# Methods for the Reconstruction of Large Scale Anisotropies of the Cosmic Ray Flux

## Abstract

In cosmic ray experiments the arrival directions, among other properties, of cosmic ray particles from detected air shower events are reconstructed. The question of uniformity in the distribution of arrival directions is of large importance for models that try to explain cosmic radiation. In this thesis, methods for the reconstruction of parameters of a dipole-like flux distribution of cosmic rays from a set of recorded air shower events are studied. Different methods are presented and examined by means of detailed Monte Carlo simulations. Particular focus is put on the implications of spurious experimental effects. Modifications of existing methods and new methods are proposed. The main goal of this thesis is the development of the horizontal Rayleigh analysis method. Unlike other methods, this method is based on the analysis of local viewing directions instead of global sidereal directions. As a result, the symmetries of the experimental setup can be better utilised. The calculation of the sky coverage (exposure function) is not necessary in this analysis. The performance of the method is tested by means of further Monte Carlo simulations. The new method performs similarly good or only marginally worse than established methods in case of ideal measurement conditions. However, the simulation of certain experimental effects can cause substantial misestimations of the dipole parameters by the established methods, whereas the new method produces no systematic deviations. The invulnerability to certain effects offers additional advantages, as certain data selection cuts become dispensable.

## Zusammenfassung

In Experimenten zur kosmischen Strahlung werden, neben anderen Eigenschaften, die Ankunftsrichtungen von Teilchen der kosmischen Strahlung von detektierten Luftschauer-Ereignissen rekonstruiert. Die Frage der Gleichverteilung der Ankunftsrichtungen ist von entscheidender Bedeutung für die Modelle zur Erklärung kosmischer Strahlung. Gegenstand dieser Arbeit sind Methoden zur Rekonstruktion von Parametern einer dipolartigen Flussverteilung kosmischer Strahlung aus einem Satz aufgezeichneter Luftschauer-Ereignisse. Verschiedene Methoden werden vorgestellt und mittels detaillierter Monte Carlo Simulationsstudien untersucht. Besonderes Augenmerk wird auf die Auswirkungen störender experimenteller Effekte gerichtet. Es werden Modifikationen der existierenden Methoden und neue Methoden vorgeschlagen. Das Hauptziel dieser Arbeit ist die Entwicklung der horizontalen Rayleigh Analysemethode. Im Gegensatz zu anderen Methoden basiert diese Methode auf der Analyse lokaler Blickrichtungen anstatt globaler siderischer Richtungen. Dadurch können die Symmetrien des Experimentaufbaus besser ausgenutzt werden. Eine Berechnung der Himmelsabdeckung ist zur Durchführung dieser Analyse nicht erforderlich. Anhand weiterer Monte Carlo Simulationen wird die Leistungsfähigkeit der neuen Methode erprobt. Im Falle idealer Messbedingungen ist die neue Methode ähnlich gut oder nur unwesentlich schlechter als etablierte Analysemethoden. Die Simulation bestimmter experimenteller Effekte kann jedoch massive Fehler bei der Einschätzung der Dipolparameter durch die etablierten Methoden hervorrufen, wohingegen die neue Methode keine systematischen Abweichungen hervorruft. Die fehlende Anfälligkeit für bestimmte Effekte bringt weitere Vorteile mit sich. So kann bei der Analyse auf bestimmte Datenschnitte verzichtet werden.

# Contents

*"And the more I see, the more I know.*
*The more I know, the less I understand."*

*Paul Weller — The Changingman*

# Chapter 1

# Introduction

Almost a century has passed since the experiments of Victor Hess in 1912, which marked the beginnings of cosmic ray physics. At the time when Hess undertook his balloon flights to measure the intensity of the ambient ionising radiation at higher altitudes, it was commonly assumed that the origin of that radiation was the Earth's crust with its natural radioactive materials. However, Hess' results suggested that the Earth is also hit by ionising radiation from above, thus from the cosmos. Since then substantial advances have been made in the field of cosmic ray physics, as well as in particle physics and cosmology. Many experiments have been conducted, from the early coincidence measurements carried out by Kolhörster and later by Pierre Auger, to the large area Pierre Auger Observatory in Argentina, that collects a considerable amount of statistics even for the highest primary energies.

But still, many of the most essential questions have not been resolved yet. There is the question of the origin of cosmic rays. What astronomical object or mechanism is able to boost single atomic nuclei to macroscopic energies? Models exist that suggest answers: most prominently the emission of particles by supernova remnants, and the acceleration in magnetic shock fronts. Owing to their charged nature, the particles of the cosmic radiation are subject to deflection in the magnetic fields in our Galaxy. As a result, the tracks of the particles through our atmosphere do not point back to their sources. Since the emergence and the evolution of what is detected as cosmic radiation on Earth cannot be observed directly, scientists can only try to form a consistent model from measurements that can be obtained through experimental observation. One of these measurements is the energy spectrum of cosmic rays, another one is the elemental composition.

Last but not least, there is the issue of the isotropy of cosmic radiation. Current models suggest that, despite the fact, that the particles have lost their individual directional information, the cosmic rays collectively expose a large scale structure in the distribution of their arrival directions. At low particle energies, the deflection radii are so small, that the cosmic rays are diffusely contained in the Galaxy. With higher energies, the deflection radii become larger and a certain fraction of the cosmic rays escapes from the Galaxy. This leakage effect results in a non-uniformity of the distribution of arrival directions. The distribution has a significant dipole moment, as cosmic rays are more likely to arrive from the direction of the Galactic centre than from the opposite direction.

Extracting this large scale structure from experimental data is not a trivial task: cosmic ray experiments only see a certain part of the sky at a time, which moves along as the Earth rotates around its axis. The sought-after large scale structure would be revealed by a rather small variation of the measurement rate between one side of the sky and the opposite side. However, these two sides are never seen by the experiment at the same time, but half a day

apart. Unfortunately, the experimental conditions are also subject to variations. For instance, the atmospheric temperature is certainly not constant on a scale of twelve hours. The changing experimental conditions generally have greater impact on the measurement rate than the anisotropy of the cosmic ray flux. This is a fundamental problem, that the analysis methods have to tackle.

The aim of this thesis is to explain, discuss and test various methods for this analysis. The thesis features established methods, but also proposes new ones. The central achievement shall be the development of the "horizontal Rayleigh analysis method", which will offer important advantages compared with established methods.

## Outline of this Thesis

Two additional introductory chapters will follow this chapter:

- Chapter 2 will cover the topic of cosmic rays, with a special focus on the question of anisotropy, and the extensive air showers in the Earth's atmosphere, that are induced by cosmic rays, and

- Chapter 3 will contain explanations of the coordinate systems used in this thesis.

The next three chapters will feature an in-depth discussion of data analysis methods and concepts regarding dipole anisotropies:

- in Chapter 4, several established methods for dipole reconstruction will be presented, their properties will be explained and some of their implications discussed,

- Chapter 5 will contain the results of extensive Monte Carlo simulation studies for benchmarking the performance of the various available methods, and

- in Chapter 6, new methods for dipole reconstruction will be proposed and their pontential will be assessed by means of Monte Carlo simulations.

And finally,

- Chapter 7 will contain a summary of the findings and conclusions.

# Chapter 2

# Cosmic Rays

The term "cosmic rays" refers to the flux of high energy charged particles which constantly hit the Earth's atmosphere from the cosmos. More precisely, the term denotes the flux of ionised nuclei, ranging from hydrogen to iron, but also electrons and positrons. Sometimes, high energy photons are also considered part of what is referred to as cosmic rays. They are uncharged, but the reactions they induce in the Earth's atmosphere are very similar to those induced by light charged particles.

The systematic investigation of cosmic rays dates back to the year 1912, when Victor Hess, equipped with a gold leaf electroscope as radiation counter, undertook balloon flights and observed that the amount of radiation increased as he reached higher altitudes. The conclusion was, that the radiation was coming from outer space [Hes1912]. The energies of the cosmic ray particles range from few GeV to at least $10^{11}$ GeV, thus spanning more than ten orders of magnitude. The flux decreases with energy, from thousands of particles per square metre and second in the GeV range to less than one particle per square kilometre and century at the upper range of energies.

Direct measurements of cosmic rays by means of balloon and satellite experiments are only feasible up to energies of about $10^{14}$ eV, as the sensitive area of such experiments is very limited. For higher primary energies, the particle flux is too low to collect sufficient statistics during the lifetime of an experiment. Ground based experiments can occupy large areas and can be run for a long time, but they are unable to measure cosmic ray particles directly, because the particles interact with the atoms of the Earth's atmosphere. Through inelastic scattering, secondary particles are created, which again interact with the atmosphere. The cascade of particles created in this process is called an "extensive air shower".

## 2.1 Energy Spectrum

The energy spectrum of cosmic rays is shown in Figure 2.1. It spans about ten orders of magnitude in energy and 30 orders of magnitude in flux. With good precision, it can be described by a power law:

$$\frac{\mathrm{d}I}{\mathrm{d}E} \propto E^{-\gamma},$$ (2.1)

where $I$ is the flux (particles per time, area and solid angle), $E$ denotes the energy, and $\gamma$ is the spectral index. The energy spectrum is almost featureless, except for changes of the spectral index at certain energies. The spectral index $\gamma$ is approximately 2.7 at low energies. A steepening of the spectrum, thus an even more rapid decrease of flux with energy, comes into effect at an energy of approximately $4 \times 10^6$ GeV. At this energy the spectral index changes from
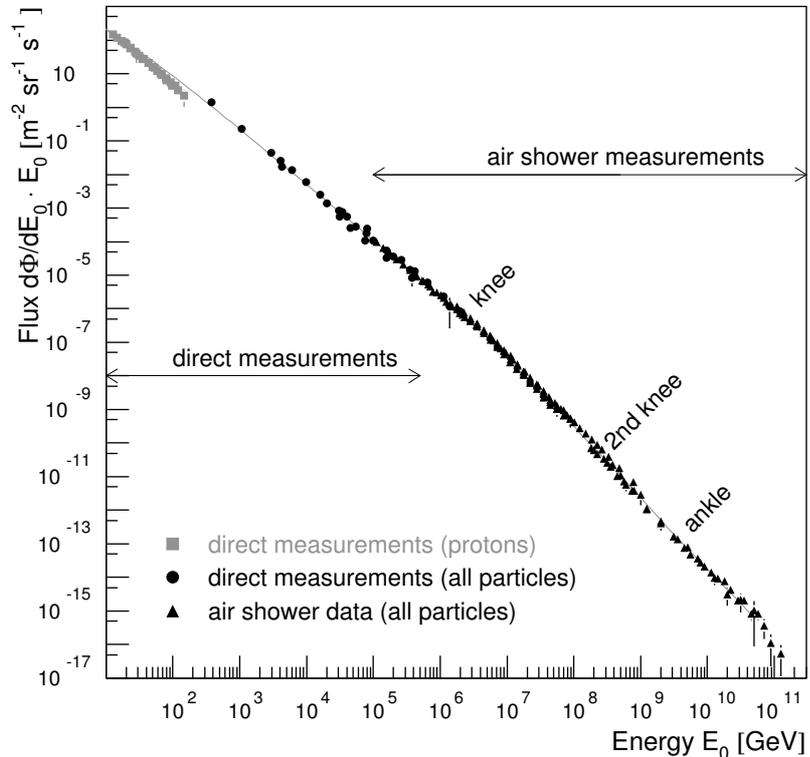
**Figure 2.1:** Energy spectrum of cosmic rays [Blu09]. Differential flux as a function of particle energy $E_0$, multiplied with $E_0$ for better visualisation.

2.7 to 3.1. This feature of the spectrum is called the "knee". At energies around $4 \times 10^8$ GeV, there appears to be a further steepening of the spectrum, a "second knee", with $\gamma$ reaching a value of about 3.3. At $4 \times 10^9$ GeV, a flattening of the spectrum is observed, with the spectral index decreasing to a value of about 2.7, which is commonly referred to as the "ankle" of the cosmic ray energy spectrum [Blu09].

The interpretation of these features of the energy spectrum is still the subject of scientific discussion. Experimental results of the KASCADE experiment [Ant03] suggest, that the knee at $4 \times 10^6$ GeV is caused by a decreasing contribution of the light elements [Ant05]. The mass composition at higher energies above the knee has not yet been exhaustively determined. A purely phenomenological model, that assumes a sequential decrease of heavier elements, at energies proportional to their charge, seems to match experimental data well. In this model, the second knee marks the end of the vanishing contributions by the stable elements [Hoe03]. Different kinds of explanations for the presence of the knee feature are discussed in literature [Hoe04]: the knee could mark the maximum energy achievable through the acceleration mechanism in the Galaxy, it could be the effect of leakage of particles from the Galaxy, it could be caused by interactions of the cosmic rays with background particles (photons, neutrinos), or it could be not a feature of the cosmic radiation at all, but put forth by the shower development in the Earth's atmosphere instead, through the creation of heavy exotic particles.

There exist different ideas to explain the energy spectrum in the range above the knee. The ankle could mark the transition from galactic to extra-galactic cosmic rays [Wib05]. The energy range up to the ankle would be attributed to acceleration in the shock waves of exploding supernovae in the Galaxy. At the ankle energy, the flux of extra-galactic protons, originating from powerful radio galaxies, would become dominant [Bie97]. However, the model of diffusive shock acceleration alone yields too low fluxes at several times $10^8$ GeV, as compared

with the accurate measurements available in this range, when it is fitted with the KASCADE results in the knee region [Hil05]. The additional flux would have to be the result of sources or acceleration processes in the Galaxy, that have not been accounted for, or it would have to be of extra-galactic origin. There are models that propose the latter, which implies, that the transition from galactic to extra-galactic cosmic rays gradually takes place in the energy region of the second knee [Ber06].

The energy spectrum of cosmic rays is expected to be suppressed above $6 \times 10^{10}$ GeV. The suppression, sometimes referred to as cut-off, is due to the interaction of the cosmic ray particles with the photons of the cosmic microwave background. This effect was predicted by Greisen and independently by Zatsepin and Kuzmin in 1966, and hence it is called the GZK limit [Gre66, Zat66]. At this energy, the center-of-mass energy of a background photon and a cosmic ray nucleon exceeds the threshold for photo-pion production [Hil85]. Accidentally, photodisintegration of nuclei leads to a flux suppression with a similar energy threshold [Ste99]. The predictions seem to be confirmed by data from the Fly's Eye [Bir94], HiRes [Abr08b] and Auger [Abb08a] experiments. The data of the AGASA experiment appear to be in contradiction to the GZK cut-off hypothesis, as too many super-GZK particles were detected [Shi06]. However, taking the systematic uncertainty of the primary energy estimation into account, the discrepancy could indeed be insignificant [DM03] (see also the references in [Blu09]).

In summary, the energy spectrum of cosmic rays has been determined by a variety of experiments. At lower energies, up to the knee, the sources of cosmic rays are considered to be in the local Galaxy. The model of diffusive shock acceleration can explain the overall shape of the spectrum. For the highest energies, the sources are considered to be extra-galactic. Evidence for the validity of the theoretical predictions concerning the interactions of cosmic ray particles with the cosmic microwave background has been found recently. However, there is no generally accepted model for the energy range between the knee and the ankle. It has not yet been found out, at what energy the transition from galactic to extra-galactic sources takes place. The determination of the elemental composition in this energy range can yield valuable information. The flux of galactic cosmic rays is considered to be dominated by heavy elements, whereas the extra-galactic particles are believed to be mainly protons. The knowledge of the distribution of arrival directions may be equally revealing, which shall be the subject of the next section.

## 2.2   Distribution of Arrival Directions

The question of the distribution of the cosmic rays' arrival directions being isotropic or not involves two different aspects. On the small scale, local variations of the cosmic ray intensity, such as hot spots, would suggest the existence of distinct sources or acceleration regions. However, the nature of cosmic rays, being charged particles and hence being subject to deflection by the magnetic fields in the Galaxy, renders the idea of cosmic ray astronomy difficult. Except for the highest primary energies, the particles lose virtually all of their directional information while travelling through the Galaxy. The second aspect is the large scale isotropy, raising the question of whether the cosmic ray flux reveals structures spanning the whole of the sky, such as a dipole.

The angular scale, down to which structures can be resolved in the cosmic ray flux, depends on the energies of the cosmic rays and the distance to their origin. The deflection of cosmic ray particles is characterised by the gyroradius, or Larmor radius, which can be calculated
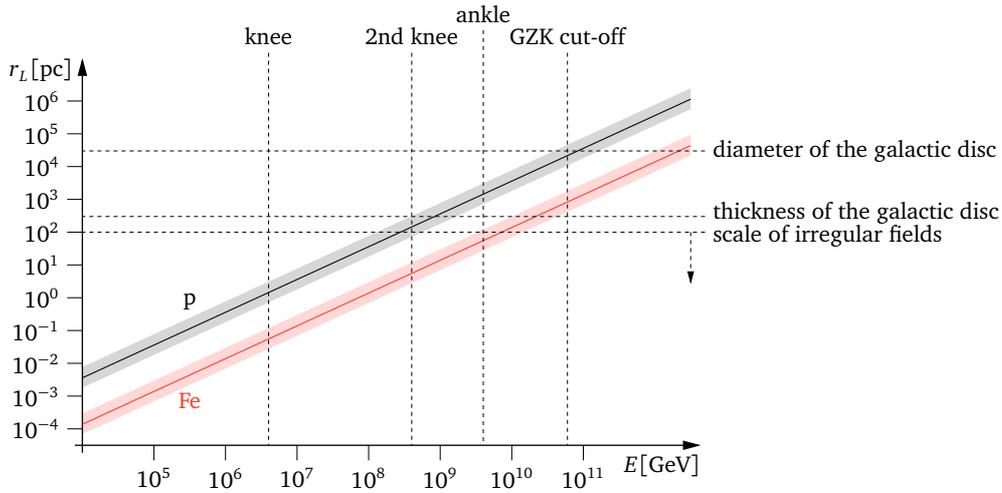
**Figure 2.2:** Gyroradii of protons and iron nuclei as a function of energy: magnetic fields of $3\,\mu G$ (solid lines), $1.4\,\mu G$ (upper edges of shaded areas) or $6\,\mu G$ (lower edges) were assumed.

according to:

$$r_L = \frac{p_\perp}{|q| \cdot B} \approx 1.08\,\mathrm{pc} \cdot \frac{E/(10^6\,\mathrm{GeV})}{Z \cdot B/\mu G}\,, \tag{2.2}$$

with $q$ denoting the charge of the particle, $B$ denoting the magnetic field strength, and $p_\perp$ denoting the component of the particle's momentum perpendicular to the magnetic field. The first equality can be easily derived by identifying the centripetal force, that keeps the particle on a circular path, with the Lorentz force, that the particle is subjected to in the surrounding magnetic field. The final approximation assumes the ultra-relativistic case, where $p = E \cdot c$, assuming the orientation of the magnetic field being perpendicular to the direction of the particle motion. ($E$ is the energy of the cosmic ray, $Z$ is the charge in units of the elementary charge, and $c$ is the speed of light.) If the magnetic field happens to be perpendicular to the particle's momentum, the particle is deflected onto a circular path. Otherwise, the particle follows a spiralling path, with a spiral radius smaller than the one given by the equation above, as only the energy of the perpendicular motion has to be considered. Figure 2.2 illustrates the relation between particle energy and Larmor radius.

In the majority of cases, the nature of the magnetic field is not known well enough to precisely reconstruct the motion of the cosmic ray. Rather, the above equation shall give a scale for the deflection of cosmic rays. If the Larmor radius at a given energy is of the same order as the dimension of a region with constant magnetic field, then particles of that energy are diffusely contained in that region. If high energy particles have a Larmor radius much larger than the coherence length of the magnetic fields they traverse, their directional information is maintained to a good degree.

To relate a particle energy to a Larmor radius, the magnitude of the magnetic field has to be known. The magnetic fields in the Galaxy are still under debate. Among the techniques for the determination of the galactic magnetic field are the measurement of starlight polarisation by interstellar dust and the measurement of the Zeeman splitting of radio spectral lines. Either method depends on model assumptions for the matter density, and so the conclusions drawn from available methods have been subject to changes over the past years. While the best estimation fifteen years ago suggested a local field strength of $1.4\,\mu G$ [Hei95] (a value often found in literature), recent publications tend to report larger values around $6\,\mu G$ [Bec09]. The

local field near the Sun is a superposition of a regular and turbulent (irregular) magnetic fields. The regular component is reported to increase exponentially towards the galactic center. The strength of this large scale field is currently estimated as $2.1\,\mu$G in the vicinity of the Sun. There is no consensus about the field strength in the galactic centre. It might reach the order of mG, or only tens of $\mu$G [Han09]. The field lines are expected to follow the direction of the spiral arms [Hei96, Sof86].

### 2.2.1 Small Scale Anisotropy

The resolution of small structures is only possible at high cosmic ray energies. The Larmor radius of a cosmic ray particle at $10^{10}\,$GeV is of the order of a few kilo parsec, which is much larger than the scale length of the random component of the galactic magnetic field. Such a particle would retain much of its directional information, and so the arrival direction, with which it is observed on Earth, points approximately back to the source region. The effect of deflection by the regular component of the galactic magnetic field cannot be completely neglected. However, it may be possible to apply corrections to the observed arrival directions, based on the knowledge of the large scale galactic magnetic field. On the other hand, the galactic magnetic field could be probed with ultra-high energy cosmic rays, if their source can be identified by correlation with known powerful astrophysical sources [Sta97].

One class of candidates as sources for ultra-high energy cosmic rays are active galactic nuclei (AGNs). The Pierre Auger Collaboration has found evidence for this hypothesis [Aug07, Abr08a]. Cosmic rays with and energy above $5.7 \times 10^{10}\,$GeV were found to be correlated with a selection of AGN sources at 99% confidence level. However, the correlation could not be confirmed by the HiRes collaboration using the parameters prescribed by the Pierre Auger Collaboration [Abb08b]. It remains to be seen, whether the finding of the Pierre Auger Collaboration was a random coincidence or a true correlation.

With more statistics becoming available at the highest energies, the search for point sources has certainly become very promising. The identification of the sources of the highest energy cosmic rays would be a breakthrough, and could mark the beginning of the new field of cosmic ray astronomy. However, further discussion of this topic is beyond the scope of this thesis.

### 2.2.2 Large Scale Anisotropy

At the lower end of the energy spectrum, cosmic rays are highly isotropic. Interstellar magnetic fields, regular and stochastic, isotropise the distribution of arrival directions. The Larmor radius of cosmic rays around the knee region is of the order of one parsec in the case of protons. Heavier nuclei have even smaller radii. Thus, the flux of cosmic rays in this energy regime is diffusive. However, leakage from the Galaxy introduces a certain anisotropy, which should generally become more pronounced with higher energy. This is a distinctive feature of galactic cosmic rays. The anisotropy evolving at higher energies should favour arrival directions from the galactic plane, as long as these particles are of galactic origin. Particles from extra-galactic sources should not have arrival directions that correlate with galactic features. They are expected to be isotropic [Hil84].

The magnitude of the anisotropy of galactic cosmic rays is predicted by the models that describe sources, acceleration and propagation of cosmic rays in the Galaxy. The current standard model, based on diffusive shock acceleration, however, predicts notably too high anisotropy amplitudes. These models assume, that galactic sources emit cosmic rays with an energy spectrum proportional to $E^{-2.1}$. However, the locally observed spectrum is proportional to $E^{-2.7}$. The large difference is accounted for in the model by a rapid outflow of particles

from the Galaxy at very high energies [Hil05]. This would result in a noticeable large scale anisotropy, which has not been observed until now. The reason for the remarkable isotropy of galactic cosmic rays could be a small diffusion coefficient in the Local Bubble, where the Sun is located. As a result, cosmic rays would be isotropised in the local vicinity of the Sun. Thus, the observed low anisotropy does not necessarily rule out the diffusive shock acceleration model [Zir05].

Another effect, that causes an anisotropic distribution of arrival directions, is the Compton-Getting effect [Com1935]. It is caused by the motion of the Solar System around the galactic centre, through the interstellar medium, which is considered to be the rest frame of galactic cosmic rays. It yields a small excess in the direction of motion, and a deficit in the opposite direction. The Compton-Getting effect produces a dipolar anisotropy with an amplitude of ca. 0.04% [Str07].

In the following, a brief overview of important experimental on large scale anisotropy searches shall be given.

The Milagro Collaboration analysed seven years' worth of data, comprising 95 billion events with a median energy of $6 \times 10^3$ GeV. The dominant feature is a deficit of about 0.25% in the direction of the Galactic North Pole. In terms of the first harmonic in sidereal time, an anisotropy amplitude of 0.04% was found, with a phase $\alpha = 104°$ [Abd09]. The data can be interpreted as a dipole anisotropy, pointing to a well defined direction in the North Galactic hemisphere. The deficit could also be caused by local magnetic fields [Bat09].

The Super-Kamiokande Collaboration analysed more than 250 million downward muon events, taken from June 1996 until May 2001, induced by cosmic rays with a median energy of $10^4$ GeV. A variation of the cosmic ray flux along the right ascension coordinate with an amplitude of $(6.64 \pm 0.98\text{stat} \pm 0.55\text{syst}) \times 10^{-4}$ was found, with the excess at $\alpha = 33.2° \pm 8.2°\text{stat} \pm 5.1°\text{syst}$ [Gui07].

The Tibet AS$\gamma$ Collaboration analysed 30 billion events in the energy range between $10^3$ and $10^5$ GeV, taken from 1999 until 2003. The sidereal daily variation showed an excess around 4–7 a.m. sidereal time and a deficit around 12 p.m.. In terms of the first harmonic, a primary energy dependent phase between $-20°$ and $24°$ was obtained, with amplitudes between 0.054% and 0.113% [Ame05].

The Large Area Air Shower (LAAS) group collected about 12.5 million events in the energy range between $5 \times 10^4$ GeV and $10^6$ GeV. The first harmonic of the right ascension distribution was found to have an amplitude of ca. 0.23%, the excess being located at $\alpha = 6°$ [Tad06].

The EAS-TOP collaboration performed an analysis of 1.3 billion events in the energy range around $2 \times 10^5$ GeV. The first harmonic in sidereal time showed an excess at $\alpha = 27°$ with an amplitude of approximately 0.037% [Agl96].

The KASCADE Collaboration analysed a data set containing 100 million showers in the energy range between $7 \times 10^5$ GeV and $6 \times 10^6$ GeV. No evidence for anisotropy was seen: neither in the complete data set, nor in subsets enriched with light or heavy primaries. Limits for the right ascension variation amplitude were set. At the lower boundary of the energy range the limit is 0.1%, at the upper boundary the limit is 1% [Ant04].

The KASCADE-Grande Collaboration performed an analysis of a data set with 2.8 million events, in subsets with different ranges of estimated primary energy between $10^{6.7}$ GeV and $10^{8.3}$ GeV, using different methods. The amplitude of the variation in the right ascension distribution was found to range between 0.1% at low energies and 10% at high energies. The phases in the different energy bins showed no common tendency, which suggests, that the anisotropy signals found are not significant. Methods for three-dimensional reconstruction of the dipole mainly yielded dipole vectors pointing very close to the Earth's North Pole. The

results for the highest energy bins pointed less far towards North, but were derived from relatively small data sets [Stu07].

The AGASA Collaboration found a 4% amplitude in the energy bin above $10^9$ GeV, which contained 27,600 events, with the excess at $\alpha = 293°$. In a three-dimensional analysis, a $4\sigma$ excess near the galactic centre was found [Hay99].

The Pierre Auger Collaboration could not confirm the findings of the AGASA experiment. About 70,000 events with primary energies above $10^9$ GeV were analysed, and the results were compatible with the isotropy hypothesis [Arm08].

To summarise, low, but very significant anisotropy amplitudes in the sub-percent range could be found by experiments taking data at lower primary energies. With the exception of the AGASA experiment, no significant hints for an anisotropy could be found in the higher range of primary energies. Owing to the steeply falling energy spectrum, the decrease of available statistics with energy is more rapid than the increase of the anisotropy. Additionally, the transition from galactic to extra-galactic sources could lead to even smaller amplitudes at high energies. At this point, the degree of isotropy of the distribution of arrival directions cannot conclusively be determined in the energy range around and above the knee.

## 2.3   Detection Techniques at High Energy

Cosmic rays at energies above $10^5$ GeV are measured indirectly through the detection of extensive air showers they initiate in the Earth's atmosphere. An air shower consists of three components: the electromagnetic, the hadronic and the muonic component. The primary particle, being a nucleus, establishes the hadronic component with the first interaction, which typically takes place in an altitude between 15 km and 20 km above sea level. The hadronic component consists of baryons, mesons and core fragments. Most of the particles created in hadronic interactions are charged and neutral pions. Almost 100% of the charged pions at low energy decay to muons and neutrinos and thereby feed the muonic component of the air shower. Neutral pions decay in 98.8% of the cases to two photons, which initiate the electromagnetic component. Highly energetic photons from the decay of neutral pions initiate electromagnetic cascades of pair production and bremsstrahlung processes. These processes take place alternatingly and cause an exponential increase of the number of electrons and photons with time, as long as the mean electron energy exceeds a critical energy (84.2 MeV for electrons in air), at which the energy loss due to ionisation begins to dominate over the radiation loss. The muons produced in decays of charged pions do almost not interact with the atmosphere, as muons barely lose energy in bremsstrahlung processes due to their larger mass.

The depth of the Earth's atmosphere amounts to approximately $1,000$ g/cm$^2$. When comparing this number with the radiation length in air of $37.1$ g/cm$^2$, and with the atmospheric attenuation lengths of hadrons ($120$ g/cm$^2$ for nucleons, $160$ g/cm$^2$ for pions, $180$ g/cm$^2$ for kaons), it is obvious that almost no primary cosmic ray particle reaches sea level. The penetration depths of the avalanche of secondary particles depends on the primary energy. The cascade processes induced by primary particles with energies lower than $10^4$ GeV die out before reaching sea level in the majority of cases, whereas the extended air showers of primary particles with energies above $10^7$ GeV typically contain millions of secondary particles that reach ground level. (For references, see e.g. [Gai90, Rao98, Gru00].)

The measurement of extensive air showers can make use of a variety of techniques: relativistic particles create Cherenkov photons in the atmosphere, or they excite atoms, which then emit fluorescence light. Particles reaching ground level can be detected by means of scin-
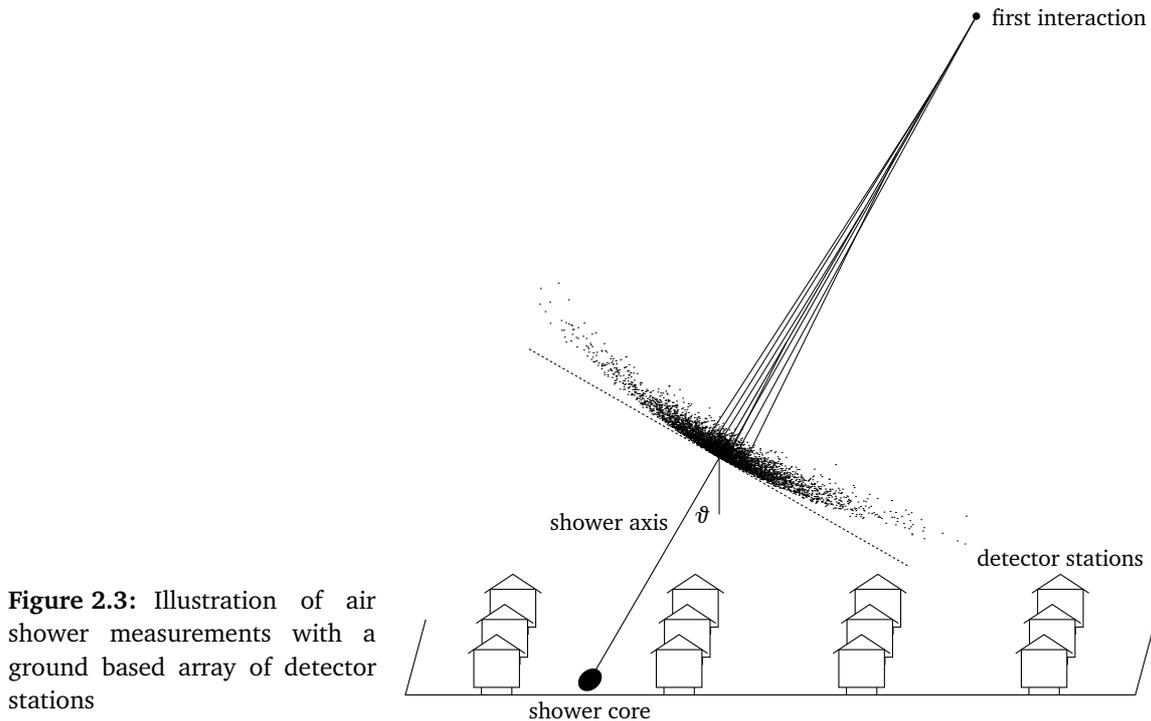
**Figure 2.3:** Illustration of air shower measurements with a ground based array of detector stations

tillators, Cherenkov detectors (e.g. employing water tanks), calorimeters or wire chambers. Figure 2.3 illustrates the detection of an extensive air shower with a ground based array of detector stations. The prolongation of the track of the primary particle is called the shower axis. The position of the shower core, i.e. the intersection point of the shower axis and the ground plane, can be reconstructed from recorded data through evaluation of the energy deposits in the individual stations. The zenith angle $\vartheta$, i.e. the shower inclination, and the azimuth angle $\varphi$ (corresponding to the compass direction, not shown in the figure) can be determined through a geometrical reconstruction of the shower disc from the relative timings of the detector signals.

The typical angular resolution of the arrival direction reconstruction of air shower experiments is in the range of a few or even below one degree. E.g. the Pierre Auger Obervatory [Abr04] quotes its angular resolution as about 0.5° for air shower events that are jointly reconstructed by the fluorescence detectors and the surface array, and as better than 2.2° for events that are detected by only three surface detector stations. Events that trigger six or more surface detectors can be reconstructed with an accuracy better than 1° [Bon09]. The KASCADE experiment, with its dense placement of detector stations, provides an angular resolution of better than 0.8°. Showers with more than $10^5$ electrons at observation level can be reconstructed with an angular resolution of ca. 0.2°. The resolution depends only mildly on the shower inclination [Mai04].

The experimental conditions are subject to continuous variations. Barometric pressure, temperature and density can influence the shower development, the reconstruction of shower properties and can shift trigger thresholds. This has only moderate consequences for the search for small scale anisotropies. The potential sources are always seen together with their surroundings. A significant excess in flux within a defined, small angular region results in higher counting rates for that region as compared to its environment. Atmospheric variations will effect the particular source candidate region as well as its surrounding region within the current field of view. Large scale structures, on the other hand, span the whole sky, of which

only a part can be seen at a time. Excess and deficit regions are never seen simultaneously. An isotropy amplitude of the order of one percent is easily superimposed by variations of the measurement rate due to experimental effects of the same or much higher order.

The Pierre Auger Collaboration has investigated the impact of changing atmospheric conditions. On a seasonal scale, variations of the order of 10% were observed. Variations during a day led to variations of 2% on average. The modulation can be related to atmospheric parameters, so that the effects can partially be corrected for [Abr09]. However, atmospheric properties can change in a variety of ways, and not all of them can be monitored. It is probably impossible to fully account for all kinds of experimental effects. The impact of these systematic effects begin to outweigh the statistical uncertainties. As a consequence, the accuracy of anisotropy analyses is limited by the knowledge of systematic effects, more than by the amount of statistics avaliable. It is desirable to find analysis methods, that are insensitive to these systematic uncertainties. The assessment of available methods for the analysis of large scale anisotropies, and the development of new ones, shall be the subject of the following chapters.

# Chapter 3

# Coordinate Systems

## 3.1 Spherical Coordinates

A direction in three dimensional space, such as the arrival direction of a cosmic ray particle at the location of an experiment, is mathematically represented by a three dimensional unit vector. The vector reaches from the origin of the coordinate system to a point on the unit sphere. While the vector generally extends in three dimensions, its length is fixed, which eliminates one degree of freedom. The remaining two degrees of freedom are usually specified by means of two angles. Since the problem of describing a location on the unit sphere matches the problem of describing a geographical location on Earth, it is practical to adopt the geographical terminology. Thus, the x-y-plane and the z-axis of the coordinate system are called the equatorial plane and the polar axis, respectively. The aforementioned angles can be chosen to correspond to latitude and longitude. The latitude is defined as the angle that a given unit vector and its projection onto the equatorial plane enclose, while the longitude denotes the angle between that projection and the positive x-axis. As a consequence of this definition, latitude values are contained in the range between $-\pi/2$ and $\pi/2$, whereas longitude values range between 0 and $2\pi$. The following definition of a unit vector shall be consistently used in this thesis:

$$\hat{e}(\beta, \lambda) = \begin{pmatrix} \cos\beta \cos\lambda \\ \cos\beta \sin\lambda \\ \sin\beta \end{pmatrix}, \tag{3.1}$$

with $\beta$ being the latitude-like component and $\lambda$ being the longitude-like component. The solid angle element is then given by:

$$d\Omega = \cos\beta \, d\beta \, d\lambda. \tag{3.2}$$

## 3.2 The Celestial Sphere

While the purpose of the geographical, or terrestrial, coordinate system with its latitude $\beta$ and longitude $\lambda$ is to specify places on Earth, a coordinate systems for describing points in the sky also needs be defined. When observing astronomical objects like stars or galaxies, there is no apparent way to measure their distance from Earth. From this fact evolved the concept of the celestial sphere. The celestial sphere is an imaginary sphere of infinite radius, with the Earth at its centre point. Now, all astronomical objects are thought to lie on this imaginary sphere. From this point, the distances of those objects are not taken into consideration anymore, but only the directions from which they appear. In order to do so, a coordinate system on the
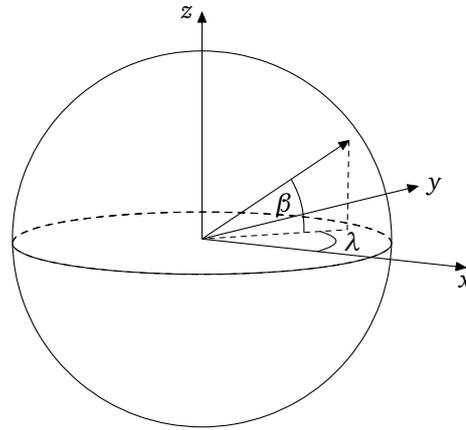
**Figure 3.1:** Definition of the unit vector: the latitude-like angle $\beta$ is measured from the equatorial plane.
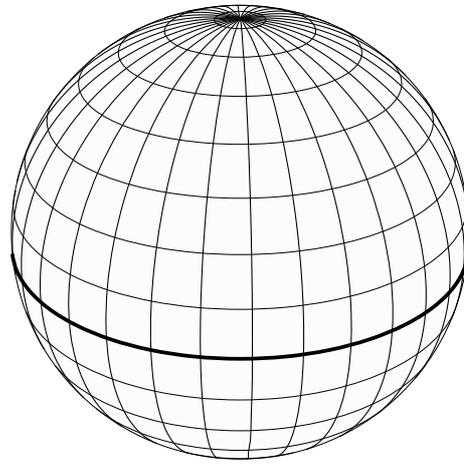


**Figure 3.2:** Spherical coordinate system: latitude circles lie in planes that are parallel to each other. Only one latitude circle is a great circle, which is the equator (thick line). Longitude circles are great circles, that all coincide in both North and South poles of the coordinate system.

celestial sphere is defined. In fact, there exist several such definitions. Some are bound to an observer on Earth, providing constant coordinates for fixed viewing directions. Others are bound to the sky and maintain constant coordinates for the fix stars.

Because of the celestial sphere's arbitrary large radius, not only the Earth but the whole solar system virtually concentrates in a single point in the centre of the sphere, which effectively renders both the position of the observer on Earth and the seasonal motion of the Earth around the Sun meaningless with regard to parallax effects. This obviously only holds true for the observation of remote astronomical objects, for which the approximation of infinite distances is valid. However, for close-by objects such as the Sun, the Moon and the planets of our solar system, the situation is much more complicated. The calculation of neither their actual positions nor their representations in celestial coordinates are trivial. However, such nearby objects shall remain out of consideration, as they are not suitable sources of the high energy cosmic rays that are subject of this thesis.

While parallax effects are irrelevant, the observer's location on Earth does still enter the calculation, as it determines the field of view. It is due to the Earth orbitting the Sun that the Earth in fact performs 366.24 revolutions during one astronomical year of 365.24 days (more precisely, solar days). Thus, the Earth's rotation around the Sun adds up to the rotation around its axis and results in one additional revolution every year. Therefore, one full revolution of the Earth with respect to the celestial sphere lasts shorter than one solar day, namely only one sidereal day, corresponding to 23 hours, 56 minutes and 4.1 seconds in solar time.
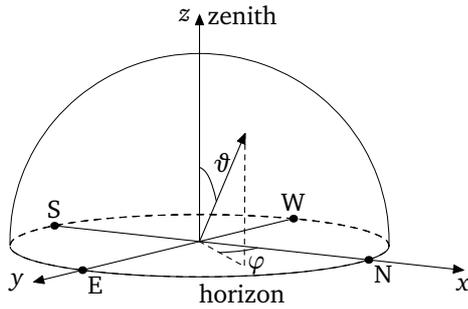
**Figure 3.3:** Horizontal coordinate system: the horizontal plane corresponds to the ground plane at the location of the observer. The zenith denotes the direction straight from above. The azimuth angle specifies the compass direction.

## 3.3 Horizontal Coordinates

The horizontal coordinate system relates points on the celestial sphere with viewing directions for an observer on Earth. The horizontal coordinates of a specific astronomical object therefore depend on the location of the observer, as well as on the time of the observation. The local horizon, i.e. a tangential plane touching Earth at the place of the observer, corresponds to the equatorial plane of this spherical coordinate system. The latitude-like component is the altitude $a$. Points with an altitude of 0 lie on the horizon, whereas an altitude of $\pi/2$ marks the direction straight from above and is called the zenith (i.e. the North Pole of this spherical coordinate system). The opposite direction, pointing down to the centre of the Earth, is called the nadir and is characterised by an altitude value of $-\pi/2$. The longitude-like component is the azimuth $\varphi$, with an azimuth of zero being defined as looking North, and then turning clockwise, i.e. through East–South–West, as the azimuth ranges from 0 to $2\pi$.

In cosmic ray experiments, horizontal coordinates are the natural choice for specifying arrival directions of cosmic rays, as reconstructed from experimental data. It has become common practice to use the zenith distance $\vartheta = \pi/2 - a$ instead of the altitude $a$, thus measuring the latitude-like angle from the zenith instead of the horizon, as this corresponds to the inclination of the cosmic ray particle with respect to the Earth's atmosphere. Systematic effects, of the detector setup as well as of the reconstruction, depend on local viewing directions rather than on the area of the sky that is being looked at. The most dominant effect emanates from the zenith angle; the more inclined a shower is, the longer is its path through the atmosphere. The shower reaches ground on average at a later stage of development when it is more inclined. It is a delicate task to rid the shower reconstruction and analysis from zenith angle dependent systematic effects, especially for experiments that solely comprise surface based detectors.

## 3.4 Equatorial Coordinates

The equatorial coordinate system aims to eliminate the dependence on the observer's time and location when describing a point on the celestial sphere. One defining feature of this system is the celestial equatorial plane, which is the projection of the Earth's equatorial plane onto the celestial sphere. Likewise, the celestial North and South poles are the intersections of the celestial sphere with the prolongation of the Earth's polar axis. As for all spherical coordinate systems, the definition of an equatorial plane alone yields the latitude-like coordinate, the declination $\delta$. In addition to the usual geometric definition of the latitude-like coordinate, being the angular distance between a given point and the equator, the declination of an astronomical object can be thought of as the geographical latitude on Earth, at which the object can appear in the zenith. E.g. all points with a declination of $-30°$ will only ever appear in the zenith in locations at $30°$ South latitude.

The longitude-like component of the equatorial coordinates is called the right ascension $\alpha$. In order to have a time independent coordinate system, the grid of equatorial coordinates on the celestial sphere does not corotate with the Earth. Thus, fixed astronomical objects retain constant declination and right ascension. Further on, in equatorial coordinates, the path of the Sun over the course of a year shapes a great-circle on the celestial sphere, which is called the ecliptic. The Earth's equator is inclined at an angle of approximately 23° to the plane of the ecliptic, and so is the celestial equator. Therefore, the Sun's path crosses the equator twice a year. The intersection point that occurs in spring, when the Sun travels from the Southern to the Northern celestial hemisphere, is called the vernal equinox. The right ascension of the vernal equinox is defined to be zero, thereby completing the definition of the equatorial coordinate system.

In cosmic ray experiments, equatorial coordinates are the natural choice for carrying out statistical analyses of arrival direction distributions. This is mainly because of the simplicity of the conversion from local viewing directions (horizontal coordinates) to equatorial coordinates; given the place of the observer, any viewing direction corresponds to a constant declination and a right ascension that uniformly traverses the range of values, increasing by $2\pi$ during one sidereal day.

## 3.5   Ecliptic Coordinates

Ecliptic coordinates are not used in this thesis, and are listed here only for completeness. The ecliptic coordinate system is obtained by skewing the equatorial system such that the ecliptic becomes the equatorial plane of the coordinate system. The components are called celestial latitude and celestial longitude. The zero point of the celestial longitude is again the vernal equinox.

## 3.6   Galactic Coordinates

The galactic coordinate system uses the projection of the plane of our Galaxy onto the celestial sphere as its equatorial plane. Thus, points on the galactical plane have a galactical latitude $b$ of 0°, with the galactic centre at a galactical longitude $l$ of 0°.

## 3.7   Precession, Nutation, Aberration and Refraction

The definitions of some of the coordinate systems given here, involve features such as the obliquity of the ecliptic and the position of the vernal equinox. These are by no means constant. Gravitational effects of the Sun and the Moon cause the precession of the Earth's axis, resulting in the equinox constantly moving Westward at a rate of about 50″ per year. By definition, such higher order effects do not affect the horizontal coordinate system, because its definition is entirely geometric and does not involve any variable properties. The conversion from horizontal coordinates to equatorial coordinates is a geometric transformation, that only depends on the observer's geographic location and the sidereal time of day. The resulting equatorial coordinates declination and right ascension, however, must be put in context with the time of the observation. Fixed astronomical objects have slowly changing equatorial coordinates owing to higher order effects. Therefore the time of the observation has to be given along with the equatorial coordinates, which is usually done by means of the astronomical epoch. An epoch defines a reference time for the equatorial coordinate system used, and is

defined as reference to the beginning of an Besselian or Julian year. Commonly used epochs are e.g. B1950.0 (the beginning of the Besselian year 1950), or nowadays especially J2000.0 (the beginning of the Julian year 2000). Given the epoch, equatorial coordinates can be converted to galactic coordinates. As the definition of the galactic coordinate system features no properties of the Earth, galactic coordinates are meant to be constant for fixed astronomical objects throughout time.

## 3.8   Conversion Between Coordinate Systems

The coordinates in different systems are converted into each other by means of rotations of the coordinate system. The rotation can either be specified by the direction of the rotational axis and the amount of rotation, or more commonly by a set of up to three angles for consecutive rotations around a given sequence of coordinate system axes. The transformation from or to the horizontal coordinate system also requires a change of sign of one of the components, because of the longitudinal component (the azimuth) being defined as turning clockwise, i.e. the mathematical negative sense.

   The conversion from equatorial coordinates (declination $\delta$, right ascension $\alpha$) to horizontal coordinates (zenith $\vartheta$, azimuth $\varphi$) can be implemented as follows: the unit vector in equatorial coordinates ($\hat{e}(\delta, \alpha)$) is first mirrored at the $xz$-plane (yielding $\hat{e}(\delta, -\alpha)$), then rotated around the $z$-axis by the angle of the local mean sidereal time plus $180°$ (yielding $\hat{e}(\delta, lmst - \alpha + \pi)$), and then rotated around the $y$-axis by an amount of $\pi/2 - \beta$, with $\beta$ being the geographical latitude of the observer. The result is the unit vector of the given direction in horizontal coordinates ($\hat{e}(\pi/2 - \vartheta, \varphi)$). The first of these three transformations is responsible for the transition from a left-handed coordinate system (horizontal coordinates), to a right-handed one (equatorial coordinates). The second transformation normalises the rotational state of the Earth with respect to the fix stars. The third transformation shifts the zenith direction to the North Pole of the coordinate system. The transformation can be written as:

$$\vec{r}^H = \hat{e}(\tfrac{\pi}{2} - \vartheta, \varphi) = \mathbf{R_y}(\tfrac{\pi}{2} - \beta)\,\hat{e}(\delta, h + \pi)$$

$$h = local\ mean\ sidereal\ time - \alpha = global\ mean\ sidereal\ time - \lambda - \alpha\,,$$

(3.3)

with $\mathbf{R_y}(\psi)$ being the matrix, that rotates the vector on the right hand side around the $y$-axis by the angle $\psi$, and $h$ being the hour angle. Accordingly, the conversion back from horizontal to equatorial coordinates can be achieved by reversing the sequence of transformations.

   The conversion from and to galactic coordinates involves a similar series of rotations. However, the angular values are not constant, but depend on the epoch, in which the equatorial coordinates are acquired. The values can be found in astronomical tables, and are not given here, as this conversion is not required in this thesis.

# Chapter 4

# Reconstruction of Large Scale Anisotropies

The arrival direction of a primary cosmic ray particle is among the properties, that are reconstructed from the data of extensive air shower experiments. The distribution of reconstructed arrival directions is affected by two distinct effects. Firstly, there are the experimental circumstances, such as geographical location and measurement times, that affect the set of recorded cosmic ray events. At any given time, cosmic ray air showers from different directions traverse the Earth's atmosphere with different inclinations. As a result, showers from certain directions are more likely to remain undetected or be discarded during reconstruction or analysis than showers from other directions, which clearly influences the resulting direction distributions. Secondly, cosmic rays may reach the Earth with a non-uniform distribution. While the latter influence is much less pronounced in recorded data sets than the experimental effects, it actually is the one of interest.

In mathematical terms, the recorded distribution is a convolution of the true distribution with a set of experimental features (field of view, measurement times, experimental efficiencies, reconstruction errors). This chapter describes methods to perform the de-convolution, thus deducing the flux distribution from the recorded arrival directions. Especially the limited field of view of a typical experiment is a challenge for the analysis, as it causes the coverage of the sky not only to be inhomogeneous, but also incomplete.

## 4.1 Flux Distributions

In order to describe a flux distribution, it is necessary to choose a parametrisation of the flux as a function of the direction. In this context, directions are specified by equatorial coordinates (declination $\delta$ and right ascension $\alpha$). The flux shall generally be described by an isotropic component and a direction dependend function representing the anisotropy:

$$\Phi(\delta, \alpha) = \Phi_0 \cdot ( \underbrace{1}_{\substack{\text{isotropic} \\ \text{component}}} + \underbrace{f(\delta, \alpha)}_{\substack{\text{anisotropic} \\ \text{component} \\ \ll 1}} ). \tag{4.1}$$

The simplest of such functions is given by the isotropy hypothesis, thus assuming a constant flux for all directions:

$$\Phi_{\text{isotropy}}(\delta, \alpha) = \Phi_0 . \tag{4.2}$$
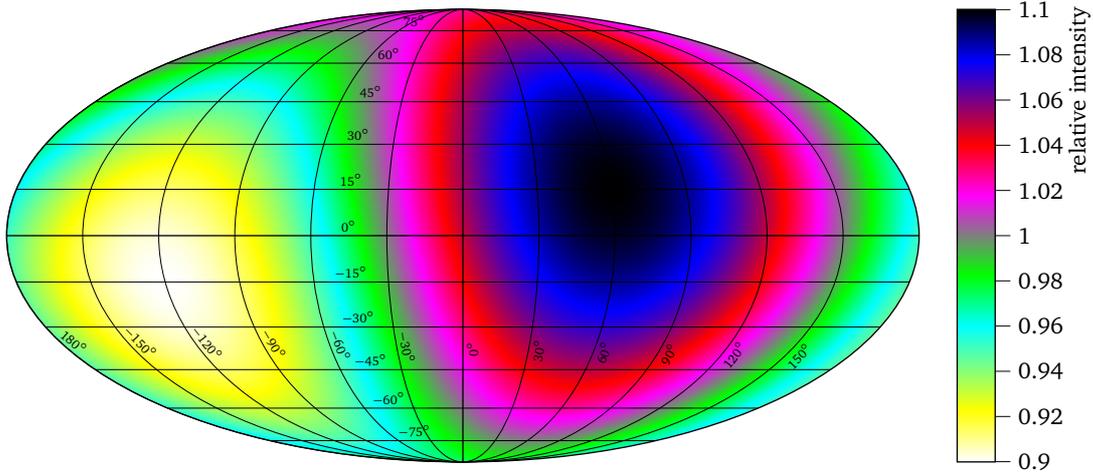
**Figure 4.1:** Example of a dipole distribution. The dipole vector points to 15° latitude and 60° longitude. The magnitude is 0.1. The Mollweide projection [Mol1805] has been used for visualisation. As features of this projection technique, latitudes are straight horizontal parallel lines, and equal solid angles are represented by equal areas in the projection.

While this model leaves apparently no room for the analysis of large scale anisotropies, it is possible to examine local deviations from the otherwise constant flux and treat them as candidates for point sources of cosmic rays. As a matter of fact, it is most common to assume an isotropic background flux for the search for point sources, as those sources should outweigh the large scale flux variations.

The most basic approach to a large scale variation of the cosmic ray flux is the assumption of a dipole:

$$\Phi_{\text{dipole}}(\delta, \alpha) = \Phi_0 \cdot \left( 1 + \hat{e}(\delta, \alpha) \cdot \vec{D} \right), \quad \vec{D} = D \cdot \hat{e}(\delta_{\text{dipole}}, \alpha_{\text{dipole}}), \tag{4.3}$$

with $\vec{D}$ being the dipole vector, defined by its magnitude $D$ and its orientation $\delta_{\text{dipole}}, \alpha_{\text{dipole}}$. ($\hat{e}$ denotes the unit vector.) The right hand side of this equation ranges from $\Phi_0(1 - D)$ to $\Phi_0(1 + D)$. It reaches its maximum value in the direction of the dipole, and its minimum in the opposite direction. An example dipole distribution is shown in Figure 4.1.

The next step towards a more precise and general description of the flux map is to introduce a quadrupole moment, then a sextupole, an octupole, and so forth. By including terms of higher and higher order, the number of parameters increases as the model resembles the recorded data set better and better, eventually leading to a full expansion in spherical harmonics. However, while it is mathematically possible to reproduce the data set precisely with such an expansion, it is questionable whether this expansion can yield valuable information on the nature of the anisotropy. The data set itself suffers from experimental inaccuracies and, much more severe, statistical fluctuations, rendering the higher order terms of the expansion virtually meaningless. The flux distribution can be expressed by means of spherical harmonics by

$$\Phi_{\text{s.h.}}(\delta, \alpha) = \Phi_0' \sum_{\ell=0}^{\infty} \sum_{m=-\ell}^{\ell} a_{\ell m} Y_{\ell m}(\delta, \alpha), \tag{4.4}$$

with $a_{\ell m}$ being the sought-after coefficients, and $Y_{\ell m}$ being the spherical harmonic functions of degree $\ell$ and order $m$. The spherical harmonic functions can be defined in different ways. The classical spherical harmonics are complex functions, but by recombining the different degrees

of one order, it is possible to obtain a modified set of spherical harmonics, that only comprises real functions, and therefore only yields real coefficients, when the function being expanded is purely real. For a full definition of the spherical harmonics used in this thesis, see Appendix A. The choice of these functions simplifies the calculations substantially. Firstly, the absence of complex numbers renders complex conjugation unnecessary. Secondly, the following identity is valid:

$$\hat{e}(\delta, \alpha) = \begin{pmatrix} \cos\delta\cos\alpha \\ \cos\delta\sin\alpha \\ \sin\delta \end{pmatrix} = \frac{1}{\sqrt{3}} \begin{pmatrix} Y_{11}(\delta,\alpha) \\ Y_{1-1}(\delta,\alpha) \\ Y_{10}(\delta,\alpha) \end{pmatrix} . \tag{4.5}$$

Since $Y_{00}(\delta,\alpha)$ is identically equal to one, the flux distribution can be transformed to

$$\begin{aligned} \Phi_{\text{s.h.}}(\delta,\alpha) &=& \Phi_0' \cdot \left( a_{00} + \sum_{\ell=1}^{\infty} \sum_{m=-\ell}^{\ell} a_{\ell m} Y_{\ell m}(\delta,\alpha) \right) \\ &=& \underbrace{\Phi_0' a_{00}}_{\Phi_0} \cdot \left( 1 + \sum_{\ell=1}^{\infty} \sum_{m=-\ell}^{\ell} \frac{a_{\ell m}}{a_{00}} Y_{\ell m}(\delta,\alpha) \right) , \end{aligned} \tag{4.6}$$

by which the original form is re-obtained.

The dipole distribution as given by Equation 4.3 can be expressed in terms of a spherical harmonics expansion with non-zero coefficients only in degree one. Thus, a dipole distribution can be described by means of the dipole vector, or equivalently by three coefficients $a_{1m}$. Applying Identity 4.5 to Equation 4.3 yields

$$\Phi_{\text{dipole}}(\delta,\alpha) = \Phi_0 \cdot \left( 1 + \hat{e}(\delta,\alpha) \cdot \vec{D} \right) = \Phi_0 \cdot \left( 1 + \frac{1}{\sqrt{3}} \begin{pmatrix} Y_{11}(\delta,\alpha) \\ Y_{1-1}(\delta,\alpha) \\ Y_{10}(\delta,\alpha) \end{pmatrix} \cdot \vec{D} \right) , \tag{4.7}$$

which is identical to Equation 4.6, if the coefficients are chosen as follows:

$$\begin{aligned} a_{00} &>& 0 , \\ \sqrt{3}/a_{00} \cdot a_{11} &=& D_x &=& D\cos\delta_{\text{dipole}}\cos\alpha_{\text{dipole}} , \\ \sqrt{3}/a_{00} \cdot a_{1-1} &=& D_y &=& D\cos\delta_{\text{dipole}}\sin\alpha_{\text{dipole}} , \\ \sqrt{3}/a_{00} \cdot a_{10} &=& D_z &=& D\sin\delta_{\text{dipole}} , \\ a_{\ell m} &=& 0 \ \ (\ell > 1) . \end{aligned} \tag{4.8}$$

## 4.2 Calculation of the Exposure

In order to interpret a set of recorded data in view of an assumed parametrisation, it is necessary to know the sky coverage which underlies the experimental data. Depending on the geographical location of the experiment, only certain parts of the sky are visible at all. Depending on the precise measurement periods, some parts of the sky have been seen more often than others. This section covers the calculation of the exposure, which is a measure for the sky coverage. The exposure is a function, that takes the experiment's geometry and the actual measurement times into account. As a function of declination and right ascension, it yields the product of the surface area, that has been exposed to the cosmic rays from this direction, multiplied by the measurement time, during which the given direction has been visible. In this context, the term "visible" refers to a field of view, that is defined by the maximum zenith angle $\vartheta_{\text{max}}$, up to which the showers are considered well reconstructable, see Figure 4.2. The exposure can be most generally calculated as follows:

**Figure 4.2:** Field of view of an experiment at 49° North latitude and with a zenith limit of 42°. As the Earth rotates around the polar axis, so does the cone that marks off the field of view. After one revolution, i.e. after one sidereal day, most of the Northern hemisphere of the sky has been seen. Only the part of the sky with declinations South of +7° remains unseen. On the other hand, a small area around the celestial North Pole lies continually within the experiment's field of view.
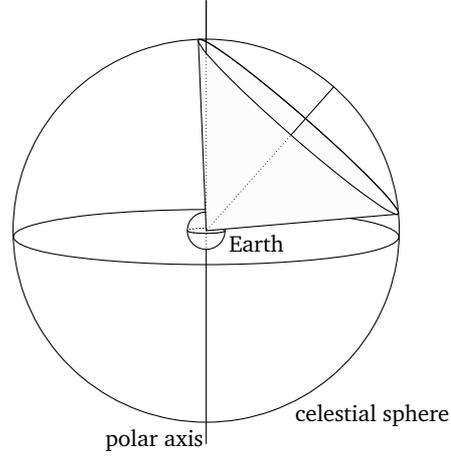


$$\omega(\delta, \alpha) = \int dt \cdot A(\vartheta, \varphi, t) \cdot \varepsilon(\vartheta, \varphi, t), \tag{4.9}$$

where the viewing direction (zenith $\vartheta$, azimuth $\varphi$) is calculated from (and therefore mathematically depends on) the celestial direction $(\delta, \alpha)$ and time $t$. $A(\vartheta, \varphi, t)$ denotes the area that is exposed to the particular viewing direction at the time $t$. $\varepsilon(\vartheta, \varphi, t)$ marks the efficiency for detecting cosmic rays from the given viewing direction and at the given time. The integration is carried out over the actual measurement periods in time.

Assuming a plane ground based experiment, and no bizarre geometrical features, the effectively exposed area only depends on the zenith angle $\vartheta$. The more inclined a shower is, the smaller is the projection of the experiment's ground area onto the shower's normal plane. That is to say, the experiment looks "narrower" to a more inclined shower:

$$A(\vartheta) = A_{\text{surf}} \cdot \cos \vartheta. \tag{4.10}$$

In order get rid of the efficiency term in the exposure calculation, it is most common to apply cuts to the data set ensuring full efficiency within the selected subset. With respect to the arrival directions, this leads to an upper limit for the zenith angle $(\vartheta_{\text{max}})$. These two assumptions simplify the former equation to

$$\omega(\delta, \alpha) = \int dt \cdot A_{\text{surf}} \cdot \cos \vartheta(\delta, \alpha, t) \cdot H(\vartheta_{\text{max}} - \vartheta(\delta, \alpha, t)), \tag{4.11}$$

with $H(x)$ being the Heaviside step function[1]. The presence of the step function term effectively reduces the integration range to those parts of the measurement periods, for which the given celestial direction corresponds to a zenith angle not greater than $\vartheta_{\text{max}}$.

Looking at the conversion from equatorial to horizontal coordinates, the zenith angle $\vartheta$ is calculated from the equatorial coordinates $(\delta, \alpha)$ and the time $t$ as follows:

$$\vartheta(\delta, \alpha, t) = \arccos \left( \sin \delta \sin \beta + \cos \delta \cos \beta \cos h(\alpha, t) \right), \tag{4.12}$$

with $\beta$ being the geographical latitude of the experiment, and $h$ being the hour angle, which in turn relates the right ascension $\alpha$ to the local (thus depending on the geographical longitude) mean sidereal time. The geographical location of the experiment is considered static, which is

---

[1]$H(x)$ is defined as an antiderivative of the Dirac function, $H(x) = \int_{-\infty}^{x} \delta(x')dx'$, which leads to $H(x) = 0$ for $x < 0$ and $H(x) = 1$ for $x > 0$.

(a)



(b)
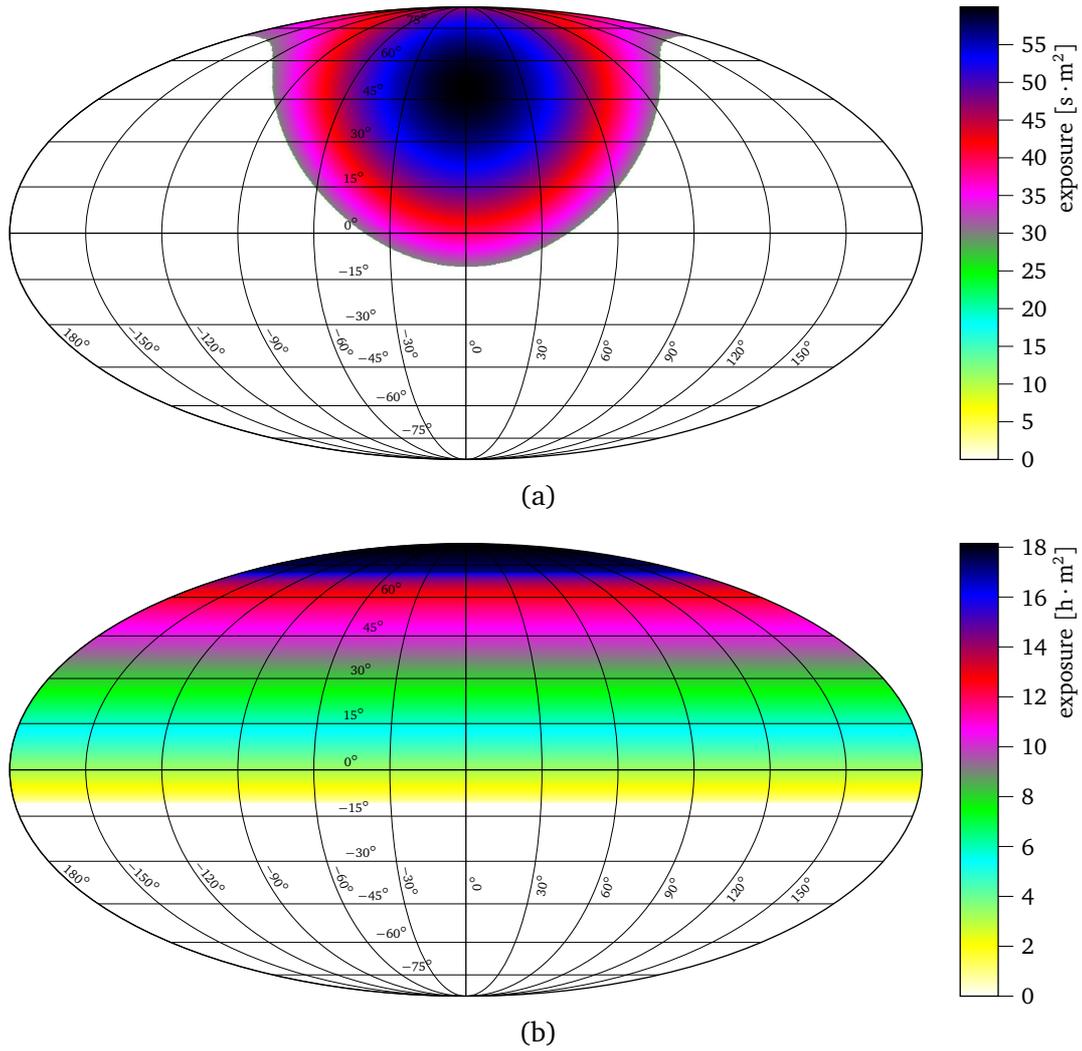
**Figure 4.3:** Exposure maps of an experiment at 49° North latitude with a detection area of one square metre. For illustration purposes, a zenith limit of 60° was chosen. (a) shows a measurement period of one sidereal minute, beginning from 12:00 a.m. local mean sidereal time. A region around the North Pole ($\delta \geq 71°$) is continually contained in the field of view. (b) shows the exposure for one full sidereal day. Source directions with a declination less than $-11°$ have zero exposure.

why dependencies on latitude and longitude are not explicitly quoted in the formula. During the course of one sidereal day, the zenith angle corresponding to any given celestial direction changes, but the time dependency enters the calculation only via the hour angle:

$$\cos\vartheta(t) = \sin\delta\sin\beta + \cos\delta\cos\beta\cos h(\alpha, t). \tag{4.13}$$

This function is illustrated in Figure 4.4. The value of the hour angle in fact sweeps out the whole range of 0 to $2\pi$ during one sidereal day, making its cosine perform between $-1$ and 1. This defines the range of possible values for $\cos\vartheta$ and, as a result, for the zenith angle $\vartheta$: [2]

$$\sin\delta\sin\beta - \cos\delta\cos\beta \leq \cos\vartheta(t) \leq \sin\delta\sin\beta + \cos\delta\cos\beta. \tag{4.14}$$

---

[2]As the ranges of values of both $\delta$ and $\beta$ are $[-\pi/2; \pi/2]$, their respective cosines are never negative.

**Figure 4.4:** Variation of the zenith angle $\vartheta$ (shown here is its cosine) of a fixed celestial direction over the course of one sidereal day.
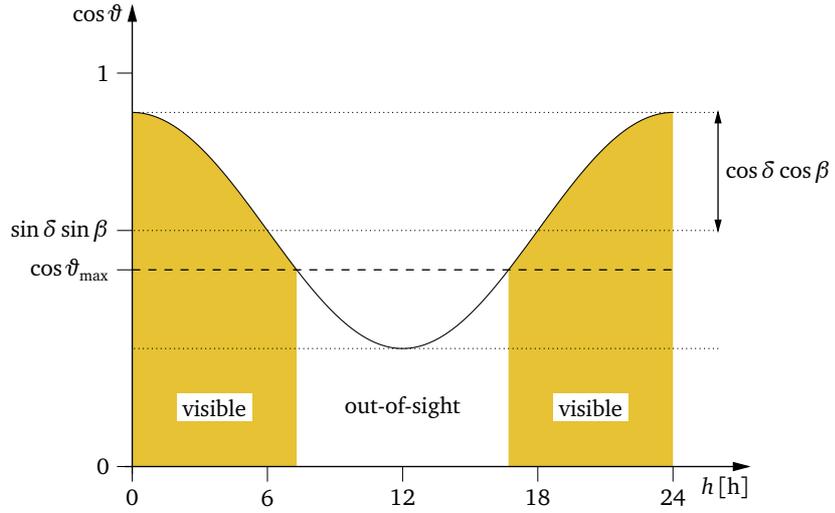
Applying angle sum and difference identities yields

$$-\cos(\delta + \beta) = \cos(\delta + \beta + \pi) \leq \cos\vartheta(t) \leq \cos(\delta - \beta). \tag{4.15}$$

With respect to the visibility of a celestial direction $(\delta, \alpha)$ and depending on the declination $\delta$ alone, three cases can be distinguished:

1. The direction never lies within the experiment's field of view.

   This is the case, if for all times $t$, $\vartheta > \vartheta_{\mathrm{max}}$ (thus[3] $\cos\vartheta < \cos\vartheta_{\mathrm{max}}$) holds, which is true if the upper limit of $\cos\vartheta(t)$ is less than $\cos\vartheta_{\mathrm{max}}$:

   $$\cos\vartheta(t) \leq \cos(\delta - \beta) < \cos\vartheta_{\mathrm{max}} \rightsquigarrow \left|\delta - \beta\right| > \vartheta_{\mathrm{max}}. \tag{4.16}$$

   Obviously, the exposure for such directions is zero.

2. The direction always lies within the experiment's field of view.

   This is the case, if for all times $t$, $\vartheta \leq \vartheta_{\mathrm{max}}$ (thus $\cos\vartheta \geq \cos\vartheta_{\mathrm{max}}$) holds, which is true if the lower limit of $\cos\vartheta(t)$ is greater than $\cos\vartheta_{\mathrm{max}}$:

   $$\cos\vartheta(t) \geq -\cos(\delta + \beta) \geq \cos\vartheta_{\mathrm{max}} \rightsquigarrow \left|\delta + \beta\right| \geq \pi - \vartheta_{\mathrm{max}}. \tag{4.17}$$

3. The direction sometimes lies within the experiment's field of view.

   This is the case if neither of the previous two conditions is fulfilled:

   $$\left|\delta - \beta\right| \leq \vartheta_{\mathrm{max}} < \pi - \left|\delta + \beta\right|. \tag{4.18}$$

Given the set of measurement periods, the exposure can finally be calculated as follows:

$$\omega(\delta, \alpha) = \int dt \cdot A_{\mathrm{surf}} \cdot \left[\sin\delta \sin\beta + \cos\delta \cos\beta \cos h(\alpha, t)\right] \cdot H(\vartheta_{\mathrm{max}} - \vartheta(\delta, \alpha, t)). \tag{4.19}$$

The Heaviside term turns out to be trivial for directions that continually lie outside ($H = 0$ and consequently $\omega = 0$) or within ($H = 1$) the field of view. Otherwise, the integration

---

[3]The zenith angle is defined to range within $[0; \pi]$. Therefore $\vartheta \leq \vartheta'$ is equivalent to $\cos\vartheta \geq \cos\vartheta'$.

has to be carried out over the intersection of measurement and visibility periods. Given the geographical location of the experiment, the field of view (in terms of the maximum zenith angle $\vartheta_{\max}$), and the precise measurement periods, an exposure map can be generated by performing this calculation for many different directions. Figure 4.3 shows an example of such a map.

Given a carefully calculated exposure map and assuming a certain form of the flux distribution, it is possible to extract the parameters of the distribution from a set of measured arrival directions. The following paragraphs describe different methods for the extraction.

## 4.3 Rayleigh Analysis

One very common approach, many times a first step in anisotropy considerations, is the Rayleigh analysis. Often, it has been declared as a method for dipole reconstruction. However, its main result—the Rayleigh amplitude—is only indirectly connected with the dipole amplitude. Its value is not determined by the flux distribution alone, but also by features of the experiment, namely geographical location and field of view. It will be shown later in more detail, that the value of the Rayleigh amplitude has only limited meaning with regard to quantitative considerations. Nevertheless, the Rayleigh analysis is able to falsify the hypothesis of an isotropic distribution. This, and the simplicity of the procedure, justify the deployment of the Rayleigh analysis as a first step for anisotropy studies.

### 4.3.1 The Formalism

The Rayleigh analysis takes only the right ascension values of the arrival directions into account. Sines and cosines of the right ascensions are added separately:

$$C = \frac{2}{N} \sum_{i=1}^{N} \cos \alpha_i, \quad S = \frac{2}{N} \sum_{i=1}^{N} \sin \alpha_i, \tag{4.20}$$

with $N$ being the number of observations. This step can be thought of as adding up the $N$ two-dimensional unit vectors representing the right ascension values, with $C$ and $S$ being the $x$ and $y$ coordinates of the sum, divided by $2N$ for normalisation. The length and the orientation of the resulting vector are called Rayleigh amplitude $R$ and Rayleigh phase $\alpha_R$, respectively, and are defined as:

$$R = \sqrt{C^2 + S^2}, \quad \alpha_R = \arg(C + iS). \tag{4.21}$$

The right ascension, being the longitude-like component of the equatorial coordinate system, is a periodic variable, that can take values in the range between $0$ and $2\pi$. If the set of right ascension values $\alpha_i$ favours certain directions over others, the resulting amplitude $R$ may differ from zero significantly, whereas for a perfectly homogeneous distribution of $\alpha_i$-values the quantities $S$ and $C$ should only differ from zero owing to statistical fluctuations. The probability to obtain an amplitude not less than $R$ from an uniform distribution is given by [Ray1880][4]

$$p(R) = \exp\left(-R^2 N/4\right). \tag{4.22}$$

This comparably simple formalism allows for a check of the isotropy hypothesis against a set of observed right ascension values: First, the Rayleigh amplitude of the data set is computed.

---

[4]The equation is an approximation for $N \to \infty$, but has proven to work adequately for values of $N$ as small as three.

Then, according to the previous equation, the probability, that a uniform distribution yields an amplitude at least as high, is evaluated. Demanding that this probability falls below a value that was set a priori, anisotropy is considered evident.

### 4.3.2   Exposure Based Weighting

A non-uniform distribution of right ascension values does not necessarily have to be caused by an anisotropy of the cosmic ray flux. Instead, it can be the result of systematic effects. Obviously, an exposure, that varies with the right ascension, will severely distort the data set. There are two ways to deal with this problem: either force the exposure map to be homogeneous in right ascension, or introduce weighting factors in the formulas above, that account for the differences in exposure. The first approach can be realised by reducing the data set to measurement periods of full sidereal days only: the measurement periods of the data start at arbitrary times, but go uninterrupted for an integer number of sidereal days. This produces an exposure map that is perfectly homogeneous along the right ascension like the one shown in Figure 4.3(b), at the cost of a (typically large) amount of data being discarded.

The second approach does not restrain the analysis to full sidereal days, hence it uses the full set of statistics. An exemplary exposure map for such a case is shown in Figure 4.5(a). It requires a modification of the Rayleigh formalism, that was proposed by Mollerach and Roulet [Mol05]. Based on the exposure previously computed $\omega(\delta, \alpha)$, each addend in the sum formulas of the Rayleigh formalism is furnished with a weighting factor, that solely depends on the direction of the observation. The weighting factor could have been the inverse exposure $1/\omega(\delta, \alpha)$, but Mollerach and Roulet decided to use

$$W(\delta, \alpha) = \frac{\bar{\omega}(\delta)}{\omega(\delta, \alpha)}, \tag{4.23}$$

with $\bar{\omega}(\delta)$ being the average exposure of declination $\delta$

$$\bar{\omega}(\delta) = \frac{1}{2\pi} \int_0^{2\pi} \mathrm{d}\alpha\, \omega(\delta, \alpha). \tag{4.24}$$

Figure 4.5(b) depicts the weighting factors that correspond to the exposure map in Figure 4.5(a).

The inverse exposure as weighting factor would generally weight observations from directions of low exposure more strongly. Celestial directions, that only scratch the field of view once each sidereal day for a short time (which then automatically happens with great inclination), will receive dramatically high weights. This would, however, provide the exposure effectively being the same for all directions. But with the Rayleigh analysis only taking the right ascension into account, it is not necessary to level the exposure with weighting factors in a way that it becomes constant over the whole field of view. Instead, Mollerach and Roulet homogenise the exposure only in right ascension. While the reasons for two arbitrary celestial directions having different exposures are the different zenith angles under which they appear as well as a possibly different number of observations during the actual measurement periods, only the latter of the two reasons applies if the two directions have the same declination and only differ in right ascension. Therefore, the weighting factors needed for balancing the exposure in right ascension only are of order unity, by which means the problem of introducing large weighting factors and overpronouncing regions with small exposure is circumvented.

The refined Rayleigh analysis after Mollerach and Roulet uses the following formulas:

$$C = \frac{2}{\tilde{N}} \sum_{i=1}^{N} W(\delta_i, \alpha_i) \cos \alpha_i, \quad\quad S = \frac{2}{\tilde{N}} \sum_{i=1}^{N} W(\delta_i, \alpha_i) \sin \alpha_i, \tag{4.25}$$

(a)



(b)
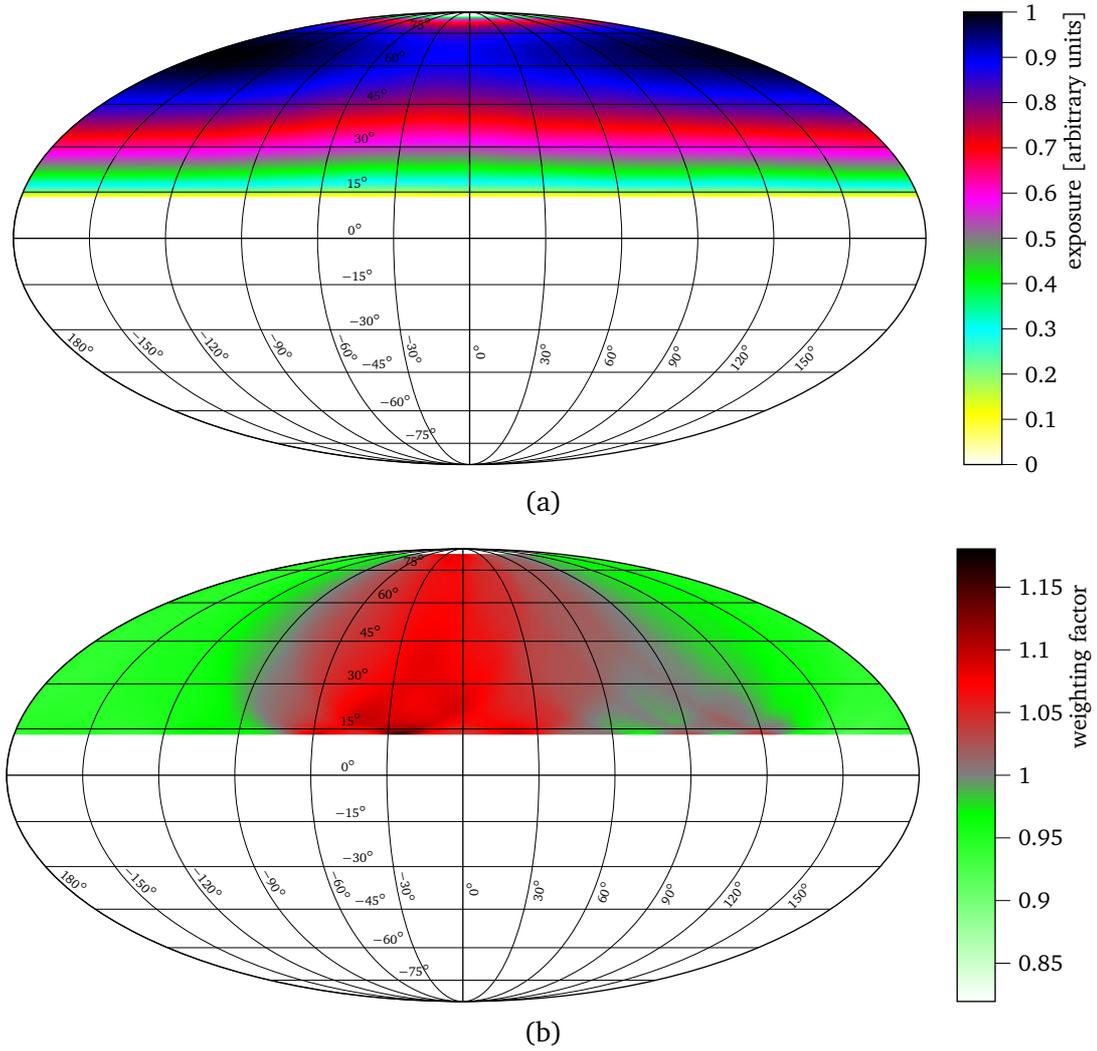
**Figure 4.5:** (a) Exemplary exposure map for an experiment at 49° North latitude with a zenith limit of 36°. Interruptions of the measurement cause the exposure to be inhomogeneous in right ascension, too.
(b) Weighting factors corresponding to the above exposure map.

$$R = \sqrt{C^2 + S^2}, \quad \alpha_R = \arg(C + iS), \quad (4.26)$$

with $W(\delta, \alpha)$ being the direction dependent weighting factor, and $\tilde{N}$ being the sum of the weighting factors for all observations, which should not differ very much from the number of observations $N$:

$$W(\delta, \alpha) = \frac{\bar{\omega}(\delta)}{\omega(\delta, \alpha)}, \quad \tilde{N} = \sum_{i=0}^{N} W(\delta_i, \alpha_i). \quad (4.27)$$

In the case of an already right ascension independent exposure, i.e. measurement periods of full sidereal days, all weighting factors equal one and these equations conform to the previous ones.

### 4.3.3 Applying the Rayleigh Formalism to a Two-Dimensional Dipole Distribution

So far, the Rayleigh formalism has been introduced with no assumptions about the particular form of the flux distribution. In order to identify the results of the Rayleigh analysis, the amplitude $R$ and the phase $\alpha_R$, with features of the distribution, it is necessary to analytically track their calculation. As an intermediate first step, this shall be done for the two-dimensional case: instead of examining distributions on the unit (or celestial) sphere, represented by declination and right ascension coordinates, this section covers distributions on the unit circle, represented by the periodic coordinate $\alpha$ alone.

The Rayleigh analysis takes a set of observation coordinates $\alpha_i$ as input. For the purpose of an analytic calculation, the set of observations is considered infinitely large and represented by a continuous, dimensionless function $I(\alpha)$, which acts as observation density function. It is proportional to both the flux $\Phi(\alpha)$ and the exposure $\omega(\alpha)$, as these are the quantities that determine the expected numbers of observations from the given direction:

$$I(\alpha) = I_0 \omega(\alpha) \Phi(\alpha), \tag{4.28}$$

where the constant $I_0$ has the dimension needed to ensure $I(\alpha)$ is dimensionless. The absolute value of $I_0$ is meaningless for the following considerations. It is customary to set $I_0 = 1/(\bar{\omega}\Phi_0)$, with $\bar{\omega}$ being the mean exposure and $\Phi_0$ an arbitrary constant flux.

Instead of summing over all observations, an integration is carried out over the coordinate space, with the number of observations from that coordinate ($I(\alpha)\mathrm{d}\alpha$) as additional factor:

$$C = \frac{2}{\tilde{N}} \int_{\alpha=0}^{2\pi} I(\alpha)\,\mathrm{d}\alpha\,W(\alpha)\cos\alpha, \quad S = \frac{2}{\tilde{N}} \int_{\alpha=0}^{2\pi} I(\alpha)\,\mathrm{d}\alpha\,W(\alpha)\sin\alpha, \tag{4.29}$$

$$W(\alpha) = \frac{\bar{\omega}}{\omega(\alpha)}, \quad \tilde{N} = \int_{\alpha=0}^{2\pi} I(\alpha)\,\mathrm{d}\alpha\,W(\alpha). \tag{4.30}$$

With the definitions of $I(\alpha)$ and $I_0$ given above, the exposure completely cancels out, which proves, that the exposure correction of the refined Rayleigh formalism works: the results do only depend on the real flux distribution, and not on the exposure. The equations can be simplified to:

$$C = \frac{2}{N} \int_{\alpha=0}^{2\pi} \Phi(\alpha)\,\mathrm{d}\alpha\,\cos\alpha, \quad S = \frac{2}{N} \int_{\alpha=0}^{2\pi} \Phi(\alpha)\,\mathrm{d}\alpha\,\sin\alpha, \quad \tilde{N} = \int_{\alpha=0}^{2\pi} \Phi(\alpha)\,\mathrm{d}\alpha. \tag{4.31}$$

Applying to these equations a two-dimensional dipole distribution

$$\Phi_{\mathrm{dipole}}(\alpha) = \Phi_0 \cdot \left[1 + D \cdot \cos\left(\alpha - \alpha_{\mathrm{dipole}}\right)\right], \tag{4.32}$$

yields:

$$\tilde{N} = 2\pi\Phi_0, \quad C = D \cdot \cos\alpha_{\mathrm{dipole}}, \quad S = D \cdot \sin\alpha_{\mathrm{dipole}}, \quad R = D, \quad \alpha_R = \alpha_{\mathrm{dipole}}. \tag{4.33}$$

Thus, for the two-dimensional case and an infinite number of observations, the Rayleigh analysis correctly reproduces the features of a dipole distribution. The Rayleigh amplitude amounts to the dipole's amplitude, and the Rayleigh phase reflects the dipole's orientation.
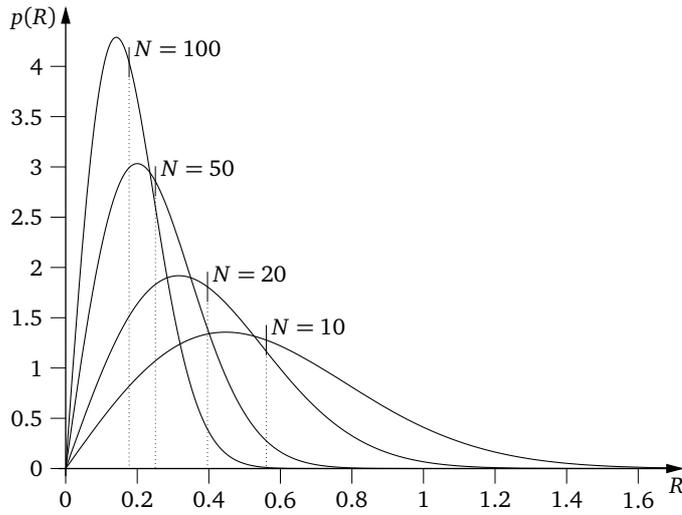
**Figure 4.6:** Probability density functions of the Rayleigh amplitude for isotropic data, for different numbers of observations $N$. The markers denote the respective mean values.

However, when working with a data set of finite extent, these quantities are subject to statistical fluctuations. Given the number of observations $N$, a dipole of magnitude $D$ would yield a Rayleigh amplitude in the range between $R$ and $R + dR$ with a probability of [Lin75]

$$p(R)dR = \frac{RN}{2} \exp\left[-N(R^2 + D^2)/4\right] I_0(RDN/2)\,dR\,, \tag{4.34}$$

where $I_0$ is the modified Bessel function of order zero. Notably, the true dipole amplitude $D$ is neither the expectation value nor the most probable value of $R$, as the statistical fluctuations tend to overpronounce the anisotropy. The most obvious example for this behaviour is a perfectly isotropic distribution, thus a dipole amplitude of $D = 0$, for which the probability density function is given by

$$p(R) = \frac{RN}{2} \exp\left(-NR^2/4\right)\,. \tag{4.35}$$

Figure 4.6 shows the graphs of this function for different numbers of observations $N$. The expectation value of $R$ is $\sqrt{\pi/N}$. With $N$ as big as 10,000, the expected Rayleigh amplitude is no less than 1.5%, no matter what the underlying distribution is, as the lower limit for this number is of course given by the case of perfect isotropy. The probability density function for the Rayleigh phase is given by

$$p(\psi) = \frac{1}{2\pi} \exp(-k)\left[1 + \sqrt{\pi k}\cos\psi \exp\left(k\cos^2\psi\right) \cdot \left[1 + \mathrm{erf}\left(\sqrt{k}\cos\psi\right)\right]\right]\,, \quad k = D^2N/4\,, \tag{4.36}$$

with $\psi$ being the Rayleigh phase relative to the true dipole direction, or the reconstruction error, thus $\psi = \alpha_R - \alpha_{\mathrm{dipole}}$. The distribution is symmetrical and peaks at zero, i.e. the expectation value for the reconstructed phase is indeed the dipole direction. The more observations taken into account, and the greater the dipole amplitude, the narrower the peak. For a zero amplitude—the case of isotropic data—the phase is meaningless and so the distribution is completely flat. See Figure 4.7 for an illustration.

### 4.3.4 The Rayleigh Analysis in Three Dimensions

In order to make use of these findings for the Rayleigh analysis in cosmic ray physics, which processes the arrival directions of the cosmic ray particles coming from three-dimensional space, the distribution of right ascension values, as used for the Rayleigh analyses, needs to

**Figure 4.7:** Probability density functions of the Rayleigh phase for different combinations of dipole amplitude $D$ and number of observations $N$ ($k = D^2N/4$). For instance, for a dipole amplitude of 2%, the curves (from wide to narrow) correspond to $10^2$, $10^3$, $10^4$, $10^5$ and $10^6$ events, respectively. On the other hand, for a given number of 10,000 observations, these curves (again from wide to narrow) correspond to dipole amplitudes of 0.2%, 0.63%, 2%, 6.3% and 20%, respectively.
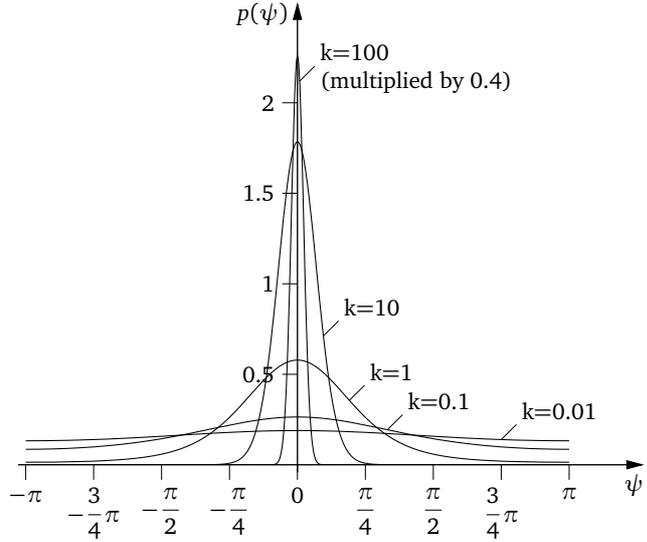
be related to the original, thus three-dimensional, flux distribution. It will turn out, that the results of the Rayleigh analysis will not be mere projections of the three-dimensional quantities onto the equatorial plane. Given an arbitrary flux as function of declination and right ascension $\Phi(\delta, \alpha)$, averaging over the declination yields the right ascension distribution $\bar{\Phi}(\alpha)$:

$$\bar{\Phi}(\alpha) = \frac{\int_{\delta=-\pi}^{\pi} \Phi(\delta, \alpha) \cos \delta \, \mathrm{d}\delta}{\int_{\delta=-\pi}^{\pi} \cos \delta \, \mathrm{d}\delta} = \frac{1}{2} \int_{\delta=-\pi}^{\pi} \Phi(\delta, \alpha) \cos \delta \, \mathrm{d}\delta \, . \tag{4.37}$$

While this calculation can be carried out for any kind of flux distribution, it only makes sense to consider a dipole distribution at this point. Returning only one amplitude and one phase, the Rayleigh analysis cannot produce information on higher orders. Substituting $\Phi(\delta, \alpha)$ with the dipole distribution as given in Equation 4.3, and carrying out the integration leads to

$$\bar{\Phi}_{\mathrm{dipole}}(\alpha) = \Phi_0 \cdot \left[ 1 + \frac{\pi}{4} D \cos \delta_{\mathrm{dipole}} \cos(\alpha - \alpha_{\mathrm{dipole}}) \right] \, . \tag{4.38}$$

The form of this equation is the one of a two-dimensional dipole, which means that the considerations in the previous section are valuable in the three-dimensional situation, too. At the first sight, it may look like the disregard of the third dimension leaves the original dipole vector projected onto, or even skewed into the equatorial plane. However, while the resulting direction of the two-dimensional dipole is indeed coincident with the right ascension of the original dipole vector, the dipole amplitude is weakened by two effects. Firstly, the projection effect: the $z$-component of the dipole vector has no influence on the two-dimensional distribution. Projecting onto the $xy$-plane, i.e. the equatorial plane, adds the factor of $\cos \delta_{\mathrm{dipole}}$ in the above equation. Secondly, the dimensional effect: Even when the dipole vector lies in the equatorial plane, so that no further projection onto that plane is necessary ($\cos \delta_{\mathrm{dipole}} = 1$), the reduction to two-dimensions weakens the dipole. Looking at slices of the unit sphere of constant declination $\delta$, the two-dimensional distributions in all slices are dipole-like. But only one slice—the equatorial plane ($\delta = 0$)—carries a dipole that has an amplitude as great as $D$. In all other slices, the respective dipole amplitudes are smaller, namely only $D \cos \delta$, see

(a)  (b)  (c)
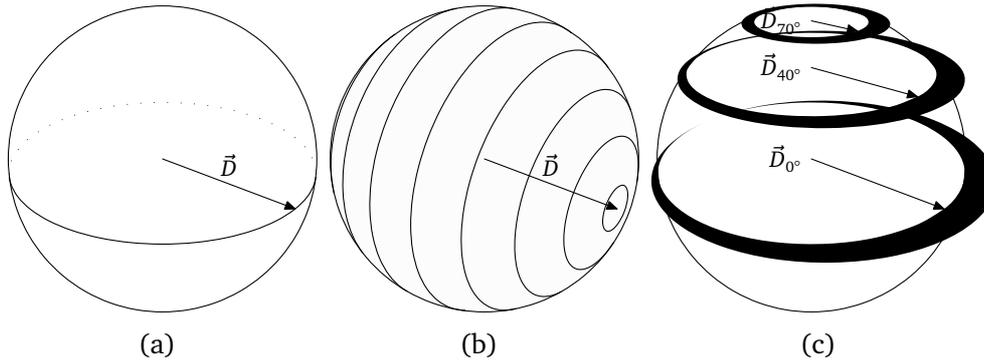
**Figure 4.8:** Dimensional weakening effect acting on a three-dimensional dipole distribution. Considering the case of the dipole vector lying in the equatorial plane, with dipole vector $\vec{D}$, as depicted in Figure (a), and in Figure (b) showing lines of equal intensity on the unit sphere. Looking at the two-dimensional distributions in slices of constant declination, of all the slices only the equatorial one ($\delta = 0$) has a dipole identical to $\vec{D}$. Figure (c) shows the intensity distributions in three exemplary slices by means of line thickness. Off-equator slices have less pronounced dipoles.

Figure 4.8. Averaging over all the slices introduces an additional factor of

$$
\frac{\int_{\delta=-\pi}^{\pi} \overbrace{\cos\delta}^{\text{weakening factor}} \overbrace{\cos\delta}^{\substack{\text{geometrical factor} \\ \text{(off-equator slices} \\ \text{contribute less)}}} \mathrm{d}\delta}{\underbrace{\int_{\delta=-\pi}^{\pi} \cos\delta\,\mathrm{d}\delta}_{\text{normalisation}}} = \frac{\pi/2}{2} = \frac{\pi}{4}. \tag{4.39}
$$

For reasons of clearness, this illustrative explanation has only dealt with the special case of an equatorial dipole. However, the factor of $\pi/4$ turns out to be the same, regardless of the dipole's orientation.

A brief summary of the findings so far: Assuming a dipole-like intensity distribution, the Rayleigh analysis can correctly reproduce the dipole vector's right ascension, whereas it does not provide the declination. The reconstructed dipole amplitude is suppressed by a factor of $\pi/4 \cdot \cos\delta_{\text{dipole}}$, which depends on the (unknown) declination of the dipole vector.

In fact, the situation is even worse. What has remained disregarded here is the issue of inhomogeneous and incomplete sky coverage, i.e. the exposure. It has been shown, that the Rayleigh analysis correctly reconstructs dipole amplitude and direction in two-dimensions. The problem of unequal exposure has been dealt with by means of weighting factors. When looking upon the three-dimensional dipole as superposition of slices containing two-dimensional dipoles, for each of which the above considerations apply, the question is how this superposition works. So far, no weighting factors have been used, implying that the exposure is constant for all slices, i.e. over all declinations, which usually is not the case. There are two ways for circumventing this problem: The first possibility is to introduce another set of weighting factors, in order to make the contributions of each of the declination slices correctly represented. The weighting for any of the declination slices would be $1/\bar{\omega}(\delta)$. As a matter of fact, the term $\bar{\omega}(\delta)$ appears in the numerator of the weighting factors that are already in place for right ascension correction (see Equation 4.23), and therefore is cancelling out. As a result, each observation would be weighted with the inverse exposure of its reconstructed

arrival direction $(1/\omega(\delta, \alpha))$. It has been discussed in Section 4.3.2 that this would be an un-favourable choice owing to the fact that these factors are not of the order of one. In addition, this idea requires coverage of the full sky, as zero-exposure in any direction would entail an infinite weighting factor.[5] However, following this approach would mean that the resulting Rayleigh amplitude could be identified with the term $\pi/4 \cos \delta_{\text{dipole}} D$.

The second possibilty is to keep the weighting as it is, avoiding the negative implications, at the cost of changing the meaning of the Rayleigh amplitude. Not correcting for the declination dependency of the exposure means that in the superposition of the declinations slices, some slices have more impact than others. The right ascension distribution, i.e. the input of the Rayleigh procedure, becomes:

$$\bar{\Phi}(\alpha) = \frac{\int_{\delta=-\pi}^{\pi} \Phi(\delta, \alpha)\, \bar{\omega}(\delta) \cos \delta \, \mathrm{d}\delta}{\int_{\delta=-\pi}^{\pi} \bar{\omega}(\delta) \cos \delta \, \mathrm{d}\delta} \, . \tag{4.40}$$

Applying this to the dipole distribution $\Phi_{\text{dipole}}(\delta, \alpha)$ yields:

$$\bar{\Phi}_{\text{dipole}}(\alpha) = \Phi_0' \cdot \left[ 1 + D' \cos(\alpha - \alpha_{\text{dipole}}) \right] \, ,$$

$$D' = \frac{D \cos \delta_{\text{dipole}}\, C_{20}}{1 + D \sin \delta_{\text{dipole}}\, C_{11}} \, , \qquad C_{ij} = \frac{\int_{\delta=-\pi/2}^{\pi/2} \bar{\omega}(\delta) \cos^i \delta \, \sin^j \delta \, \mathrm{d}\delta}{\int_{\delta=-\pi/2}^{\pi/2} \bar{\omega}(\delta) \cos \delta \, \mathrm{d}\delta} \, , \tag{4.41}$$

which in turn is a two-dimensional dipole distribution.[6] However, the relationship between the original dipole amplitude $D$ and the dipole amplitude in the resulting right ascension distribution $(D')$ , on which the Rayleigh analysis works, is anything but trivial. Figure 4.9 illustrates that relationship.

### 4.3.5  Summary

The Rayleigh analysis extracts the amplitude and the phase of the first harmonic from the distribution of right ascension values of a set of measured cosmic ray observations. It aims at reconstructing features of a dipole anisotropy. However, since it completely disregards the declination coordinates, it is unable to do a full reconstruction of the three-dimensional dipole. It can only detect the equatorial component of the anisotropy. In order to retrieve meaningful results from the Rayleigh analysis, either the data set has to be restricted to periods of full side-real days with constant measurement conditions, or—if the exposure of the experiment can be calculated—weighting factors have to be introduced, that account for the variations of the exposure in right ascension. With either of these measures in place, the Rayleigh analysis can correctly reproduce the right ascension of the dipole vector. On the other hand, the Rayleigh amplitude relates only indirectly to the amplitude of the dipole. Generally, the dipole ampli-tude is greater than the amplitude of the right ascension distribution. The Rayleigh amplitudes computed in cosmic ray analyses are usually so small that they could be a product of statistical fluctutations alone. From a statistical point of view, they serve as an upper limit for the true right ascension amplitude, which in turn is a lower limit for the sought-after dipole amplitude. Therefore, the meaning of the Rayleigh amplitude in view of the actual dipole amplitude is

---

[5]Although the actual calculation can be written in a way that these infinite weighting factors do not enter, it will not give correct results in that case.

[6]This formula has a different flux constant $\Phi_0'$, which adds a constant factor to $\Phi_0$ that depends on $\delta_{\text{dipole}}$ and integrals of $\bar{\omega}(\delta)$. The precise definition is not of importance, hence it shall be omitted here for reasons of clarity.
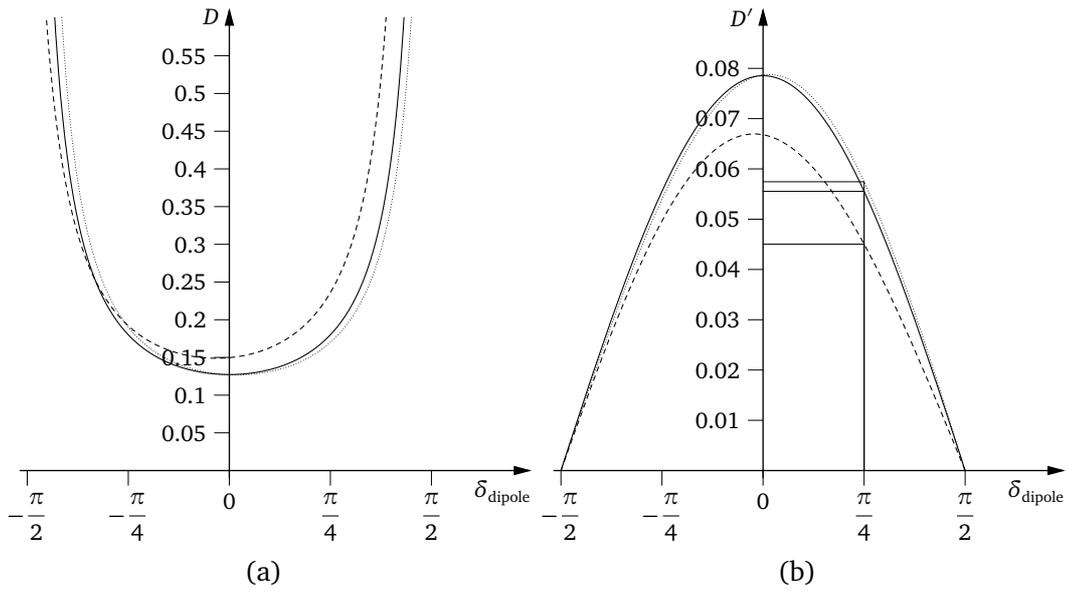
**Figure 4.9:** Relationship between dipole amplitude and Rayleigh amplitude. Shown here are curves for an ideal experiment with uniform exposure (solid lines), for the exposure depicted in Figure 4.5(a) (dashed lines), and for an experiment on the Southern hemisphere (35° South latitude) with a zenith limit of 60° (dotted lines). (a) refers to a Rayleigh amplitude of 10%. The actual dipole amplitude is plotted. It depends on the skew of the dipole and cannot be determined by the Rayleigh analysis alone. However, a given Rayleigh amplitude can set a lower limit for the dipole amplitude (about 12.7% in this example). (b) refers to a dipole amplitude of 10%. The amplitude of the right ascension distribution ranges from zero to approximately 7.9%, again depending on the skew of the dipole vector. The experiment's location and zenith limit have an influence, too: a 10% dipole with $\delta_{\text{dipole}} = 45°$ would correspond to a Rayleigh amplitude of 4.5% and 5.7%, respectively, for the two hypothetic experiments discussed here.

very limited. Much more than an estimate of the dipole amplitude, the Rayleigh amplitude is a measure for the precision and the confidence of the determination of the Rayleigh phase. Still, a Rayleigh amplitude, that does significantly exceed the statistical fluctuations, provides clear evidence for anisotropy, although a quite significant anisotropy is needed to achieve this.

## 4.4 The SAP Method for Dipole Reconstruction

The previous section has made the need for a three-dimensional reconstruction algorithm obvious. A more sophisticated analysis procedure should take the full available information into account, and therefore not neglect the declination values altogether. Moreover it should yield an absolute magnitude of the dipole. In 2001, Sommers published an article discussing the possibilities of anisotropy analyses with an observatory with full sky coverage [Som01]. The method that he proposed for a dipole reconstruction was very much a generalisation of the concept of the Rayleigh analysis to the three dimensions. While the Rayleigh amplitude works on the sum of two-dimensional unit vectors of the measured right ascension values, Sommers' method adds up the three-dimensional unit vectors of the reconstructed arrival directions:

$$\vec{R} = \frac{3}{\tilde{N}} \sum_{i=1}^{N} \frac{\hat{e}(\delta_i, \alpha_i)}{\omega(\delta_i, \alpha_i)}, \quad \tilde{N} = \sum_{i=1}^{N} \frac{1}{\omega(\delta_i, \alpha_i)}. \tag{4.42}$$

Every addend is divided by the direction's exposure, thereby accounting for unequal sky coverage. It is obvious that, if the directions are drawn from an isotropic distribution, the expected value of this quantity is zero, as the items of the summation cancel out. As for the Rayleigh amplitude, a value significantly differing from zero would indicate an anisotropy. In case of a dipole distribution, the vector $\vec{R}$ in fact reproduces the dipole vector. However, this method entirely depends on a full sky coverage. With gaps in the exposure, the isotropic component of the flux fails to cancel out in $\vec{S}$, because the summation lacks the terms of those missing directions.

   Thus for a data set of an experiment with partial sky coverage, $\vec{R}$ as defined above cannot be identified with the dipole vector. However, this quantity is still related to the properties of the dipole distribution. In 2005, Aublin and Parizot published an article in which they described a way to generalise Sommers' method to work with partial sky coverage [Aub05]. This method is commonly known as the SAP method, named after its developers Sommers, Aublin and Parizot. Like before, the unit vectors of the reconstructed arrival directions are weighted with the direction's inverse exposure and added up. The notation is chosen slightly differently:

$$\vec{S} = \sum_{i=1}^{N} \frac{\hat{e}(\delta_i, \alpha_i)}{\omega(\delta_i, \alpha_i)}, \quad S_0 = \sum_{i=1}^{N} \frac{1}{\omega(\delta_i, \alpha_i)}. \tag{4.43}$$

In case of full sky coverage, the term $3\vec{S}/S_0$ (which is equal to $\vec{R}$ in the previous definition) reconstructs the dipole vector. In the more general case, that the field of view is limited to declinations in the range between $\delta_{\min}$ and $\delta_{\max}$, the relation between the computed quantities $\vec{S}$ and $S_0$ and the dipole vector is much more complicated, but can be derived analytically. The analogue for the two-dimensional case has been shown in Section 4.3.3, and this derivation goes along the same lines: the quantities $\vec{S}$ and $S_0$ are written as integrals of the flux and these integrals are calculated under the assumption of a dipole-like flux distribution. The resulting values for $\vec{S}$ and $S_0$ depend on the features of the dipole distribution, as well as on the choice of the integration range ($\delta_{\min}$ and $\delta_{\max}$). Making the reconstructed dipole vector $\vec{R}$ the subject of the system of equations leads to

$$
\begin{aligned}
R_x &= \frac{S_x}{sS_z - 2\gamma S_0} \cdot \frac{\gamma - p}{\gamma - 1}, \\
R_y &= \frac{S_y}{sS_z - 2\gamma S_0} \cdot \frac{\gamma - p}{\gamma - 1}, \\
R_z &= \frac{sS_0 - 2S_z}{sS_z - 2\gamma S_0},
\end{aligned}
\tag{4.44}
$$

with

$$d = \sin\delta_{\max} - \sin\delta_{\min}, \quad s = \sin\delta_{\max} + \sin\delta_{\min}, \quad p = \sin\delta_{\max} \cdot \sin\delta_{\min}, \quad \gamma = \frac{s^2 - p}{3}. \tag{4.45}$$

These equations attribute a reconstructed dipole vector to a data set, even when the data set spans only a part of the sidereal sphere. The specific declination range can be chosen freely by the analyser, as long as the exposure is greater than zero for all directions within this range. The natural choice would be to take $\delta_{\min}$ and $\delta_{\max}$ as determined by the geographical location and the zenith limit of the experiment, thereby making use of all visible parts of the sky. However, it can be favourable to exclude the outward regions with low exposure. Disregarding these regions reduces the number of observations only marginally, but can improve the stability

of the result, as the events to be discarded have excessively high weightings. Artificially decreasing the declination range will change the specific values of $\vec{S}$ and $S_0$, as it will also change their meaning. However, the conversion formulas given here account for these changes. Mathematically, the correct dipole vector can be reconstructed from an arbitrarily small declination range. Assuming that the real flux distribution indeed is a dipole distribution, the knowledge of the true distribution in a small band of declination angle contains enough information for the precise reconstruction of the dipole vector. However, these analytical considerations always imply unlimited statistics. In reality, the optimal choice of the declination range for this analysis is a trade-off between maximising the amount of data by taking the full available declination range, and getting rid of the fluctuations induced by individual observations with excessively high weightings.

## 4.5 Multipole Reconstruction

A different and more general approach employs an expansion of the flux distribution in spherical harmonics. The flux distribution can be written as linear combination of the spherical harmonic functions $Y_{\ell m}$, with coefficients $a_{\ell m}$, as shown in Equation 4.4. The coefficients can be easily obtained in the case of full and uniform sky coverage:

$$\bar{a}_{\ell m} = \frac{1}{N} \sum_{i=1}^{N} Y_{\ell m}(\delta_i, \alpha_i), \tag{4.46}$$

where $\bar{a}_{\ell m}$ stands for an estimator of the true coefficient $a_{\ell m}$. In the case of unlimited statistics, these estimators will be identical to the true coefficients, whereas in real world situations the estimators suffer from statistical fluctuations. While non-uniformities of the exposure can still be dealt with by means of weighting factors, the method as it is does not work with partial sky coverage. However, in 2008 Billoir and Deligny published an article on obtaining estimates for the multipolar coefficients based on data sets acquired with non-uniform or even partial sky coverage [Bil08].

Let $I(\delta, \alpha)$ be the density of observations from a given direction. This quantity is not identical to the cosmic ray flux from the given direction, as it also involves the exposure. In fact, it is proportional to both the flux and the exposure:

$$I(\delta, \alpha) = I_0 \omega(\delta, \alpha) \Phi(\delta, \alpha). \tag{4.47}$$

If the data set covers the whole of the sky, the exposure is greater than zero for all directions. In this case, the flux $\Phi$ can be obtained by dividing the number of observations from any given direction by the exposure towards that direction. A multipole expansion can be performed in a straight forward way. However, for partial sky coverage, the exposure for some directions is zero. The flux for these directions is undefined, as it cannot be extracted from the data with the above equation.

In their article, Billoir and Deligny describe two different methods to deal with that situation. The first method is based on a multipolar expansion of the function $I(\delta, \alpha)$. This function is well defined for all directions. For regions of the sky that are not seen by the experiment, $I(\delta, \alpha)$ simply amounts to zero. Let $b_{\ell m}$ be the set of coefficients to the spherical harmonic functions that describe the function $I(\delta, \alpha)$, then its estimators can be obtained by

$$\bar{b}_{\ell m} = \frac{1}{N} \sum_{i=1}^{N} Y_{\ell m}(\delta_i, \alpha_i). \tag{4.48}$$

These coefficients are related to the sought-after coefficients $a_{\ell m}$ through a kernel $[K]_{\ell\ell'}^{mm'}$, that can be computed from the exposure function $\omega(\delta, \alpha)$:

$$[K]_{\ell\ell'}^{mm'} = \int \cos\delta \, \mathrm{d}\delta \, \mathrm{d}\alpha \, Y_{\ell m}(\delta, \alpha) \, \omega(\delta, \alpha) \, Y_{\ell'm'}(\delta, \alpha). \tag{4.49}$$

The kernel $[K]_{\ell\ell'}^{mm'}$ has to be inverted in order to finally calculate estimators for the multipolar coefficients $a_{\ell m}$ of the cosmic ray flux $\Phi(\delta, \alpha)$:

$$\bar{a}_{\ell m} = \sum_{\ell', m'} [K^{-1}]_{\ell\ell'}^{mm'} \, \bar{b}_{\ell'm'}. \tag{4.50}$$

The second method is based on developing a set of orthogonal functions $Z_{\ell m}$, that incorporate the exposure function $\omega(\delta, \alpha)$ in such a way, that expanding $I(\delta, \alpha)$ over the $Z_{\ell m}$ functions directly yields estimators for the sought-after coefficients $a_{\ell m}$:

$$\bar{a}_{\ell m} = \frac{1}{N} \sum_{i=1}^{N} Z_{\ell m}(\delta_i, \alpha_i). \tag{4.51}$$

The derivation of the functions $Z_{\ell m}$ is considerably more complex than the first method, especially when the exposure function does not solely depend on declination but also on right ascension. It shall not be shown here.

The results, that these two methods produce, are not identical. However, the differences are typically much smaller than the statistical uncertainty. Both methods can return the multipolar coefficients up to an arbitrary order, but the maximum order $L$ has to be set a priori. The choice of $L$ also influences the results for lower orders. As for the first of the two methods, the maximum order $L$ determines the range of $\ell'$ in the sum formula 4.50, which means that, for example, even the dipole coefficients depend on whether the expansion is carried out up to the quadrupole or sextupole order. While this may be irritating at the first sight, it turns out to be logical and in fact not circumventable: Firstly, owing to the fact that parts of the sky are not visible at all to the experiment, the information contained in any data set is not sufficient to reconstruct the true flux distribution up to order infinity. It is mathematically possible to construct a hypothetic flux distribution that resembles well a dipole distribution in a part of the sky (which could be the part visible to the experiment), but which has an overall shape that considerably differs from a dipole. Such an intentionally misleading distribution would involve contributions in many orders, which could obviously not be reconstructed from measured data. Without setting a bound on the number of orders involved to construct the flux distribution, it is impossible to determine any coefficients for the flux distribution, when it is not defined for all directions. Secondly, any measurement suffers from statistical fluctuations owing to which even an isotropic flux distribution, or a plain dipolar one, will have non-zero contributions of higher order in the data set. The question is whether to interpret these higher orders as true contributions or statistical artefacts. The value of $L$ defines the highest order that is still regarded as true contribution. By setting $L = 1$ the multipole reconstruction is reduced to a dipole reconstruction, and is based on the assumption that the true flux distribution has a dipolar shape. When this assumption is correct, the methods presented here are able to reconstruct the dipole vector. However, when this assumption is false, the dipole vector returned may not correctly reflect the dipolar component of the flux distribution.

## 4.6   The East-West Method

A new method, that has recently been proposed, is the East-West method [Arm08, Ghi07, Bon07]. It utilises only the information from each reconstructed air shower event, whether its arrival direction lies within the Eastern or the Western half of the field of view. The observed frequency of air shower events in either of the two halves varies during a sidereal day. The variation may be caused by changes of measurement conditions during data taking, such as temperature changes, and by different cosmic ray fluxes from the different parts of the sky, that can be seen by the experiment as the field of view follows the Earth's rotational motion. While the latter is the effect of the anisotropy, the former is an interfering experimental effect. It can be reduced by carrying out the measurement for a long time and throughout the year, so that it eventually averages out to a certain degree. The East-West method has been developed with the hope to get rid of these effects by solely using the difference of the counting rates of the Eastern and Western hemispheres. This difference is subject to oscillations, and its first harmonic relates to a dipole anisotropy. As the Earth rotates Eastwards, the Eastern sky is closer to the dipole excess region for half a day each day. After the field of view has traversed the excess region, the Western sky is now closer to the excess and therefore bears higher counting rates than the Eastern sky.

The following considerations do not originate from the citations given above, but reflect the author's views. The counting rates at a time $t$ for the two halves of the sky can be computed from the cosmic ray flux as:

$$
\begin{aligned}
E(t) &= \int_{\varphi=0}^{\pi} \int_{\vartheta=0}^{\vartheta_{\max}} \mathrm{d}\varphi\, \sin\vartheta\, \mathrm{d}\vartheta \quad\quad \cos\vartheta \quad\quad \eta(\vartheta,t) \quad\quad A \quad\quad \Phi(\vartheta,\varphi,t) \quad, \\
W(t) &= \int_{\varphi=\pi}^{2\pi} \int_{\vartheta=0}^{\vartheta_{\max}} \underbrace{\mathrm{d}\varphi\, \sin\vartheta\, \mathrm{d}\vartheta}_{\substack{\text{solid angle} \\ \text{element}^{7}}} \underbrace{\cos\vartheta}_{\substack{\text{geometrical} \\ \text{acceptance}}} \underbrace{\eta(\vartheta,t)}_{\substack{\text{experimental} \\ \text{effects}}} \underbrace{A}_{\substack{\text{surface} \\ \text{area}}} \underbrace{\Phi(\vartheta,\varphi,t)}_{\text{flux}} \quad.
\end{aligned}
\tag{4.52}
$$

The experimental effects are represented in the efficiency function $\eta(\vartheta,t)$. In the ideal case this function equals one at all times within the considered range of $\vartheta$, thus for $\vartheta < \vartheta_{\max}$. This reflects the assumption of having full efficiency in the chosen zenith angle range, and having no variation of the measurement rate other than that caused by the actual anisotropy. Experimental effects, however, may lead to a different function $\eta$, which may depend on either or both zenith angle $\vartheta$ and time $t$. Metereological variations, for instance, may add a time dependent component to $\eta$, whereas efficiency shortcomings are likely to depend on the zenith angle. Generally, $\eta$ may depend on $\vartheta$ and $t$ simultaneously. Azimuthal symmetry is assumed, so that $\eta$ is independent from the azimuth angle $\varphi$. The function $\eta$ is meant to represent the true impact of experimental effects. Most of the time, this impact cannot be quantified. Therefore $\eta(\vartheta,t)$ is treated as an unknown quantity, and the aim is to get rid of this quantity in the equations.

Since the integration is carried out over horizontal coordinates, the flux function $\Phi$ depends on those coordinates, and also on the time $t$. Of course, the flux distribution itself is meant to be time-independent. However, the conversion between celestial and horizontal coordinates is time-dependent. Consequently, the flux from a specific viewing direction $(\vartheta,\varphi)$ depends on the time $t$. A dipolar cosmic ray flux distribution shall again be assumed. The direction

---

[7]The zenith angle $\vartheta$ is measured from the zenith, i.e. the North Pole of the coordinate system, not from the horizontal plane. Hence, the solid angle element contains a sine instead of a cosine.

of the dipole vector is constant in equatorial coordinates $(\delta_{\mathrm{dipole}}, \alpha_{\mathrm{dipole}})$, and therefore time-dependent in horizontal coordinates $(\vartheta_{\mathrm{dipole}}(t), \varphi_{\mathrm{dipole}}(t))$:

$$\Phi(\vartheta, \varphi, t) = \Phi_0 \cdot \left(1 + \hat{e}\left(\frac{\pi}{2} - \vartheta, \varphi\right) \cdot \vec{D}^H(t)\right) , \qquad (4.53)$$

with $\vec{D}^H(t)$ being the dipole vector in horizontal coordinates:

$$\vec{D}^H(t) = \begin{pmatrix} D_x^H(t) \\ D_y^H(t) \\ D_z^H(t) \end{pmatrix} = D \cdot \begin{pmatrix} \sin\vartheta_{\mathrm{dipole}}(t)\cos\varphi_{\mathrm{dipole}}(t) \\ \sin\vartheta_{\mathrm{dipole}}(t)\sin\varphi_{\mathrm{dipole}}(t) \\ \cos\vartheta_{\mathrm{dipole}}(t) \end{pmatrix} . \qquad (4.54)$$

On the other hand, $\vec{D}^H(t)$ can also be defined via transforming the dipole vector from equatorial coordinates $(\vec{D})$ to horizontal coordinates. With $\vec{D}$ being defined as $D \cdot \hat{e}(\delta_{\mathrm{dipole}}, \alpha_{\mathrm{dipole}})$, the transformation reads:

$$\begin{aligned}
\vec{D}^H(t) &= \mathbf{R_y}(\tfrac{\pi}{2} - \beta)\, D \cdot \hat{e}(\delta_{\mathrm{dipole}}, h_{\mathrm{dipole}}(t) + \pi) \\[4pt]
&= D \cdot \begin{pmatrix} \cos\beta\,\sin\delta_{\mathrm{dipole}} - \sin\beta\,\cos\delta_{\mathrm{dipole}}\,\cos h_{\mathrm{dipole}}(t) \\ -\cos\delta_{\mathrm{dipole}}\,\sin h_{\mathrm{dipole}}(t) \\ \sin\beta\,\sin\delta_{\mathrm{dipole}} + \cos\beta\,\cos\delta_{\mathrm{dipole}}\,\cos h_{\mathrm{dipole}}(t) \end{pmatrix} , \\[4pt]
h_{\mathrm{dipole}}(t) &= \textit{local mean sidereal time}(t) - \alpha_{\mathrm{dipole}} ,
\end{aligned} \qquad (4.55)$$

with $h_{\mathrm{dipole}}(t)$ being the hour angle of the dipole vector at the location of the experiment and at the time $t$, and $\mathbf{R_y}(\psi)$ being the matrix that rotates the vector on the right hand side around the $y$-axis by the angle $\psi$. $\beta$ denotes the geographical latitude of the experiment.

Plugging the dipole distribution into the definitions of $E(t)$ and $W(t)$, as given above, yields:

$$\begin{aligned}
E(t) &= \int_{\varphi=0}^{\pi} \int_{\vartheta=0}^{\vartheta_{\mathrm{max}}} \mathrm{d}\varphi\,\sin\vartheta\,\mathrm{d}\vartheta\,\cos\vartheta\,\eta(\vartheta, t) \cdot A \cdot \Phi_0 \cdot \\
&\qquad \left(1 + D_x^H(t)\sin\vartheta\,\cos\varphi + D_y^H(t)\sin\vartheta\,\sin\varphi + D_z^H(t)\cos\vartheta\right) ,
\end{aligned} \qquad (4.56)$$

and analogously for $W(t)$ with the $\varphi$ integration ranging from $\pi$ to $2\pi$. For the $\vartheta$ integration, it is convenient to introduce the following set of functions:

$$\mathscr{E}_{ij}(t) = \int_{\vartheta=0}^{\vartheta_{\mathrm{max}}} \sin^i\vartheta\,\cos^j\vartheta\,\eta(\vartheta, t)\,\mathrm{d}\vartheta . \qquad (4.57)$$

At any given time $t$, these $\mathscr{E}_{ij}$ are constants, that reflect the $\vartheta$-dependence of the experiment's efficiency. If the efficiency function $\eta(\vartheta, t)$ actually depends on the time $t$, the $\mathscr{E}_{ij}$ terms are not constant but also time dependent. The $\vartheta$-integration in the above definition of $E(t)$ yields:

$$\begin{aligned}
E(t) = A \cdot \Phi_0 \cdot &\left(\mathscr{E}_{11}(t)\int \mathrm{d}\varphi + D_x^H(t)\mathscr{E}_{21}(t)\int \cos\varphi\,\mathrm{d}\varphi + \right. \\
&\left. D_y^H(t)\mathscr{E}_{21}(t)\int \sin\varphi\,\mathrm{d}\varphi + D_z^H(t)\mathscr{E}_{12}(t)\int \mathrm{d}\varphi\right) ,
\end{aligned} \qquad (4.58)$$

with all integrals over $\varphi$ ranging from $0$ to $\pi$. The function $W(t)$ is identical, except for the different integration range for $\varphi$ from $\pi$ to $2\pi$. The $D_x^H$-contribution vanishes in both $E(t)$

and $W(t)$, whereas the $D_y^H$-contribution stays in both functions, but with different signs. The integrations over $\varphi$ yields:

$$
\begin{aligned}
E(t) &= A \cdot \Phi_0 \cdot \left( \pi \mathscr{E}_{11}(t) + 2D_y^H(t)\,\mathscr{E}_{21}(t) + \pi D_z^H(t)\,\mathscr{E}_{12}(t) \right), \\
W(t) &= A \cdot \Phi_0 \cdot \left( \pi \mathscr{E}_{11}(t) - 2D_y^H(t)\,\mathscr{E}_{21}(t) + \pi D_z^H(t)\,\mathscr{E}_{12}(t) \right).
\end{aligned}
\tag{4.59}
$$

These functions relate to the original dipole parameters in rather complex ways. However, most of these dependencies vanish, when $W(t)$ is subtracted from $E(t)$:

$$
E(t) - W(t) = 4A \cdot \Phi_0 \cdot D_y^H(t)\,\mathscr{E}_{21}(t). \tag{4.60}
$$

Thus, the difference of the event rates in the Western and Eastern halves of the sky is proportional to the total average flux $\Phi_0$, the surface area of the experiment $A$, and last but not least to the $y$-component of the dipole vector in local horizontal coordinates, which in fact is the East-West component. Replacing $D_y^H(t)$ with the definition stated above leads to:

$$
E(t) - W(t) = -4A \cdot \Phi_0 \cdot D \cos \delta_{\text{dipole}} \, \sin h_{\text{dipole}}(t)\,\mathscr{E}_{21}(t). \tag{4.61}
$$

Neglecting the potential time dependency of $\mathscr{E}_{21}(t)$ for a moment, the function $E(t) - W(t)$ performs a harmonic oscillation with a period of one sidereal day, induced by the term $\sin h_{\text{dipole}}(t)$. The amplitude of that oscillation is proportional to $D \cos \delta_{\text{dipole}}$, which denotes the equatorial component of the dipole vector. But it is also still proportional to $\mathscr{E}_{21}(t)$, which generally is time-dependent, and possibly not exactly known for the experiment. Assuming the ideal case of constant and full efficiency, $\mathscr{E}_{21}(t)$ can be computed and amounts to $\sin^3 \vartheta_{\text{max}}/3$. Using that value, the equatorial component of the dipole amplitude can be extracted from the amplitude of $E(t) - W(t)$. However, by making this assumption, the advantages of the East-West method disappear, as it now relies on the same kind of assumption as the other analysis methods. Variations of the efficiency with time, e.g. caused by changing weather conditions, can have the same hazardous effect on this method as on others. If a sudden change of weather conditions leads to a reduction of the total event rate, the same reduction does not only apply to the rates of events from the Eastern and from the Western sky, but also to the difference of the rates.

## 4.7 Summary

The reconstruction of large scale anisotropies, i.e. the deduction of a directional distribution of the cosmic ray flux from a set of measured data, faces several obstacles. The non-uniform coverage of the sky, especially when parts of the sky are not visible at all, which is always the case for a single, ground-based cosmic ray experiment, demands special methods. These methods cannot extract the nature of a possible anisotropy from the data alone. Instead, they imply assumptions on the overall shape of the anisotropy and then reconstruct specific features of it from the data. The most basic assumption, that can be made, apart from the flux being perfectly isotropic, is a dipolar anisotropy. Methods to detect and reconstruct such a dipole have been presented: The Rayleigh analysis is a simple, well understood procedure, that can yield evidence for anisotropy, although it can hardly produce quantitative information. The SAP method is a procedure dedicated to the reconstruction of a dipolar anisotropy. A multipolar expansion of experimental data is possible, although with certain limitations. If an infinite amount of statistics were available, the methods presented here would yield correct results, when applied to flux distributions that suit the assumptions contained therein. However, all

of these methods suffer from the limited availability of statistics. The examination of their potential, in terms of reconstruction accuracy under realistic conditions, shall be the subject of the next chapter.

# Chapter 5

# Monte Carlo Simulation Studies

Several methods for estimating the anisotropy, that is contained in a set of recorded cosmic ray air shower observations, have been described in the preceding chapter. The results are always influenced by the shortcomings of the recorded data, many of which are inevitable. The amount of data available is limited, so that statistical fluctuations distort the results. Even the development of individual air showers in the atmosphere and their detection are influenced by statistical fluctuations, which is one of the reasons, why the arrival directions of the cosmic ray particles can only be determined with finite precision. Shortcomings are not only in the measured data, but also in the methods, as assumptions are made about the shape of the flux distribution, that may or may not meet reality. While it has been shown, that the methods work well under ideal circumstances, more realistic checks are necessary to assess the potential of these methods and interpreting their results.

One way of checking is the creation of sets of simulated data, that reflect a given flux distribution and incorporate effects that would be caused by the experimental circumstances in a real measurement. The creation of such simulated data sets and their application to the reconstruction procedures is the subject of this chapter.

## 5.1   Display of Data Sets

In this chapter and the rest of the thesis, the data on the unit sphere, such as sets of arrival directions, are shown as histograms. It has to be pointed out, that histogramming is only utilised for the presentation of the data sets. The analyses are always carried out with the original list of simulated (or measured) directions, not with the histogrammed data. Dealing with a spherical parameter space has some implications: unlike any Euclidian parameter space, it is impossible to divide the sphere into bins of the same size and shape. The arrangement of bins on the unit sphere used in this thesis is illustrated in Figure 5.1. This method achieves that every bin covers approximately the same solid angle on the sphere. Deviations are of the order of one percent. In addition, the shape of the area of any bin is approximately quadratic (perfectly circular in the case of the top and bottom cap bins). The display of the histograms is based on the Mollweide projection, see the caption of Figure 4.1 for details. Whenever extensive quantities (i.e. quantities that vary with bin sizing, e.g. number of events per bin) are plotted, the colour coding is corrected for the slightly different solid angle coverage of the bins. Not performing this correction would sometimes lead to visible patterns in the plots, that would merely be effected by the binning and have no scientific meaning. For reasons of clarity and readability, the scales printed next to the histograms quote uncorrected (average) numbers, instead of giving values in units of quantity per steradian (solid angle). While the

**Figure 5.1:** Binning of the unit sphere. The sphere is divided into a number of slices of equal size along the declination axis. At the top and the bottom of the sphere two caps remain. Their diameter equals the width of declination slices. Each of the caps forms one bin. Each of the slices inbetween the caps is divided into a variable number of bins, the boundaries being lines of constant right ascension. The number of bins inside one declination slice is chosen such, that the solid angle covered by any of the bins approximates the solid angle of one of the cap bins.
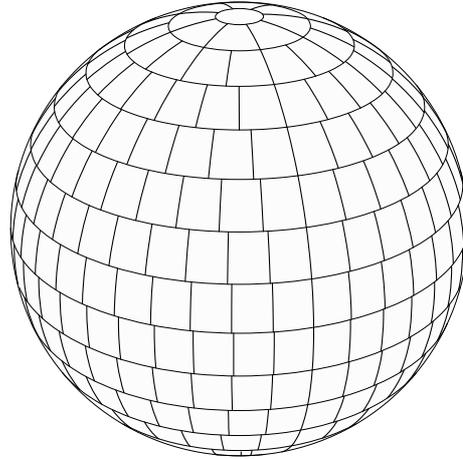
latter would technically be more precise, the former provides the reader with more descriptive indications such as "1,000 events inside one bin" instead of "23.7 events per steradian", and facilitates judging the effect of statistical fluctuations.

## 5.2   The Monte Carlo Generator

The software for producing the sets of simulated data, i.e. the Monte Carlo generator, was developed as a part of this thesis. It is based on the usage of pseudo random numbers, for the creation of which standard library routines are available. These pseudo random numbers are the outcome of an iterative chain of non-linear calculations, which are deterministic and therefore the sequence of random numbers is reproducible. Calling the generator will modify its internal state and return a number that is regarded as being random. The initial state of the generator is called the seed. Each time the Monte Carlo generator software is run, the seed has to be set to a different value at the beginning, since otherwise the generator would produce exactly the same data set again and again. The feature of reproducibility can be very helpful during the development of the Monte Carlo generator software, as along with the random numbers also errors and crashes become reproducible, enabling the developer to test modifications of the source code, that should prevent such errors. The numbers returned by the random number generator are then normalised to lie in the range between 0 and 1. It is inevitable that the distribution of the random floating point numbers has a certain granularity, owed to the fact that these numbers are stored with finite precision. Apart from that, the random numbers are considered equally distributed.

Let $X$ be a random variable with the said characteristics. Let $p_X(X')$ denote the probability that the value of $X$ is less than $X'$. The uniformity of the distribution is then expressed through

$$\frac{\mathrm{d}p_X}{\mathrm{d}X'} = \text{const.}, \quad 0 \le X' < 1. \tag{5.1}$$

Normalisation of the probability function demands that

$$\int_{X'=0}^{1} \frac{\mathrm{d}p_X}{\mathrm{d}X'}\,\mathrm{d}X' = 1 \rightsquigarrow \frac{\mathrm{d}p_X}{\mathrm{d}X'} = 1. \tag{5.2}$$

Random variables with different distributions will be used below. To obtain values for those from the random number generator, mapping functions need to be found, that convert the standard random numbers. That means, for a random variable $Y$ whose behaviour is defined by the integral probability distribution $p_Y(Y')$, the function $Y(X)$ has to be found. Another possibility to obtain random variables with an arbitrary probability distribution is to employ the rejection technique. Each number retrieved from the random number generator is discarded (i.e. rejected) with a probability that depends upon its value. By choosing the rejection probability appropriately, the resulting set of output random numbers will reflect the desired probability distribution. Although the former method cannot always be applied, as it may be impossible to find a suitable mapping function, it should be used whenever possible. The latter method is generally more CPU time consuming, as more random numbers have to be generated and rejection tests have to be performed. It can be very unfavourable, when the fraction of rejected numbers is large. These two methods can be combined, by using mapping functions, which do not effect the intended probability distribution themselves, but allow for the usage of more efficient rejection functions.

The Monte Carlo needs to draw points on the unit sphere (representing the arrival directions) with a given distribution. The points are described by means of two variables: latitude $\beta$ and longitude $\lambda$. Therefore, obtaining one direction requires to obtain two random numbers $X_1$ and $X_2$, which are then transformed to a pair of coordinates:

$$(X_1, X_2) \mapsto (\beta, \lambda). \tag{5.3}$$

The transformation is done with a mapping function that shall reproduce the desired distribution. If no mapping function can be found, that fully achieves this, a mapping will be used that produces a distribution which resembles the wanted distribution as closely as possible, and additionally a rejection function $Rej(\beta, \lambda)$ is applied: a third random number $X_3$ determines whether the obtained coordinates are accepted. This is the case when the value of $X_3$ is larger than the rejection probability $Rej(\beta, \lambda)$. The higher the value of $Rej(\beta, \lambda)$, the smaller the probability that $X_3$ exceeds that value and the obtained coordinates are accepted. Rejection of the coordinates means that the procedure is repeated as many times as necessary with new sets of random variables $X_1, X_2, X_3$.

### 5.2.1 Isotropic Distribution

The isotropic distribution is characterised by the probability of a point lying within a given area being proportional to that area's solid angle:

$$\frac{\mathrm{d}p_{\beta\lambda}}{\mathrm{d}\Omega} = \text{const.}. \tag{5.4}$$

Owing to the symmetry, the probability for a pair of coordinates can be factorised into independent probabilities for latitude and longitude ($p_{\beta\lambda} = p_\beta p_\lambda$). Plugging in the correct term for the solid angle element yields:

$$\frac{\mathrm{d}p_{\beta\lambda}}{\mathrm{d}\Omega} = \frac{\mathrm{d}p_\beta}{\mathrm{d}\beta \cos\beta} \cdot \frac{\mathrm{d}p_\lambda}{\mathrm{d}\lambda} = \text{const.}. \tag{5.5}$$

The following ansatz satisfies this condition:

$$X_1 = \frac{1}{2}(\sin\beta + 1), \quad X_2 = \frac{\lambda}{2\pi}, \tag{5.6}$$

with $X_1$ and $X_2$ being standard random numbers ($dX_1 = dp_\beta$, $dX_2 = dp_\lambda$). Therefore:

$$
\begin{aligned}
\frac{dp_\beta}{d\beta \cos\beta} &= \frac{1}{\cos\beta} \cdot \frac{dX_1}{d\beta} = \frac{1}{\cos\beta} \cdot \left( \frac{1}{2}\cos\beta \right) = \frac{1}{2} = \text{const.}, \\
\frac{dp_\lambda}{d\lambda} &= \frac{dX_2}{d\lambda} = \qquad\qquad\qquad\qquad \frac{1}{2\pi} = \text{const.,} \quad \text{q.e.d..}
\end{aligned}
\tag{5.7}
$$

Because so far only the derivatives have been considered, the boundary values of this mapping have to be checked separately:

$$
X_1 = 0 \Leftrightarrow \beta = -\frac{\pi}{2}, \quad X_1 = 1 \Leftrightarrow \beta = \frac{\pi}{2}, \quad X_2 = 0 \Leftrightarrow \lambda = 0, \quad X_2 = 1 \Leftrightarrow \lambda = 2\pi.
\tag{5.8}
$$

The range of values of $X_1$ and $X_2$ are therefore correctly mapped to those of $\beta$ and $\lambda$. Converting the definitions of $X_1$ and $X_2$ to definitions of $\beta$ and $\lambda$ leads to:

$$
\beta = \arcsin(2X_1 - 1), \quad \lambda = 2\pi X_2.
\tag{5.9}
$$

### 5.2.2 Dipole Distribution

While the probability per solid angle is constant for the isotropic distribution, it depends on the direction for any anisotropic distribution. It is proportional to the flux distribution, but normalised such, that the integral of the probability over the whole unit sphere amounts to one. For the dipole distribution follows:

$$
\frac{dp_{\beta\lambda}}{d\Omega} = \frac{1}{4\pi} \cdot \left[ 1 + \vec{D} \cdot \hat{e}(\beta, \lambda) \right] \propto \Phi_{\text{dipole}}(\beta, \lambda).
\tag{5.10}
$$

A dipole distribution is characterised by its dipole vector $\vec{D}$, the length of which corresponds to the dipole magnitude. The distribution has its maximum in the direction of the dipole vector, where it takes the value $(1 + |\vec{D}|)/4\pi$. The probability distribution's mean value is $1/4\pi$. To obtain random directions with a dipolar distribution, the isotropic mapping function can be used together with the rejection technique. The rejection function needed would be:

$$
Rej(\beta, \lambda) = 1 - \frac{\left. \dfrac{dp_{\beta\lambda}}{d\Omega} \right|_{\beta, \lambda}}{\max\left\{ \dfrac{dp_{\beta\lambda}}{d\Omega} \right\}} = 1 - \frac{1 + \vec{D} \cdot \hat{e}(\beta, \lambda)}{1 + |\vec{D}|}.
\tag{5.11}
$$

The efficiency of the procedure is the mean acceptance $(1 - \overline{Rej})$, the reciprocal of which is the mean number of additional iterations. It turns out, that for a dipole amplitude $D$, $D$ is also the exact amount of the computational overhead. E.g. generating a 30% dipole will need 130% as many sets of random numbers as for the isotropic distribution. Since employing the rejection technique also requires one additional random number $X_3$ (the rejection probability) per iteration, the computational overhead introduced by the increased demand of random numbers amounts to a total of 95%. Therefore it is worthwhile to seek a suitable mapping function, such that dipole-like distributed random directions can be drawn without employing the rejection technique.

Generally, the dipole distribution function depends on both latitude and longitude. It cannot be split into two factors, each of which only depending on latitude or longitude. However,

the situation can be substantially simplified by choosing the dipole vector to be parallel to the $z$-axis, thus perpendicular to the equatorial plane of the coordinate system. This approach does not entail a loss of generality, as the coordinate system used can always be rotated such, that the dipole vector coincides with the $z$-axis. The probability distribution is then given by:

$$\frac{\mathrm{d}p_{\beta\lambda}}{\mathrm{d}\Omega} = \frac{\mathrm{d}p_\beta}{\mathrm{d}\beta\cos\beta} \cdot \frac{\mathrm{d}p_\lambda}{\mathrm{d}\lambda} = \frac{1}{4\pi} \cdot (1 + D\sin\beta) \,. \tag{5.12}$$

It does not depend on the longitude $\lambda$ at all. The following ansatz is made:

$$\frac{\mathrm{d}p_\beta}{\mathrm{d}\beta\cos\beta} = \frac{1}{2}\left(1 + D\sin\beta\right) \,, \quad \frac{\mathrm{d}p_\lambda}{\mathrm{d}\lambda} = \frac{1}{2\pi} \,. \tag{5.13}$$

Two standard random numbers $X_1$, $X_2$ ($\mathrm{d}X_1 = \mathrm{d}p_\beta$, $\mathrm{d}X_2 = \mathrm{d}p_\lambda$) shall be drawn and mapped onto spherical coordinates. Integration of the above ansatz yields:

$$\int\limits_{X_1'=0}^{X_1} \mathrm{d}X_1' = X_1 = \int\limits_{\beta'=-\pi/2}^{\beta} \frac{1}{2}\left(1 + D\sin\beta'\right)\cos\beta'\,\mathrm{d}\beta' = \frac{D}{4}\sin^2\beta + \frac{1}{2}\sin\beta - \frac{D}{4} + \frac{1}{2} \tag{5.14}$$

$$\int\limits_{X_2'=0}^{X_2} \mathrm{d}X_2' = X_2 = \int\limits_{\lambda'=0}^{\lambda} \frac{1}{2\pi}\mathrm{d}\lambda' = \frac{\lambda}{2\pi} \,. \tag{5.15}$$

Rewriting these equations for $\beta$ and $\lambda$ yields:

$$\beta = \arcsin\frac{\sqrt{D^2 + 2D(2X_1 - 1) + 1} - 1}{D} \,, \quad \lambda = 2\pi X_2 \,. \tag{5.16}$$

The boundary conditions are the same as for the isotropic distribution. They are fulfilled by this mapping function.

In order to generate dipoles pointing to an arbitrary direction $(\beta_{\mathrm{dipole}}, \lambda_{\mathrm{dipole}})$, the coordinates obtained through the above mapping have to be rotated by an angle of $\beta_{\mathrm{dipole}} - \pi/2$ around the $y$-axis and subsequently rotated by the angle $\lambda_{\mathrm{dipole}}$ around the $z$-axis.

In order to test the dipole generator, a series of dipole distributions was simulated, see Figure 5.2. When performing simulations with identical parameters, the obtained data sets are by no means identical. The finite amount of simulated directions in a data set leads to statistical fluctuations. Also, the input parameters cannot be reconstructed from the data set with arbitrary precision. This is shown in the histograms in Figures 5.2(e) and 5.2(f). For these histograms, $20,000$ data sets with identical input parameters (3% dipole amplitude, $15°$ declination, $75°$ right ascension) were generated and underwent a Rayleigh analysis. According to Equation 4.38, the right ascension distribution of the simulated dipole has dipolar shape, pointing to $75°$ right ascension. The amplitude is less than the one of the original three-dimensional dipole because of the inclination of the dipole and the dimensional weakening effect, and amounts to $3\% \cdot \cos 15° \cdot \pi/4 \approx 2.3\%$. As can be seen in the histograms, the results of the Rayleigh analyses scatter around their expected values of 2.3% and $75°$. The probability density functions for the outcome of the Rayleigh analysis, as given by Equations 4.34 and 4.36, are plotted as black curves. It has to be emphasised, that those black curves are not the result of a fit. They are theoretical predictions, based on the input parameters of the simulation alone. The good agreement of the histogrammed data and the plotted probability density functions is a strong argument in favour of the correctness of the whole simulation procedure.
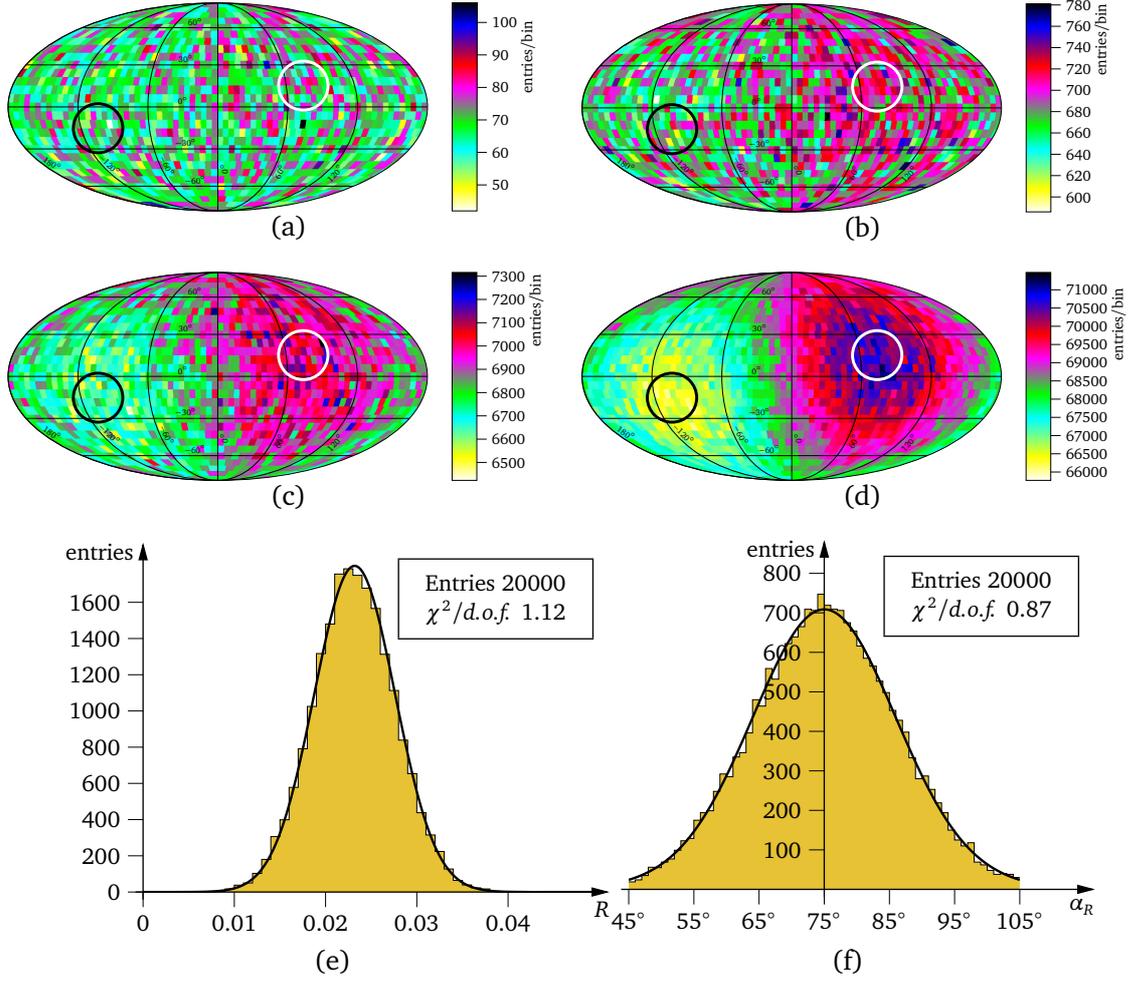
**Figure 5.2:** Monte Carlo simulation of a dipole: four data sets, containing $10^5$ (a), $10^6$ (b), $10^7$ (c) and $10^8$ (d) simulated observations. The entries were drawn from a dipole distribution with an amplitude of 3%. The dipole points towards 15° declination, 75° right ascension (white circles). While the statistical fluctuations outweigh the effect of the dipole in figure (a), the latter becomes more pronounced the larger the data set. The excess in direction of the dipole vector and the deficit in the opposite direction (black circles) are clearly visible in figure (d).

20,000 data sets with 100,000 events each, like the one depicted in Figure (a), were generated. The histograms show the distributions of the obtained Rayleigh amplitudes (e) and Rayleigh phases (f). The black curves are theoretical predictions, according to Equations 4.38, 4.34 and 4.36.

### 5.2.3 Higher Order Multipoles

Multipoles of higher order can generally only be simulated with the rejection technique. The probability is distributed according to

$$\frac{\mathrm{d}p_{\beta\lambda}}{\mathrm{d}\Omega} = \frac{1}{4\pi a_{00}} \sum_{\ell=0}^{\ell_{\max}} \sum_{m=-\ell}^{\ell} a_{\ell m} Y_{\ell m}(\beta,\lambda) \propto \Phi_{\text{s.h.}}(\beta,\lambda). \tag{5.17}$$

The strategy for obtaining a mapping function, that has been used above for deriving the mapping functions of the isotropic and dipolar distributions, does not work in the more general

case here, as the probability distribution cannot be factorised to separate the $\beta$ and $\lambda$ dependencies. The dipole along the $z$-axis is one of the few special cases in which this approach does work. However, the higher order components usually have small coefficients. Therefore the computing overhead introduced by employing the rejection technique should not significantly exceed the value of 50%, which is inevitable owing to the demand of an additional random number to test against the rejection probability.

### 5.2.4 Generation of Experiment-Like Data Sets

The distributions, that have been looked at so far, are meant to reflect the direction dependent cosmic ray intensity. At this point, experimental circumstances have not yet entered the calculations. The most influential experimental property is the inhomogeneous sky coverage, entailed by the limited field of view. The actual sky coverage of an experiment can be calculated and expressed as the direction dependent exposure function $\omega(\delta, \alpha)$. The expected number of observations from any direction is proportional to a function $I(\delta, \alpha)$, which is defined as the product of the exposure function and the assumed flux distribution:

$$I(\delta, \alpha) = \omega(\delta, \alpha)\Phi(\delta, \alpha). \tag{5.18}$$

This observation density function could be used as a probability distribution function for the Monte Carlo generator. This would require an estimate of the upper limit for the values of $I(\delta, \alpha)$, $I_{\max}$. Drawing directions from an isotropic distribution and employing $Rej(\delta, \alpha) = 1 - I(\delta, \alpha)/I_{\max}$ as rejection function would reliably produce a simulated data set, which by construction would reflect the assumed flux and exposure functions. However, the capabilities of this approach are very limited as it is based on the assumption that all experimental effects are exhaustively described by the exposure function. The outcome of the simulation procedure is prescribed by the input probability density function. Actually carrying out the simulation only adds the effect of statistical fluctuations.

The Monte Carlo generator, that was developed for this thesis, follows a different approach. It is modelled on the operation of a cosmic ray experiment. When recording data with an experiment, the set of measured arrival directions (in equatorial coordinates) is influenced by the geographical location of the experiment, by the precise measurement times, by the efficiencies of the detector components, by the reconstruction performance and by the cuts applied to the data set. A calculated exposure map does not enter in the process of data taking and reconstruction at any point. It ought not to enter in the process of simulating a data set, either. Instead, the exposure function is a consequence of the aforementioned aspects. The Monte Carlo programme reproduces those aspects. The analysis routines that work on the data set (either simulated or measured) to reconstruct the properties of the anisotropy, however, take the exposure map into account.

The procedure is divided into six steps. Step 1: an arrival direction (in equatorial coordinates) is drawn from the assumed flux distribution. This direction is considered the true arrival direction $\delta_{\text{true}}$, $\alpha_{\text{true}}$, since it has been drawn from the distribution that stands for the true flux distribution of cosmic rays within the framework of this simulation. In addition to the arrival direction, a sidereal time of the day $t$ is chosen randomly, either from a flat distribution, or from a distribution that represents the measurement periods of the experiment. The former alternative assumes, that the measurement is conducted in periods of full sidereal days, whereas the latter allows, that the experiment is operated during arbitrary periods. The idea behind this first step is, that the Earth is constantly being hit by cosmic ray particles, and that the arrival directions of those comply with the given distribution. In this first part of

the simulation chain, the arrival times and directions of particles hitting the Earth (and not necessarily the experiment) are drawn. The flux has implicitly been assumed as constant in time.

Step 2: the equatorial coordinates $\delta_{\text{true}}$, $\alpha_{\text{true}}$ are transformed into local viewing directions (horizontal coordinates) $\vartheta_{\text{true}}$ (zenith angle), $\varphi_{\text{true}}$ (azimuth angle). This transformation depends on the sidereal time of the day, which is also the reason why it is generated in Step 1, as well as on the geographical location of the experiment. Since the directions are generated in Step 1 from the true flux distribution, they are by no means confined to the field of view of the experiment. Therefore, many of the viewing directions computed here lie outside the field of view or even below the horizon.

Step 3: directions, that lie way outside the field of view, are discarded. The field of view is defined by an upper limit of the zenith angle $\vartheta$, $\vartheta_{\text{max}}$.

Step 4: the true arrival direction $\vartheta_{\text{true}}$, $\varphi_{\text{true}}$ is reconstructed by the experiment as $\vartheta_{\text{rec}}$, $\varphi_{\text{rec}}$. The limited accuracies of measurement and reconstruction are simulated in this step. The reconstructed coordinates are chosen from a Gaussian distribution around the true coordinates. For a realistic emulation of the experiment, the width of the Gaussian distribution (i.e. the angular resolution) has to be assessed by means of full air shower and detector simulations beforehand. Taking into account, that the reconstruction error could shift observations from outside to inside the defined field of view, only those events must be discarded in Step 3, that practically cannot be misreconstructed into the field of view.

Step 5: applying the detector, reconstruction and analysis efficiency. The simplest approach is, that the efficiency is considered to be 100% for all events with zenith angles smaller than $\vartheta_{\text{max}}$. More inclined events are discarded in the analysis, which is due to a cut on the zenith angle, and therefore are also discarded here. Basically, this is a strict cut on zenith angle, but in contrast to Step 3, this cut is on the reconstructed zenith angle, not the true one. However, it is possible to simulate more complicated scenarios, e.g. a small efficiency defect for highly inclined showers.

Step 6: transformation back to equatorial coordinates $(\delta_{\text{rec}}, \alpha_{\text{rec}})$. These constitute the final result of the simulation chain and enter the data set.

A great share of the simulated particles is discarded in Steps 3 and 5, most often because the particle in question cannot be seen by the experiment. It is vital, that the simulation restarts at Step 1, so that a new direction and a new time are drawn from their corresponding distributions, once a particle gets rejected. Keeping the direction of the discarded event and only reassigning the time, or vice versa, would lead to distortions in the resulting data set. E.g., if the Monte Carlo generator did reuse the chosen time across rejections until the particle finally got accepted, the output distribution of incident times would equal the distribution the times were drawn from. This, however, is not intended. While the cosmic ray flux is assumed to be constant in time, this does not necessarily apply to the observation rate of the experiment. While the experiment is facing regions of the sky that expose an excess or deficit in flux, the event rate of the experiment experiences modulation. The procedure described above implicitly takes account of this modulation, as it is reproduced by the rejection of events in Steps 3 and 5. The assumption that lies in the approach taken here is, that not the experiment but the Earth is hit by cosmic rays with a constant rate.

Data sets of arbitrary size can be generated by repeating this simulation chain. The distributions of arrival directions in the so obtained data sets should resemble the function $I(\delta, \alpha)$, that has been defined earlier. However, when experimental effects are simulated, that are not considered in the calculation of the exposure function, the outcome of this more sophisticated simulation procedure may differ from the analytically obtained function $I(\delta, \alpha)$.
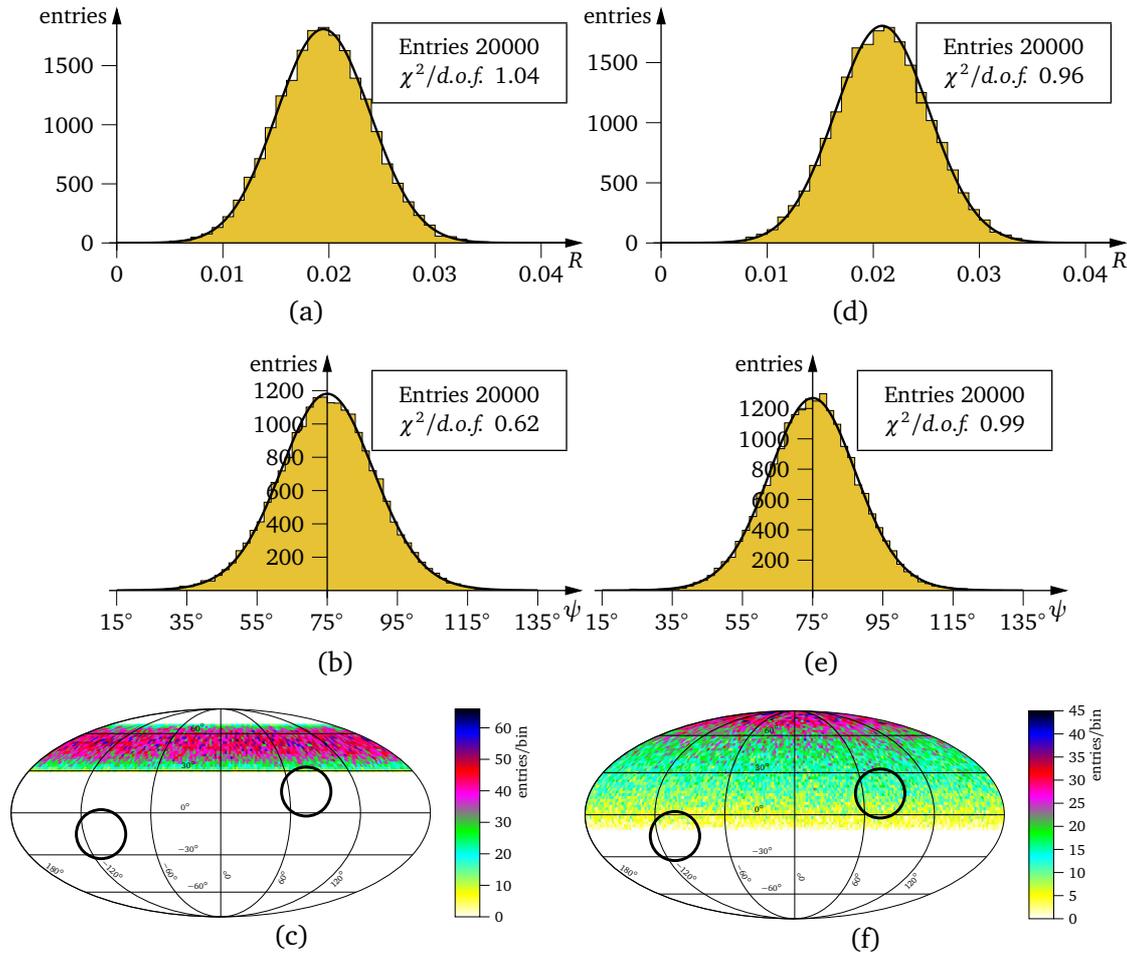
**Figure 5.3:** Reconstructed Rayleigh amplitudes (a) and phases (b) for simulated data sets. Subject of the simulations is a hypothetic experiment located at 49° North latitude with a zenith limit of 20°, which is exposed to a dipole flux distribution with an amplitude of 3%, pointing towards 75° right ascension at 15° declination. Each of the 20,000 simulated data sets comprises 100,000 observations. One such data set is depicted in Figure (c), in which the upper and lower circles mark the excess and deficit regions of the dipole, respectively. Figures (d), (e) and (f) show the corresponding plots for a zenith limit of 60°.

The black curves are theoretical predictions, according to Equations 4.41, 4.34 and 4.36.

### 5.2.5 Tests of the Monte Carlo Generator

In addition to the checks of the dipole generator discussed above and illustrated in Figure 5.2, the Monte Carlo generator can be tested for those cases which can also be explained analytically. There is an analytical description for the result of a Rayleigh analysis in the case of partial sky coverage, provided that the exposure does not depend on the right ascension coordinate. Given a dipole-like flux distribution, the geographical location of the experiment and its opening angle, and assuming precise reconstruction and full efficiency for all observations within the defined field of view, the distribution of recorded right-ascension values is also dipolar and can be predicted according to Equation 4.41. When perfoming a series of Monte Carlo simulations, the sample of reconstructed amplitudes and phases shall be distributed according to Equations 4.34 and 4.36.

Such a test was carried out and the results are shown in Figure 5.3. The configuration of the simulated dipole was the same as in the test of the dipole generator in Section 5.2.2: amplitude 3%, declination 15°, right ascension 75°. The expected Rayleigh amplitude depends on experimental features. The geographic location of the experiment used in the Monte Carlo simulations is 49° North latitude. Assuming a very narrow field of view, with a maximum zenith angle of only 20°, the sky coverage of the experiment is characterised by the following values of the $C_{ij}$ constants, as outlined in Section 4.3.4:

$$C_{20} \approx 0.658 \, , \quad C_{11} \approx 0.733 \, .$$

These values have been obtained by numerical integration of the exposure function of this scenario. Accordingly, the Rayleigh amplitude of the right ascension distribution is expected to be approximately 1.90% (see Equation 4.41). The black curve in Figure 5.3(a) describes the distribution of obtained Rayleigh amplitudes when working with data sets with finite size, here 100,000 events, according to Equation 4.34. In total, 20,000 of such simulated data sets were produced. The histogram in the same figure shows the outcome of the Monte Carlo simulations. It is practically coincident with the theoretical prediction. So is the distribution of the phase values, as shown in Figure 5.3(b).

A second set of Monte Carlo simulations was carried out with identical parameters, except for the zenith limit, which was set to 60°. Even though the underlying flux distribution is the same as for the former set, the expected Rayleigh amplitude is different. The broader field of view results in a different sky coverage, this time characterised by:

$$C_{20} \approx 0.706 \, , \quad C_{11} \approx 0.588 \, .$$

The correct Rayleigh amplitude in this scenario amounts to approximately 2.04%, which is slightly higher than in the former case. Along with these quantities, the distributions of the individual results of Rayleigh analyses have changed. These are depicted in Figure 5.3(d) and Figure 5.3(e). Again, the obtained samples conform perfectly with the analytical predictions.

The conclusion to be drawn from these tests is, that the Monte Carlo generator correctly reproduces the effect of a constrained field of view. Not all of the six steps of the event simulation, that have been described in the previous section, could be reviewed in this test. The reconstruction has been treated as perfectly accurate (thus Step 4 was bypassed), and no efficiency defects have been simulated (in Step 5), as there is no way to incorporate these effects into the analytical predictions. For the same reason, this test has been restricted to the case of data taking during full sidereal days with constant measurement conditions. However, where comparisons to analytical considerations are possible, the Monte Carlo generator has been proven to work. In the following sections, more situations will be studied, that cannot be handled analytically: either because the experimental effects are too complex, or because reconstruction algorithms other than the Rayleigh analysis will be used, for which the output distributions are not known. These situations can only be accessed by means of Monte Carlo simulations.

## 5.3   Tests of Reconstruction Methods

In this section, data sets created with the Monte Carlo generator, that has been introduced above, are analysed with different methods. The aim is to evaluate the potential of the methods in terms of correctness and accuracy. The data sets all reflect the ideal experimental case: the exposure function does not vary with right ascension, the reconstruction of arrival directions

is perfectly accurate, and the detection takes place with full efficiency. These are the ideal circumstances, that are implicitly assumed by the reconstruction methods.

### 5.3.1 A Quantitative Measure of the Reconstruction Quality

In order to assess the quality of the reconstruction techniques, that are applied in the sections below, it is necessary to have a quantitative measure of the reconstruction quality, that can be obtained through Monte Carlo simulations. The accuracy of the reconstruction of properties of the original flux distribution is affected by the amount of statistics available, but may vary subject to the reconstruction method used. In the realisitic case of the amount of available statistics being limited, the reconstruction results are subject to fluctuations. Therefore, the production and analysis of a single data set cannot give conclusive information on the general accuracy of the method used. Instead, a series of Monte Carlo data sets with common input parameters has to be produced. The individual analyses will yield different results. The values obtained for any of the properties will behave according to a certain (usually unknown) distribution, of which the series of Monte Carlo simulations reveals a sample. From this sample, the distribution's mean value and scatter can be estimated. The mean value should comply within its errors with the true value, i.e. the input value to the Monte Carlo simulation, of the considered property. Otherwise, the reconstruction method introduces a systematic deviation, or bias. The width of the distribution is desired to be as small as possible, as it corresponds to the statistical error of the reconstruction of a single data set. A reconstruction method can generally be regarded as good, when the mean reconstructed value matches the true value, and the scatter around this mean value is small. A suitable measure to quantify the combination of these two aspects is the second algebraic moment of the distribution $x - x_{\text{true}}$, with $x$ representing the property being reconstructed (e.g. dipole amplitude) and $x_{\text{true}}$ being its corresponding true value. The second algebraic moment $\mu'_2$ shall henceforth be called the quality measure $q^2$ and is defined as

$$q^2 = \mu'_2 = \overline{(x - x_{\text{true}})^2}, \tag{5.19}$$

thus being the mean square deviation of the reconstructed values of $x$ with respect to the true value $x_{\text{true}}$. In the ideal case of an unbiased reconstruction, the mean value of $x$ matches $x_{\text{true}}$, so that the $x - x_{\text{true}}$-distribution has a mean value very close to zero. If so, the quality parameter $q^2$ is the same as the variance $\sigma^2$ of the $x - x_{\text{true}}$-distribution, which is identical to the variance of the $x$-distribution itself. However, when the reconstructed values $x$ show a systematic deviation from the true value, the quality parameter $q^2$ combines the scatter of the distribution and its deviation from the true value:

$$\begin{aligned} \sigma^2 &= \text{V}\left[x - x_{\text{true}}\right] = \overline{(x - x_{\text{true}})^2} - \overline{(x - x_{\text{true}})}^2 = q^2 - (\overline{x} - x_{\text{true}})^2 \\ \Rightarrow q^2 &= \sigma^2 + (\overline{x} - x_{\text{true}})^2. \end{aligned} \tag{5.20}$$

It turns out, that $q^2$ is the squared sum of the standard deviation and the offset of the mean value with respect to the true value.

The quality of a reconstruction method shall be estimated from a series of Monte Carlo simulations. Such a series has to consist of Monte Carlo simulations that have been carried out with identical input parameters. For each of the reconstructed properties, the quality measure $q^2$ shall be estimated. Therefore, the obtained values of $q^2$ are only valid for the input parameters used. Repeating this procedure with varying input parameters may reveal a systematic relationship between input parameters and reconstruction quality. To give an example, the reconstruction quality of the dipole amplitude might depend on the inclination

of the dipole with respect to the equatorial plane. However, in order to investigate such relationships, it is crucial that not only the quality measure $q^2$ can be estimated from a series of Monte Carlo simulations, but also that the statistical error of this estimation can be quantified.

An unbiased estimator for $q^2$ can be calculated from a sample of $N$ reconstructed values $x_i$ as follows:

$$q^2_{\text{est}} = m'_2 = \frac{1}{N} \sum_{i=1}^{N} (x_i - x_{\text{true}})^2 . \tag{5.21}$$

The statistical error of this estimator is given by the square root of its variance. An unbiased estimator of the variance is given by:

$$\text{V}\left[m'_2\right]_{\text{est}} = \frac{1}{N-1} \cdot \left(m'_4 - m'^2_2\right) , \quad m'_4 = \frac{1}{N} \sum_{i=1}^{N} (x_i - x_{\text{true}})^4 . \tag{5.22}$$

While this expression estimates the variance correctly, its square root is not an unbiased estimator for the distribution's standard deviation. However, it is not possible to formulate an unbiased estimator for the standard deviation without making assumptions on the precise shape of the underlying distribution. For a normal distribution, which the samples encountered here closely resemble, and for $N$ greater than 10, the term $\frac{1}{4}/(N-1)$ is a good approximation of the necessary relative correction [Joh94]. The magnitude of the underestimation turns out to be negligible for the sample sizes used here. Hence, $q^2$ can finally be estimated as

$$q^2_{\text{est}} = m'_2 \pm \sqrt{\frac{1}{N-1} \cdot \left(m'_4 - m'^2_2\right)} . \tag{5.23}$$

For the full derivation of these estimators, see Appendix B. It is convenient to quote the square root of $q^2$, thus $q$, as the final result, because it is dimensionally consistent with the quantity in question. The corresponding error can be derived by error propagation from the former expression, leading to the final formula:

$$q_{\text{est}} = \sqrt{m'_2} \pm \frac{1}{2}\sqrt{\frac{1}{N-1} \cdot \frac{m'_4 - m'^2_2}{m'_2}} , \quad m'_r = \frac{1}{N} \sum_{i=1}^{N} (x_i - x_{\text{true}})^r . \tag{5.24}$$

Again, the square root of $m'_2$ is not an unbiased estimator for $q = \sqrt{\mu'_2}$. The same considerations as above apply.

To summarise, the quality estimator $q$ is a quantity that evaluates the quality of the reconstruction of a parameter $x$, on the basis of a series of $N$ Monte Carlo simulated data sets. The parameter $x$ is reconstructed from each of the $N$ data sets with a given method, yielding $N$ individual results $x_i$ $(i = 1, \ldots, n)$. The quality estimator $q$ can be computed from the obtained sample of $x_i$-values and the true value of $x$ $(x_{\text{true}})$, which is an input parameter to the Monte Carlo simulation. The meaning of $q$ is closely related to that of the standard deviation $\sigma$. In fact, if the reconstruction of the $x$-parameter is completely unbiased, i.e. its mean value coincides with the true value, $q$ and $\sigma$ are identical. In case of a systematic deviation called forth by the reconstruction procedure, the offset between mean reconstructed value and true value contributes to $q$ as an additional penalty. Therefore, $q$ reflects the reconstruction accuracy of any one individual data set: the inaccuracy may stem from either or both systematic deviation and statistical fluctuation.

By definition, the quality value $q$ can never be smaller than the standard deviation $\sigma$. However, when estimating $q$ and $\sigma$ from the available samples, the estimation of $q$ can yield

slightly smaller values than that of $\sigma$. For a sample of $N$ values, the calculation of the standard deviation $\sigma$ features a factor $N/(N-1)$, which accounts for the fact, that $\sigma$ is calculated with respect to the sample mean instead of the true mean value of the distribution. This penalty does not occur in the calculation of $q$, which is done with respect to the true parameter value, which is a given, error-free number.

### 5.3.2 The Standard Parameters for Simulated Data Sets

The following sections will present the results obtained from many thousand simulated data sets. The standard configuration, with which the sets were created, are the following:

- a dipole distribution with an amplitude of 3%, with the dipole excess located at $\delta_{\text{dipole}} = 30°$ and $\alpha_{\text{dipole}} = 75°$,

- an experiment located at $\beta = 49°$ Northern latitude,

- a field of view spanning from the vertical to a maximum inclination of $\vartheta_{\text{max}} = 60°$,

- an uninterrupted measurement, thus constant coverage of the sidereal day,

- no spurious experimental effects, i.e. full efficiency for all arrival directions, and constant measurement conditions,

- and a data set size of 1 million events.

First, the reconstruction results obtained for 1,000 data sets, that were generated with this configuration, shall be presented for the different reconstruction methods. Then, single properties of this configuration shall be varied and the effect on the reconstruction quality examined.

### 5.3.3 Rayleigh Analysis

The Rayleigh analysis reconstructs the Rayleigh amplitude and phase from a data set. While the latter directly estimates the right ascension coordinate of the dipole vector, the former quantity is only indirectly related to the dipole amplitude. The reconstruction quality of the Rayleigh amplitude therefore is of minor interest, as the quantity itself can only be interpreted with the knowledge of the dipole vector's declination coordinate, which cannot be determined through a Rayleigh analysis. However, the reconstruction quality of the right ascension is indeed of interest, as other reconstruction methods compete with the Rayleigh analysis in this field. The distributions of the Rayleigh amplitudes and phases obtained for the 1,000 simulated data sets with the standard parameters are shown in Figure 5.4. Both amplitude and phase values scatter around their true values. In both distributions, the mean values are compatible with the corresponding true value. Therefore, the values of the standard deviations, that are computed from each of the samples, are practically identical to the corresponding values of the quality measure $q$. For the given standard dipole configuration, the Rayleigh procedure estimates the Rayleigh amplitude with an error of ca. 0.14% and the phase with an error of ca. 4.4°.

### 5.3.4 The SAP Method

The SAP method yields estimates for both dipole amplitude and three-dimensional direction. Figure 5.5 shows the distributions of obtained dipole amplitudes, declinations and right ascensions. Again, all quantities scatter around their true values, which are compatible with the

| Entries | 1000 |
|---|---|
| Sample mean | $1.817 \pm 0.0045$ |
| Sample std. dev. | $0.141 \pm 0.0032$ |
| $q$ | $0.141 \pm 0.0031$ |

| Entries | 1000 |
|---|---|
| Sample mean | $74.78 \pm 0.14$ |
| Sample std. dev. | $4.45 \pm 0.099$ |
| $q$ | $4.45 \pm 0.096$ |

(a)                                                    (b)
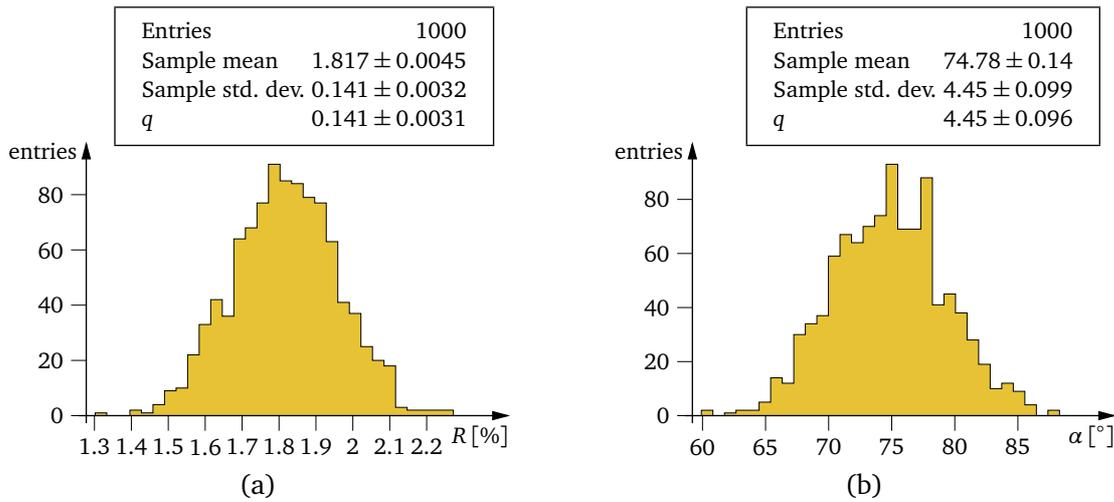
**Figure 5.4:** Rayleigh analysis applied to simulated data sets: 1,000 data sets with 1 million events each were simulated and analysed. Figure (a) displays the obtained Rayleigh amplitudes, which scatter around the expected value, which amounts to approximately 1.82% for the chosen configuration (see Section 5.3.2). The distribution of obtained Rayleigh phases is shown in Figure (b).

statistical means of the samples. In case of the standard dipole configuration used here, the amplitude is estimated by the SAP method with an error of about 0.30%. The error of the declination and right ascension estimates are 8.5° and 5.4°. The reconstruction of the right ascension value works slightly less precisely than with the Rayleigh analysis, which produced an error of only 4.4°.

Figure 5.5(d) shows the distribution of the angles between true and reconstructed dipole directions, thus combining declination and right ascension reconstruction. The reconstructed direction is off by ca. 8° on average. The quality measure $q$ is computed with respect to 0 as true value, because a fully correct reconstruction returns the true direction and corresponds to an angular difference of 0° (being the "true" value of this quantity). The resulting quality measure, thus the error of the reconstructed direction, amounts to 9.4°.

### 5.3.5   Multipole Expansion For Dipole Reconstruction

Like the SAP method, the multipole expansion method reconstructs both amplitude and three-dimensional direction of the dipole. The reconstruction results for the present series of 1,000 simulated data sets with standard configuration are depicted in Figure 5.6. In this configuration, the multipole expansion method outperforms the SAP method in all categories. The error of the dipole amplitude reconstruction amounts to ca. 0.24%, as opposed to 0.32% for the SAP method, which is a statistically significant difference of more than $9\sigma$. It should be noted, that the better performance of the multipole expansion method is characterised by the information that its error of the amplitude reconstruction, in the case of the specific configuration used here, is smaller than that of the SAP method by about one third. The statement that the difference corresponds to a statistical significance of $9\sigma$ is to underline the safety of this conclusion only. The value of $9\sigma$ is not a property of the reconstruction methods, as it can be raised further by carrying out more Monte Carlo simulations. However, the number of 1,000 Monte Carlo data sets is sufficient to conclude safely, that the multipole expansion yields more precise results for the dipole amplitude than the SAP method.

| Entries | 1000 |
|---|---|
| Sample mean | $3.016 \pm 0.0096$ |
| Sample std. dev. | $0.304 \pm 0.0068$ |
| $q$ | $0.304 \pm 0.0066$ |

(a)

| Entries | 1000 |
|---|---|
| Sample mean | $28.5 \pm 0.27$ |
| Sample std. dev. | $8.40 \pm 0.19$ |
| $q$ | $8.5 \pm 0.20$ |

(b)

| Entries | 1000 |
|---|---|
| Sample mean | $74.75 \pm 0.17$ |
| Sample std. dev. | $5.38 \pm 0.12$ |
| $q$ | $5.38 \pm 0.12$ |

(c)

| Entries | 1000 |
|---|---|
| Sample mean | $8.43 \pm 0.15$ |
| Sample std. dev. | $4.88 \pm 0.11$ |
| $q$ | $9.74 \pm 0.18$ |

(d)
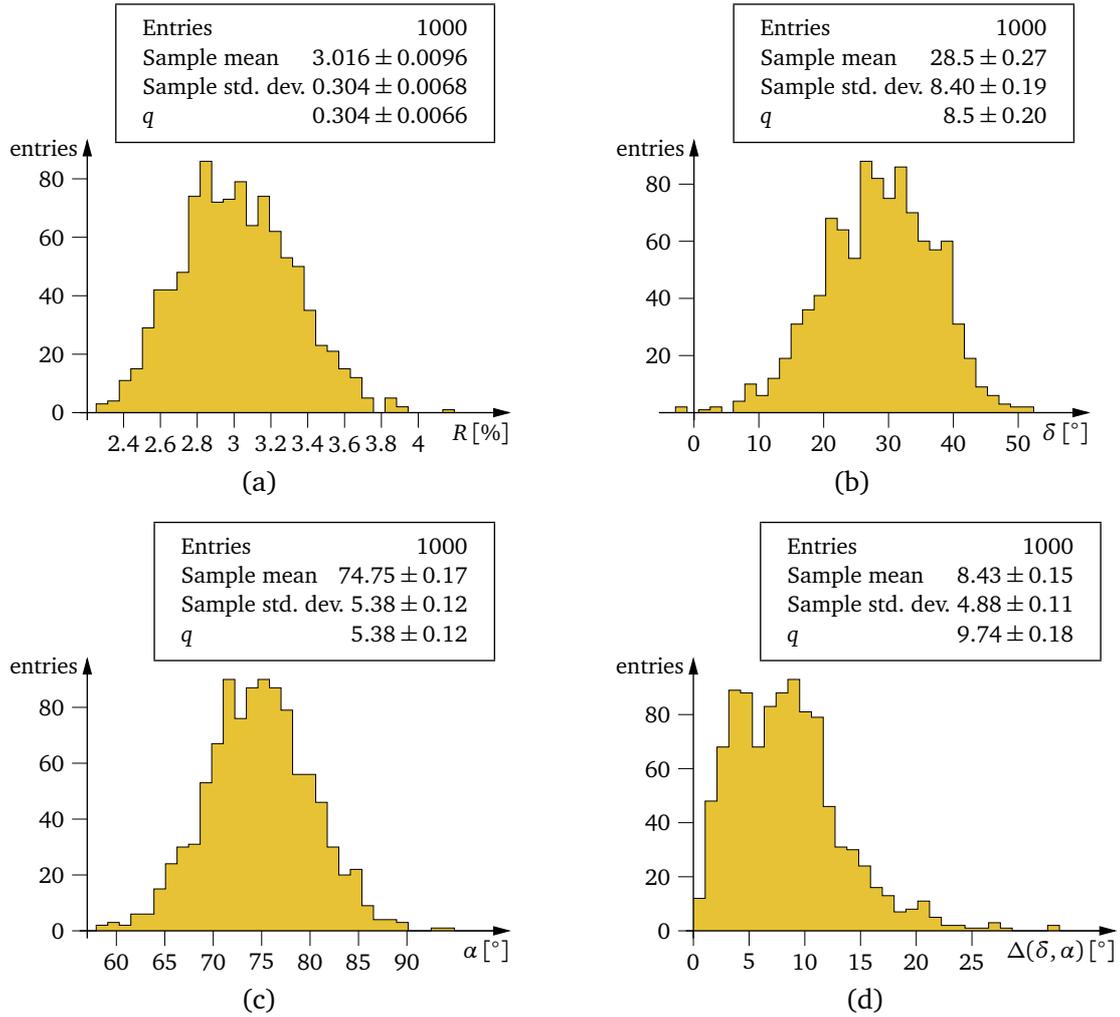
**Figure 5.5:** SAP method applied to simulated data sets: 1,000 data sets comprising 1 million events each were simulated with standard configuration (see Section 5.3.2). The obtained dipole amplitudes are displayed in Figure (a), declination values are shown Figure (b), and right ascension values are shown in Figure (c). Figure (d) displays the distribution of angular distances between the reconstructed dipole direction and the true one.

The error of the declination reconstruction amounts to 5.6° (SAP method: 8.1°, difference $> 10\sigma$), and the error of the right ascension reconstruction amounts to 4.1° (SAP method: 5.4°, difference $> 8\sigma$). The overall error of the dipole direction is 6.6° (SAP method: 9.4°, difference $> 10\sigma$).

## 5.4 The Influence of Configuration Parameters

The results, that have been presented in the previous section, have been obtained with the standard configuration for Monte Carlo production, as given in Section 5.3.2. That configuration fully defines the simulation scenario, including a number of experimental properties and the shape of the simulated cosmic ray flux distribution. The experimental properties include geographical location of the experiment and the boundary of the field of view, represented by the maximum shower inclination $\vartheta_{\mathrm{max}}$. Another experimental property is the measurement
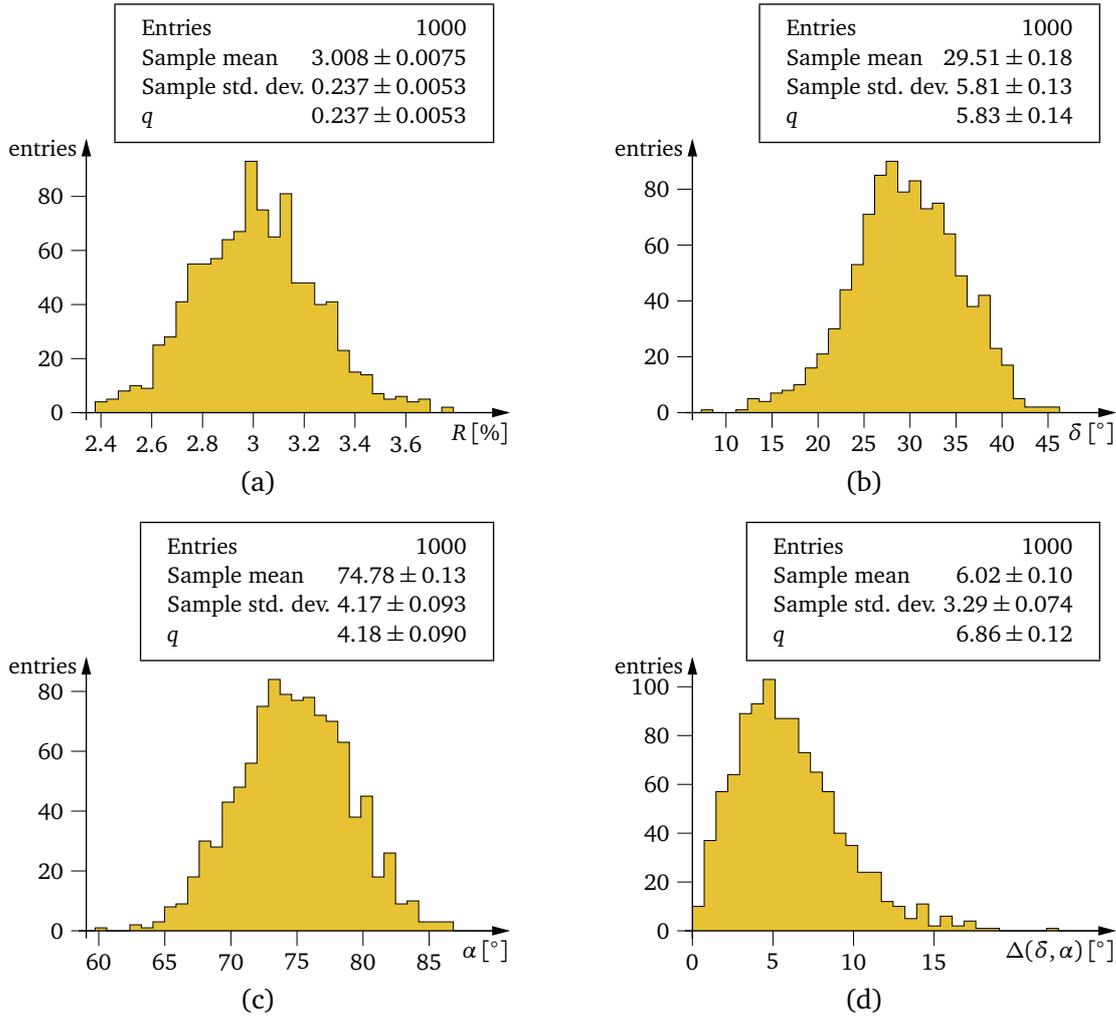
| Entries | 1000 |
|---|---|
| Sample mean | $3.008 \pm 0.0075$ |
| Sample std. dev. | $0.237 \pm 0.0053$ |
| $q$ | $0.237 \pm 0.0053$ |

(a)

| Entries | 1000 |
|---|---|
| Sample mean | $29.51 \pm 0.18$ |
| Sample std. dev. | $5.81 \pm 0.13$ |
| $q$ | $5.83 \pm 0.14$ |

(b)

| Entries | 1000 |
|---|---|
| Sample mean | $74.78 \pm 0.13$ |
| Sample std. dev. | $4.17 \pm 0.093$ |
| $q$ | $4.18 \pm 0.090$ |

(c)

| Entries | 1000 |
|---|---|
| Sample mean | $6.02 \pm 0.10$ |
| Sample std. dev. | $3.29 \pm 0.074$ |
| $q$ | $6.86 \pm 0.12$ |

(d)

**Figure 5.6:** Multipole expansion method applied to simulated data sets: 1,000 data sets comprising 1 million events each were simulated with standard configuration (see Section 5.3.2) and analysed. The obtained dipole amplitudes are displayed in Figure (a), declination values are shown Figure (b), and right ascension values are shown in Figure (c). Figure (d) displays the distribution of angular distances between the reconstructed dipole direction and the true one.

time, which is represented here by the size of a single data set, thus the number of events each data set comprises. While these properties are input parameters to and being accounted for by the SAP and multipole expansion method, the Rayleigh analysis ignores them. As a result, SAP and multipole expansion method produce results which do not depend on these properties (their precision, however, may), whereas the amplitude value returned by the Rayleigh procedure varies for different experimental configurations. In the following sections, the simulation parameters are varied one at a time, and the impact on the reconstruction accuracies of dipole amplitude and declination (as provided by the SAP and the multipole expansion method) as well as the dipole right ascension (as provided by all three methods) are investigated. Furthermore, the configuration parameters of the simulated dipole distribution are varied as well. For each individual set of configuration parameters, a series of 1,000 Monte Carlo data sets was simulated and analysed with the SAP and multipole expansion method, and with the Rayleigh
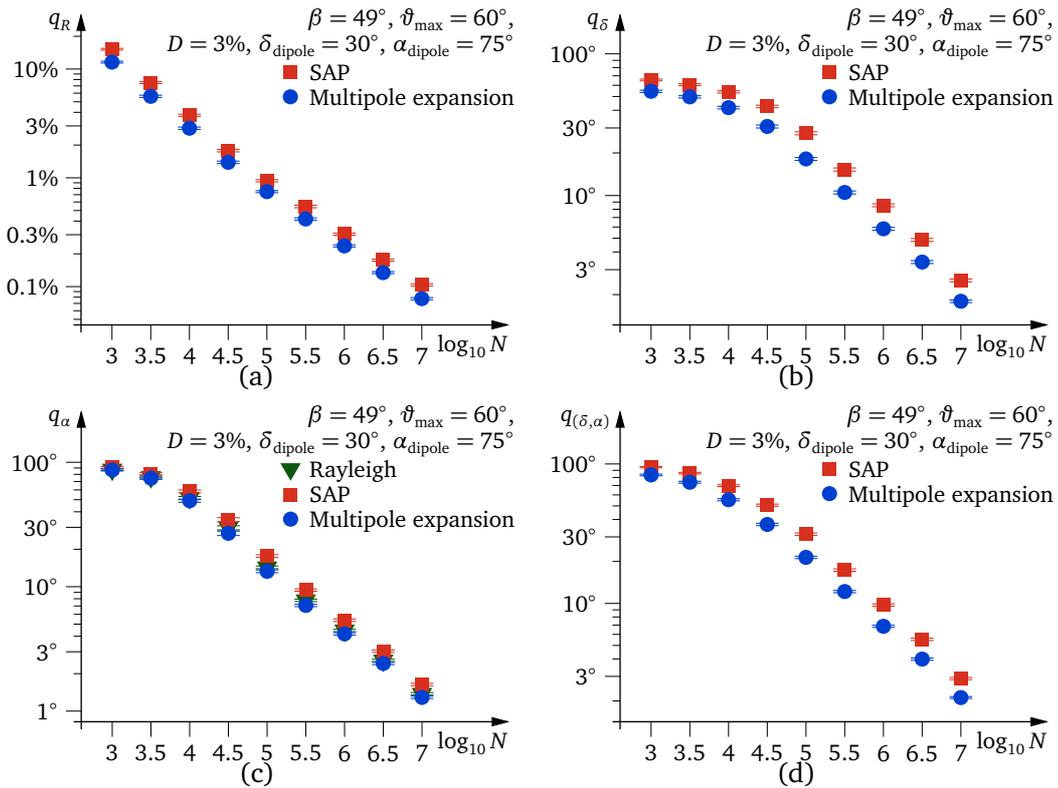
**Figure 5.7:** Reconstruction quality subject to number of simulated events

analysis where applicable. The dependency on each of the configuration parameters is illustrated by plots showing the values of the quality measure $q$ for dipole amplitude, declination, right ascension and direction (combined declination and right ascension) for a series of different values for the respective parameter on the x-axis. For every one of these values, another series of 1,000 Monte Carlo data sets was generated. Both (or all three) methods act on the same data sets: the differently coloured points inside the same column of the plots are highly correlated. The error bars shown represent statistical errors of the determination of the value of $q$ from the sample of 1,000 reconstruction results with respect to the true value.

### 5.4.1 Number of Simulated Events

Figure 5.7 depicts the relation between reconstruction quality and the number of simulated events per data set. Data set sizes range from $10^3$ to $10^7$ events. The amplitude reconstruction, the quality of which is displayed on a double-logarithmic scale in Figure 5.7(a), follows a power law for both SAP and multipole expansion method: the quality improves by a factor of ten as the statistics increases by a factor of 100. Thus, the amplitude error is proportional to one over the square root of the number of events. The multipole expansion method keeps being the favourable method over the whole range, with errors approximately 25% lower than those of the SAP method.

Declination, right ascension and combined direction reveal a similar power law behaviour. Owing to the directional nature of these quantities, their errors cannot be infinitely large. Going to very small data set sizes, the error saturates at a maximum value as the results become virtually arbitrary. The power law behaviour sets in at a size of about 30,000 events. Again, the SAP method is constantly outperformed by the multipole expansion method, except
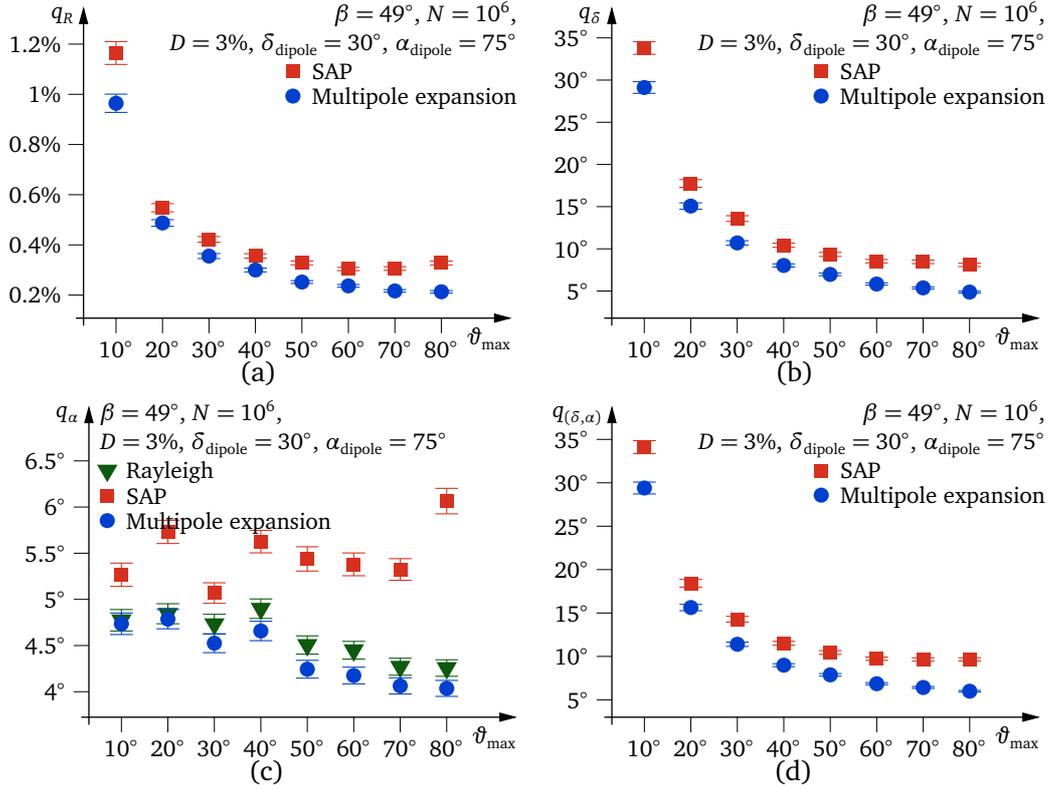
**Figure 5.8:** Reconstruction quality subject to zenith angle limit

for the reconstruction of the right ascension coordinate with very small data sets of less than 30,000 events, where SAP and multipole expansion method deliver comparable results. For such small data sets, the Rayleigh analysis yields slightly more precise results. However, with that little statistics available, none of the methods can narrow down the direction of the dipole vector very well. With larger data sets, the right ascension precision of the Rayleigh analysis is equal to that of the multipole expansion method.

In case of the simulation parameters used here, most importantly with a dipole amplitude of 3%, a data set with at least 100,000 events is necessary to determine the dipole amplitude at a percent level. One million events are needed to identify the dipole direction with an error better than 10°.

### 5.4.2 Zenith Angle Limit

Figure 5.8 illustrates the influence of the extent of the field of view towards inclined directions. The overall trend is that the reconstruction of each of the dipole parameters improves the larger the field of view. Zenith angle limits below 30° are strongly disfavoured. Above 40°, the additional gain in quality is less substantial. There might even be the effect that the quality of the SAP method degrades with very large zenith angle limits. However, the error bars suggest that the indication of this effect is not very significant. It might be a case of a random statistical artefact.

All data sets, that were simulated for Figure 5.8, contain one million events. It should be noted, that for a given experiment the choice of a larger field of view automatically results in a larger amount of statistics being available for analysis. The number of events scales with $\sin^2 \vartheta_{\max}$, taking into account the geometric circumstances only. Experimental effects
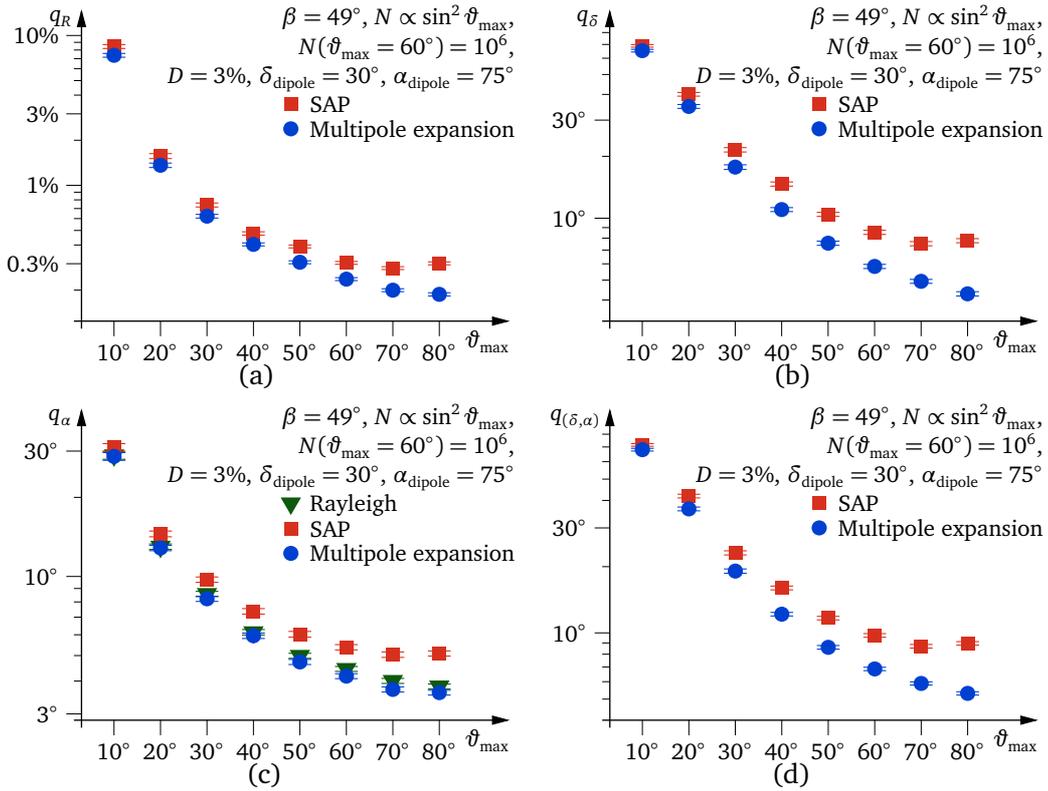
**Figure 5.9:** Reconstruction quality subject to zenith angle limit with the corresponding reduction of statistics taken into account

and a possible anisotropy of the flux are neglected. However, for the purpose of these plots, a misestimation of the data set sizes in the percent range is irrelevant. Figure 5.9 displays the relations between reconstruction qualities and the choice of the zenith angle limit. With $\vartheta_{\max} = 60°$, each simulated data set contains one million events. The numbers of events in other data sets range from 40,205 ($\vartheta_{\max} = 10°$) to approximately 1.3 millions ($\vartheta_{\max} = 80°$). It should be noticed, that unlike in Figure 5.8, where all data sets contain one million events, the axes in Figure 5.9 are logarithmic. The influence of the choice of the maximum zenith angle is indeed dominated by the decrease of statistics for narrower fields of view.

### 5.4.3 Geographical Latitude

The plots in Figure 5.10 suggest, that all of the methods investigated here prefer an experiment located close to the Earth's equator. The advantage of a equatorial location is that a larger fraction (in terms of covered solid angle) of the sky can be seen by the experiment. The reconstruction qualities vary with factors between two and three over the range of geographical latitudes: this effect is certainly less severe than other effects discussed here. Despite the fact, that the dipole vector points to the Northern hemisphere of the sky, there seems to be no significant difference between experiments located on the Northern and Southern hemispheres.
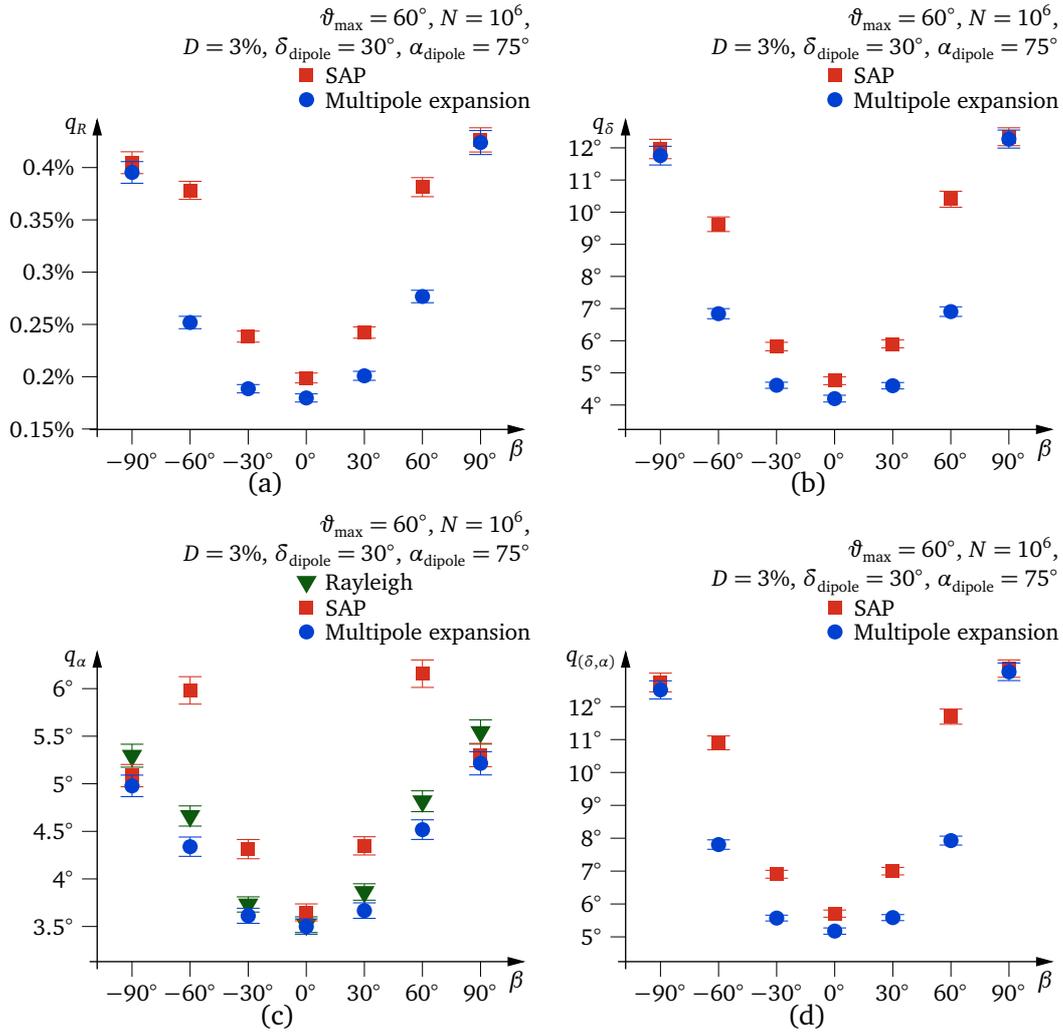
**Figure 5.10:** Reconstruction quality subject to experiment's geographical latitude

### 5.4.4  Dipole Amplitude

The previous sections have dealt with parameters that can be chosen by the experimenter. Finally, two properties of the cosmic ray flux shall be varied and examined. Firstly the dipole amplitude, and secondly the dipole declination. Varying the right ascension of the dipole vector cannot lead to systematical effects, given the longitudinal symmetry of the situation.

Figure 5.11 depicts the reconstruction qualities for dipole amplitudes between 0.1% and 30%. Generally, the reconstruction is more precise the higher the dipole amplitude. The absolute error of the estimated amplitude increases with higher amplitudes for amplitudes larger than 1%. However, the relative error (amplitude error over amplitude) keeps decreasing with higher amplitude. For a data set with one million events, a dipole amplitude of at least about 3% is needed to achieve a precision better than 10° for the determination of the dipole direction. For amplitudes below 1%, the error of the amplitude estimate is not or not considerably lower than the amplitude value itself. Therefore, the dipole signal cannot reliably be discriminated from the isotropy hypothesis.
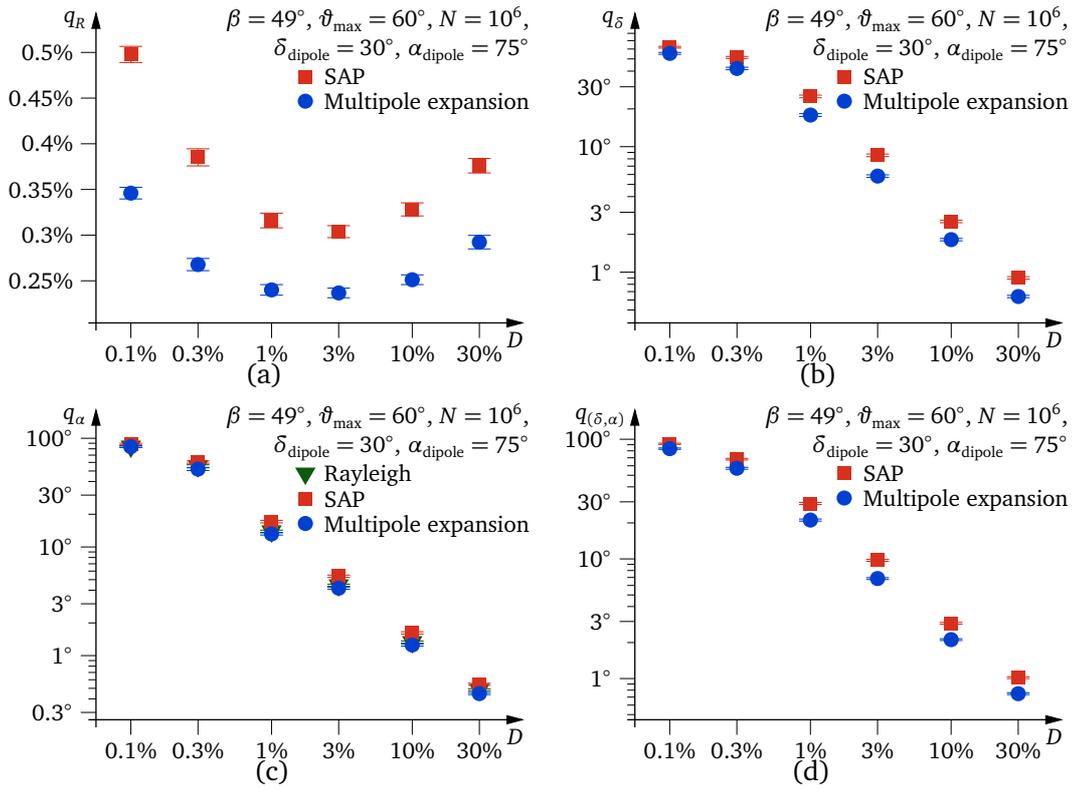
**Figure 5.11:** Reconstruction quality subject to dipole amplitude

### 5.4.5 Dipole Declination

As can be seen in Figure 5.12, the dipole vector's declination influences the accuracies of the amplitude and the direction estimates quite differently. For the estimation of the dipole amplitude, a dipole vector near the equatorial plane would be beneficial. The same applies to the estimation of the dipole vector's right ascension, which works best if the dipole vector lies in the equatorial plane. The quality declines drastically for dipole vectors pointing closer to the poles. However, this is mainly a geometric effect, as the longitude circles are denser near the poles. The reconstruction of the dipole declination performs best when the true declination value is in the medium range between the equator and either of the poles. The precision of the reconstruction of the overall dipole direction, however, is better for dipole vectors that point towards polar regions: the direction of a dipole vector parallel to the Earth's polar axis can be identified with ca. $5°$ precision by means of the multipole expansion method. An equatorial dipole leads to a precision of only $7°$.

## 5.5 The Impact of Experimental Effects

So far, the performances of the reconstruction methods have been examined with respect to quantities that the reconstruction procedures account for. The number of recorded events and the geographical location of the experiment are known values. The zenith angle, up to which detected air shower events are recorded and analysed, can be set by the experimenter. The dipole amplitude and declination are sought-after quantities, for the determination of which the reconstruction methods are designed. However, there may be additional experimental
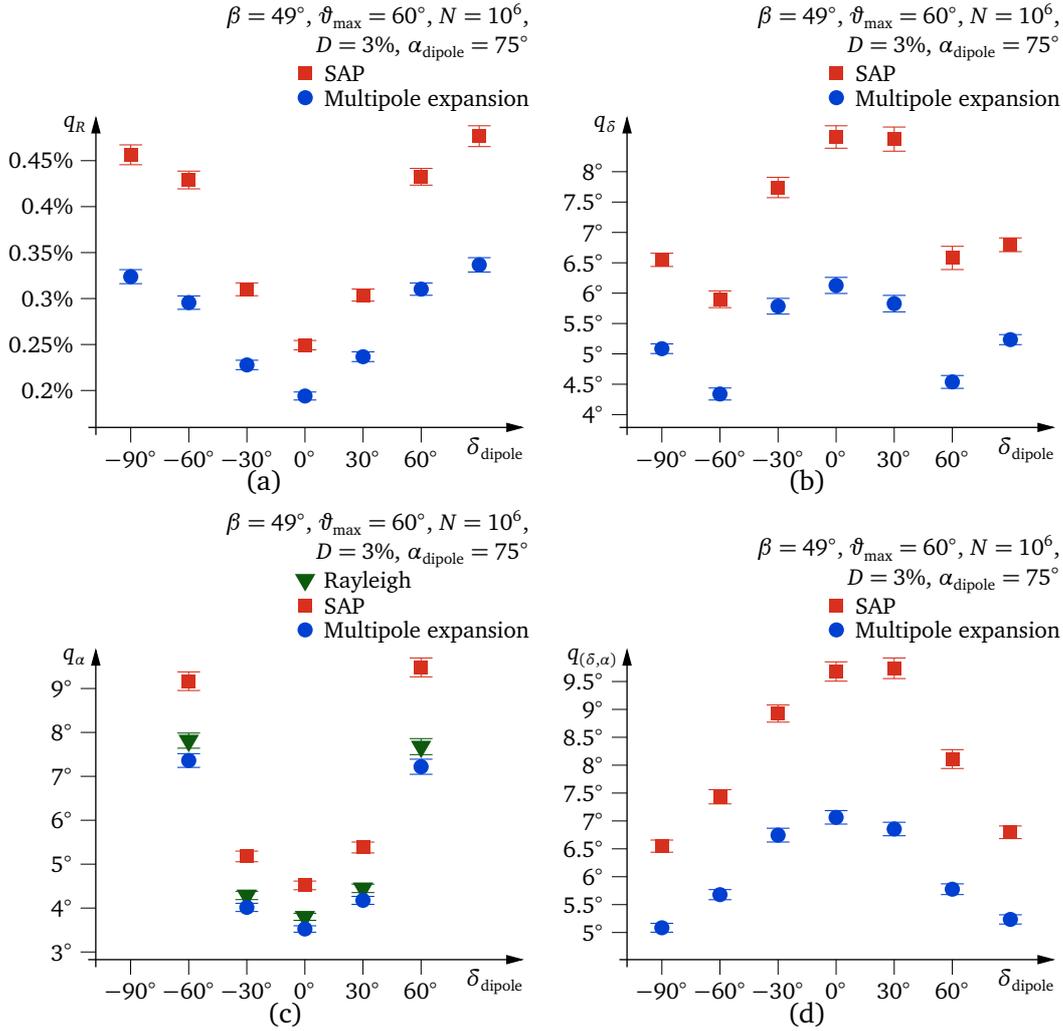
**Figure 5.12:** Reconstruction quality subject to dipole declination

effects that affect the data taking.

So far, an ideal case has been assumed, where all periods of the sidereal day are equally well covered by the data set. This is the case of an right ascension independent exposure function: $\omega(\delta, \alpha) \equiv \bar{\omega}(\delta)$. In a more realistic scenario, the measurement is interrupted from time to time, e.g. for maintenance of the detector hardware. Another experimental effect, that has not yet been considered, is the variability of temperature, barometric pressure and further atmospheric conditions. Variations of the event rate would only occur on a small scale and due to the change of the visible cosmic ray flux as the field of view follows the Earth's rotational motion and covers different parts of the anisotropic sky. As a matter of fact, rate variations do occur much more pronounced and are mostly due to variations of the measurement conditions, such as caused by the weather and the day-night cycle. In addition, the individual air shower arrival directions can only be reconstructed from the recorded data with a certain precision. Introducing a finite angular resolution in the Monte Carlo simulation may have an effect on the dipole reconstruction quality. Another assumption, that has implicitly been made, is that of full, or at least constant, efficiency for the complete field of view of the experiment. If, however, certain parts of the visible sky are not seen with full efficiency, the corresponding regions are underrepresented in the data set, leading to a distortion of the dipole reconstruction. These
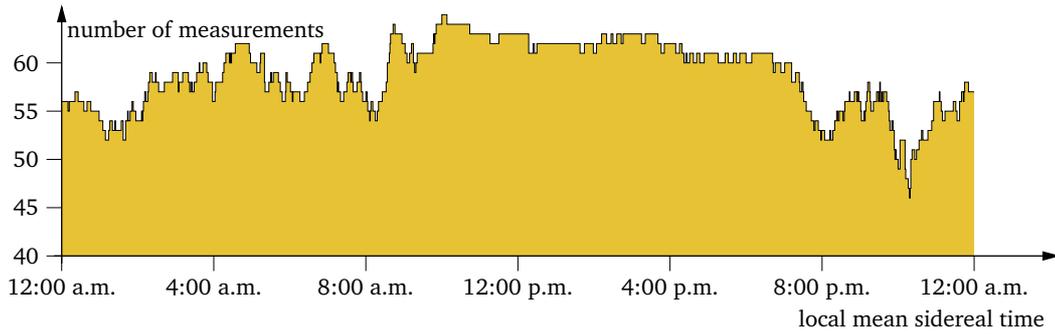
**Figure 5.13:** Temporal coverage of the sidereal day: occasional interruptions of the experiment's operation lead to an irregular coverage of the sidereal day.

effects shall be the subject of the following sections.

### 5.5.1 Interruptions of the Measurements

Occasional interruptions of the measurements lead to an irregular temporal coverage of the sidereal day by the recorded data set. A coverage, that could have been achieved by an experiment, is shown in Figure 5.13. It is meant to be an example with a typical extent of fragmentation of the measurement periods. In this example, the measurement periods cover any given moment of the sidereal day between 46 and 65 times. The coverage variation is roughly of the order of 10%. Experiments record the duration of their measurement periods, so that the equivalent of the histogram in Figure 5.13 is known for any experimental data set at the time it is analysed. The exposure function $\omega(\delta, \alpha)$ is computed from this information. Inhomogeneous coverage of the sidereal day results in an exposure function that actually depends on the right ascension. Rayleigh analysis, SAP method and multipole expansion method all account for the effect of the measurement interruptions: either by means of weighting factors, that are derived from the exposure function (Rayleigh and SAP), or through incorporating the exposure function into the procedure (multipole expansion). Therefore, these methods do not report fake dipole signals induced by this effect. However, the additional weighting may change the statistical properties in the sense, that the effect of fluctuations may get more pronounced. Figure 5.14 compares the reconstruction quality for data sets of different sizes with and without the effect of measurement interruptions. The open symbols present the same data as displayed in Figure 5.7. The filled symbols mark the reconstruction accuracies for data sets with interrupted measurements. The coverage of the sidereal day used for the simulation is the one depicted in Figure 5.13. The effect does not give rise to any noticeable change of the reconstruction qualities, not even for very small data sets.

The effect described here breaks the right ascension symmetry of the exposure function. Hence, the simulated scenario is no longer fully symmetric with respect to right ascension, and so the reconstruction accuracy could possibly depend on the right ascension component of the dipole vector. Figure 5.15 displays the reconstruction qualities for different right ascension values of the dipole vector. All simulations were carried out with the time coverage shown in Figure 5.13. Again, no noticeable effect can be seen, which underlines the point, that this variation has no impact on reconstruction qualities. These plots also exclude the possibility, that no effect was seen in the previous plots because by chance the chosen right ascension coordinate of the dipole vector ($\alpha_{\text{dipole}} = 75°$, according to the standard configuration as given in Section 5.3.2) matches the time coverage histogram in a favourable way.
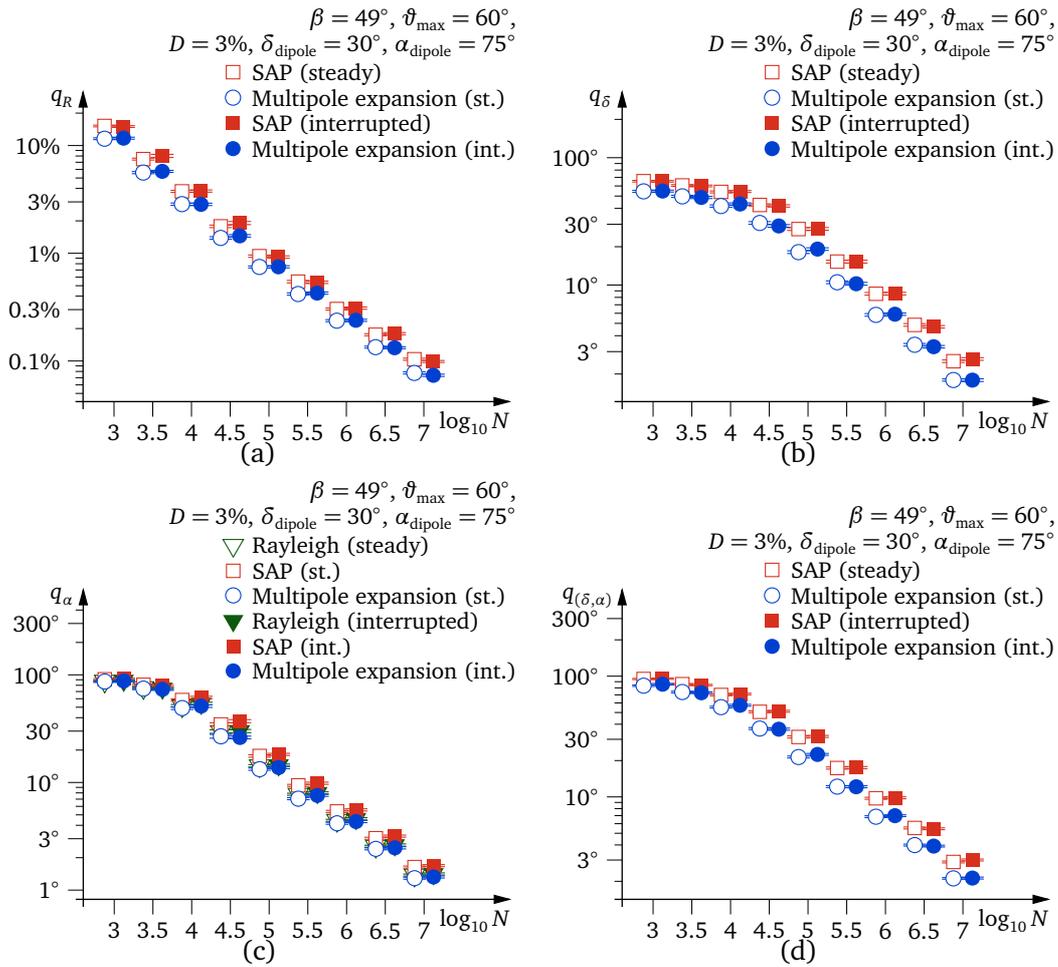
**Figure 5.14:** Reconstruction quality with measurement interruptions, subject to the data set size (filled symbols). The open symbols display the same data as in Figure 5.7. For better visibility, the open symbols are displaced to the left and the filled symbols are displaced to the right.

### 5.5.2 Rate Variations Due To Metereological Effects

Even when performing an uninterrupted measurement, that lasts exactly one sidereal day, the actual sky coverage may be inhomogeneous along the right ascension coordinate. Variations of temperature and barometric pressure can have an effect on the frequency of detected air shower events. The lower temperatures during the night could result in different intensities, with which the day sky and the night sky are observed. With a measurement of only one sidereal day, the day-night cycle would probably create a fake dipole in the data set. Conducting measurements over a longer period of time, one or more years, is a means of lowering the effect, as it should average out over time to a large degree. The night sky in summer is seen at day during winter, and vice versa. Changes of the weather conditions are unlikely to happen coherently with respect to sidereal time. On the other hand, the intensity of the day-night effect may vary with season, so that it never fully cancels out.

The reconstruction methods, as they have been described, do not account for a potential variation of the observation intensity. Additional mechanisms can be introduced to correct for this shortcoming. Temperature and air pressure can be recorded during the operation of the
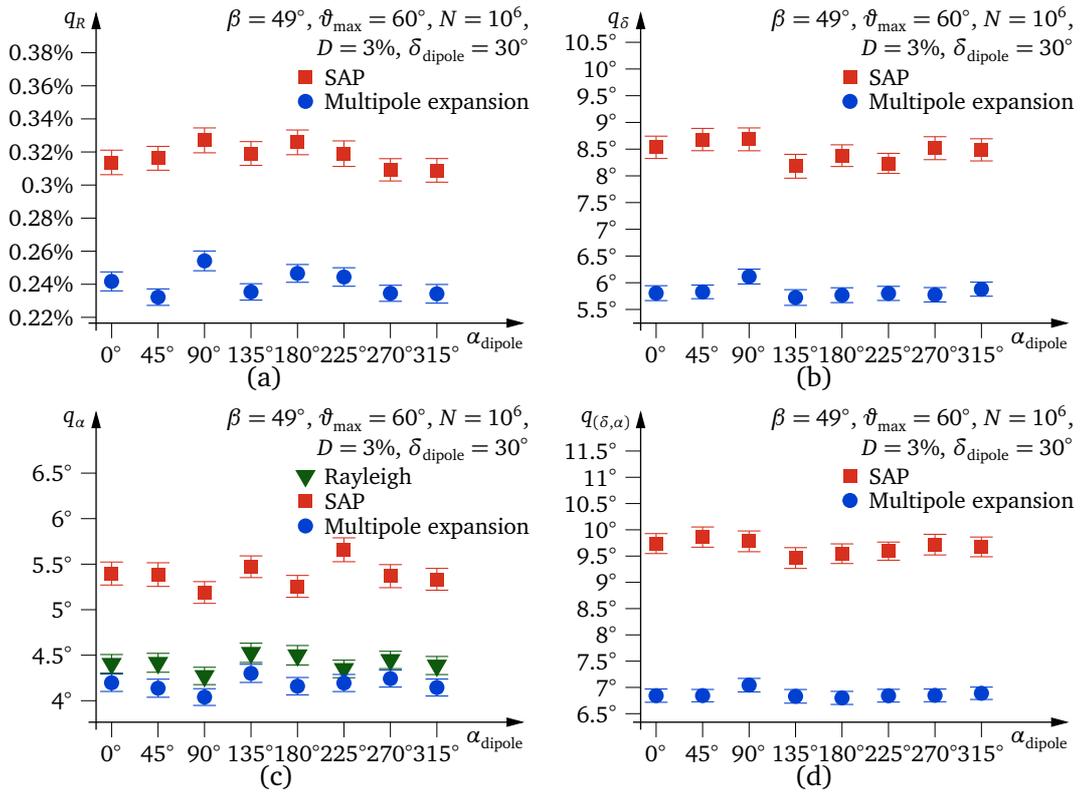
**Figure 5.15:** Reconstruction quality subject to dipole right ascension

experiment. Additional weights can be applied to the individual air shower events in the data set, in order to compensate for metereological effects: events recorded during periods with e.g. high barometric pressure can be weighted up to compensate for the higher attenuation of the atmosphere during such periods. Weighting factors can be obtained by studying the mean event rates subject to temperature, barometric pressure and whatever atmospheric information is available. However, there is the risk of worsening the quality of the data set: firstly, the atmospheric conditions cannot be fully described by means of a few atmospheric observables. Typically, temperature and barometric pressure are measured at ground, but the conditions in the higher atmosphere may vary independently. Consequently, the weighting factors applied do not match the atmospheric conditions correctly, and the original problem subsists. Secondly, the determination of the weighting factors could interfere with the actual cosmic ray anisotropy. If so, the weighting factors would also compensate for the anisotropy to a certain degree, thereby weakening the signal of the true anisotropy in the data set.

Compensating for weather effects is a delicate issue. Even when applying corrections, a certain variation of the effective observation intensity may remain. The variation may average out to a certain degree if the data taking is performed over a long period of time. However, a fraction of the variation may persist and cause that parts of the sidereal day are overrepresented in the data set, whilst others are underrepresented. For the simulation of this effect, a simple model of the variation is used: a harmonic variation of the observation intensity in sidereal time. The strength of the effect is characterised by the amplitude $A_{\text{weather}}$ of the variation. The variation as a function of sidereal time has the shape of a sine function. The event rate at 6 a.m. sidereal time is enhanced by a factor $1 + A_{\text{weather}}$, whereas the rate at 6 p.m. sidereal time is multiplied with $1 - A_{\text{weather}}$, thus decreased. It should be noted, that a typical variation
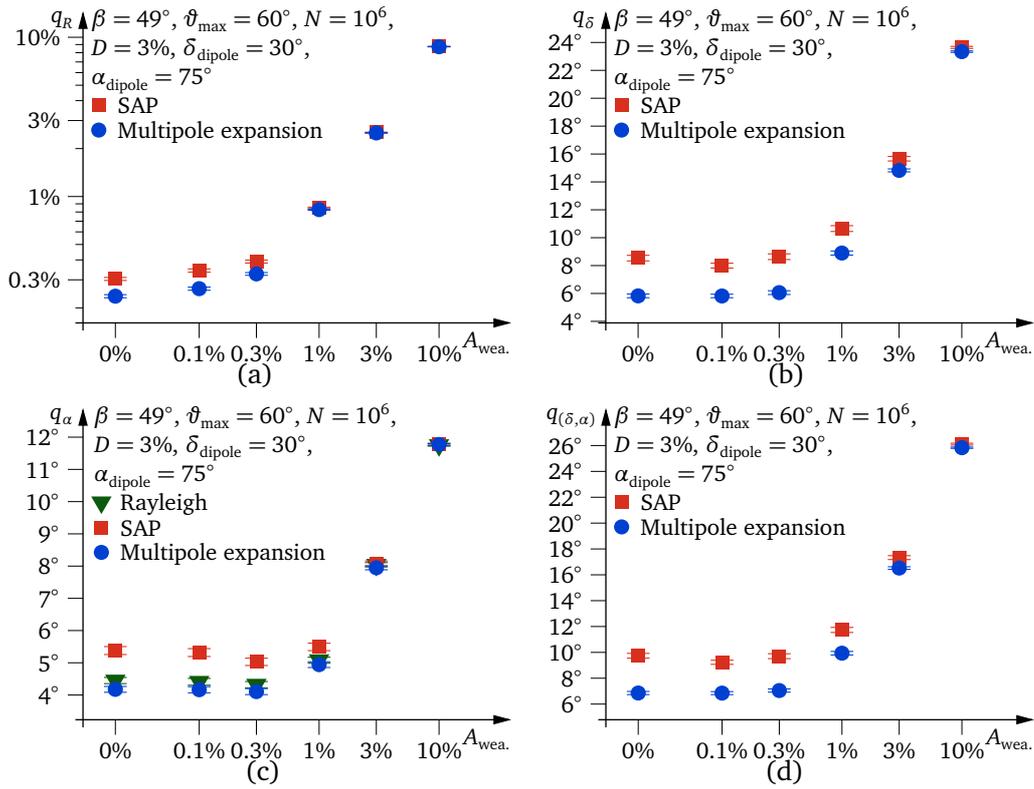
**Figure 5.16:** Reconstruction quality subject to the amplitude of a spurious rate variation

of the measurement rate during the operation of the experiment of the order of 10% does not necessarily result in an amplitude $A_{\text{weather}}$ of 10%. The weather effects mostly correlate to solar time, or are completely random. Therefore they tend to average out when looking at the net effect as a function of sidereal time. What remains in sidereal time (after metereological corrections, if such are applied) is denoted by $A_{\text{weather}}$.

Figure 5.16 illustrates the influence of this effect on the reconstruction accuracies. The simulations were carried out with the standard configuration (see Section 5.3.2) and with an additional harmonic variation of the event rates in sidereal time with amplitude $A_{\text{weather}}$, that was not accounted for by the reconstruction procedures. Several of such amplitudes in the range between 0.1% and 10% were simulated. In the case of the standard simulation configuration, spurious rate variations up to 0.3% have no or only little effect on the accuracies. However, with larger variations the reconstruction qualities drastically degrade. In contrast to any of the simulation sets, that have been shown before, this effect can cause the SAP method and multipole expansion method to perform with the same accuracy. For values of 1% or greater for $A_{\text{weather}}$, the amplitude reconstruction of those two methods is equally accurate with an error of about the value of $A_{\text{weather}}$. The multipole expansion method continues to provide better precision of the dipole reconstruction until $A_{\text{weather}}$ reaches 10%. Summarising briefly, the presence of weather effects can badly diminish the reconstruction quality. Reducing these variations to the lowest possible level is very important.

### 5.5.3  Angular Resolution

The effect of limited resolution of the arrival direction reconstruction can be simulated as described as Step 4 in the simulation procedure (see Section 5.2.4). A Gaussian point spread
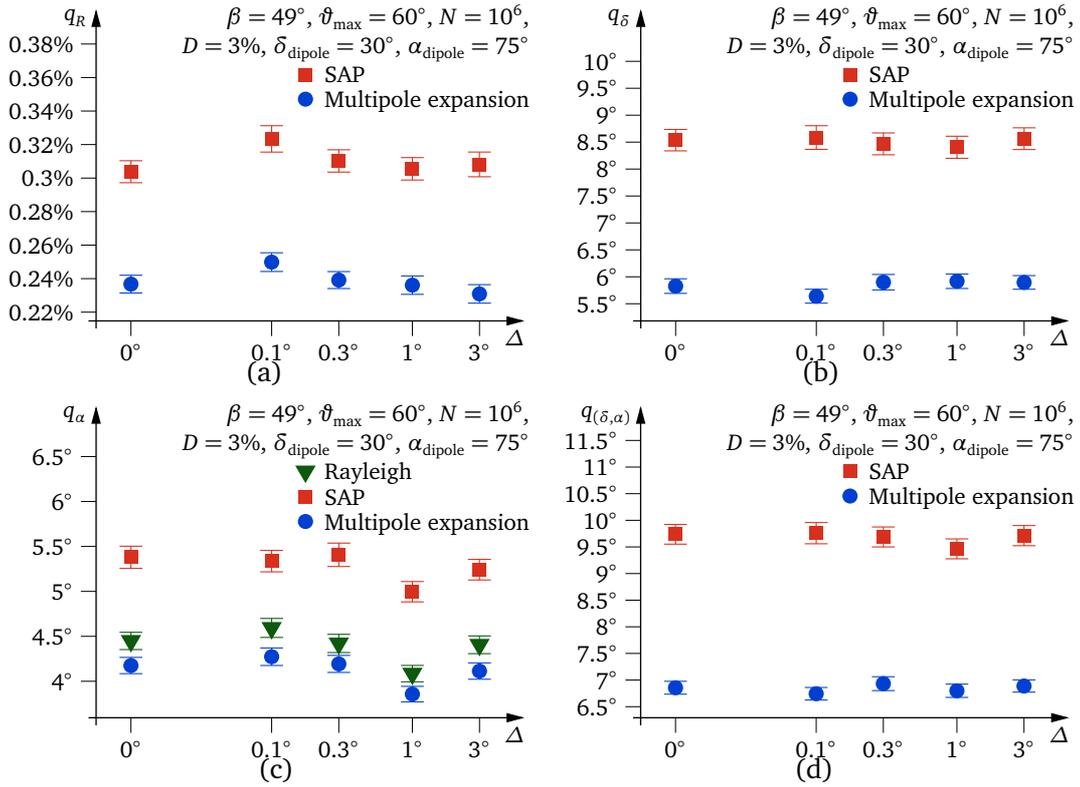
**Figure 5.17:** Reconstruction quality subject to the experiment's angular resolution

function is applied to the true arrival direction of each individual event to obtain the reconstructed arrival direction, which is input to the dipole reconstruction methods. The angular resolution $\Delta$ denotes the standard deviation $\sigma$ of the Gaussian point spread function. Thus, 68% of the recorded events are reconstructed with an angular error less than $\Delta$. The angular resolution of a cosmic ray experiment is typically better than $1°$. Figure 5.17 displays the reconstruction accuracies for data sets generated with angular resolutions between $0.1°$ and $3°$. Every quality value obtained in these simulations is statistically compatible with the case of perfect angular resolution ($\Delta = 0°$). Thus, the effect of limited angular resolution is irrelevant, at least with the standard Monte Carlo configuration used here, and for a resolution better than $3°$.

### 5.5.4 Inclination Dependent Efficiency Defect

The final experimental effect, that shall be discussed here, concerns the assumption of full efficiency over the whole field of view. When calculating the exposure function $\omega(\delta, \alpha)$, the field of view of the experiment is usually characterised by the maximum zenith angle $\vartheta_{\max}$ up to which recorded data are used for analysis. Typical values for $\vartheta_{\max}$ are $40°$ or $60°$. A value must be chosen, up to which the reconstruction of the arrival direction is known to work properly. The calculation of the exposure implies, that no events with inclination greater than $\vartheta_{\max}$ are contained in the data set (a data selection cut is applied to ensure this), and that incident cosmic ray particles with inclinations less than $\vartheta_{\max}$ are recorded and properly reconstructed. Thus, full detection and reconstruction efficiency is assumed for the whole field of view. This requirement is not trivial to accomplish: inclined particles traverse the Earth's atmosphere on a longer path than vertically moving particles. Owing to the atmospheric attenuation, the
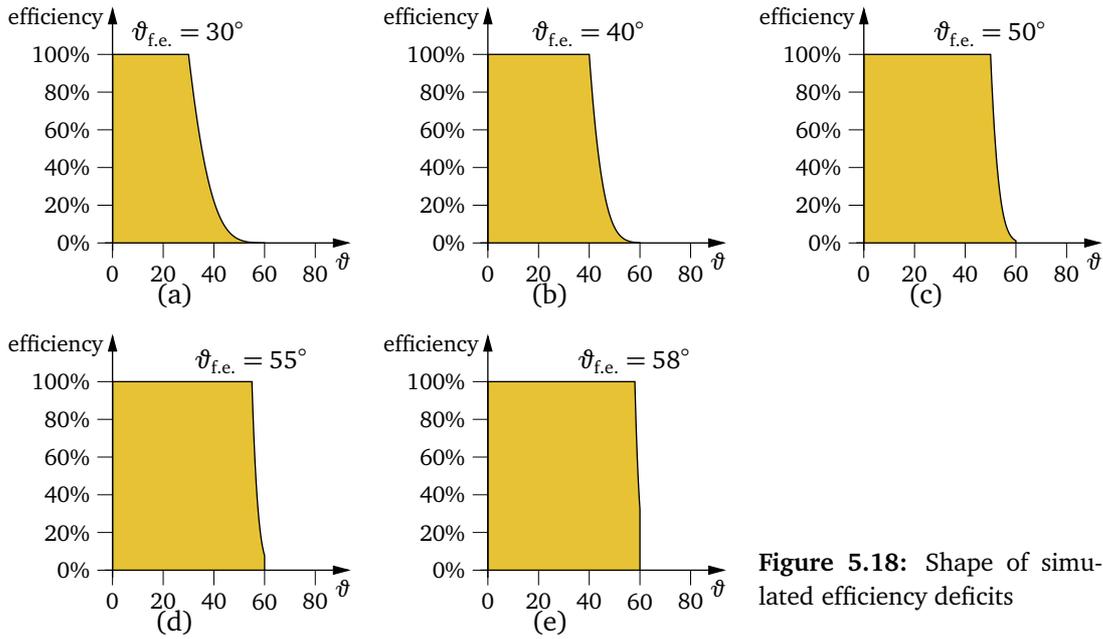
**Figure 5.18:** Shape of simulated efficiency deficits

detection efficiency for particles of a given primary energy and element depends on the shower inclination. Full efficiency is reached at a certain energy threshold. Additional cuts have to be applied to the data set to ensure that the analysis is restricted to particles above that energy threshold. The energy can only be estimated through observable quantities, which are subject to statistical fluctuations. Should the energy estimator be sensitive to the inclination angle, then the cut on the energy estimator may introduce different energy thresholds for different shower inclinations. Since the energy spectrum of the cosmic radiation is a steeply falling power law, a small change of the energy threshold can have a substantial influence on the resulting population of the data set.

For the simulation of the effect of misestimated efficiency, a simple model was chosen to describe the efficiency as a function of the zenith angle: the Earth's atmosphere is considered to be 10 interaction lengths thick. Since inclined air showers travel on a longer path through the atmosphere, the number of interaction lengths, that an air shower has to overcome, depends on the zenith angle $\vartheta$, and amounts to $10 \sec\vartheta$. Up to a maximum zenith angle of $\vartheta_{\text{f.e.}}$ showers are detected with full efficiency. In the context of this simple model, this means that $10 \sec\vartheta_{\text{f.e.}}$ interaction lengths can be traversed with full detection efficiency being ensured. For showers even more inclined, the efficiency drops by a factor of $1/e$ as the path length gains one additional interaction length. The efficiency function can then be written as:

$$\text{efficiency}(\vartheta) = \min\left(100\%; \exp(10 \sec\vartheta_{\text{f.e.}} - 10 \sec\vartheta)\right) . \qquad (5.25)$$

The function is displayed in Figure 5.18 for different values of $\vartheta_{\text{f.e.}}$ between $30°$ and $58°$. The zenith angle cut is applied at $\vartheta_{\max} = 60°$. Data sets were simulated with the given values for $\vartheta_{\text{f.e.}}$. The severity of the effect depends strongly on the choice of $\vartheta_{\text{f.e.}}$. Full efficiency only up to $30°$ entails that virtually no showers are recorded with inclinations above $50°$, which would certainly not go unnoticed. On the other hand, with $\vartheta_{\max} = 58°$, there is only a deficit within the last $2°$ of the field of view.

The reconstruction accuracies subject to $\vartheta_{\text{f.e.}}$ are displayed in Figure 5.19. The reconstruction qualities of dipole amplitude and declination undergo a substantial degradation when an efficiency defect is present. A lack of efficiency between $58°$ and $60°$ zenith angle alone gives
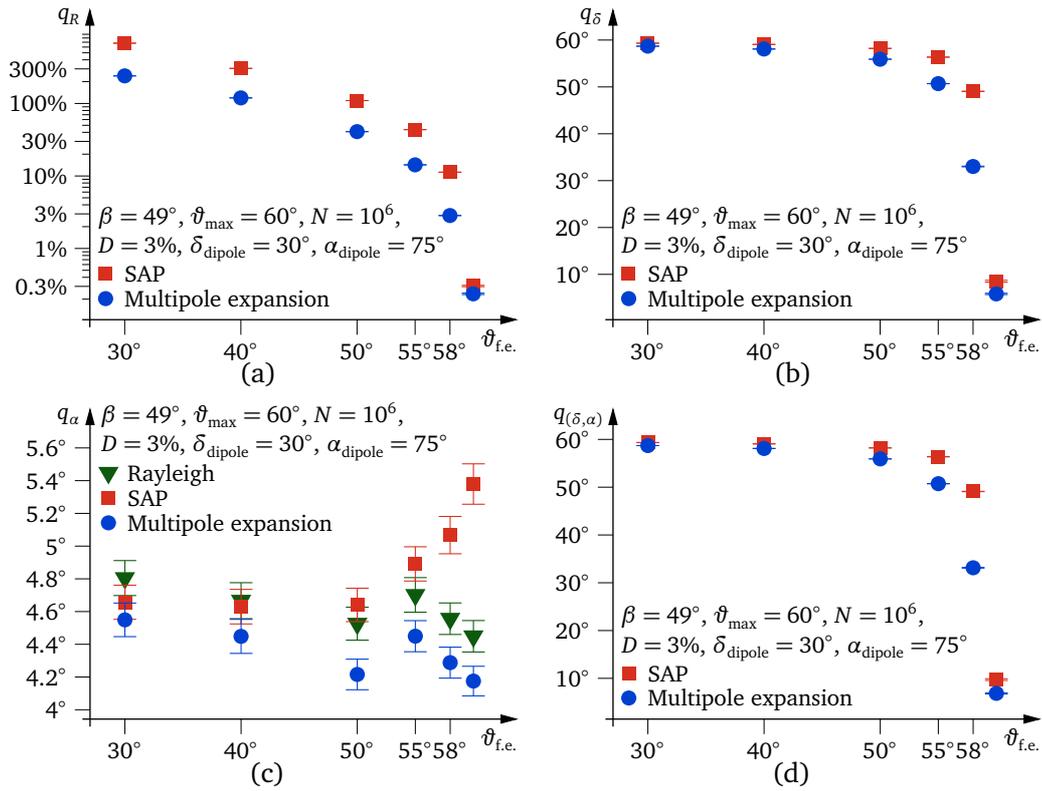
**Figure 5.19:** Reconstruction quality subject to the extent of the efficiency defect: the rightmost data point in each of the plots refers to the case of full efficiency for the whole field of view, thus for the absence of the efficiency defect.

rise to a worsening of the amplitude reconstruction accuracy from 0.3% to 3% in case of the multipole expansion method. The declination accuracy decreases similarly. If the efficiency drop sets in at 55°, the reconstruction basically yields no valid information on the dipole amplitude and declination.

The right ascension reconstruction, however, is almost unaffected by this effect. On the contrary, the SAP method seems to profit from the lack of highly inclined events in the data set. Since each of the simulated data sets contains the same number of events, a lack of highly inclined events results in a surplus of less inclined events provided by the simulation. As a consequence, the data set contains fewer events that receive very high weighting factors by the SAP method. With a more homogeneous weighting, the SAP method delivers more accurate results for the dipole right ascension. It must be noted, that apart from the added efficiency defect the standard configuration was used for the creation of the data sets shown here. As one point of the specification of the standard configuration, an uninterrupted measurement was simulated, i.e. the exposure is independent from right ascension. If the effect of interrupted measurement cycles, as discussed in Section 5.5.1, is added, the right ascension reconstruction degrades as well, as a cause of the fact, that the calculated exposure map does not correctly reflect the circumstances. The efficiency defect leads to an effective exposure map that differs from the assumed and calculated one. This has no effect in the case of homogeneous coverage of the sidereal day, because both the assumed and the effective exposure function do not depend on the right ascension coordinate. This symmetry is broken, when the measurement periods cover the sidereal day unevenly. A plot illustrating the right ascension reconstruction quality under these conditions is shown in the next Chapter, see Figure 6.3(b).

Figure 5.20 shows the distributions of reconstructed amplitudes and declinations, obtained with both the SAP and the multipole expansion method, for two series of Monte Carlo simulations. The first series was generated with $\vartheta_{\mathrm{max}} = 58°$ (Figures 5.20(a) to (d)), the second with $\vartheta_{\mathrm{max}} = 50°$ (Figures 5.20(e) to (h)). As can be seen in these plots, the cause of the bad reconstruction qualities is not a widening of the distributions, but a systematic deviation. The width of the distributions is not larger than in the case of a correctly working reconstruction. Instead, both amplitude and declination values are systematically reconstructed too large: the dipole vector is dragged towards the North Pole. The effect is more pronounced for the SAP method than for the multipole method, and increases with the severity of the efficiency defect. Apparently, the actual anisotropy signal is overshadowed by an artificial dipole induced by the efficiency deficit. The artificial dipole points towards the North and its amplitude depends on the extent of the efficiency deficit. The more dominant it is, the further the resulting dipole points towards North. Since the simulated experiment is located on the Northern hemisphere at $\beta = 49°$ and records air shower events with inclinations up to 60°, the sky coverage reaches from the North Pole down to $\delta = 49° - 60° = -11°$. Those regions of the sky close to the Southern boundary are only ever seen at high inclinations. The lack of highly inclined events leads to too few events at the Southern boundary in the data set. This North-South divide creates the said artificial dipole. Since the SAP method equips observations at the Southern boundary of the visible sky with much higher weightings than the multipole expansion method (owing to the low exposure of that region), the impact on the SAP method is worse than on the multipole expansion method.

## 5.6   Summary

In this chapter, the performances of the SAP method and the multipole expansion method have been evaluated by means of Monte Carlo simulation studies. The Monte Carlo generator used for the creation of data sets has been described in detail. This generator allows to simulate the acquisition of data sets with different parameters, including the emulation of certain experimental effects. As a result of these studies, parameters and effects have been identified, that have significant impact on the accuracy and the functioning of the reconstruction methods. Generally, the multipole expansion method tends to be more precise than the SAP method. It is also less prone to spurious effects than the SAP method. A geographical position close to the equator is beneficial with respect to the dipole reconstruction accuracy. The accuracy does also depend on the true values of the dipole parameters. The reconstruction of the dipole amplitude works better if the dipole points to equatorial directions. On the other hand, the reconstruction of the dipole direction works better if the dipole points somewhere near the North or South Pole.

Of the experimental effects, two have turned out to have no significant impact on the dipole reconstruction. Neither the resolution with which the air showers' arrival directions can be reconstructed (relevant values assumed), nor occasional interruptions of the measurement (provided they are monitored and accounted for during analysis) have a noticeable effect. Two other effects have been investigated, and those have substantial meaning for the functioning of the dipole reconstruction. Firstly, variable measurement conditions, which may be caused by the weather for instance, can degrade the reconstruction quality. Accounting for the changing atmospheric conditions is delicate, and a remaining disturbance of 1% in the data set is enough to increase the reconstruction errors substantially. As a side effect, the reconstruction quality of the multipole method is no longer superior to the SAP method. Secondly, a misestimation of the detection efficiency can severely distort the dipole reconstruction. A zenith

angle dependent detection efficiency was simulated. It has been shown, that a lack of highly inclined events in the data set can lead to a considerable misestimation of dipole parameters. The effect may cause the finding of large dipole anisotropies, pointing very close to one of the Earth's poles.

It would be desirable to have reconstruction methods at hand, that are less prone to such effects. The improvement of the available methods, and the development of new ones, will be the subject of the next chapter.
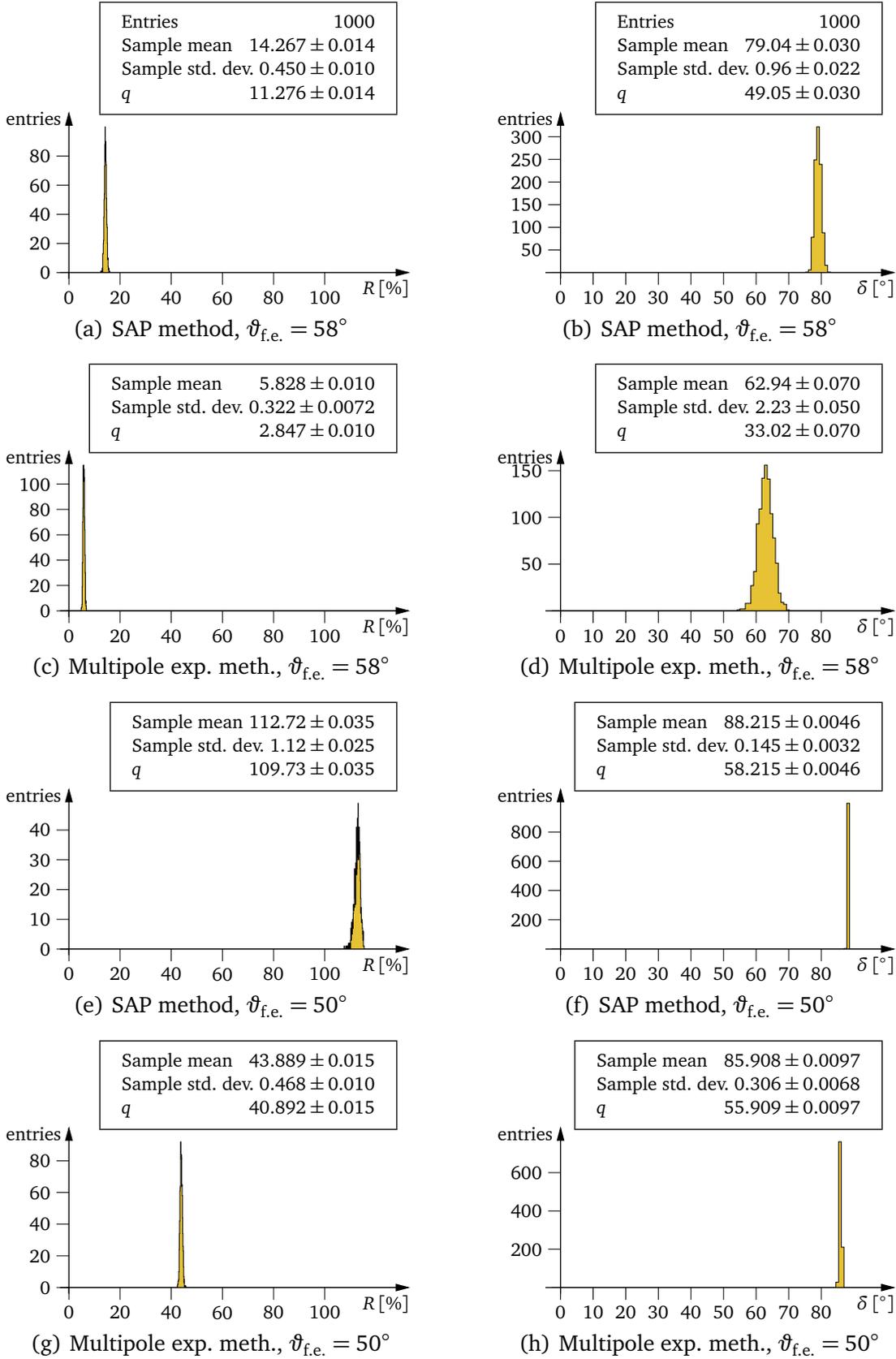
**Figure 5.20:** SAP and multipole expansion method applied to data sets with efficiency defects

# Chapter 6

# New Methods for Dipole Reconstruction

Several methods for the reconstruction of large scale anisotropies in data sets of cosmic ray experiments have been presented and evaluated in the previous two chapters. Those methods mostly concentrate on large scale structures of the first order only: they reconstruct the parameters of a dipole shaped cosmic ray flux. It has been shown, that the methods generally deliver correct results in "ideal world scenarios". With only limited amounts of statistics available, the results are subject to statistical fluctuations and therefore only offer a certain degree of precision. An optimisation of the statistical treatment of the data sets may help to improve this precision. However, systematic effects have proven to be much more severe, as they can lead to large measurement uncertainties of the dipole parameters. It is desirable to find methods that are resistant to such experimental effects. This chapter aims at modifying and thereby improving existing methods and proposing new ones.

## 6.1 Time Based Weighting

Both the Rayleigh analysis, when applied to data sets taken with right ascension dependent exposure, and the SAP method use weighting techniques in order to account for the underlying inhomogeneous sky coverage. While the SAP method uses a weighting that levels the share of all directions of the visible part of the sky in the data set, the weighting used for the Rayleigh analysis only aims at balancing the difference between directions of the same declination. In both cases, the weighting factors depend on the reconstructed arrival directions of the showers. For the Rayleigh analysis, the weighting factors have been given in Equation 4.23:

$$W(\delta, \alpha) = \frac{\bar{\omega}(\delta)}{\omega(\delta, \alpha)}, \tag{6.1}$$

with $\omega(\delta, \alpha)$ being the exposure function and $\bar{\omega}(\delta)$ denoting the average exposure of declination $\delta$ (see Section 4.3.2 for details). In case of a right ascension independent exposure, all weights are identically equal 1, since $W(\delta, \alpha) = \bar{\omega}(\delta)$. See Figure 4.5 for a graphical representation of an example exposure function and the corresponding weighting factors. The weighting factors result from the exposure function alone, which is computed from the list of measurement periods of the experiment. It can be computed very efficiently from a histogram like the one shown in Figure 5.13, which displays for every minute of the sidereal day the number of times that the measurement was active at the given minute. Like the exposure map

shows the coverage of the regions of the sky, and thereby the amount of representation of the regions in the data set, such a histogram reveals the coverage by time of the sidereal day in the data set. In order to reflect the data set correctly, very small amounts of data have to be discarded from the data set at the start and end of every measurement period, so that every measurement period effectively starts and ends at the boundary of a sidereal minute. The amount of data being discarded can be reduced by chosing an even finer binning of the sidereal day. However, with single measurements typically lasting hours or days, the gain will be marginal. Apart from the histogrammed sidereal day coverage, only the geographical location of the experiment and the shape of its field of view is needed to compute the exposure map. The latter is usually specified by the zenith angle limit $\vartheta_{\text{max}}$.

Instead of deriving the weighting factors from the exposure map, they can be taken from the sidereal day coverage histogram directly. Let $m(t)$ denote the number of measurements, that were active during the same sidereal time of day as the time $t$. $m(t)$ is a functional representation of the data in the sidereal day coverage histogram shown in Figure 5.13. The directional weightings can be replaced with time based ones according to:

$$W(\delta, \alpha) = \frac{\bar{\omega}(\delta)}{\omega(\delta, \alpha)} \longrightarrow W(t) = \frac{\bar{m}}{m(t)}, \tag{6.2}$$

where $\bar{m}$ stands for the average number of measurement:

$$\bar{m} = \frac{\displaystyle\int_{\substack{1 \\ \text{sidereal} \\ \text{day}}} m(t)\,\mathrm{d}t}{1\,\text{sidereal day}}. \tag{6.3}$$

Using these weighting factors, the sidereal day is evenly represented in the data set. Therefore, the effective sky coverage is homogeneous in right ascension, as well. While the weightings for individual events can differ from those obtained with direction dependent weighting, the overall effects on the data set are the same with both variants. A conceptual advantage of time based weighting is, that weighting factors do not depend on reconstructed observables like the arrival direction, which are subject to reconstruction inaccuracies. The event time is recorded by the data acquisition software, without need for considerable precision, since the weighting only depends on the sidereal minute an event belongs to.

The following section will test the performance of the time based weighting by means of Monte Carlo simulations. A noteworthy improvement as a result of the time based weighting is not expected. On the contrary, in the specific scenario simulated, the time based weighting factors range between 0.905 and 1.279, whereas the direction based weighting factors are contained in the range between 0.916 and 1.181. With the weighting factors spanning a larger range, the weighting is probably more inhomogeneous and might lead to larger statistical fluctuations. Whether this effect is noticeable and significant, remains to be seen. The advantage of the time based weighting lies in the simplicity of the procedure, as it allows to perform a Rayleigh analysis without calculating an exposure map at all. It also allows to create a method for three-dimensional dipole reconstruction, that is completely independent of the exposure function, which will be discussed below in Section 6.3.

### 6.1.1   Monte Carlo Simulations

Figure 6.1 displays the reconstruction qualities of the Rayleigh amplitude and phase for Rayleigh analyses with weightings based on direction and on time. The simulated param-
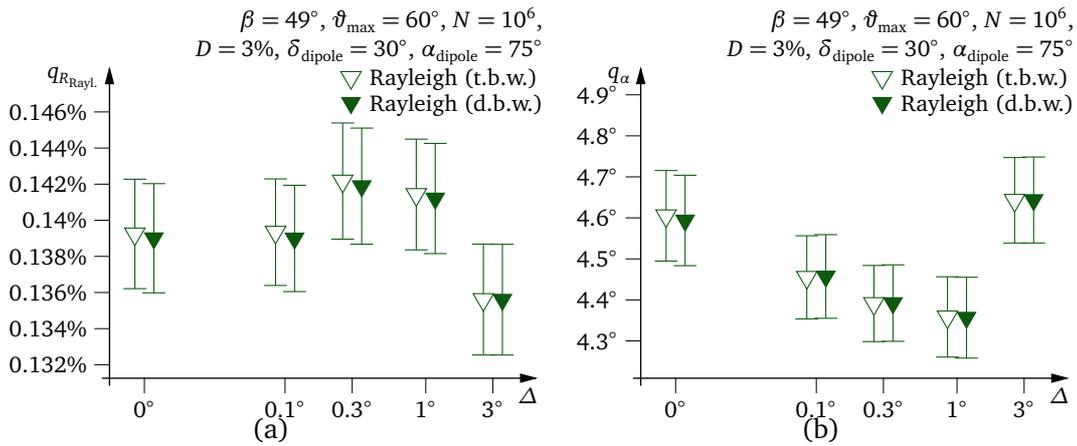
**Figure 6.1:** Reconstruction quality of the Rayleigh analysis with time based weighting (t.b.w.), opposed to conventional, direction based weighting (d.b.w.), subject to angular resolution: the quality measure $q$ is displayed, as introduced in Section 5.3.1. The true value of the Rayleigh amplitude in this scenario amounts to 1.82%. For reasons of clarity, the open symbols are displaced to the left and the solid symbols are displaced to the right.

eters are those of the standard configuration, as introduced in Section 5.3.2, except that a measurement was simulated with occasional interruptions. The sidereal day coverage used is the one depicted in Figure 5.13. The effect of an interrupted measurement has been discussed and examined in Section 5.5.1. Without this effect, the exposure function is independent from the right ascension, and both direction and time based weighting factors are all identically equal 1. Because one of the weighting methods utilises the reconstructed arrival directions of individual air showers, the resolution of the arrival direction reconstruction may influence the results here. However, as it turns out, it does not. The results obtained for resolutions between $0.1°$ and $3°$, as well as for perfectly precise reconstruction, are all identical within their errors. For each configuration, thus for each angular resolution value shown, one series of 1,000 data sets was simulated. The same data were used for the analysis with the two different methods, which is why the solid and the corresponding open data points in the plot are highly correlated. The difference between the analysis of the data sets with time based weighting and direction based weighting is smaller than the statistical precision with which the qualities can be determined with 1,000 data sets. Apparently, weighting with individual, slightly misreconstructed arrival directions has no negative impact on the overall reconstruction quality. Neither does the slightly wider range of values of the time based weights, as opposed to direction based ones, lead to noticeably larger statistical fluctuations. In case of the simulation configuration used here, it does not matter whether direction based or time based weightings are used.

However, other experimental effects may have an impact. Of the various effects discussed in Chapter 5, two can be regarded as a misestimation of the experiment's exposure function: firstly, metereological effects can lead to spurious variations of the event rate. Owing to changing atmospheric conditions, the sky is not seen with constant intensity. As an effect, the data in the sidereal day coverage histogram, which only counts the number of observations at a sidereal time of day, may not reflect the correct experimental circumstances. Consequently, the exposure computed from that histogram is erroneous, and so are the direction based weighting factors derived from it. However, the time based weighting factors are calculated from the same histogram, and therefore should expose the same problems. The results of the corresponding Monte Carlo simulations are depicted in Figure 6.2. The plots correspond to those
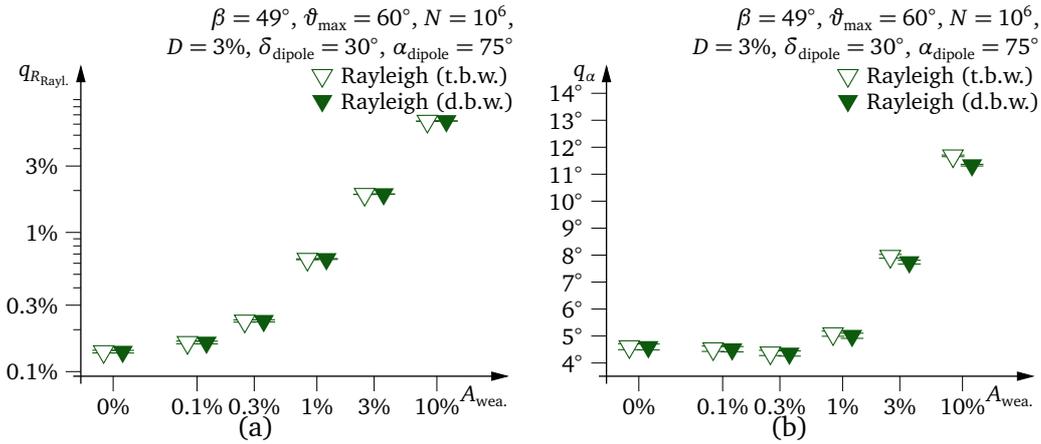
**Figure 6.2:** Reconstruction quality of the Rayleigh analysis with direction and time based weighting subject to the amplitude of a spurious rate variation
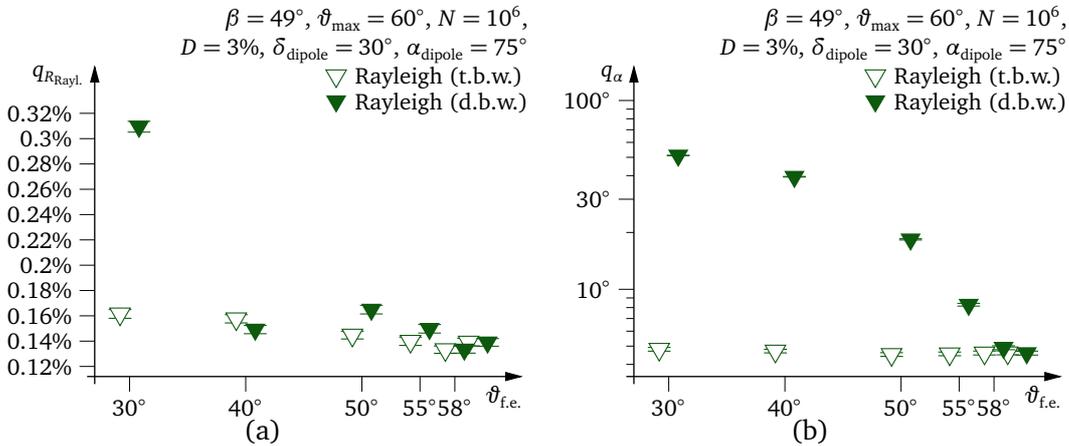


**Figure 6.3:** Reconstruction quality of the Rayleigh analysis with direction and time based weighting subject to the extent of the efficiency defect: the rightmost data points in both plots refer to the case of full efficiency for the whole field of view.

shown in Figure 5.16 and discussed in Section 5.5.2, except that the simulations shown here were generated with occasional measurement interruptions. The impact of the metereological effects is basically the same here as in Section 5.5.2. The reconstruction quality degrades, leading to a considerable decrease for rate variation amplitudes of 1% or more. For the highest simulated amplitude, the reconstruction of the dipole right ascension is even slightly worse with time base weighting compared with direction based weighting. While the gap between the two methods is indeed statistically significant, the difference is so small that is not really relevant. It could well be the consequence of a random interference within the example sidereal day coverage histogram. However, it is safe to say, that with both conventional, direction based weighting and time based weighting, the Rayleigh analysis is similarly prone to metereological effects.

Secondly, the simulation of an efficiency deficit for highly inclined showers has lead to systematic measurement uncertainties of the dipole parameters. See Section 5.5.4 for an in-depth discussion of this effect. While the sidereal day coverage histogram can still be considered correct, when this effect is active, the calculation of the exposure map from the histogram is per-

formed under the incorrect assumption of full efficiency. Hence, the calculated exposure map does not reflect the actual experimental circumstances. A weighting based on the (erroneous) exposure map is not favourable in comparison with a weighting based on the (correct) sidereal day coverage histogram. This case is the subject of another series of Monte Carlo simulations, the results of which are depicted in Figure 6.3. The reconstruction quality of the dipole vector's right ascension is not influenced by this effect at all, when time based weighting is utilised. However, with direction based weighting, the accuracy of the reconstruction degrades badly. The reason for the bad values of $q$ is not an increase of statistical fluctuations, but a strong bias. As can be seen in Table C.14, the distributions of the reconstructed right ascension values have all the same width (in terms of their standard deviations), but their mean values begin to differ substantially from the true value. In the discussion of the effect of the zenith angle dependent efficiency defect in Section 5.5.4, the reconstruction of the right ascension variable has been found to be insensitive to the efficiency effect. The simulations shown here were carried out with an inhomogeneous coverage of the sidereal day, as it is caused by occasional interruptions of the measurement. On the other hand, the plots in Section 5.5.4 are based on the simulation of a measurement that runs uninterruptedly for an integer number of sidereal days and with constant measurement conditions, in which case all weighting factors are 1, no matter which weighting method is used.

The plot shown in Figure 6.3(a) displays the reconstruction accuracy of the Rayleigh amplitude. As can be seen, with time based weighting, the accuracy decreases gradually while going towards larger efficiency deficits, thus going towards lower values of the full efficiency threshold zenith angle $\vartheta_{\text{f.e.}}$. The behaviour of the solid data points in this plot, illustrating the performance of the Rayleigh analysis with conventional, direction based weighting, looks self-contradictory. Going towards lower values of $\vartheta_{\text{f.e.}}$, the inaccuracy increases, with one exception: at $\vartheta_{\text{f.e.}} = 40°$ the quality is remarkably good, even outperforming the time based weighting. This behaviour can only be explained with some additional information on the distributions, from which the data points were extracted. Table C.14 lists not only the $q$-values but also mean values and standard deviations of the distributions represented by each of the data points. According to these data, the widths of all distributions (all $\vartheta_{\text{f.e.}}$ values, with both time and direction based weighting) are the same. The different $q$-values result from mismatches between the distributions' mean values and the true value. For the chosen simulation configuration, the true value of the Rayleigh amplitude amounts to approximately 1.82%. However, the Rayleigh amplitude is not a universal quantity in the sense that it only depends on properties of the cosmic ray flux. Instead, it is also influenced by the experiment's geographical location and the shape of its field of view. The calculation of the true value incorporates the declination behaviour of the exposure function, as it composes the result from the amplitudes within the different declination slices. In this sense, even the calculation of the true value, which assumes a homogeneous field of view up to $\vartheta = 60°$, does not match the experimental conditions, when the zenith efficiency defect is included in the simulation. The shift of the sample mean values for time and direction based weighting can be interpreted as follows: it is evident from the right ascension reconstruction, that the direction based weighting method has problems in the case of right ascension dependent exposure functions that falsely rely on the assumption of full efficiency. The larger the extent of the efficiency deficit, the further the reconstructed dipole right ascension is dragged towards a false value. The direction, it is dragged to, is a property of the specific sidereal day coverage histogram used. The structures therein determine the extent of the misreconstruction and the direction towards which the reconstruction tends to deviate. The sidereal day coverage histogram used here (depicted in Figure 5.13) is an arbitrary example. Rather than drawing quantitative conclusions from it,

it should only be noted, that a non-flat sidereal day coverage indeed has an effect. It also affects the reconstruction of the Rayleigh amplitude: the interference of the specific sidereal day coverage histogram with the efficiency defect leads to a underestimation of the Rayleigh amplitude as the full efficiency threshold goes from $\vartheta_{\text{f.e.}} = 60°$ (full efficiency) to 50°. At $\vartheta_{\text{f.e.}} = 30°$, it turns into an overestimation. In the intermediate range at $\vartheta_{\text{f.e.}} = 40°$, the reconstructed amplitude happens to be very close to the expected value. The resulting bias at $\vartheta_{\text{f.e.}} = 40°$ is very small, which is the reason for the unexpectedly low position of this data point in the plot in Figure 6.3(a). On the other hand, the performance of the time based weighting can be interpreted as following: the right ascension reconstruction is equally accurate, and unaffected by the effectively incorrect exposure map. This is plausible, because the Rayleigh analysis is carried out without the exposure function entering the calculation. The mean value of obtained Rayleigh amplitudes shifts towards lower values with smaller ranges of zenith angle with full efficiency. Rather than a misreconstruction, this reflects the changing declination composition of the data set, caused by the increasing lack of highly inclined events.

It does not make sense to investigate the reconstruction quality of the Rayleigh amplitude. The Rayleigh amplitude is not a property of the cosmic ray flux alone. It also depends on experimental features. Moreover, it depends on the position of the dipole vector relative to the equatorial plane. Since the Rayleigh analysis cannot determine the position, it cannot provide conclusive information on the anisotropy. Rather than being a quantitative measure of the strength of the anisotropy, a positive Rayleigh amplitude can yield evidence for anisotropy. The evidence can be judged on the basis of the absolute value of the Rayleigh amplitude and the number of the events in the data set. However, a significantly non-zero Rayleigh amplitude is a sufficient condition for anisotropy, but not a necessary one. In that sense, even the concept of a "true value" for the Rayleigh amplitude is of limited use. There certainly is an expected value for the Rayleigh amplitude for a given simulation configuration. However, the calculation of the expected value requires precise knowledge of the simulation configuration. In contrast, three-dimensional reconstruction methods aim to extract estimates for dipole amplitude, declination and right ascension. These are universal quantities, of which the accuracy can easily be judged by comparison with the true values, which are defined unambiguously. This is the reason, why the Rayleigh amplitude was not considered in the extensive simulation studies, which have been described in Chapter 5.

### 6.1.2   Summary

An alternative way of weighting the individual events in a data set for performing a Rayleigh analysis has been presented. The alternative offers certain conceptual advantages over the conventional weighting method. While the latter determines the weighting factors from reconstructed quantities (the arrival directions), the new method proposed here only relies on a quantity that can be measured directly, namely the event time. In case of ideal measurement conditions, both methods perform equally well. However, experimental effects can cause problems for the conventional weighting method, that the new, time based weighting avoids. The conventional, direction based weighting relies on the correctness of the sky exposure map, which is calculated from the coverage histogram of the sidereal day, taking into account the experiment's geographical location and field of view. The time based weighting, on the other hand, only relies on the correctness of the sidereal day coverage. Hence, it avoids one potential point of failure: if the field of view is assumed incorrectly, the calculated exposure map does not reflect the experimental conditions properly. While the conventional weighting method is prone to this kind of error, the time based weighting is not.

The time based weighting method is meant to be an additional alternative, not a replace-

ment for the direction based weighting. The analysis of actual data should be carried out with both methods in parallel. In case, that the experimental conditions under which the data set was acquired, are fully understood, both method should yield similar results. However, substantial differences between the results delivered by the two methods would indicate incomplete understanding of the characteristics of the recorded data.

In the following section, a modified version of the SAP method will be developed, which uses the same weighting mechanism as the Rayleigh analysis. Consequently, the modified method can be operated with either direction or time based weighting as well.

## 6.2 A Modified SAP Method

The SAP method for dipole reconstruction has been introduced in Section 4.4. The basic idea of this method is to derive the dipole's amplitude and direction from the sum of the unit vectors of the reconstructed arrival directions. The relation between the sum of unit vectors ($\vec{S}$) and the estimated dipole vector ($\vec{R}$) in the simplest case of complete and uniform sky coverage can be written as:

$$\vec{R} = 3\frac{\vec{S}}{N}, \quad \vec{S} = \sum_{i=1}^{N} \hat{e}(\delta_i, \alpha_i),$$

(6.4)

with $N$ being the number of air shower observations. In this case, the estimator for the dipole vector is the arithmetic mean of the unit vectors representing the arrival directions, multiplied by 3 for normalisation. When applying this procedure on a set of isotropically distributed directions, the addends will essentially cancel out. The result will only differ from zero owing to statistical fluctuations.

The formula above is very similar to the Rayleigh formalism. The Rayleigh formalism reconstructs a dipole-like anisotropy in a distribution of right ascension values. In the special case of full and uniform sky coverage, the equatorial component of the dipole vector can be identified with the arithmetic mean of the two-dimensional unit vectors representing the right ascension values, multiplied by $\pi/2$ for normalisation:

$$\vec{R}_{\text{eq.}} = \frac{\pi}{2} \cdot \frac{\vec{S}_{\text{r.a.}}}{N}, \quad \vec{S}_{\text{r.a.}} = \sum_{i=1}^{N} \hat{e}(\alpha_i).$$

(6.5)

Both methods, two and three-dimensional, can be generalised to non-uniform sky coverages by means of weighting factors [Som01]. By weighting each air shower event with the inverse of the exposure function at the arrival direction, all regions of the sky give an equally large contribution to the sum:

$$\vec{R} = 3\frac{\vec{S}}{S_0}, \quad \vec{S} = \sum_{i=1}^{N} \frac{\hat{e}(\delta_i, \alpha_i)}{\omega(\delta_i, \alpha_i)}, \quad S_0 = \sum_{i=1}^{N} \frac{1}{\omega(\delta_i, \alpha_i)}.$$

(6.6)

In the case of full, but non-uniform sky coverage, the dipole vector is estimated by the weighted mean of the individual unit vectors, again multiplied by 3. Apart from the arithmetic mean having been replaced by a weighted mean, the form the original equation has been preserved.

The same weighting factors can be applied to the Rayleigh formalism. However, it has become customary to use different weighting factors. Instead of the inverse exposure at the arrival direction, the ratio of the average exposure at the arrival direction's declination and the exposure at the arrival direction serves as weighting factor:

$$\vec{S}_{\text{r.a.}} = \sum_{i=1}^{N} \frac{\bar{\omega}(\delta_i)}{\omega(\delta_i, \alpha_i)} \hat{e}(\alpha_i), \quad S_{0\,\text{r.a.}} = \sum_{i=1}^{N} \frac{\bar{\omega}(\delta_i)}{\omega(\delta_i, \alpha_i)}.$$

(6.7)
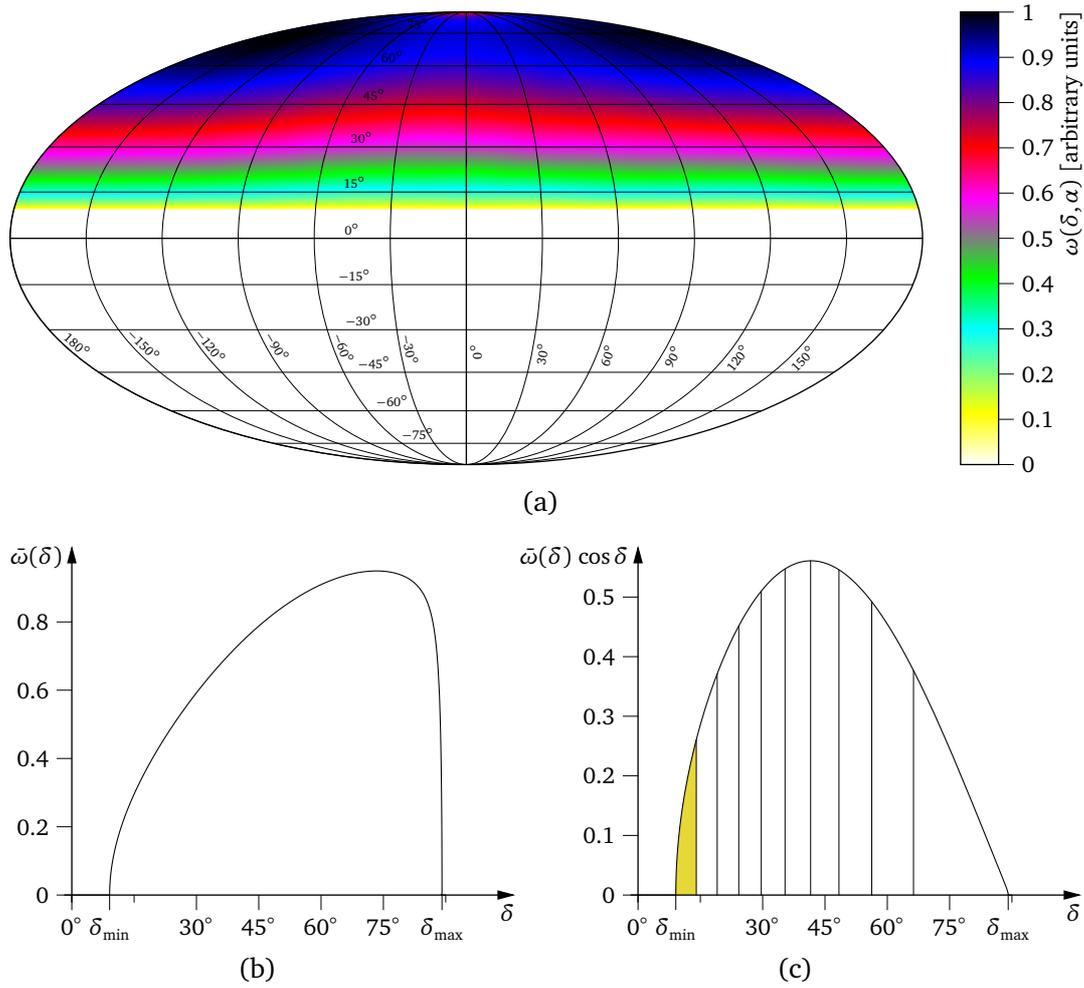
**Figure 6.4:** Figure (a) shows the exposure map of an experiment at 49° North latitude with a zenith limit of 40°. The field of view spans declinations from 9° to 89°. A typical extent of variation of the exposure with right ascension has been simulated. In Figure (b), the averaged exposure function $\bar{\omega}(\delta)$ is plotted. This function is multiplied with $\cos \delta$ to account for the solid angle coverage of the declination, and depicted in Figure (c). This curve represents the distribution of declination values in the data set, that would be expected under ideal measurement conditions, if the flux were perfectly isotropic. The total declination range from $\delta_{\min} = 9°$ to $\delta_{\max} = 89°$ is divided into ten sections of equal solid angle. The first of the sections (shaded area) covers approximately 2.8% of the area under the curve, which means that about 2.8% (statistical fluctuations and possible variations due to actual anisotropy aside) of the data set falls into this declination range. The original SAP method weights the data in a way, that this first section constitutes 10% of the eventual result, in compliance with its fraction of the solid angle. The modified SAP method presented here, uses different weighting factors and thereby achieves, that the first section composes only 2.8% of the final result, compliant with its share of the data set.

These weighting factors do not balance the contributions of all directions in the sky. Instead, they only equalise the contributions of different directions with the same declination. Thus, the strength of the contribution of a direction is not constant for all directions, but it does only depend on the declination, not on the right ascension. A detailed discussion of the choice of the weighting factors is given in Section 4.3.4. The conceptual difference of these two weightings

is illustrated in Figure 6.4.

Three aspects of that discussion shall be revisited here. Firstly, owing to the rotation of the Earth around its axis, the exposure depends much more on the declination than on the right ascension. While the inverse exposure can span several orders of magnitude, the weighting factors are of the order of one, typically in the range between 0.8 and 1.2. This prevents that few observations from regions with low exposure introduce large statistical fluctuations due to their huge weights. Secondly, the weighted mean $(\vec{S}/S_0)$ of the directions' unit vectors (multiplied by a constant factor) can no longer be identified as an estimator for the equatorial component of the dipole vector. There is a functional relation between the dipole vector and the weighted mean, which depends on $\bar{\omega}(\delta)$ (Eq. 4.41). Thirdly, this procedure can handle cases where the exposure is zero for certain declination ranges. The absence of contributions from such regions is correctly considered in the formalism. The procedure is therefore applicable to data sets of experiments with non-uniform and partial sky coverage.

The last aspect is taken into account by the SAP method [Aub05]. Since each air shower observation is weighted with the inverse of the exposure at its direction, all regions of the sky with declinations between $\delta_{\min}$ and $\delta_{\max}$ are equally represented. Regions outside the declination range do not contribute at all. However, the dipole vector is not estimated by the term $3\vec{S}/S_0$, but by more complex formulas (Eq. 4.44), that account for the incomplete coverage of the sky. This relation does solely depend on the field of view of the experiment, in terms of the declination range, expressed by $\delta_{\min}$ and $\delta_{\max}$. As the weighting factors do fully account for the possibly inhomogeneous sky coverage between $\delta_{\min}$ and $\delta_{\max}$, the exposure function does not enter in the transformation of the weighted mean into a dipole estimator.

It is desirable to realise also the first of the three aforementioned aspects for the three-dimensional reconstruction. The usage of weighting factors of order one would reduce the effect of statistical fluctuations. Using the same weighting factors as for the Rayleigh formalism, the weighted sum $(\vec{S})$ of the three-dimensional unit vectors representing the reconstructed cosmic ray arrival directions, and the sum of the weights $(S_0)$ is given by:

$$\vec{S} = \sum_{i=1}^{N} \frac{\bar{\omega}(\delta_i)}{\omega(\delta_i, \alpha_i)} \, \hat{e}(\delta_i, \alpha_i), \quad S_0 = \sum_{i=1}^{N} \frac{\bar{\omega}(\delta_i)}{\omega(\delta_i, \alpha_i)} \,. \tag{6.8}$$

In the following section, formulas for calculating a dipole estimator from the modified versions of $\vec{S}$ and $S_0$ will be derived.

### 6.2.1 Derivation of a Dipole Estimator

In order to find the functional relation between the dipole vector and the expectation values for $\vec{S}$ and $S_0$, an analytic calculation of $\vec{S}$ and $S_0$ is carried out, for which the sum over all observations is replaced by an integral over the directions:

$$\vec{S} = \int d\Omega \, I(\delta, \alpha) \, \frac{\bar{\omega}(\delta)}{\omega(\delta, \alpha)} \, \hat{e}(\delta, \alpha), \quad S_0 = \int d\Omega \, I(\delta, \alpha) \, \frac{\bar{\omega}(\delta)}{\omega(\delta, \alpha)} \,. \tag{6.9}$$

The set of reconstructed arrival directions is represented by a continiuous function $I(\delta, \alpha)$, that corresponds to the density of observations from the given direction. It is given by the product of the flux and the exposure:

$$I(\delta, \alpha) = \omega(\delta, \alpha) \Phi(\delta, \alpha). \tag{6.10}$$

The flux is assumed to have dipolar shape:

$$\Phi_{\text{dipole}}(\delta, \alpha) = \Phi_0 \cdot \left( 1 + \hat{e}(\delta, \alpha) \cdot \vec{D} \right), \quad \vec{D} = D \cdot \hat{e}(\delta_{\text{dipole}}, \alpha_{\text{dipole}}). \tag{6.11}$$

Using the definitions of $\Phi(\delta, \alpha)$ and $I(\delta, \alpha)$ yields:

$$\begin{aligned}
\vec{S} &= \int \mathrm{d}\Omega\,\omega(\delta, \alpha)\,\Phi_0 \cdot \left(1 + \hat{e}(\delta, \alpha) \cdot \vec{D}\right) \frac{\bar{\omega}(\delta)}{\omega(\delta, \alpha)}\, \hat{e}(\delta, \alpha), \\
S_0 &= \int \mathrm{d}\Omega\,\omega(\delta, \alpha)\,\Phi_0 \cdot \left(1 + \hat{e}(\delta, \alpha) \cdot \vec{D}\right) \frac{\bar{\omega}(\delta)}{\omega(\delta, \alpha)}\, .
\end{aligned}$$

$$(6.12)$$

In both these equations, the exposure function $\omega(\delta, \alpha)$ appears twice: once it stems from $I(\delta, \alpha)$ and represents the dependency of the frequency of observations from a certain direction on the exposure. The higher the exposure towards a direction, the more observations from that direction are contained in the data set. The second occurence of the exposure function is in the denominator of the weighting factor, which is designed to compensate for the former dependency. These two terms cancel out, so that the values of $\vec{S}$ and $S_0$ will not depend on the specific shape of the exposure function. However, both equations contain the averaged exposure function $\bar{\omega}(\delta)$, and consequently the result will depend on it. In fact, the presence of $\bar{\omega}(\delta)$ is one of two differences to the conventional SAP method. The other difference is the integration range: while the SAP method integrates over declinations from $\delta_{\min}$ to $\delta_{\max}$, the integration in this modified version can generally be carried out over the whole sky ($\delta$ ranging from $-\pi/2$ to $\pi/2$), as the term $\bar{\omega}(\delta)$ effectively narrows down the integration range to declinations with non-zero exposure. The right ascension $\alpha$ is always integrated over its range of values from $0$ to $2\pi$. For improved readability, these integration ranges are not written in the following calculations. Expanding and using the definition of the solid angle element gives:

$$\begin{aligned}
\vec{S} &= \underbrace{\Phi_0 \iint \cos\delta\,\mathrm{d}\delta\,\mathrm{d}\alpha\,\bar{\omega}(\delta)\,\hat{e}(\delta, \alpha)}_{\vec{S}^i} + \underbrace{\Phi_0 \iint \cos\delta\,\mathrm{d}\delta\,\mathrm{d}\alpha\,\left(\hat{e}(\delta, \alpha) \cdot \vec{D}\right)\bar{\omega}(\delta)\,\hat{e}(\delta, \alpha)}_{\vec{S}^a}, \\
S_0 &= \underbrace{\Phi_0 \iint \cos\delta\,\mathrm{d}\delta\,\mathrm{d}\alpha\,\bar{\omega}(\delta)}_{S_0^i} + \underbrace{\Phi_0 \iint \cos\delta\,\mathrm{d}\delta\,\mathrm{d}\alpha\,\left(\hat{e}(\delta, \alpha) \cdot \vec{D}\right)\bar{\omega}(\delta)}_{S_0^a}\, .
\end{aligned}$$

$$(6.13)$$

The terms $\vec{S}^i$ and $S_0^i$ describe the contributions of the isotropic component (the background) of the flux to $\vec{S}$ and $S_0$, respectively. Accordingly, the anisotropic component (the signal) is reflected in $\vec{S}^a$ and $S_0^a$. In the special case of complete and uniform sky coverage, the isotropic contribution to the sum of unit vectors fully cancels out. Therefore, $\vec{S}^i$ equals zero and $\vec{S}^a$ corresponds to the dipole vector (apart from a constant normalisation factor). In that case, $S_0$, which is defined as the sum of all weighting factors, can be identified with the number of recorded events. Because the excess of events in one direction and the deficit in the opposite direction cancel each other out perfectly, the anisotropic component does not influence the number of recorded events. Thus $S_0^a$ is zero, and the number of events $S_0$ equals $S_0^i$.

Even in the case of an arbitrary sky coverage, the $x$ and $y$-components of $\vec{S}^i$ always vanish, because their integrands of the $\alpha$-integration are $\cos\alpha$ and $\sin\alpha$, respectively. This is no surprise, as these quantities correspond to the equatorial component of the weighted sum of the arrival directions. Bearing in mind that $\vec{S}^i$ only comprises the isotropic component of the flux, and that differences of the exposure in right ascension are levelled out by the weighting factors, the equatorial component ($S_x^i$ and $S_y^i$) is expected to cancel out completely. The $z$-component does generally not cancel out and is given by:

$$S_z^i = 2\pi\Phi_0 \int \cos\delta\,\mathrm{d}\delta\,\bar{\omega}(\delta)\sin\delta = 2\pi\Phi_0 C_{11}^*\, . \qquad (6.14)$$

Integrals of the averaged exposure function $\bar{\omega}(\delta)$ multiplied by powers of the cosine and sine functions will repeatedly occur in the following calculations. The values of these integrals are properties of the exposure function. Hence they are constants for the analysis of a given data set, generically defined by:

$$C_{ij}^* = \int\limits_{\delta=-\pi/2}^{\pi/2} \bar{\omega}(\delta) \cos^i \delta \, \sin^j \delta \, \mathrm{d}\delta \, . \tag{6.15}$$

Based on these, a second set of constants $C_{ij}$ is defined, which is normalised to $C_{10}^*$:

$$C_{ij} = \frac{C_{ij}^*}{C_{10}^*} \, . \tag{6.16}$$

In contrast to $C_{ij}^*$, the $C_{ij}$ constants are dimensionless. By definition of $C_{ij}$, the following identities are true:

$$C_{10} = 1 \, , \qquad \frac{C_{ij}^*}{C_{i'j'}^*} = \frac{C_{ij}}{C_{i'j'}} \, . \tag{6.17}$$

In the final result of the following derivation, the $C_{ij}^*$ constants only appear in ratios, so that the result can be given with the dimensionless constants $C_{ij}$ alone. This is preferable, because unlike the unnormalised constants, the $C_{ij}$ constants do not depend on the amount of measurement time of the experiment. The averaged exposure function $\bar{\omega}(\delta)$ is proportional to the amount of measurement time, and so are the $C_{ij}^*$ constants. However, this dependency cancels out through the normalisation. The number of constants used in the formulas can be reduced by means of the following identity:

$$\cos^i \delta \, \sin^j \delta = \cos^{i-2} \delta \, \sin^j \delta \cdot \underbrace{(1 - \sin^2 \delta)}_{\cos^2 \delta} = \cos^{i-2} \delta \, \sin^j \delta - \cos^{i-2} \delta \, \sin^{j+2} \delta \, , \tag{6.18}$$

which can be applied to the integrand in the above definition and thus yields:

$$C_{ij}^* = C_{i-2;j}^* - C_{i-2;j+2}^* \, , \qquad C_{ij} = C_{i-2;j} - C_{i-2;j+2} \, . \tag{6.19}$$

Specifically, the identity $C_{30}^* = C_{10}^* - C_{12}^*$, which can also be written as $C_{30} = 1 - C_{12}$, will be used.

The vector $\vec{S}^a$ corresponds to the anisotropy signal in the data set. However, it cannot be identified with the dipole vector directly, because it may be distorted due to the inhomogeneous sky coverage. Its definition contains the scalar product $\hat{e}(\delta, \alpha) \cdot \vec{D}$, for the calculation of which it is most convenient to express the dipole vector through its Cartesian components $D_x$, $D_y$ and $D_z$:

$$\hat{e}(\delta, \alpha) \cdot \vec{D} = D_x \cos \delta \, \cos \alpha + D_y \cos \delta \, \sin \alpha + D_z \sin \delta \, . \tag{6.20}$$

This scalar quantity is one of the factors in the integrand of $\vec{S}^a$. It enters the calculations of $S_x^a$ and $S_y^a$ as well as $S_z^a$. However, the integration over $\alpha$ entails, that each of the three components of the dipole vector eventually only appears in the corresponding components of $\vec{S}^a$. In the scalar product, the $\alpha$-dependent part is $\cos \alpha$ in the $D_x$-term, $\sin \alpha$ in the $D_y$-term and 1 in the $D_z$-term. The same $\alpha$-dependencies appear in the three components of the unit vector, which is the only other term in the integrand that depends on $\alpha$. For integration over

$\alpha$ from 0 to $2\pi$, these three functions form an orthogonal system. Hence there are no mixed terms in the result. The integrations yields:

$$
\begin{array}{rcrclcl}
S_x & = & 0 & + & \pi\Phi_0 C_{30}^* D_x & = & \pi\Phi_0\cdot(C_{10}^* - C_{12}^*)D_x\,, \\
S_y & = & 0 & + & \pi\Phi_0 C_{30}^* D_y & = & \pi\Phi_0\cdot(C_{10}^* - C_{12}^*)D_y\,, \\
S_z & = & \underbrace{2\pi\Phi_0 C_{11}^*}_{\vec{S}^i} & + & \underbrace{2\pi\Phi_0 C_{12}^* D_z}_{\vec{S}^a} & = & 2\pi\Phi_0\cdot(C_{11}^* + C_{12}^* D_z)\,.
\end{array}
\tag{6.21}
$$

The quantity $S_0$ stands for the sum of the weights of all observations. Since the weights are of the order of one, $S_0$ should be approximately the number of observations. The formula given above breaks $S_0$ down into an isotropic and an anisotropic part. The isotropic part ($S_0^i$) corresponds to the number of events that would be recorded if there were no anisotropy effect. The anisotropic part ($S_0^a$) denotes the (possibly negative) number of events, that the anisotropy effect adds to the data set. In case of full and uniform sky coverage, the latter is zero. However, with non-uniform sky coverage, the experiment can have more or less exposure towards the excess region as compared to the deficit region. Carrying out the integration of $S_0$ gives:

$$
S_0 = \underbrace{2\pi\Phi_0 C_{10}^*}_{S_0^i} + \underbrace{2\pi\Phi_0 C_{11}^* D_z}_{S_0^a} = 2\pi\Phi_0\cdot(C_{10}^* + C_{11}^* D_z)\,.
\tag{6.22}
$$

A brief summary of the procedure so far: a set of variables ($\vec{S}$, $S_0$) has been defined. These variables can be computed for any set of arrival directions, provided that the underlying exposure function is known. Based on a flux of dipolar shape, characterised by a dipole vector ($\vec{D}$), the quantities $\vec{S}$ and $S_0$ have been analytically calculated. The results depend on the properties of the dipole distribution. At this point, there is a system of four equations (those defining $S_x$, $S_y$, $S_z$ and $S_0$) and a total of four unknown variables ($D_x$, $D_y$, $D_z$ and $\Phi_0$).

The derivation, as it has been carried out so far, could be accomplished with any arbitrary definition of the variables $\vec{S}$ and $S_0$. Different weightings could be used, or the definitions could have a completely different form. However, there are two more requirements, that have to be met. Firstly, the obtained system of equations must be solvable, i.e. it must be possible to extract solutions for the three components of $\vec{D}$ from the computed values of $\vec{S}$ and $S_0$. If this condition is fulfilled, it is ensured, that the obtained analytic formulas, when applied to a dipole-like flux distribution, would correctly reconstruct the dipole vector, if infite statistics were available. This leads to the second requirement to be fulfilled: the procedure has to perform well with a limited amount of statistics.

The set of variables chosen here fulfills the first of the requirements: the equation system can be solved. However, when this analysis is applied to a real data set, i.e. one of finite size, it cannot deliver the true dipole vector $\vec{D}$, but only an estimate $\vec{R}$. Therefore, the final result of the derivation shall be given as a set of equations that defines $\vec{R}$:

$$
\begin{aligned}
R_x & = \frac{2S_x}{1 - C_{12}}\cdot\frac{C_{12} - C_{11}^2}{C_{12}S_0 - C_{11}S_z}\,, \\[2mm]
R_y & = \frac{2S_y}{1 - C_{12}}\cdot\frac{C_{12} - C_{11}^2}{C_{12}S_0 - C_{11}S_z}\,, \\[2mm]
R_z & = \frac{C_{11}S_0 - S_z}{C_{11}S_z - C_{12}S_0}\,.
\end{aligned}
\tag{6.23}
$$

The validation of the second requirement is subject to tests by means of Monte Carlo simulations. These were performed, and the results will be presented below. First, however, the correctness of the above formulas shall be reassessed by plausibility considerations.

### 6.2.2 Plausibility Checks

The formulas obtained in the previous section correspond to the very general case of inhomogeneous, and possibly incomplete sky coverage. When applied to special cases, they can be reduced to simpler formulas. Particularly the formulas of [Som01] and the SAP method [Aub05] can be extracted from the ones above.

Assuming a complete and uniform sky coverage ($\omega(\delta, \alpha) = \omega_0$), the $C_{ij}$ constants can be calculated in the following way:

$$
\begin{aligned}
C_{ij} &= \frac{C_{ij}^*}{C_{10}^*} = \frac{\int_{\delta=-\pi/2}^{\pi/2} \bar{\omega}(\delta) \cos^i \delta \sin^j \delta \, \mathrm{d}\delta}{\int_{\delta=-\pi/2}^{\pi/2} \bar{\omega}(\delta) \cos \delta \, \mathrm{d}\delta} = \frac{\omega_0 \int_{\delta=-\pi/2}^{\pi/2} \cos^i \delta \sin^j \delta \, \mathrm{d}\delta}{\omega_0 \int_{\delta=-\pi/2}^{\pi/2} \cos \delta \, \mathrm{d}\delta} \\
&= \frac{\omega_0 \int_{\delta=-\pi/2}^{\pi/2} \cos^i \delta \sin^j \delta \, \mathrm{d}\delta}{2\omega_0} = \frac{1}{2} \int_{\delta=-\pi/2}^{\pi/2} \cos^i \delta \sin^j \delta \, \mathrm{d}\delta .
\end{aligned}
\tag{6.24}
$$

The constants have the following values:

$$
C_{11} = 0 , \quad C_{12} = \frac{1}{3} .
\tag{6.25}
$$

When plugging these values into Equation 6.23, the formulas become much simpler:

$$
\vec{R} = 3 \frac{\vec{S}}{S_0} .
\tag{6.26}
$$

Thus, in the special case of complete and homogeneous sky coverage, the modified SAP method yields the same dipole estimator as in [Som01]. This is the expected behaviour, as in that special case these two approaches are equivalent. Each single event is weighted equally. The weighting factor in [Som01] takes the constant value $1/\omega_0$, whereas in the modified SAP method $\omega_0$ cancels out and the weighting factor is 1. The specific values of $\vec{S}$ and $S_0$ are not identical with both methods (in [Som01], both carry an additional factor of $1/\omega_0$). However, their ratio, which appears in the formula for the dipole estimator, is the same. When generalising towards the case of full, but inhomogeneous sky coverage, the two methods take on different ways, regarding both the calculation of $\vec{S}$ and $S_0$ and their interpretation as dipole estimator.

An incomplete and homogeneous sky coverage is defined by

$$
\omega(\delta, \alpha) = \begin{cases} \omega_0 & \delta_{\min} < \delta < \delta_{\max} \\ 0 & \text{otherwise} \end{cases} .
\tag{6.27}
$$

In this case, the modified SAP method is expected to be equivalent to the original SAP method [Aub05]. The considerations regarding the weighting factors are the same as in the previous case. The calculation of the $C_{ij}$ constants goes along the same lines, only with the integration range being reduced to $\delta_{\min}$ to $\delta_{\max}$, finally leading to the following results:

$$
C_{11} = \frac{\sin \delta_{\max} + \sin \delta_{\min}}{2} , \quad C_{12} = \frac{\sin^2 \delta_{\max} + \sin^2 \delta_{\min} + \sin \delta_{\max} \sin \delta_{\min}}{3} .
\tag{6.28}
$$

Comparing these with the constants used in the original SAP method (Eq. 4.44) leads to:

$$
s = 2C_{11} , \quad \gamma = \frac{s^2 - p}{3} = \frac{(\sin \delta_{\max} + \sin \delta_{\min})^2 - \sin \delta_{\max} \sin \delta_{\min}}{3} = C_{12} ,
$$
$$
p = s^2 - 3\gamma = 4C_{11}^2 - 3C_{12} .
\tag{6.29}
$$

With these identities, the formulas for the dipole estimator of the original SAP method (Eq. 4.44) and the modified SAP method (Eq. 6.23) are equivalent.

### 6.2.3  Time Based Weighting

The time based weighting factors, introduced in Section 6.1, can also be used with the modified SAP method. The change only regards the summations of the quantities $\vec{S}$ and $S_0$ (Eq. 6.8). With time based weighting in place, the modified formulas read:

$$\vec{S} = \sum_{i=1}^{N} \frac{\bar{m}}{m(t)}\,\hat{e}(\delta_i, \alpha_i), \quad S_0 = \sum_{i=1}^{N} \frac{\bar{m}}{m(t)}, \tag{6.30}$$

where $m(t)$ is the function describing the coverage of the sidereal day, as defined in Section 6.1, and $\bar{m}$ is its average value. The formulas for calculating the dipole vector estimate $\vec{R}$ from $\vec{S}$ and $S_0$ stay unchanged. The section below on Monte Carlo simulations with the modified SAP method will feature results obtained with both direction and time based weighting.

### 6.2.4  Comparison of the Modified SAP Method and the Multipole Expansion Method

The advantage of the modified SAP method over the original SAP method lies in the reduction of statistical fluctuations due to the more regular weighting of events within the data set. If the data set spans only full sidereal days and invariant measurement conditions can be assumed, the exposure function $\omega(\delta, \alpha)$ does not depend on the right ascension $\alpha$, so that

$$\omega(\delta, \alpha) = \bar{\omega}(\delta) \Rightarrow \frac{\bar{\omega}(\delta)}{\omega(\delta, \alpha)} = 1. \tag{6.31}$$

In this special case, all events are evenly weighted. The formulas for $\vec{S}$ and $S_0$ can then be simplified to:

$$\vec{S} = \sum_{i=1}^{N} \hat{e}(\delta_i, \alpha_i), \quad S_0 = \sum_{i=1}^{N} 1 = N. \tag{6.32}$$

On the other hand, the multipole expansion method, as described in Section 4.5, can be used as a pure dipole reconstruction method. In this case, the maximum number for the order $\ell$ amounts to one, and the summation can be written as:

$$\bar{b}_{00} = \frac{1}{N}\sum_{i=1}^{N} Y_{00}(\delta_i, \alpha_i) = \frac{1}{N}\sum_{i=1}^{N} 1 = 1, \tag{6.33}$$

$$\begin{pmatrix} \bar{b}_{11} \\ \bar{b}_{1-1} \\ \bar{b}_{10} \end{pmatrix} = \frac{1}{N}\sum_{i=1}^{N} \begin{pmatrix} Y_{11}(\delta_i, \alpha_i) \\ Y_{1-1}(\delta_i, \alpha_i) \\ Y_{10}(\delta_i, \alpha_i) \end{pmatrix} = \frac{1}{N}\sum_{i=1}^{N} \sqrt{3}\,\hat{e}(\delta_i, \alpha_i) = \frac{\sqrt{3}}{N}\vec{S} = \frac{\sqrt{3}}{S_0}\vec{S}. \tag{6.34}$$

Thus, the three multipole coefficients $b_{1m}$, that represent the dipole moment of the data set, equal (apart from a constant factor $\sqrt{3}/N$) the components of the vector $\vec{S}$, that is used in the modified SAP method. In the same way as the vector $\vec{S}$ is transformed into a dipole estimator, the set of $b_{\ell m}$ coefficients is subject to a transformation that yields a set of estimators for the $a_{\ell m}$ coefficients, which are meant to describe the cosmic ray flux distribution. With $\ell_{\max}$ set to one, the set of $b_{\ell m}$ coefficients forms a dipole estimator. The question is, how the dipole

estimators, that are retrieved with these two methods, the modified SAP method and the multipole expansion method, relate to each other.

The inverse of the kernel $[K]_{\ell\ell'}^{mm'}$ transforms the $\bar{b}_{\ell m}$ coefficients (from the summation of the arrival directions' unit vectors) into the $\bar{a}_{\ell m}$ coefficients (the dipole estimator). The kernel's definition is given in Equation 4.49. Dealing with the special case of right ascension independent exposure, the definition can be slightly simplified and written as:

$$[K]_{\ell\ell'}^{mm'} = \int \cos\delta \, d\delta \, d\alpha \, Y_{\ell m}(\delta,\alpha) \, \bar{\omega}(\delta) \, Y_{\ell'm'}(\delta,\alpha). \tag{6.35}$$

The $Y_{\ell m}$ functions consist of sine and cosine terms of $\delta$ and $\alpha$. The precise definitions are given in Appendix A. Since $\ell$ only ranges between zero and one, the kernel consists of 16 elements, many of which amount to zero due to the integration over $\alpha$. The remaining terms are:

$$
\begin{aligned}
[K]_{00}^{00} &= \int \cos\delta \, d\delta \, d\alpha \, \bar{\omega}(\delta) &&= C_{10}^*, \\
[K]_{11}^{11} &= \int \cos\delta \, d\delta \, d\alpha \, \bar{\omega}(\delta) \, 3\cos^2\delta \, \cos^2\alpha &&= 3\pi C_{30}^*, \\
[K]_{11}^{-1-1} &= \int \cos\delta \, d\delta \, d\alpha \, \bar{\omega}(\delta) \, 3\cos^2\delta \, \sin^2\alpha &&= 3\pi C_{30}^*, \\
[K]_{11}^{00} &= \int \cos\delta \, d\delta \, d\alpha \, \bar{\omega}(\delta) \, 3\sin^2\delta &&= 6\pi C_{12}^*, \\
[K]_{01}^{00} = [K]_{10}^{00} &= \int \cos\delta \, d\delta \, d\alpha \, \bar{\omega}(\delta) \, \sqrt{3}\sin\delta &&= 2\pi\sqrt{3} C_{11}^*.
\end{aligned}
\tag{6.36}
$$

Inverting the kernel and applying it to the set of $\bar{b}_{\ell m}$ coefficients leads to the set of estimators for the $a_{\ell m}$ coefficients:

$$
\begin{aligned}
\bar{a}_{00} &= \frac{3 C_{12}^* \bar{b}_{00} - \sqrt{3}\, C_{11}^* \bar{b}_{10}}{6\pi \cdot \left( C_{10}^* C_{12}^* - C_{11}^{*\,2} \right)}, &\quad \bar{a}_{1-1} &= \frac{\bar{b}_{1-1}}{3\pi C_{30}^*}, \\[2ex]
\bar{a}_{10} &= \frac{\sqrt{3}\, C_{11}^* \bar{b}_{00} - C_{10}^* \bar{b}_{10}}{6\pi \cdot \left( C_{10}^* C_{12}^* - C_{11}^{*\,2} \right)}, &\quad \bar{a}_{11} &= \frac{\bar{b}_{11}}{3\pi C_{30}^*},
\end{aligned}
\tag{6.37}
$$

from which the dipole estimator can be constructed according to Equation 4.8[1]. Its components are given by:

$$
\begin{aligned}
R_x &= \frac{\sqrt{3}}{\bar{a}_{00}} \bar{a}_{11} &&= \frac{2\bar{b}_{11}}{1 - C_{12}} \cdot \frac{C_{12} - C_{11}^2}{\sqrt{3}\, C_{12}\bar{b}_{00} - \bar{b}_{10} C_{11}}, \\[2ex]
R_y &= \frac{\sqrt{3}}{\bar{a}_{00}} \bar{a}_{1-1} &&= \frac{2\bar{b}_{1-1}}{1 - C_{12}} \cdot \frac{C_{12} - C_{11}^2}{\sqrt{3}\, C_{12}\bar{b}_{00} - \bar{b}_{10} C_{11}}, \\[2ex]
R_z &= \frac{\sqrt{3}}{\bar{a}_{00}} \bar{a}_{10} &&= \frac{\sqrt{3}\, C_{11}\bar{b}_{00} - \bar{b}_{10}}{C_{11}\bar{b}_{10} - \sqrt{3}\, C_{12}\bar{b}_{00}}.
\end{aligned}
\tag{6.38}
$$

The $\bar{b}_{\ell m}$ terms can be expressed by means of $\vec{S}$ and $S_0$, as described above in Equations 6.33 and 6.34. The resulting formulas are identical to those of the modified SAP method (Eq. 6.23).

Thus, in the case of an exposure function that is independent from the right ascension, the modified SAP method is identical to the multipole expansion up to dipole order ($\ell_{\max} = 1$). The two methods, however, do differ in the way that they handle exposure functions, that do depend on right ascension. While the modified SAP methods applies different weightings to the events in order to account for the irregularities, the multipole expansion incorporates

---

[1]Equation 4.8 relates the true dipole vector $\vec{D}$ to the true multipole coefficients $a_{\ell m}$. The dipole estimator $\vec{R}$ can be derived from the estimated multipole coefficients $\bar{a}_{\ell m}$ in the same way.
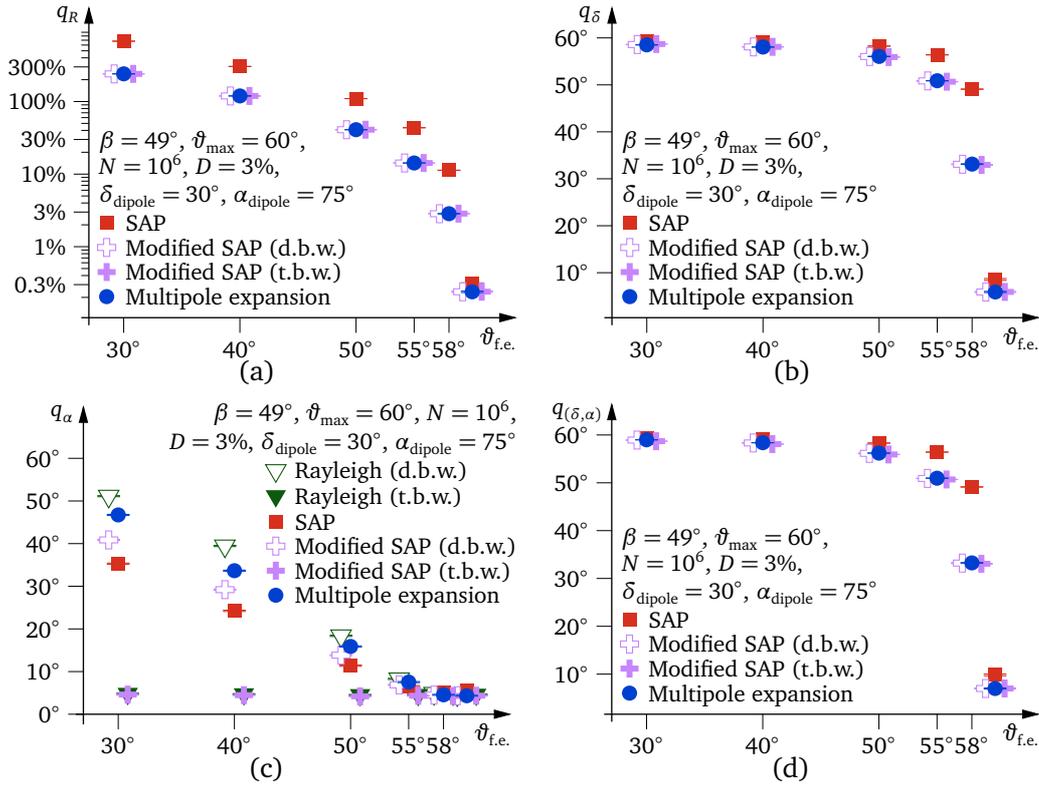
**Figure 6.5:** Reconstruction quality of the modified SAP method subject to the extent of the efficiency defect: the rightmost data points in each of the plots refer to the case of full efficiency for the whole field of view, thus for the absence of the efficiency defect.

the precise exposure function into the transformation $[K]$ between the coefficients describing the dipole in the cosmic ray flux ($a_{\ell m}$) and that in the data set ($b_{\ell m}$). In the same sense that the modified SAP method is preferable over the original SAP method from the statistics point of view, the multipole expansion method is even more favourable for dipole reconstruction. However, after changing the weighting from using arbitrarily high values (original SAP method) to values of the order of one (modified SAP method), the additional benefit of abandoning weighting factors completely (multipole expansion method) is far less significant. On the other hand, the implementation of the modified SAP method can be simpler compared to that of the multipole expansion, as it can do without calculation of the precise exposure function: when using time based weightings, only the averaged exposure function $\bar{\omega}(\delta)$ needs be computed, for which an analytic expression can be used. Carrying out the multipole expansion method in the general case involves the numerical computation of two-dimensional integrals of the exposure function.

### 6.2.5 Monte Carlo Simulations

The modified SAP method is identical to the multipole expansion method in the case of a right ascension independent exposure function. Only in the case of data sets with inhomogeneous sidereal day coverage, the modified SAP method constitutes an additional option for analysis. The following Monte Carlo studies are based on the standard configuration for simulations, as introduced in 5.3.2, with the exception that the coverage of the sidereal day simulated is the one depicted in Figure 5.13. Additionally, efficiency deficits of various extents were simulated.

These deficits entail that the computed exposure maps, on which the analyses are based, do not correctly reflect the experimental situation. This may reveal different performances of the direction and time based weighting mechanism, as it has been the case in Section 6.1. Figure 6.5 shows the reconstruction accuracies for the various methods subject to the zenith angle up to which full efficiency is given. The rightmost data points in each of the plots refers to the standard configuration, with full efficiency for the complete field of view.

The accuracies of amplitude and declination reconstructions of both variants of the modified SAP method equal those of the multipole expansion method exactly. The impact of the simulated efficiency defect on amplitude and declination reconstructions is also identical for these two methods. Although the modified SAP method still uses a weighting technique to account for the right ascension dependency of the exposure function, it does not perform worse than the multipole expansion method, which assigns the same weight to all recorded events. Using weights of the order of one seems to have no effect on the strength of statistical fluctuations, whereas the weights of arbitrary magnitudes, that are used by the SAP method, result in a considerable penalty.

The situation is different for the reconstruction of the dipole's right ascension value. Here, the original SAP method performs even better than the multipole method. The zenith efficiency effect, combined with the uneven coverage of the sidereal day, leads to irregularities in the distribution of the air showers' reconstructed right ascensions. These irregularities concentrate in the medium declination range, as those regions of the sky are seen with different inclinations over the course of time. They do not affect the edges of the visible declination range, as those parts of the sky are only seen once per sidereal day and at high inclination. Since the SAP method weights the regions at the edge of the visible sky higher than other regions, owing to their low exposure, the SAP method is less obstructed by the combination of experimental effects simulated here.

A considerably better performance for right ascension reconstruction is achieved with the methods that utilise time based weightings. The weighting factors are not affected by any of the experimental effects simulated here, and so the reconstruction of the dipole vector's right ascension component works flawlessly. However, this advantage is practically irrelevant: the efficiency defect causes the declination value to be falsely reconstructed as very close to the North Pole. Being a longitudinal coordinate, the specific value of the right ascension coordinate is almost meaningless near the poles. Consequently, the better reconstruction of the right ascension by the time based weighting variants has almost no positive effect on the combined error of the dipole direction reconstruction.

### 6.2.6 Summary

A modification of the established SAP method has been proposed, which performs a more homogeneous weighting of the recorded events and therefore can reduce the statistical fluctuations of the reconstruction results. However, it has been shown that the modified SAP method is very similar to the multipole expansion method. In fact, these two methods are mathematically equivalent, thus identical, in the special case of right ascension independent exposure functions. In the more general case of right ascension dependent exposure functions, the modified SAP methods accounts for this dependency by weighting the individual events, whereas the multipole expansion method incorporates this dependency into the transformation of the summation variables to the dipole estimator. The latter demands are more sophisticated implementation, as it involves the numerical computation of several two-dimensional integral formulas. The reconstruction accuracy of the modified SAP method is as good as that of the multipole expansion method. By employing time based weightings, the modified SAP method

can avoid problems with the right ascension reconstruction introduced by the combination of two effects, namely occasional interruptions of the measurement and zenith angle dependent efficiency. I.e. the modified SAP method performs the right ascension reconstruction even better than the multipole expansion method.

## 6.3   The Slice Method for Dipole Reconstruction

The methods discussed in this chapter so far aimed at optimising the statistical properties of the dipole reconstruction. However, as the simulation studies in the previous chapter have shown, experimental, thus systematic, effects can have a much bigger impact on the results of the analyses. One of those effects is a zenith angle dependent experimental inefficiency. It has been shown, that all the methods presented so far are vulnerable to this effect. The problem emerges from the fact, that all those methods rely on the correctness of the exposure function $\omega(\delta, \alpha)$, which is computed with full efficiency up to a given zenith angle limit $\vartheta_{\max}$. If the actual exposure function, that influences the data set, differs from the assumed one, the analysis methods fail to reconstruct the correct dipole configuration. It would be particularly advantageous to have an analysis method that does not rely on the correctness of the exposure function. This is specifically the case, if the exposure function does not enter the calculations at all. The Slice method, which shall be introduced in this section, achieves this. It does not depend on the exposure function, but uses the time based weightings that have been introduced in this chapter. Therefore, it is not prone to problems caused by a direction dependent efficiency. However, the method does assume constant measurement conditions. Care has to be taken to compensate for e.g. metereological effects, that affect the event rate.

The basic idea behind the Slice method is to divide the data set into subsets of events with (nearly) identical declination values. In each of these narrow stripes in declination, or slices, the right ascension distribution is investigated by means of a Rayleigh analysis. Assuming that the cosmic ray flux distribution has a dipolar shape, each of the slices contains a dipolar distribution of events as well. While the excess regions in all of the slices coincide, within the limits of statistical fluctuations, with the right ascension of the global dipole vector, the reconstructed Rayleigh amplitudes in the slices will differ. The set of Rayleigh amplitudes, that are reconstructed in different declination slices, can be used to determine the amplitude and declination of the global dipole.

As usual, weighting factors are used in the Rayleigh analyses to eliminate the right ascension dependency of the exposure. By using the time based weighting factors, as introduced in Section 6.1, this can be done without explicitly calculating the exposure function. On the other hand, the declination dependency of the exposure turns out to be irrelevant for this technique. The actual amount of the exposure for any declination range influences the amount of statistics that enters the Rayleigh analysis in the corresponding slice, but does not influence the expectation values of the results of the particular Rayleigh analysis.

Let the data set be divided into $S$ subsets with indices $i = 0, \ldots, S - 1$. Each slice covers an infinitesimally small declination range around the declination $\delta_i$. The outcome of the Rayleigh analysis can be predicted using Equation 4.41 by defining the exposure function as $\bar{\omega}(\delta) = \omega_i \delta(\delta - \delta_i)$, with $\delta(x)$ denoting the Dirac delta function. According to the definition (Eq. 4.41), the $C_{ij}$ constants become $C_{11} = \sin \delta_i$ and $C_{20} = \cos \delta_i$. The Rayleigh amplitude, that is expected in slice $i$, is then given by:

$$D_i' = \frac{D \cos \delta_{\text{dipole}} \cos \delta_i}{1 + D \sin \delta_{\text{dipole}} \sin \delta_i} , \tag{6.39}$$

where $D$ is the amplitude of the global dipole, and $\delta_{\text{dipole}}$ is the declination of its excess region. The Rayleigh phase in each of the slices is expected to match the right ascension of the dipole's excess region $\alpha_{\text{dipole}}$. This formula complies with the above considerations in the sense that it contains no reference to any specific values or properties of the exposure function $\bar{\omega}(\delta)$.

For a given dipole configuration $(D, \delta_{\text{dipole}}, \alpha_{\text{dipole}})$, the expected Rayleigh amplitudes can be calculated for all slices. These can be compared with the values obtained from the data set. Since the behaviours of the Rayleigh amplitude and phase as random variables, i.e. their probability density functions, are known, the likelihood of the obtained results in a slice can be calculated, assuming a certain dipole configuration. The dipole configuration, that is contained in the data set, can be estimated by finding the configuration that maximises the combined likelihood in all slices, thus by performing a log-likelihood fit.

The probability to obtain in slice $i$ a Rayleigh amplitude between $R_i$ and $R_i + \mathrm{d}R_i$, and a Rayleigh phase between $\alpha_i$ and $\alpha_i + \mathrm{d}\alpha_i$, is given by [Lin75]:

$$p(R_i, \alpha_i)\,\mathrm{d}R_i\,\mathrm{d}\alpha_i = \frac{R_i N_i}{4\pi} \cdot \exp\left[-N_i \cdot \left(R_i^2 + D_i'^2 - 2R_i D_i' \cos(\alpha_i - \alpha_{\text{dipole}})\right)/4\right] \mathrm{d}R_i\,\mathrm{d}\alpha_i \,. \quad (6.40)$$

The product of the likelihoods has to be maximised. For practical reasons, the negative natural logarithm of the likelihood is taken. That quantity is summed over all slices, and the result is minimised by varying the assumed dipole's parameters. The implementation uses the Simplex algorithm of Nelder and Mead for minimising the log-likelihood quantity, as provided by the `nmsimplex` function of the GNU Scientific Library [Gal03].

### 6.3.1 Monte Carlo Simulations

In this section, the Slice method shall be evaluated by means of Monte Carlo simulations. First, the analysis of a single data set is illustrated with several plots. Then, a number of simulated data sets are analysed to judge the statistical significance of the results.

For the first part, a data set was simulated with 10 million events. The dipole amplitude is chosen as 10%, which should be suitably large for illustration purposes. The dipole vector points to $\delta_{\text{dipole}} = 40°$, $\alpha_{\text{dipole}} = 75°$, while the experiment is located at 49° North latitude and records air shower events up to a maximum zenith angle of 60°. For the analysis, the data set is subdivided into declination slices with a width of $1°/10$. Figure 6.6(a) and (b) show the reconstructed Rayleigh phases and amplitudes. The dots represent the individual results for the different slices, whereas solid curves indicate the expected behaviours. In case of the reconstructed Rayleigh phase, the expectation value corresponds to the true right ascension value of the dipole vector in all slices. Because of the statistical fluctuations, the reconstructed phases scatter symmetrically around this expectation value. The width of the scatter is determined by the strength of the anisotropy and the number of events within the slices. The reconstructed amplitudes scatter asymmetrically around their expected behaviour, which is marked by the curve, the shape of which is determined by the dipole amplitude and declination. The width of the scatter is again influenced by the amount of statistics available in the slices. The latter is depicted in Figure 6.6(c).

Figure 6.7 contains three additional plots for the same data set. The Slice method determines its estimate of the dipole configuration through a log-likelihood maximation. These figures show three cross sections of the three-dimensional parameter space $(D, \delta_{\text{dipole}}, \alpha_{\text{dipole}})$. Figure 6.7(a) shows the log-likelihood values for all possible dipole directions assuming the correct dipole amplitude of 10%. In Figure 6.7(b), the correct right ascension value (75°) is assumed and log-likelihood values are plotted against the range of amplitude and declination values. These two plots reveal a massive problem of the Slice method: the log-likelihood

(a)



(b)



(c)
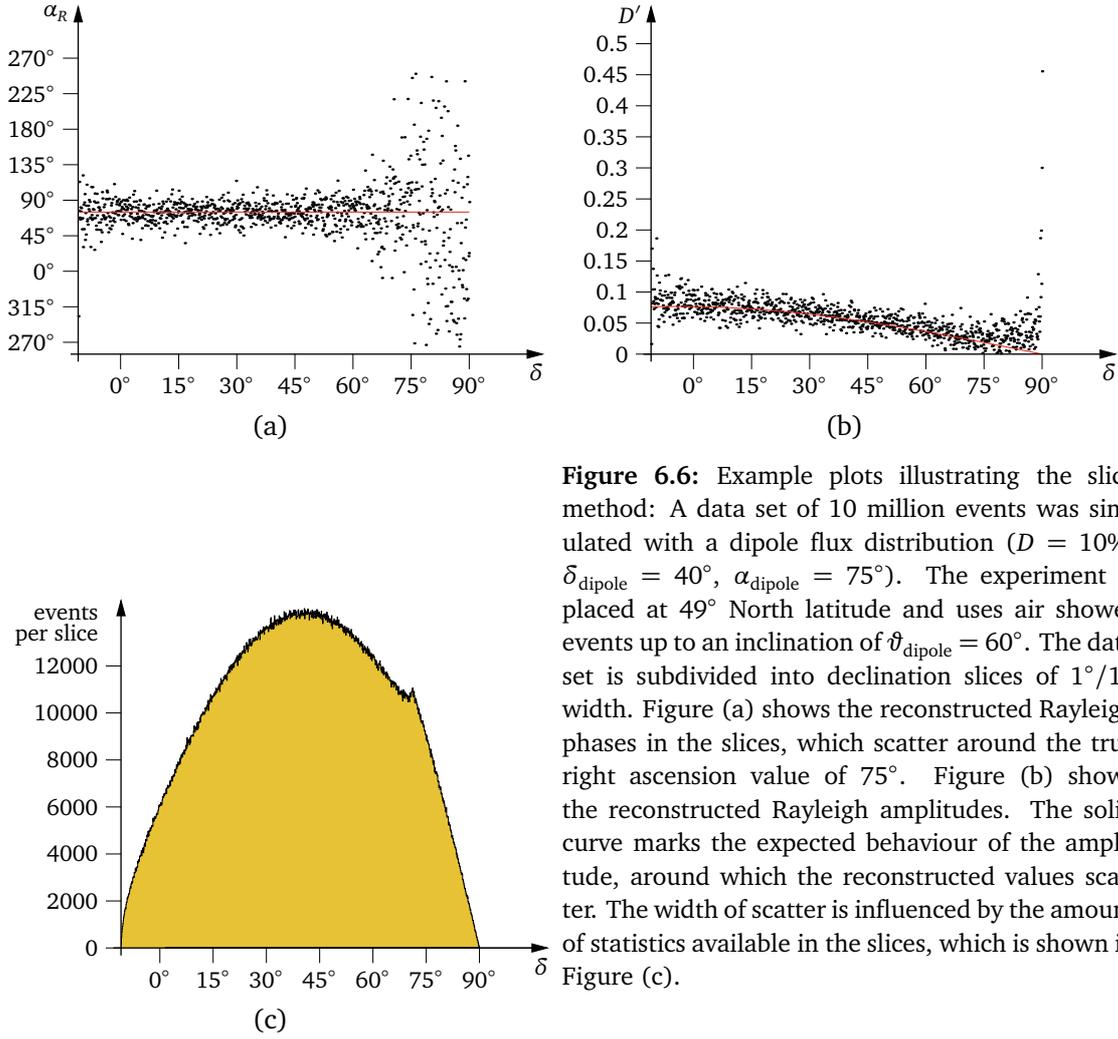
**Figure 6.6:** Example plots illustrating the slice method: A data set of 10 million events was simulated with a dipole flux distribution ($D = 10\%$, $\delta_{\text{dipole}} = 40°$, $\alpha_{\text{dipole}} = 75°$). The experiment is placed at 49° North latitude and uses air shower events up to an inclination of $\vartheta_{\text{dipole}} = 60°$. The data set is subdivided into declination slices of $1°/10$ width. Figure (a) shows the reconstructed Rayleigh phases in the slices, which scatter around the true right ascension value of 75°. Figure (b) shows the reconstructed Rayleigh amplitudes. The solid curve marks the expected behaviour of the amplitude, around which the reconstructed values scatter. The width of scatter is influenced by the amount of statistics available in the slices, which is shown in Figure (c).

values do not seem to peak clearly at or near the true parameter values. Especially in the amplitude/declination plane of the parameter space (Fig. 6.7(b)), the method fails to deliver unambiguous results, as log-likelihood values, that are comparably good, span a large area in this section of the parameter space. The fit results for this specific data set match the true values rather well, with an estimated dipole amplitude of 9.7% and direction $\delta = 37.4°$, $\alpha = 74.8\%$. However, with 10 million events and an amplitude of 10%, this data set represents a very favourable case for the dipole reconstruction. Statistical fluctuations get worse both with smaller amplitudes and smaller data sets. Especially small amplitudes are a challenge for the three-dimensional dipole reconstruction with the Slice method: for very small amplitudes $D$, the shape of the function $D'(\delta)$ can hardly characterise both dipole amplitude and declination, as the dependency of $D'$ on amplitude $D$ and declination $\delta_{\text{dipole}}$ exists in good approximation only in the form of a proportionality to the product of $D$ and $\cos \delta_{\text{dipole}}$:

$$D'_i = \frac{D \cos \delta_{\text{dipole}} \cos \delta_i}{1 + D \sin \delta_{\text{dipole}} \sin \delta_i} \approx D \cos \delta_{\text{dipole}} \cos \delta_i \,. \tag{6.41}$$

Thus, the function $D'(\delta)$, shown as the solid curve in Figure 6.6(b), looks practically the same for many different combinations of $D$ and $\delta_{\text{dipole}}$. The method often tends to produce large

(a)



(b)



(c)
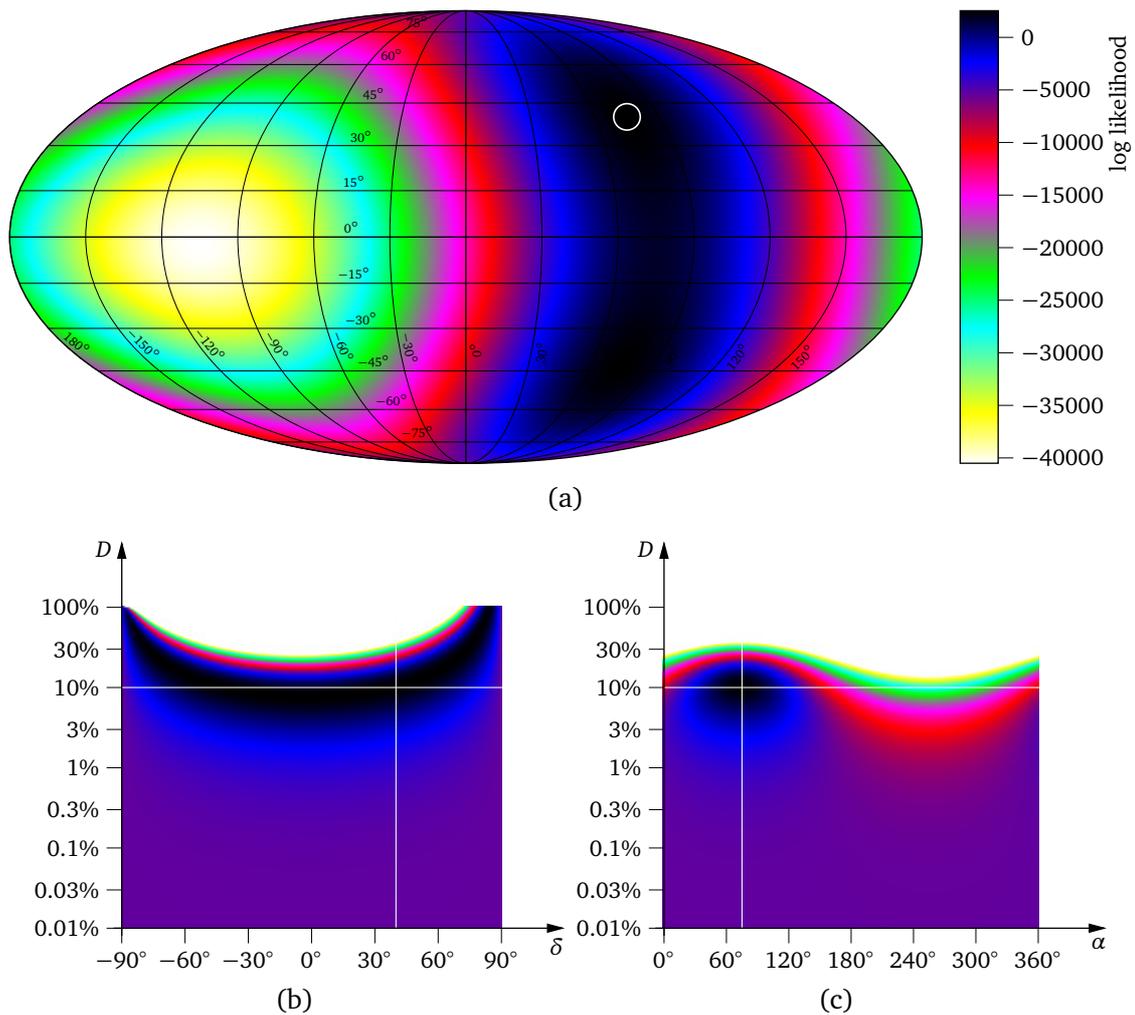
**Figure 6.7:** Log-likelihood maps for the slice method: three cross-sections of the three-dimensional parameter space are shown. In Figure (a), log-likelihood values are plotted for dipole configurations with the true amplitude value of 10%. Figure (b) shows the amplitude/declination plane of the parameter space with the true right ascension value (75°). Figure (c) depicts the amplitude/right ascension plane of the parameter space with the true declination value (40°). The fit fails to deliver unambiguous results.

amplitude values with declinations near the North Pole or South Pole. It only performs fairly stably when both the simulated amplitude and the amount of available statistics are large.

### 6.3.2 Summary

A new method for the reconstruction of the dipole parameters has been discussed. It has been designed to be insensitive to zenith angle dependent efficiency defects. The Slice method divides the set of recorded data into many declination slices, i.e. subsets of data with almost equal declination values. It then performs an individual Rayleigh analysis in each of these declination slices. The dipole parameters are obtained through a log-likelihood fit of the Rayleigh amplitudes and phases. However, as it turns out, the approach chosen here has not lead to a workable reconstruction method. The maximum likelihood hardly identifies a single dipole configuration. Instead, there are extended regions in the parameter space with similarly high

likelihood values. The fit implementation will randomly report any configuration inside that region as the result.

Results of Monte Carlo series are not shown here, because the dipole reconstruction with the Slice method often fails completely, in the sense, that the dipole amplitude parameter diverge during the fit procedure. Therefore the idea of the Slice method shall not be pursued any further in this thesis.

## 6.4   Rayleigh Analysis in Horizontal Coordinates

In this section, a better reconstruction method for a dipole anisotropy shall be proposed, that combines ideas of the Slice method and the East-West method, which has been introduced in Section 4.6. Like the East-West method, the horizontal Rayleigh analysis processes local viewing directions of the air shower events. Like the Slice method, the final result is obtained through a log-likelihood fit, taking advantage of the availability of the precise probability density functions for the Rayleigh analysis procedure. The horizontal Rayleigh analysis provides an estimate of all three dipole parameters, thus it performs a three-dimensional reconstruction. It shall be shown, that this method is insensitive to many common experimental effects, that have been discussed earlier.

Starting point is Equation 4.60, which shall be revisited here:

$$E(t) - W(t) = 4A \cdot \Phi_0 \cdot D_y^H(t) \mathscr{E}_{21}(t). \tag{6.42}$$

$E(t)$ and $W(t)$ are the air shower event counting rates of an experiment at time $t$ for the Western and Eastern halves of the field of view. Apart from being proportional to the mean cosmic ray flux $\Phi_0$ and the size of the fiducial area of the experiment $A$, this expression depends on properties of the field of view, which are contained in $\mathscr{E}_{21}(t)$. Eventually, the expression is also proportional to the $y$-component of the dipole vector in local viewing coordinates (horizontal coordinates). The latter is the object of interest. To obtain it from data, the difference of East and West counting rates must be divided by the other factors. Difficulties arise with the determination of $\mathscr{E}_{21}(t)$, which is defined according to:

$$\mathscr{E}_{ij}(t) = \int_{\vartheta=0}^{\vartheta_{\max}} \sin^i \vartheta \, \cos^j \vartheta \, \eta(\vartheta, t) \, \mathrm{d}\vartheta, \tag{6.43}$$

where $\vartheta_{\max}$ is the zenith angle limit up to which the data are used for analysis. The function $\eta(\vartheta, t)$ represents experimental effects and can be understood as the efficiency, with which cosmic ray particles hitting the experiment at time $t$ with an inclination angle $\vartheta$ are detected. Ideally, the function $\eta(\vartheta, t)$ is identically equal to one at all times and for the whole zenith angle range. However, this is exactly the same assumption, that is incorporated in other reconstruction methods, like the SAP method or the multipole expansion. Usually, this assumption is implicitly made, so that $\eta(\vartheta, t)$ does not even appear in the formulas. The assumption may not reflect the true experimental conditions, which may even be not exactly known or anyway hard to quantify. In this sense, $\eta(\vartheta, t)$ is an unknown quantity. It is desirable to find functional relations that yield information on the dipole configuration, but do not contain instances of the efficiency function $\eta(\vartheta, t)$, and therefore are not based on any such assumptions.

One obvious approach for ridding the quantity $E(t) - W(t)$ of the features determined by the experimental circumstances, would be to normalise it with $E(t) + W(t)$, i.e. the total counting rate. However, as can be seen from the calculations in Section 4.6, the expression for the total counting rate is even more complex:

$$I(t) = E(t) + W(t) = 2\pi A \cdot \Phi_0 \cdot \left( \mathscr{E}_{11}(t) + D_z^H(t) \mathscr{E}_{12}(t) \right), \tag{6.44}$$

so that the $\mathscr{E}_{ij}$ terms do not cancel out, when the normalisation is performed:

$$\frac{E(t)-W(t)}{E(t)+W(t)} = \frac{2}{\pi} \cdot \frac{D_y^H(t)\,\mathscr{E}_{21}(t)}{\mathscr{E}_{11}(t) + D_z^H(t)\,\mathscr{E}_{12}(t)}. \tag{6.45}$$

Hence, normalising with the total counting rate is not an option for acquiring a quantity that is independent of the experimental effects.

Along the lines of the calculation of the $E(t)$ and $W(t)$ functions, which have been derived in Section 4.6 by integrating a dipole-like flux distribution over the respective parts of the field of view, the counting rates for the North and the South halves of the sky can be constructed.

$$N(t) = A \cdot \Phi_0 \cdot \left( \mathscr{E}_{11}(t) \int \mathrm{d}\varphi + D_x^H(t)\,\mathscr{E}_{21}(t) \int \cos\varphi\,\mathrm{d}\varphi + \right.$$
$$\left. D_y^H(t)\,\mathscr{E}_{21}(t) \int \sin\varphi\,\mathrm{d}\varphi + D_z^H(t)\,\mathscr{E}_{12}(t) \int \mathrm{d}\varphi \right), \tag{6.46}$$

with all integrals over $\varphi$ ranging from $-\pi/2$ to $\pi/2$. The function $S(t)$ is defined identically, but with the $\varphi$-integration ranging from $\pi/2$ to $3\pi/2$. Unlike for the $E(t)$ and $W(t)$ functions, the $D_y^H$ terms vanish, whereas the $D_x^H$ terms remain. Executing the $\varphi$-integrations yields:

$$N(t) = A \cdot \Phi_0 \cdot \left( \pi\mathscr{E}_{11}(t) + 2D_x^H(t)\,\mathscr{E}_{21}(t) + \pi D_z^H(t)\,\mathscr{E}_{12}(t) \right),$$
$$S(t) = A \cdot \Phi_0 \cdot \left( \pi\mathscr{E}_{11}(t) - 2D_x^H(t)\,\mathscr{E}_{21}(t) + \pi D_z^H(t)\,\mathscr{E}_{12}(t) \right). \tag{6.47}$$

As for the two former functions, most of the terms cancel each other when the difference of these two functions is computed:

$$N(t) - S(t) = 4A \cdot \Phi_0 \cdot D_x^H(t)\,\mathscr{E}_{21}(t). \tag{6.48}$$

In fact, this difference is identical to $E(t)-W(t)$, except that the occurence of $D_y^H(t)$ is replaced with $D_x^H(t)$, which is the North-South component of the dipole vector. In order to get rid of the disturbing terms, the two differences can be divided by each other:

$$\frac{E(t)-W(t)}{N(t)-S(t)} = \frac{4A \cdot \Phi_0 \cdot D_y^H(t)\,\mathscr{E}_{21}(t)}{4A \cdot \Phi_0 \cdot D_x^H(t)\,\mathscr{E}_{21}(t)} = \frac{D_y^H(t)}{D_x^H(t)}. \tag{6.49}$$

However, not only the disturbing terms are cancelled. When dividing the $y$-component of the dipole vector by its $x$-component, the amplitude of the dipole cancels out as well. The result comprises information only on the direction of the dipole vector, more precisely on the projection of the dipole vector into the $xy$-plane of the horizontal coordinate system, i.e. the horizontal plane. In Section 4.6, two different notations for the definition of the $\vec{D}^H(t)$ vector have been given: firstly, Equation 4.54 uses the dipole direction in horizontal coordinates $(\vartheta_{\mathrm{dipole}}(t), \varphi_{\mathrm{dipole}}(t))$. Secondly, Equation 4.55 defines $\vec{D}^H(t)$ by means of the constant equatorial coordinates of the dipole vector. Both notations yield different insights: the first on the meaning, the second on the temporal development of the ratio in question. According to Equation 4.54: [2]

$$\frac{D_y^H(t)}{D_x^H(t)} = \frac{D \cdot \sin\vartheta_{\mathrm{dipole}}(t)\,\sin\varphi_{\mathrm{dipole}}(t)}{D \cdot \sin\vartheta_{\mathrm{dipole}}(t)\,\cos\varphi_{\mathrm{dipole}}(t)} \Rightarrow \varphi_{\mathrm{dipole}}(t) = \arg(D_x^H(t) + iD_y^H(t)). \tag{6.50}$$

This means, that the ratio of $E(t) - W(t)$ and $N(t) - S(t)$ determines the azimuth angle

---

[2]It has been checked, that the resulting azimuth angle always lies within the correct sector. The signs of numerator and denominator are correctly preserved. All terms cancelling out are positive definite. The zenith angle can principally range between 0 and $\pi$. Hence, its sine (as in $\sin\vartheta_{\mathrm{dipole}}$) is never negative. Provided that no events appearing from below the ground are recorded, the field of view contains only zenith angles less than $\pi/2$, which is needed to ensure that all $\mathscr{E}_{ij}$-terms are positive definite.
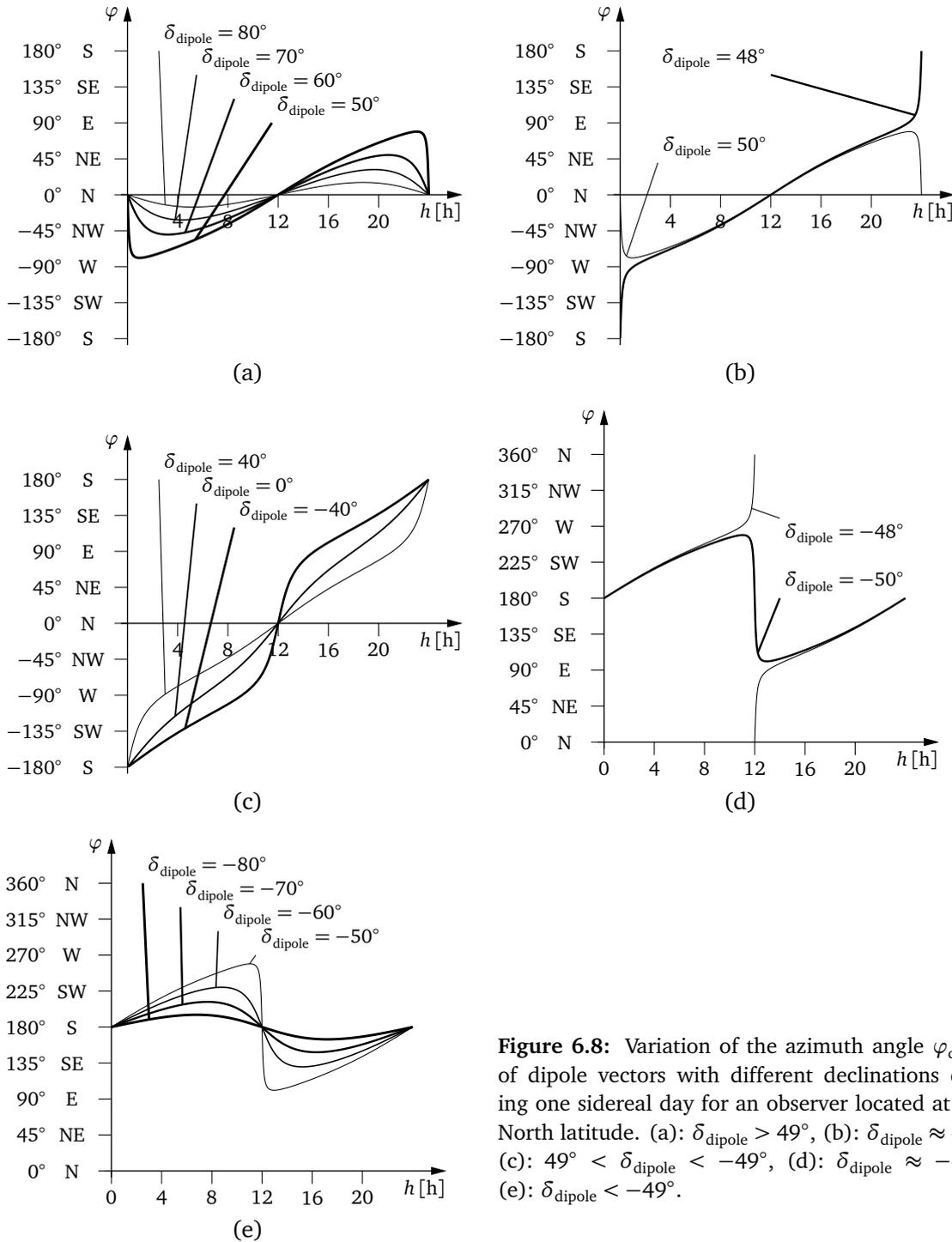
**Figure 6.8:** Variation of the azimuth angle $\varphi_{\text{dipole}}$ of dipole vectors with different declinations during one sidereal day for an observer located at 49° North latitude. (a): $\delta_{\text{dipole}} > 49°$, (b): $\delta_{\text{dipole}} \approx 49°$, (c): $49° < \delta_{\text{dipole}} < -49°$, (d): $\delta_{\text{dipole}} \approx -49°$, (e): $\delta_{\text{dipole}} < -49°$.

of the dipole vector at time $t$. It should be noticed, that this relation is not based on any assumptions about the efficiency or the absence of spurious variations of the measurement rate. The only assumption, that lies in the given formula, is the symmetry of the experiment and the measurement conditions with respect to the azimuth angle.

The second notation of the dipole vector in horizontal coordinates is given in Equa-

tion 4.55, according to which:

$$D_y^H(t) = -D \cdot \cos \delta_{\text{dipole}} \sin h_{\text{dipole}}(t),$$
$$D_x^H(t) = D \cdot \left( \cos \beta \, \sin \delta_{\text{dipole}} - \sin \beta \, \cos \delta_{\text{dipole}} \, \cos h_{\text{dipole}}(t) \right),$$

which leads to:

$$\varphi_{\text{dipole}}(t) = \arg(\cos \beta \, \sin \delta_{\text{dipole}} - \sin \beta \, \cos \delta_{\text{dipole}} \, \cos h_{\text{dipole}}(t) - i \cos \delta_{\text{dipole}} \, \sin h_{\text{dipole}}(t)).$$
(6.51)

This notation includes the dipole configuration in equatorial coordinates. The only term, that depends on the time $t$, is the hour angle of the dipole vector $h_{\text{dipole}}$, which equals the difference of local mean sidereal time and the dipole vector's right ascension. The function is shown in Figure 6.8 for different values of $\delta_{\text{dipole}}$. The horizontal axes in those plots show the hour angle $h_{\text{dipole}}$, which equals the local mean sidereal time at the experiment, if the dipole vector points to right ascension 0°, and is shifted accordingly otherwise. In Figure 6.8, the experiment is located at 49° North latitude. The different graphs show qualitative differences. If the declination of the dipole vector is further North than 49°, its azimuth varies around the North direction. This is generally the case when $\delta_{\text{dipole}} > |\beta|$, where $\beta$ is the geographical latitude of the experiment's location: the North-South component of the dipole vector $D_x^H(t)$ is constantly positive, thus pointing Northwards. On the other hand, the dipole vector's azimuth varies around the South direction, if its declination is further South than −49° in this example, or generally if $\delta_{\text{dipole}} < -|\beta|$, as $D_x^H(t)$ is constantly negative then. If neither is the case, thus if $-|\beta| < \delta_{\text{dipole}} < |\beta|$, the azimuth angle covers the whole range of directions during one sidereal day, turning clockwise (S, W, N, E, S) if the experiment is situated on the Northern Hemisphere, or anti-clockwise (N, W, S, E, N) if the experiment is located on the Southern Hemisphere. It should be possible to discriminate between those qualitatively different cases when analysing a data set.

The actual analysis of data, of course, cannot draw on the event rates as continuous functions, but can only estimate event rates for discrete time intervals by dividing the number of recorded events by the duration of the time interval. These estimators shall be called $\bar{E}$, $\bar{W}$, $\bar{N}$ and $\bar{S}$, respectively. For a time interval lasting from $t$ until $t + \Delta t$, those quantities can be written as a sum over selected events:

$$\bar{E}(t, \Delta t) = \frac{1}{\Delta t} \sum_{\substack{i \\ t < t_i < t + \Delta t \\ 0 < \varphi_i < \pi}} 1, \quad \bar{W}(t, \Delta t) = \frac{1}{\Delta t} \sum_{\substack{i \\ t < t_i < t + \Delta t \\ \pi < \varphi_i < 2\pi}} 1, \tag{6.52}$$

where $t_i$ denotes the point of time of the event $i$, and $\varphi_i$ its reconstructed azimuth angle, and analogously for $\bar{N}$ and $\bar{S}$ with corresponding ranges for $\varphi_i$. The differences $\bar{E} - \bar{W}$ and $\bar{N} - \bar{S}$

can then also be written as:

$$
\begin{aligned}
\bar{E}(t,\Delta t) - \bar{W}(t,\Delta t) &= \frac{1}{\Delta t} \sum_{\substack{i \\ t<t_i<t+\Delta t}} \begin{cases} 1 & (\text{if } 0 < \varphi_i < \pi) \\ -1 & (\text{if } \pi < \varphi_i < 2\pi) \end{cases} \\
&= \frac{1}{\Delta t} \sum_{\substack{i \\ t<t_i<t+\Delta t}} \mathrm{sign}(\sin \varphi_i)\,, \\
\bar{N}(t,\Delta t) - \bar{S}(t,\Delta t) &= \frac{1}{\Delta t} \sum_{\substack{i \\ t<t_i<t+\Delta t}} \begin{cases} 1 & (\text{if } \varphi_i < \pi/2 \vee \varphi_i > 3\pi/2) \\ -1 & (\text{if } \pi/2 < \varphi_i < 3\pi/2) \end{cases} \\
&= \frac{1}{\Delta t} \sum_{\substack{i \\ t<t_i<t+\Delta t}} \mathrm{sign}(\cos \varphi_i)\,.
\end{aligned}
\tag{6.53}
$$

The length of the time interval $\Delta t$ eventually cancels out, when calculating the ratio of those two differences. However, the choice of $\Delta t$, thus the duration of the time bins, within which the analysis is carried out, does effect the analysis. From a statistical point of view, it is favourable to choose long time intervals, in order to maximise event numbers and therefore minimise the effect of statistical fluctuations. On the other hand, the longer the time interval the worse the approximation of assuming a constant dipole vector in horizontal coordinates.

This reconstruction method looks at the ratio of "Eastness" and "Northness" of the data set taken during a short period of time. Each event is categorised as either West or East, depending on the sign of the sine of the event's reconstructed azimuth angle, and as either North or South, depending on the sign of the cosine. Eastness and Northness of a single event could also be defined as continuous quantities, namely directly as the sine and cosine of the azimuth angle, respectively. These functions shall be called $Y(t)$ (Eastness) and $X(t)$ (Northness). Unlike the counting rates previously used, they shall be normalised by the total counting rate $I(t)$. They can be analytically calculated as integrals over the experiment's field of view:

$$
\begin{aligned}
Y(t) &= \frac{2}{I(t)} \int_{\varphi=0}^{2\pi} \int_{\vartheta=0}^{\vartheta_{\max}} \mathrm{d}\varphi \, \sin\vartheta \, \mathrm{d}\vartheta \quad \cos\vartheta \quad \eta(\vartheta,t) \quad A \quad \Phi(\vartheta,\varphi,t) \quad \sin\varphi\,, \\
X(t) &= \frac{2}{I(t)} \int_{\varphi=0}^{2\pi} \int_{\vartheta=0}^{\vartheta_{\max}} \mathrm{d}\varphi \, \sin\vartheta \, \mathrm{d}\vartheta \quad \cos\vartheta \quad \eta(\vartheta,t) \quad A \quad \Phi(\vartheta,\varphi,t) \quad \cos\varphi\,, \\
I(t) &= \int_{\varphi=0}^{2\pi} \int_{\vartheta=0}^{\vartheta_{\max}} \underbrace{\mathrm{d}\varphi \, \sin\vartheta \, \mathrm{d}\vartheta}_{\substack{\text{solid angle} \\ \text{element}}} \underbrace{\cos\vartheta}_{\substack{\text{geometrical} \\ \text{acceptance}}} \underbrace{\eta(\vartheta,t)}_{\substack{\text{experimental} \\ \text{effects}}} \underbrace{A}_{\substack{\text{surface} \\ \text{area}}} \underbrace{\Phi(\vartheta,\varphi,t)}_{\text{flux}}\,.
\end{aligned}
\tag{6.54}
$$

The further calculations go along the same lines as for the East-West method, as shown in Section 4.6. However, the $\varphi$-integration is always carried out over the whole range from 0 to $2\pi$. Assuming a dipole distribution for $\Phi(\vartheta,\varphi,t)$ (Eq. 4.53) leads to:

$$
\begin{aligned}
Y(t) = {} & \frac{2}{I(t)} \int_{\varphi=0}^{2\pi} \int_{\vartheta=0}^{\vartheta_{\max}} \mathrm{d}\varphi \, \sin\vartheta \, \mathrm{d}\vartheta \, \cos\vartheta \, \eta(\vartheta,t) \cdot A \cdot \Phi_0 \cdot \\
& \left( 1 + D_x^H(t) \sin\vartheta \cos\varphi + D_y^H(t) \sin\vartheta \sin\varphi + D_z^H(t) \cos\vartheta \right) \cdot \sin\varphi\,,
\end{aligned}
\tag{6.55}
$$

and analogously for $X(t)$, except for the factor $\sin\varphi$ being replaced by $\cos\varphi$. The $\vartheta$-integration

yields:

$$
\begin{aligned}
Y(t) &= \frac{2}{I(t)} \cdot A \cdot \Phi_0 \cdot \Big( \mathscr{E}_{11}(t) \int \sin\varphi \, d\varphi + D_x^H(t) \mathscr{E}_{21}(t) \int \cos\varphi \, \sin\varphi \, d\varphi + \\
&\qquad D_y^H(t) \mathscr{E}_{21}(t) \int \sin^2\varphi \, d\varphi + D_z^H(t) \mathscr{E}_{12}(t) \int \sin\varphi \, d\varphi \Big) , \\
X(t) &= \frac{2}{I(t)} \cdot A \cdot \Phi_0 \cdot \Big( \mathscr{E}_{11}(t) \int \cos\varphi \, d\varphi + D_x^H(t) \mathscr{E}_{21}(t) \int \cos^2\varphi \, d\varphi + \\
&\qquad D_y^H(t) \mathscr{E}_{21}(t) \int \sin\varphi \, \cos\varphi \, d\varphi + D_z^H(t) \mathscr{E}_{12}(t) \int \cos\varphi \, d\varphi \Big) ,
\end{aligned}
\tag{6.56}
$$

and after the $\varphi$-integration:

$$
\begin{aligned}
Y(t) &= \frac{2\pi}{I(t)} \cdot A \cdot \Phi_0 \cdot D_y^H(t) \mathscr{E}_{21}(t), \\
X(t) &= \frac{2\pi}{I(t)} \cdot A \cdot \Phi_0 \cdot D_x^H(t) \mathscr{E}_{21}(t).
\end{aligned}
\tag{6.57}
$$

Apart from the normalisation, these functions are identical to the formerly used differences $E(t)-W(t)$ and $N(t)-S(t)$. The ratio of $Y(t)$ and $X(t)$ determines the current dipole azimuth, in the same way as said differences do:

$$
\frac{Y(t)}{X(t)} = \frac{D_y^H(t)}{D_x^H(t)} = \tan\varphi_{\text{dipole}}(t).
\tag{6.58}
$$

The advantage of the new set of functions becomes apparent when looking at the formulas of their estimators from measured data:

$$
\begin{aligned}
\bar{Y}(t,\Delta t) &= \frac{1}{\Delta t} \cdot \frac{2}{\bar{I}(t,\Delta t)} \sum_{\substack{i \\ t < t_i < t+\Delta t}} \sin\varphi_i , \\
\bar{X}(t,\Delta t) &= \frac{1}{\Delta t} \cdot \frac{2}{\bar{I}(t,\Delta t)} \sum_{\substack{i \\ t < t_i < t+\Delta t}} \cos\varphi_i , \\
\bar{I}(t,\Delta t) &= \frac{1}{\Delta t} \sum_{\substack{i \\ t < t_i < t+\Delta t}} 1 = \frac{N}{\Delta t}.
\end{aligned}
\tag{6.59}
$$

For a set of $N$ air shower observations with reconstructed azimuth angles $\varphi_i$, the functions $Y(t)$ and $X(t)$ can be estimated as:

$$
\bar{Y} = \frac{2}{N} \sum_{i=1}^{N} \sin\varphi_i , \quad \bar{X} = \frac{2}{N} \sum_{i=1}^{N} \cos\varphi_i .
\tag{6.60}
$$

These two formulas are identical to those of the Rayleigh formalism (Eq. 4.20), with the exception that the original Rayleigh formalism works on right ascension values, whereas these formulas process azimuth values. However, both right ascension and azimuth are longitudinal coordinates. Provided that the complete set of events was taken during a short period of sidereal time of day (although not necessarily all on the same sidereal day), the variation of the flux distribution in horizontal coordinates with time can be neglected. Thus, the full set is drawn from the dipolar flux distribution $\Phi(\vartheta, \varphi, t)$ at a practically fixed time $t$. The distribution

of azimuth angles in the data set can be calculated from the flux as follows:

$$\bar{\Phi}(\varphi, t) = \frac{\int_{\vartheta=0}^{\vartheta_{\max}} \Phi(\vartheta, \varphi, t)\, \eta(\vartheta, t)\, \cos\vartheta\, \sin\vartheta\, \mathrm{d}\vartheta}{\int_{\vartheta=0}^{\vartheta_{\max}} \underbrace{\eta(\vartheta, t)}_{\substack{\text{experimental} \\ \text{effects}}} \underbrace{\cos\vartheta}_{\substack{\text{geometrical} \\ \text{acceptance}}} \underbrace{\sin\vartheta\, \mathrm{d}\vartheta}_{\substack{\text{solid angle} \\ \text{element}}}}. \tag{6.61}$$

After plugging in the flux distribution, as given in Equation 4.53, the $\vartheta$-integration can be executed, which yields the following result:

$$\bar{\Phi}(\varphi, t) = \underbrace{\Phi_0 \cdot \left(1 + \frac{\mathscr{E}_{12}(t)}{\mathscr{E}_{11}(t)} D \cos\vartheta_{\text{dipole}}(t)\right)}_{\Phi_0'(t)} \cdot \left(1 + D'(t) \cos(\varphi - \varphi_{\text{dipole}}(t))\right),$$

$$D'(t) = \frac{D \sin\vartheta_{\text{dipole}}(t)\, \mathscr{E}_{21}(t)}{\mathscr{E}_{11}(t) + D \cos\vartheta_{\text{dipole}}(t)\, \mathscr{E}_{12}(t)}. \tag{6.62}$$

Therefore, at any time $t$, the distribution of azimuth values has a dipolar shape, too. Its excess coincides with the azimuth of the dipole vector at that time. The amplitude is described by the function $D'(t)$ and depends on the dipole amplitude $D$, the zenith angle of the dipole vector at time $t$, but also on the $\mathscr{E}_{ij}$-functions, that describe the field of view, the efficiency and possible experimental effects. The dipole's current azimuth angle can be estimated from the data subset by the Rayleigh phase $\varphi_R$. The Rayleigh ampltide $R^H$ is an estimator for the amplitude of the azimuth variation $D'(t)$:

$$R^H = \sqrt{\bar{X}^2 + \bar{Y}^2}, \qquad \varphi_R = \arg(\bar{X} + i\bar{Y}). \tag{6.63}$$

The advantage of using the Rayleigh formalism compared to using the ratio of East-West and North-South differences lies in the knowledge of the precise statistical behaviour of the resulting quantities. Probability density functions are available, that describe the Rayleigh amplitude and phase, both seperately and simultaneously [Lin75]. Thus, the complete data set can be subdivided into short bins of local mean sidereal time of day, the horizontal Rayleigh phases can be computed for each bin, and the direction of the dipole vector in sidereal coordinates can be obtained through a log-likelihood fit of the Rayleigh phases with the function given in Equation 6.51. While the fit function itself does not depend on the strength of the dipole, the probability density function does (in terms of $D'$):

$$p(\varphi_R) = \frac{1}{2\pi} \cdot \exp(-k) \cdot \left[1 + \sqrt{\pi k} \cos\psi\, \exp\left(k \cos^2\psi\right) \cdot \left(1 + \mathrm{erf}\left(\sqrt{k} \cos\psi\right)\right)\right],$$

$$\psi = \varphi_R - \varphi_{\text{dipole}}, \qquad k = D'^2 N/4. \tag{6.64}$$

The shape of this function is depicted in Figure 5.2(f). The maximum probability is always at $\psi = 0$, so where $\varphi_R = \varphi_{\text{dipole}}$. However, the width of the peak depends on the dipole's amplitude. The stronger the dipole, the sharper the probability density function is concentrated around the peak value. This is true for each of the time bins, so that the set of Rayleigh phases obtained from the data, generally scatter wider around the function $\varphi_{\text{dipole}}(t)$ the weaker the dipole. In turn, this means that the amount of scatter characterises the strength of the actual dipole. The dipole amplitude therefore is treated as a free parameter in the log-likelihood fit, along with the direction (declination and right ascension) of the dipole. These three parameters influence the probability density function of the Rayleigh phase in each sidereal time bin.

The fit procedure maximises the combined likelihood of the obtained Rayleigh phases by varying the dipole configuration. The dipole's declination determines the shape of the fit function $\varphi_{\text{dipole}}(t)$. The dipole's right ascension determines the offset between the hour angle (which is shown on the $x$-axes in Figure 6.8) and the local mean sidereal time. Thus, it shifts the fit function along the time axis. The dipole amplitude determines the amount of variance of the individual data points (the computed Rayleigh phases) around the fit function. If, during the fit procedure, the amplitude is assumed too high, the Rayleigh phase is outside the peak region of the probability density function in many of the sidereal time bins. On the other hand, when assuming too small an amplitude, the phase will be inside the peak region in most of the time bins, but the probability density functions are so wide, and therefore low, that the resulting likelihood can be further maximised by increasing the amplitude parameter.

Although the method only extracts azimuth directions from the data set, the exact knowledge of the statistics involved allows to extract eventually both direction and strength of the dipole from the data set. However, this benefit comes at a price. In each iteration of the fit procedure, the expected amplitudes of the azimuth distributions $D'(t)$ need be computed for the currently assumed dipole configuration for all time bins, as they appear in the likelihood function. The relation between the global dipole configuration ($D$, $\delta_{\text{dipole}}$, $\alpha_{\text{dipole}}$) and the azimuthal amplitude at a time $t$ ($D'(t)$) is given in Equation 6.62. It has been stated above, that this relation is affected by experimental effects, because it contains the $\mathscr{E}_{ij}$-functions. Therefore, it is not completely true, that the described method is insensitive to those experimental effects described by a time and zenith angle dependent efficiency function $\eta(\vartheta, t)$. However, possible variations with time are indeed irrelevant: if the experiment is at certain times generally more efficient than at other times, which is typically caused by changing metereological conditions, this affects the amount of statistics, that enters the corresponding time bins. Other than that, it does not influence the results. A zenith angle dependency of the efficiency, on the other hand, would render the calculation of the $\mathscr{E}_{ij}$-functions incorrect, which assumed, for the lack of better knowledge, full efficiency up to the zenith angle limit $\vartheta_{\text{max}}$. Therefore the expected Rayleigh amplitudes are not calculated correctly, which leads to a slight misinterpretation of the scatter. While this should not affect the estimation of the dipole vector's direction, the dipole amplitude may be misestimated. The actual impact of this effect can be evaluated by means of Monte Carlo simulations.

It is desirable, however, to ultimately get rid of the dependency on the efficiency function $\eta(\vartheta, t)$. In the derivation of the horizontal Rayleigh method, as it has been shown, that function appears first in the calculations of the Eastness and Northness weighted counting rates ($Y(t)$ and $X(t)$), but those instances of $\eta(\vartheta, t)$ fully cancel out, because only the ratio of $Y(t)$ and $X(t)$ is used for the analysis. The efficiency function $\eta(\vartheta, t)$ appears again in Equation 6.61, where the azimuth angle distribution at time $t$, $\bar{\Phi}(\varphi, t)$ is computed from the cosmic ray flux distribution $\Phi(\vartheta, \varphi, t)$ by integrating over the zenith angle $\vartheta$. The result is shown as Equation 6.62, according to which the azimuth distribution always has dipolar shape. The peak azimuth angle, i.e. the phase, coincides with the dipole vector's azimuth angle $\varphi_{\text{dipole}}(t)$. The amplitude of the azimuth distribution $D'(t)$ closely relates to the dipole's amplitude $D$. However, the specific values of $D'(t)$ depend on the shape of the experiment's field of view.

An alternative way of calculating $D'(t)$ shall be given, which can eventually be freed from the dependency on experimental features. The amplitude of the azimuthal flux variation inside a slice of the sky with a discrete zenith angle $\vartheta$ can be calculated from the flux distribution as

follows:

$$\Phi(\vartheta, \varphi, t) = \Phi_0 \cdot \left( 1 + \hat{e}(\pi/2 - \vartheta, \varphi) \cdot \vec{D}^H(t) \right)$$

$$= \Phi_0 \cdot \left( 1 + D \, \cos\vartheta_{\text{dipole}}(t) \cos\vartheta + D \, \sin\vartheta_{\text{dipole}}(t) \sin\vartheta \, \cos(\varphi - \varphi_{\text{dipole}}(t)) \right)$$

$$= \Phi_0 \cdot (1 + D \, \cos\vartheta_{\text{dipole}}(t) \cos\vartheta) \cdot \left( 1 + \frac{D \, \sin\vartheta_{\text{dipole}}(t) \sin\vartheta}{1 + D \, \cos\vartheta_{\text{dipole}}(t) \cos\vartheta} \cos(\varphi - \varphi_{\text{dipole}}(t)) \right) .$$

$$\tag{6.65}$$

At any time $t$, the amplitude of the slice with zenith angle $\vartheta$ therefore is given by:

$$A(\vartheta, t) = \frac{D \, \sin\vartheta_{\text{dipole}}(t) \sin\vartheta}{1 + D \, \cos\vartheta_{\text{dipole}}(t) \cos\vartheta} . \tag{6.66}$$

The total azimuth distribution, as given as $\bar{\Phi}(\varphi, t)$ in Equation 6.62, is a linear combination of the fluxes inside the zenith slices, all of which are dipole distributions with identical phase. Accordingly, the total azimuth amplitude $D'(t)$ is a weighted mean of the amplitudes inside the slices $A(\vartheta, t)$. The weighting depends on the intensity, with which the different slices enter the data set, which can be quantified as follows:

$$n(\vartheta, t) = \int_{\varphi=0}^{2\pi} \mathrm{d}\varphi \quad \underbrace{\Phi(\vartheta, \varphi, t)}_{\text{flux}} \quad \underbrace{\eta(\vartheta, t)}_{\substack{\text{experimental} \\ \text{effects}}} \quad \underbrace{\cos\vartheta}_{\substack{\text{geometrical} \\ \text{acceptance}}} \quad \underbrace{\sin\vartheta}_{\substack{\text{solid angle} \\ \text{element}}}$$

$$= 2\pi \quad \Phi_0 \cdot (1 + D \, \cos\vartheta_{\text{dipole}}(t) \cos\vartheta) \quad \eta(\vartheta, t) \quad \cos\vartheta \quad \sin\vartheta .$$

$$\tag{6.67}$$

The azimuthal amplitude $D'(t)$ can now be computed as:

$$D'(t) = \frac{\displaystyle\int_{\vartheta=0}^{\pi/2} A(\vartheta, t) \, n(\vartheta, t) \, \mathrm{d}\vartheta}{\displaystyle\int_{\vartheta=0}^{\pi/2} n(\vartheta, t) \, \mathrm{d}\vartheta} . \tag{6.68}$$

Unlike previously, the upper limit of the $\vartheta$-integrations is set to $\pi/2$ instead of $\vartheta_{\text{max}}$. The integration therefore covers the whole upward sky. The efficiency function $\eta(\vartheta, t)$ shall by convention be defined in such a way, that it equals zero for $\vartheta > \vartheta_{\text{max}}$. Thus, the integration is effectively carried out over the same integration range as before. It is beneficial not to include the variable $\vartheta_{\text{max}}$ in the formula, in order not to have such a dependency in the final result. Using the definitions of $A(\vartheta, t)$ and $n(\vartheta, t)$ and integrating yields:

$$D'(t) = \frac{\displaystyle\int_{\vartheta=0}^{\pi/2} D \, \sin\vartheta_{\text{dipole}}(t) \sin\vartheta \cdot 2\pi\Phi_0 \, \eta(\vartheta, t) \cos\vartheta \, \sin\vartheta \, \mathrm{d}\vartheta}{\displaystyle\int_{\vartheta=0}^{\pi/2} 2\pi\Phi_0 \cdot (1 + D \, \cos\vartheta_{\text{dipole}}(t) \cos\vartheta) \cdot \eta(\vartheta, t) \cos\vartheta \, \sin\vartheta \, \mathrm{d}\vartheta}$$

$$= \frac{D \, \sin\vartheta_{\text{dipole}}(t) \, \mathscr{E}_{21}(t)}{\mathscr{E}_{11}(t) + D \, \cos\vartheta_{\text{dipole}}(t) \, \mathscr{E}_{12}(t)} ,$$

$$\tag{6.69}$$

which is identical to the result obtained in Equation 6.62. However, defining $D'(t)$ in this way offers the possibility to remove the dependency on the generally unknown efficiency function

$\eta(\vartheta, t)$. The function $n(\vartheta, t)$ is meant to reflect the rate of air shower events at a time $t$, that arrive with a zenith angle of $\vartheta$, including the effect of the dipole anisotropy as well as the geometry and the experimental effects that are expressed by the function $\eta(\vartheta, t)$. Instead of analytically calculating $n(\vartheta, t)$ by making assumptions on the experimental effects (essentially by assuming their absence), it can be taken from the experimental data. Let $\vartheta_i$ be the zenith angles of the $N$ air shower observations in one of the time bins. The following replacement can be applied:

$$n(\vartheta, t) \longrightarrow n_0 \sum_{i=1}^{N} \delta(\vartheta - \vartheta_i), \tag{6.70}$$

where $\delta(x)$ is the Dirac delta function. The integrations in Equation 6.68 now yield:

$$D'(t) = \frac{n_0 \sum_{i=1}^{N} A(\vartheta_i, t)}{n_0 \sum_{i=1}^{N} 1} = \frac{1}{N} \sum_{i=1}^{N} A(\vartheta_i, t) = \frac{1}{N} \sum_{i=1}^{N} \frac{D \sin \vartheta_{\text{dipole}}(t) \sin \vartheta_i}{1 + D \cos \vartheta_{\text{dipole}}(t) \cos \vartheta_i}. \tag{6.71}$$

The computational effort for calculating $D'(t)$ this way is considerably higher, as a summation over all air shower events has to be carried out. This summation has to be repeated for each iteration of the fit procedure, as different values for $\vartheta_{\text{dipole}}(t)$ and $D$ are assumed. Strictly speaking, the $D'(t)$ computed here is only an estimate for the true azimuthal amplitude, as it is computed from a limited number of events. It is again subject to statistical fluctuations. However, computing this quantity from experimental data avoids the systematic bias, that a calculation based on false assumptions implicates.

The horizontal Rayleigh analysis, as it has been presented here, does not rely on assumptions about experimental properties, other than azimuthal symmetry of the experiment. A variation of the sensitivity of the experiment with zenith angle and/or time does not influence the results. Unlike many other analysis methods, measurement conditions are not assumed to be invariable. Therefore changing metereological conditions, even if the variations are repetitive (e.g. the day-night cycle), are without effect, which renders compensating for metereologically induced rate changes, e.g. by means of weighting factors, unneccessary. In the same way, zenith angle correlated effects are irrelevant. Cuts on the zenith angle do not need to assure full efficiency within their bounds. A cut on the zenith angle should still be performed, to restrict the analysis to shower inclinations at which the arrival direction reconstruction is known to work properly.

One more modification of the horizontal Rayleigh analysis method shall be suggested here. So far, the log-likelihood fit only uses the Rayleigh phases that are calculated for each time bin. Since the probability distribution as a function of both Rayleigh amplitude and phase is available as well, the fit can also be performed using phase and amplitude information simultaneously. To do so, the probability density function shown in Equation 6.64 has to be replaced with [Lin75]:

$$p(R^H, \varphi_R) = \frac{R^H N}{4\pi} \cdot \exp\left[ -N \cdot \left( R^{H 2} + D'^2 - 2R^H D' \cos(\varphi_R - \varphi_{\text{dipole}}) \right) / 4 \right]. \tag{6.72}$$

Using both the Rayleigh phase and amplitude could enhance the precision of the results, since more of the available information is used. Originally, the pure phase fit was chosen in order to reduce the dependency on amplitude values, as only the obtained phases were fully independent from all zenith angle related experimental effects. However, as an estimator for $D'$ has

become available, that is equally independent from those effects, fitting both the phase and amplitude values is a viable option.

Altogether there are four variants of the horizontal Rayleigh analysis method. The fit can either be performed with the phase values alone (probability density function according to Eq. 6.64), or with both phase and amplitude information (Eq. 6.72). Additionally, there are two different ways of estimating the azimuthal amplitudes: either by means of an analytical function, that assumes a certain shape of the field of view, and of the efficiency function (Eq. 6.62), or by the distribution of zenith angles in the data set (Eq. 6.71). The two kinds of fitting can be combined with either of the amplitude estimation methods, leading to a total of four possible variants of the analysis method:

- phase fit, combined with an analytical description of the field of view (abbreviated 'p'),

- combined phase and amplitude fit, combined with an analytical description of the field of view (abbreviated 'p&a'),

- phase fit, combined with the evaluation of zenith angles (abbreviated 'p+$\vartheta$'),

- combined phase and amplitude fit, combined with the evaluation of zenith angles (abbreviated 'p&a+$\vartheta$').

Implementations of these four variants need different input data for the analysis. All of them need to know about the geographical location of the experiment. Additionally, implementations of the variants 'p' and 'p&a' need information on the shape of the field of view (usually specified by the maximum zenith angle $\vartheta_{\text{max}}$). They process a list of air shower observations, of which only the reconstructed azimuth angles and the event times (in the form of local mean sidereal time) are considered. On the other hand, the variants 'p+$\vartheta$' and 'p&a+$\vartheta$' need both azimuth and zenith angle of the reconstructed arrival directions, together with the local sidereal time. However, these variants need no externally provided information on the extent and the shape of the field of view.

### 6.4.1 Monte Carlo Simulations

The capabilities of the new method can be assessed with the help of Monte Carlo simulations. First, however, the mode of operation of the horizontal Rayleigh analysis shall be illustrated with some simulated example data sets. Each of these data sets comprises 10 million simulated air shower events. For illustration purposes, a strong dipole was simulated, with an amplitude of 10%. The geographical latitude of the experiment ($\beta$) was set to 49° North. The zenith angle limit was chosen to amount to 60°. Figure 6.9 shows three different plots for each of the four different dipole declinations. Figures 6.9(a) to (c) correspond to a dipole declination $\delta_{\text{dipole}}$ of 40°, whereas $\delta_{\text{dipole}}$ is set to −40° in Figures 6.9(d) to (f). Both of those values for $\delta_{\text{dipole}}$ lie within the range between $+\beta$ and $-\beta$, so that the azimuth angle of the dipole vector in local viewing coordinates keeps progressing clockwise all day, thus sweeping out the full range of azimuth values. The remaining two declination values are 75° (Figures 6.9(g) to (i)) and −75° (Figures 6.9(j) to (l)). These illustrate the cases where $\delta_{\text{dipole}}$ is greater than $|\beta|$, so that the azimuth angle of the dipole oscillates around the North direction, and where $\delta_{\text{dipole}}$ is less than $-|\beta|$, causing the dipole's azimuth angle to oscillate around South. These different classes of behaviour can clearly be distinguished when looking at the simulated data. All of these four data sets are divided into 1,440 time bins. Each bin therefore corresponds to a period of one sidereal minute. The first of the three plots, which are shown for each of
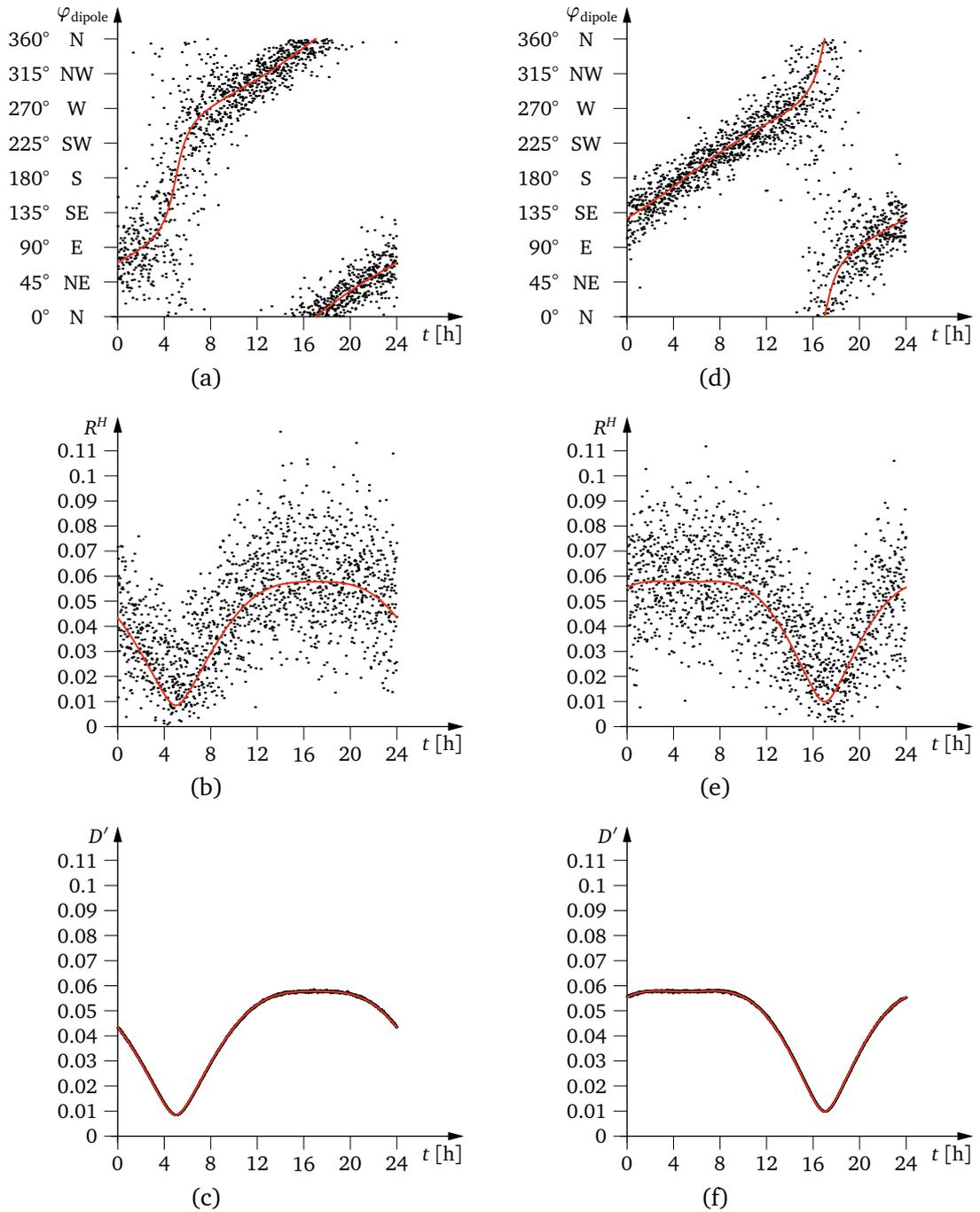
**Figure 6.9:** Example plots illustrating the horizontal Rayleigh analysis: data sets of 10 million simulated events were generated for an experiment at 49° North latitude, with a 10% dipole pointing to $\delta_{\text{dipole}} = 40°$ and $\alpha_{\text{dipole}} = 75°$. Constant measurement conditions and full efficiency over the full zenith angle range up to $\vartheta_{\text{max}} = 60°$ were simulated. The time axes show the local mean sidereal time. At 5 a.m. sidereal time the dipole excess is situated above the experiment's meridian. The data sets are divided into time bins of one sidereal minute. Figures (a) and (b) show the reconstructed horizontal Rayleigh phases and amplitudes, respectively, in each time bin. The solid curves represent the expected values for these quantities. Figure (c) shows the estimated azimuth amplitudes $D'(t)$, calculated from the events' zenith angles assuming the true dipole configuration. The curve from Figure (b) is also shown in Figure (c) for comparison. Figures (d), (e) and (f) present the same plots for a different data set, which was generated with $\delta_{\text{dipole}} = -40°$ and otherwise identical parameters.
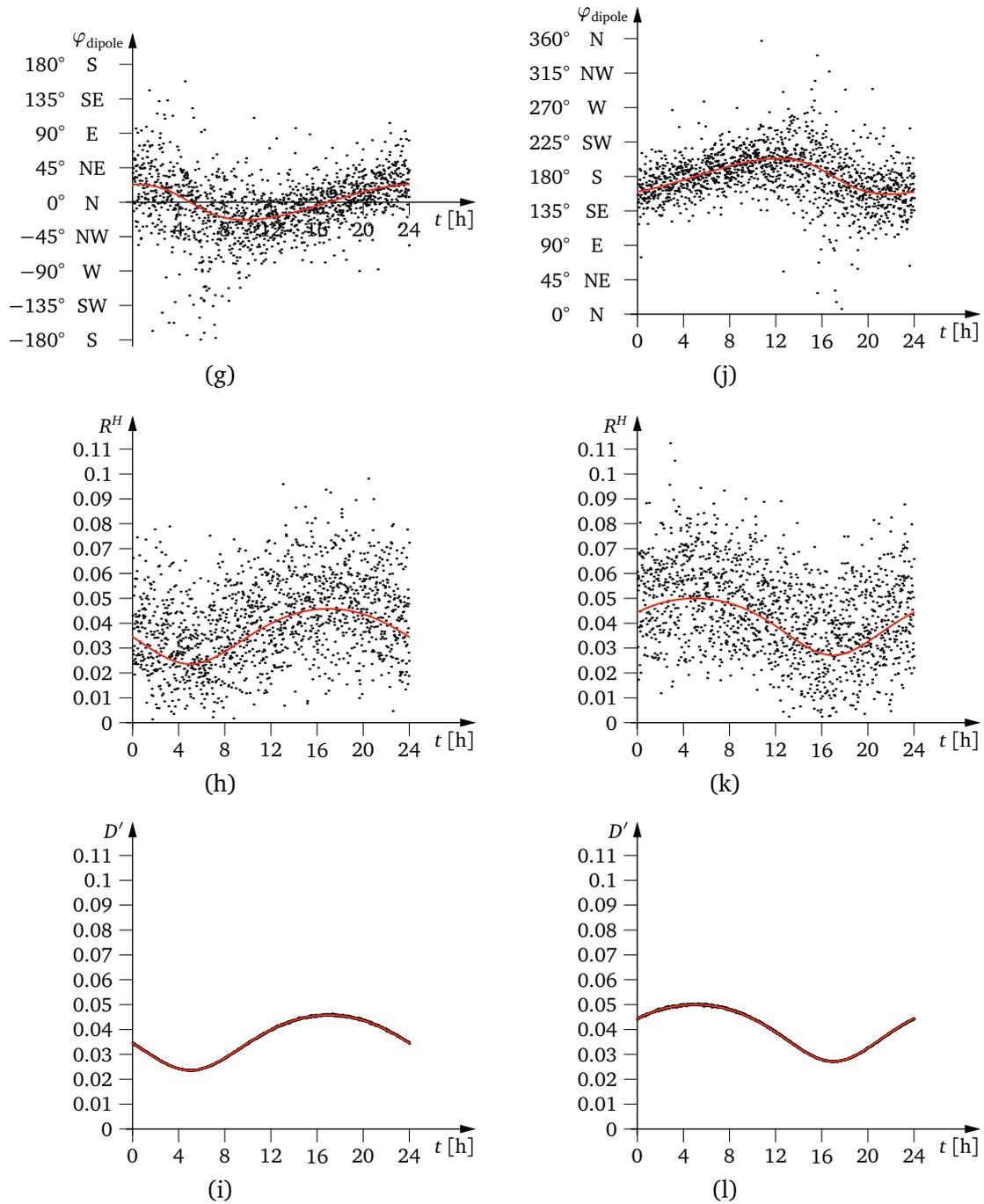
**Figure 6.9:** (cont'd) Two more dipole declination values were simulated. Figures (g), (h) and (i) were generated with $\delta_{\text{dipole}} = 75°$. Figures (j), (k) and (l) were generated with $\delta_{\text{dipole}} = -75°$.

the four example dipole configurations, features the extracted Rayleigh phases, i.e. dipole azimuths. The solid curve illustrates the true development of the dipole vector's azimuth angle. Due to the large dipole amplitude and the large number of events chosen for the simulation, it is clearly discernible that the data points scatter around that curve. The second of the three plots features the reconstructed horizontal Rayleigh amplitudes $R^H$. Again, the solid curve represents the theoretical prediction around which the data points scatter. The prediction,
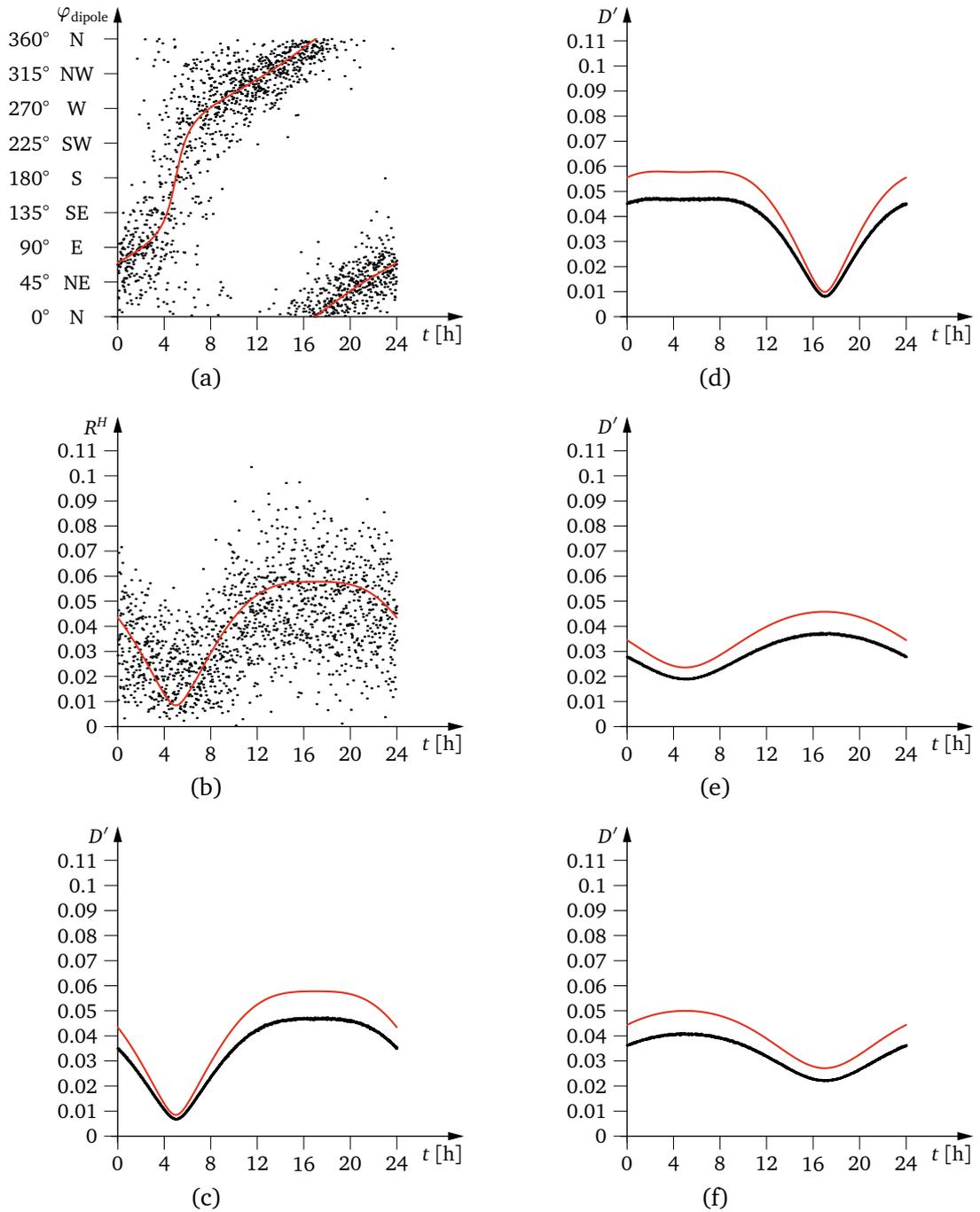
**Figure 6.10:** Impact of an efficiency deficit at high zenith angles on the horizontal Rayleigh analysis: Figures (a), (b) and (c) correspond to Figures 6.9(a), (b) and (c) ($\delta_{\text{dipole}} = 40°$). However, reduced efficiency was simulated in the zenith angle range between 40° and 60°. The upper curves in Figures (b) and (c) reflect the assumption of full efficiency. Figures (d), (e) and (f) were generated with $\delta_{\text{dipole}} = -40°$, 75° and $-75°$, respectively.

however, is based on the assumption of constant efficiency within the whole range of zenith angles up to $\vartheta_{\text{max}}$. In the case of these simulated sets, this assumption is fulfilled, because no efficiency deficit was simulated. The third in each series of plots compares the predicted az-

(a)



(b)                                                    (c)
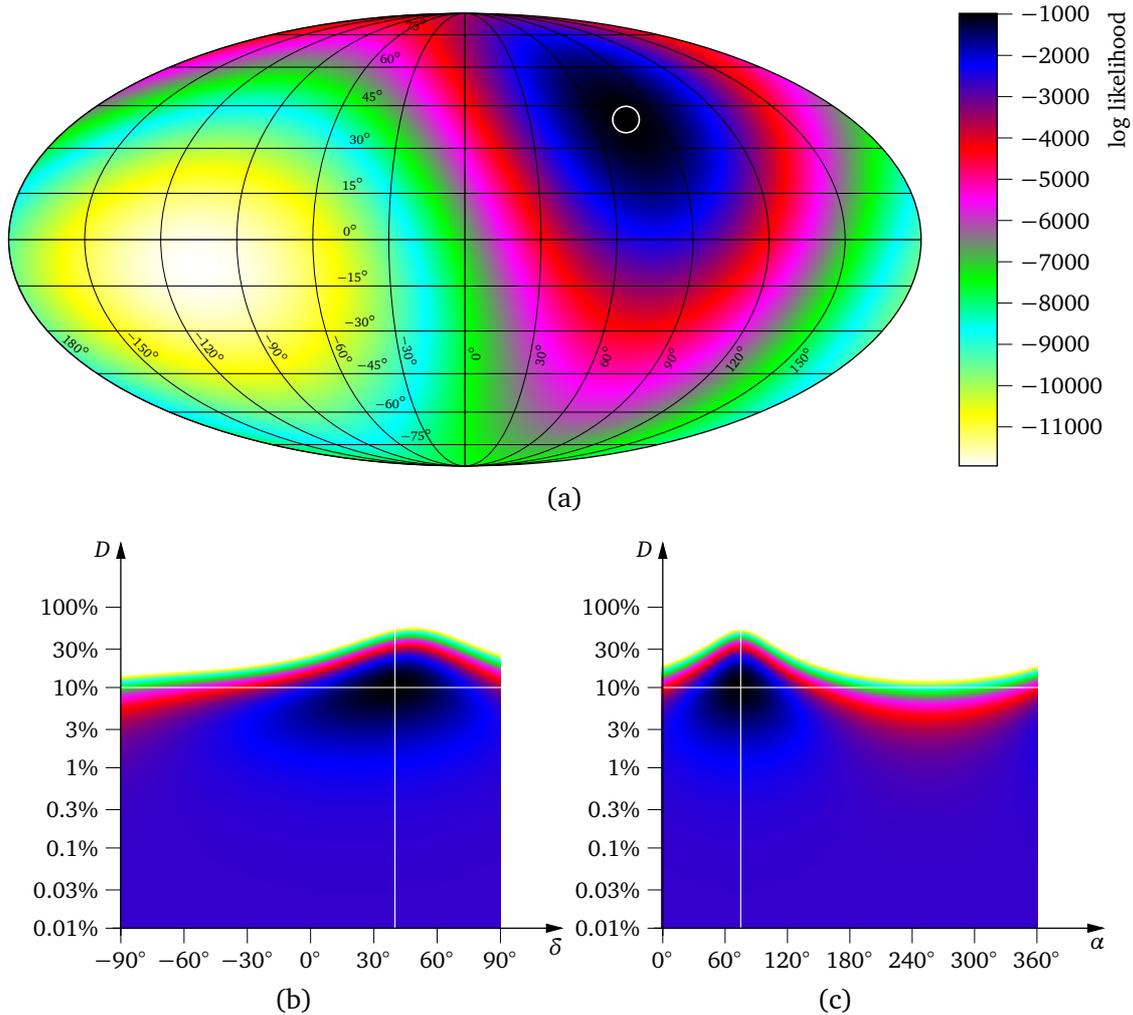
**Figure 6.11:** Horizontal Rayleigh analysis ('p'): log-likelihood map, illustrating the fit of the data displayed in Figures 6.9(a) to 6.9(c). Figure (a) displays log-likelihood values subject to dipole direction, for the true amplitude value (10%). The white circle marks the true dipole direction. Figure (b) displays log-likelihood values subject to amplitude and declination, for the true dipole right ascension (75°). Likewise, Figure (c) shows the amplitude/right ascension plane of the parameter space at $\delta = 40°$, which is the true declination value. The dotted lines mark the respective true values.

imuthal amplitudes (the curve is the same as in the second plot) with the expected amplitudes as calculated from the time bins' zenith angle distributions according to Equation 6.71. In this case, the data points generally agree with the theoretically predicted amplitudes.

Figure 6.10 shows results of the simulations of four example data sets that suffer from an efficiency defect for zenith angles between 40° and 60°. For the first data set (with $\delta_{\text{dipole}} = 40°$) the series of the three plots is shown in Figures 6.10(a) to 6.10(c). For the other three sets (again with $\delta_{\text{dipole}} = -40°$, 75° and $-75°$) only the third plot is shown in Figures 6.10(d) to 6.10(f). The underrepresentation of more inclined showers in the data set leads to smaller horizontal Rayleigh amplitudes than expected for these dipole configurations. As a result, the fit algorithm yields too low values for the dipole amplitude if the assumption of full efficiency is made. As can be seen in Figure 6.10(a), the smaller azimuthal amplitudes cause the data points to scatter slightly wider around the curve than in Figure 6.9(a),
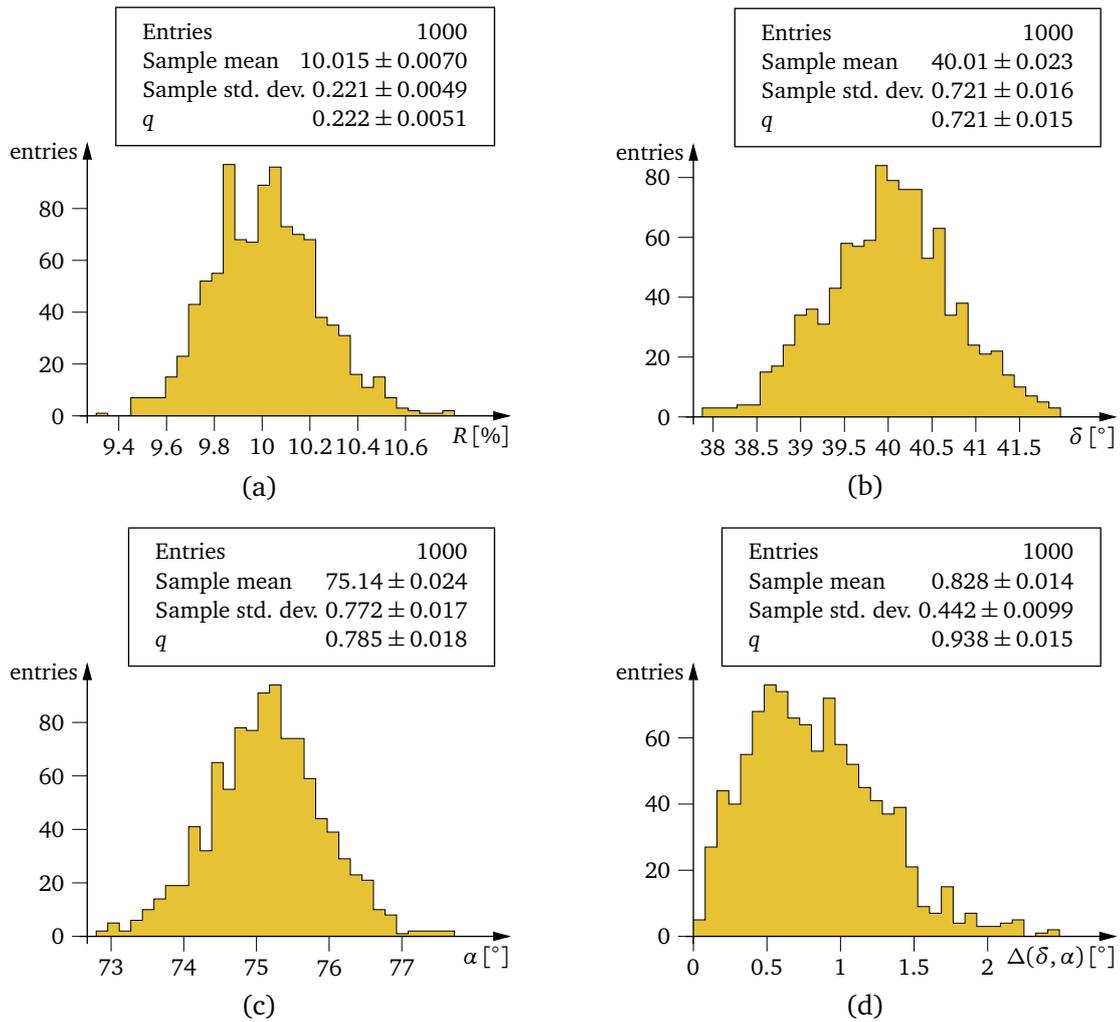
**Figure 6.12:** Horizontal Rayleigh analysis ('p') applied to simulated data sets: 1,000 data sets of the kind displayed in Figures 6.9(a) to (c) were simulated. The obtained dipole amplitudes are displayed in Figure (a), declination values are shown Figure (b), and right ascension values are shown in Figure (c). Figure (d) displays the distribution of angular distances between the reconstructed dipole direction and the true one. These plots correspond to 1,000 realisations of the fit illustrated in Figure 6.11.

where full efficiency is correctly assumed. The tendency of the data points to underestimate the expected degree of azimuthal anisotropy can be seen in Figure 6.10(b), especially when compared to Figure 6.9(b). The effect becomes even clearer in Figure 6.10(c), in which the predicted azimuthal amplitudes (solid curve, based on the assumption of full efficiency) are put in contrast with the expected amplitudes as calculated from the zenith angle distribution (dots, reflecting the actual efficiency situation). The horizontal Rayleigh analysis can be performed with either the full efficiency assumption (variants 'p' and 'p&a') or with the zenith distributions from data (variants 'p+$\vartheta$' and 'p&a+$\vartheta$').

The functioning of the horizontal Rayleigh analysis, and of the log-likelihood fit in particular, shall be illustrated by Figures 6.11 to 6.18. These figures feature log-likelihood displays and reconstruction result distributions for four different scenarios, with different combinations of variants of the method and simulation configurations. The first scenario is based on the data

(a)



(b)                                                    (c)
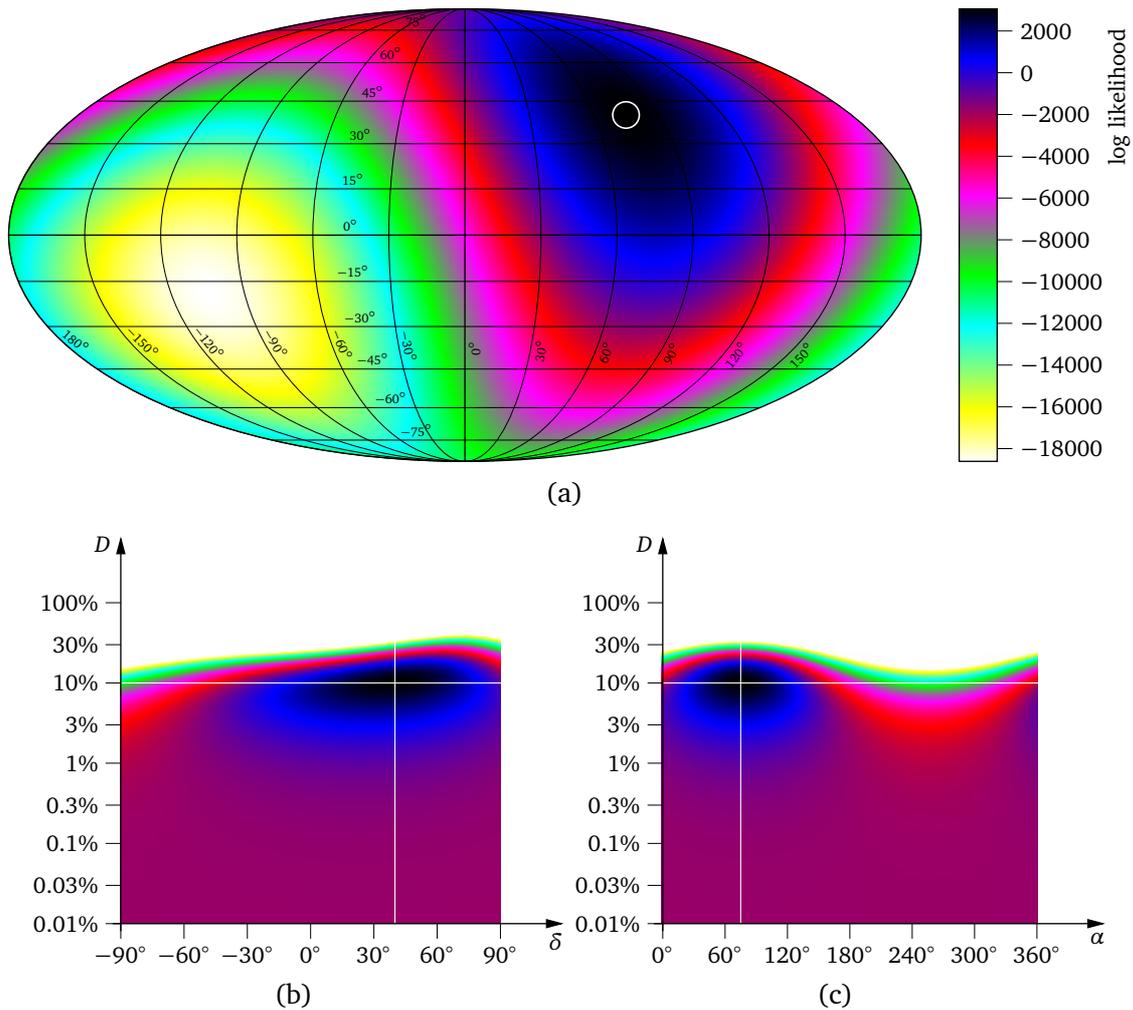
**Figure 6.13:** Horizontal Rayleigh analysis ('p&a'): log-likelihood map, illustrating the fit of the data
displayed in Figures 6.9(a) to 6.9(c). Figure (a) displays log-likelihood values subject
to dipole direction, for the true amplitude value (10%). The white circle marks the
true dipole direction. Figure (b) displays log-likelihood values subject to amplitude and
declination, for the true dipole right ascension (75°). Likewise, Figure (c) shows the
amplitude/right ascension plane of the parameter space at $\delta = 40°$, which is the true
declination value. The dotted lines mark the respective true values.

set displayed in Figures 6.9(a) to (c). It is depicted in Figures 6.11 and 6.12, the former of
which displays log-likelihood values in sections through the parameter space spanned by the
amplitude, declination and right ascension parameters. The absolute log-likelihood values
do not have a meaning on their own. However, these plots suggest, that the true dipole pa-
rameters clearly stand out inside the parameter space. A fit algorithm, that maximises the
log-likelihood value through the choice of appropriate dipole parameters, localises the true
parameter values with good accuracy. There are no pronounced secondary maxima, neither in
the vicinity of the true values, nor at distant places in the parameter space. The log-likelihood
values shown are based on the evaluation of the obtained horizontal Rayleigh phases in the
various time bins alone (variant 'p', see page 114 for an explanation of the four variants of the
horizontal Rayleigh method). The same kind of simulation and analysis was repeated 1,000
times. In Figure 6.12, the outcome of the analyses is shown in the form of four histograms.

Figure with four histograms (a), (b), (c), (d):

(a) statistics box:
| Entries | 1000 |
| Sample mean | $10.004 \pm 0.0035$ |
| Sample std. dev. | $0.110 \pm 0.0025$ |
| $q$ | $0.110 \pm 0.0025$ |

x-axis: $R\,[\%]$

(b) statistics box:
| Entries | 1000 |
| Sample mean | $40.01 \pm 0.021$ |
| Sample std. dev. | $0.655 \pm 0.015$ |
| $q$ | $0.655 \pm 0.014$ |

x-axis: $\delta\,[°]$

(c) statistics box:
| Entries | 1000 |
| Sample mean | $75.14 \pm 0.022$ |
| Sample std. dev. | $0.690 \pm 0.015$ |
| $q$ | $0.704 \pm 0.016$ |

x-axis: $\alpha\,[°]$

(d) statistics box:
| Entries | 1000 |
| Sample mean | $0.750 \pm 0.013$ |
| Sample std. dev. | $0.397 \pm 0.0089$ |
| $q$ | $0.848 \pm 0.013$ |

x-axis: $\Delta(\delta,\alpha)\,[°]$

**Figure 6.14:** Horizontal Rayleigh analysis ('p&a') applied to simulated data sets: the same data sets as used for Figure 6.12 were analysed. Instead of the phase fit, the phase and amplitude fit was used. These plots correspond to 1,000 realisations of the fit illustrated in Figure 6.13.

The distributions of reconstructed dipole amplitudes, declinations and right ascensions suggest that the method works stably. The mean values of all three obtained distributions match the respective true values. Furthermore, there are no outliers. The accuracy of the amplitude reconstruction is better than a quarter percent. The error of both declination and right ascension values reconstruction are better than 0.8°. The dipole direction is off the correct direction by ca. 0.8° on average. While these numbers sound very positive, it should be noted that the configuration of this simulation (10 million events and a dipole amplitude of 10%) is very benevolent to any analysis method. The accuracies must be evaluated through comparison with other methods, which will be discussed below.

The second scenario is depicted in Figures 6.13 (log-likelihood maps) and 6.14 (distributions). The same data sets were used as in the former scenario, but the 'p&a' variant of the horizontal Rayleigh analysis was used. This variant uses both the reconstructed horizontal Rayleigh phase and amplitude of each time bin for the calculation of the likelihood of a potential dipole configuration. The structures of the log-likelihood maps look slightly different than before, especially those of the declination/amplitude and right ascension/amplitude plots. As

a result, the accuracy is improved: the error of the amplitude reconstruction is halved, and the directional reconstruction performs slightly better. The fundamental reason for this improvement lies in the fact that the 'p&a' variant uses more information than the 'p' variant, which results in a benefit in accuracy.

The third scenario, illustrated in Figures 6.15 (log-likelihood maps) and 6.16 (distributions), uses the 'p&a' variant as well. However, unlike the first two scenarios, it is based on the data set displayed in Figures 6.10(a) to (c). This data set was simulated with reduced efficiency for showers with inclinations above $\vartheta = 40°$. It has been discussed in Section 5.5.4, that such an effect can have a substantial negative impact on the reconstruction quality of other methods. Even though the extent of the efficiency lack in the data set discussed here is drastic, it has only a mild effect on the reconstruction results. It can be seen in both the log-likelihood map in Figure 6.15(a) and the distributions in Figures 6.16(b) to 6.16(d), that there is no considerable effect on the reconstruction of the dipole direction. However, the dipole amplitude is systematically underestimated, with a mean value of 8% instead of the correct 10% (Fig. 6.16(a)). The log-likelihood maps in Figures 6.15(b) and 6.15(c) reveal this effect as well, as the region of maximum likelihood is slightly below the 10% mark. The efficiency misestimation still has an effect on the dipole reconstruction with the horizontal Rayleigh method (at least with the 'p&a' variant), although it is far from being as severe as for the SAP and multipole expansion method (see Section 5.5.4). The reason for this is, that full efficiency is still assumed, although not in such a central part as in other methods: the assumption does only effect the interpretation of azimuthal anisotropies in terms of the assumed dipole amplitude.

The issue of possible misestimation of the efficiency (usually in the sense, that constantly full efficiency is falsely assumed) is addressed by the variants 'p+$\vartheta$' and 'p&a+$\vartheta$' of the horizontal Rayleigh analysis. By extracting the zenith angle distributions for each time bin from the data, assumptions about the shape of the field of view and the efficiency are avoided. The final of the four scenarios uses the 'p&a+$\vartheta$' variant to analyse the same data sets as in the previous scenario. Figures 6.17 (log-likelihood maps) and 6.18 (distributions) show the results. As a consequence, the dipole amplitude is no more underestimated. The reconstruction error of dipole amplitude and direction are not as good as in the case of full efficiency, but this effect is of purely statistical origin: as can be seen in Figure 6.10(c), the efficiency deficit (the data points form the lower curve) leads to smaller azimuthal anisotropies in the separate time bins than in the case of full efficiency (upper curve), so that in each of the time bins, the distribution of reconstructed azimuth angles is generally less anisotropic. With lower amplitudes, the Rayleigh phases (the dipole vector's azimuth in this context) can only be determined less precise.

### 6.4.2    The Influence of Configuration Parameters and Experimental Effects

Following the approach in Section 5.3, the investigations below will be based upon a set of standard configuration parameters, as described in Section 5.3.2. First, the reconstruction accuracies in the case of that standard configuration are presented, in the same way as for the SAP method (Section 5.3.4) and the multipole expansion method (Section 5.3.5). Then, single configuration items will be varied in order to test the influence of these parameters.

#### 6.4.2.1    Standard configuration data sets

Figure 6.19 shows the distributions of amplitude, dipole declination and right ascension results, as well as the distribution of angular deviations, obtained with the horizontal Rayleigh method ('p&a+$\vartheta$') for 1,000 simulated data sets with the standard configuration, as described

(a)



(b)

(c)
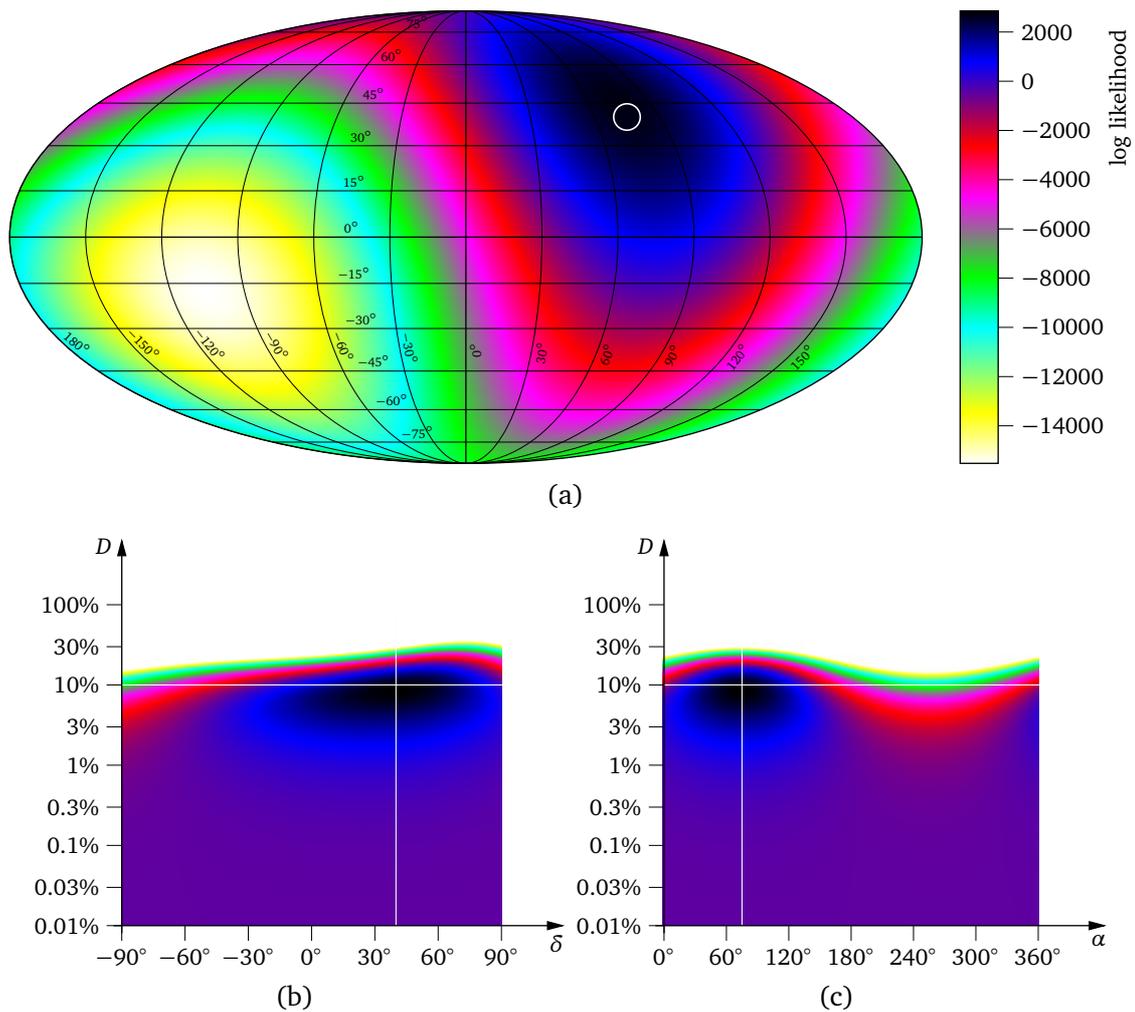
**Figure 6.15:** Horizontal Rayleigh analysis ('p&a') of a data set with an efficiency deficit at high inclinations: log-likelihood map, illustrating the fit of the data displayed in Figures 6.10(a) to 6.10(c). Figure (a) displays log-likelihood values subject to dipole direction, for the true amplitude value (10%). The white circle marks the true dipole direction. Figure (b) displays log-likelihood values subject to amplitude and declination, for the true dipole right ascension (75°). Likewise, Figure (c) shows the amplitude/right ascension plane of the parameter space at $\delta = 40°$, which is the true declination value. The dotted lines mark the respective true values.

in Section 5.3.2. The plots in this figure can directly be compared with those in Figure 5.5 (SAP method) and Figure 5.6 (multipole expansion method). Table 6.1 lists the properties of the distributions for all analysis methods discussed here. The reconstruction accuracy of the horizontal Rayleigh method is basically of the same order of magnitude than those of the SAP method and the multipole expansion method. The variants, that make use a combined fit of phase and amplitude values, are generally performing better than those using only phase information. This is indeed plausible, taking into account, that the pure phase fit variants basically ignore valid information, that the other variants include. Because more valid information is used, the results are more precise. In case of the standard configuration for simulations, full efficiency is simulated for the complete field of view. As a consequence, there is no difference between a variant using an analytical description of the field of view, based on the said assump-

| Entries | 1000 |
|---|---|
| Sample mean | $8.060 \pm 0.0035$ |
| Sample std. dev. | $0.110 \pm 0.0025$ |
| $q$ | $1.943 \pm 0.0035$ |

(a)

| Entries | 1000 |
|---|---|
| Sample mean | $40.10 \pm 0.025$ |
| Sample std. dev. | $0.791 \pm 0.018$ |
| $q$ | $0.796 \pm 0.017$ |

(b)

| Entries | 1000 |
|---|---|
| Sample mean | $75.10 \pm 0.027$ |
| Sample std. dev. | $0.849 \pm 0.019$ |
| $q$ | $0.854 \pm 0.019$ |

(c)

| Entries | 1000 |
|---|---|
| Sample mean | $0.919 \pm 0.015$ |
| Sample std. dev. | $0.466 \pm 0.010$ |
| $q$ | $1.030 \pm 0.015$ |

(d)
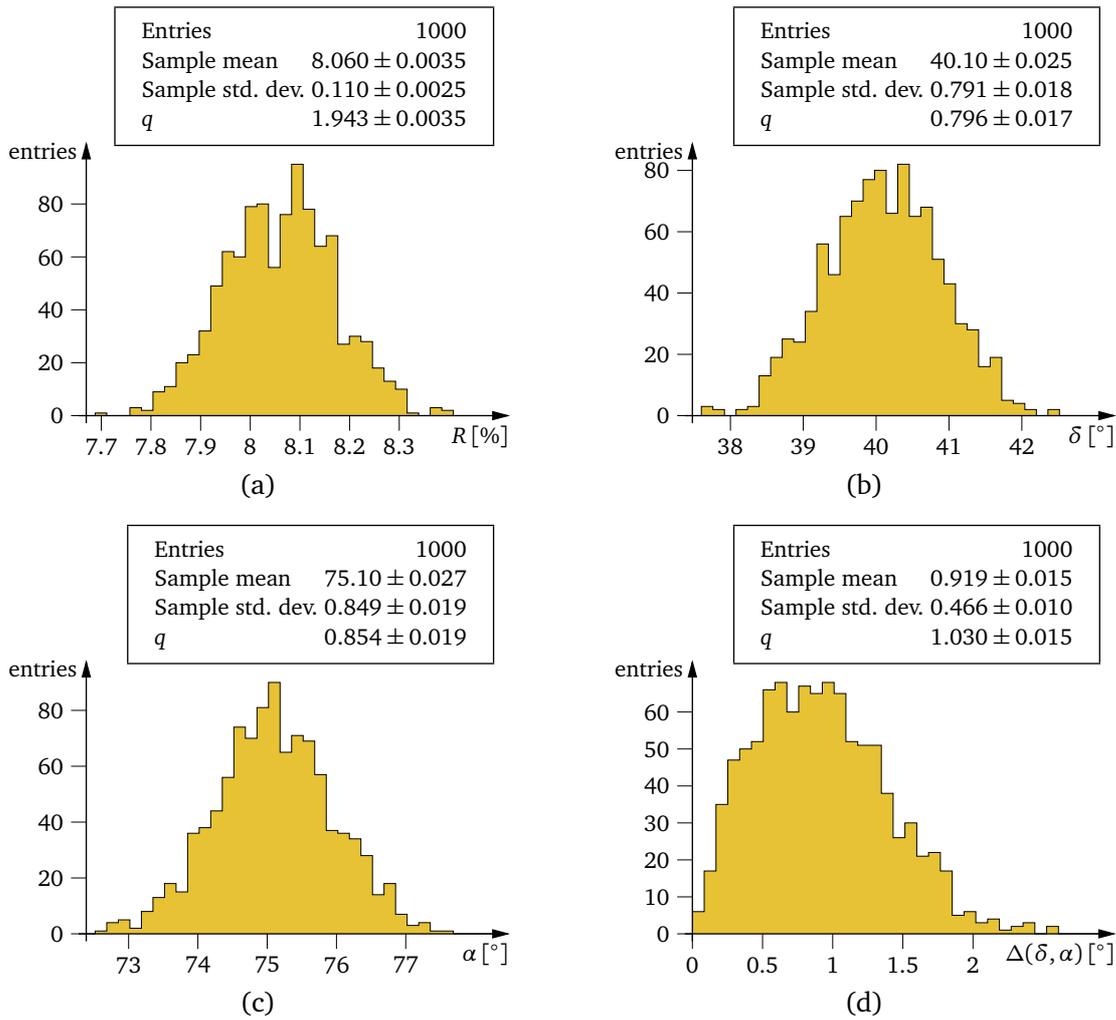
**Figure 6.16:** Horizontal Rayleigh analysis ('p&a') applied to simulated data sets with zenith efficiency defect: 1,000 data sets of the kind displayed in Figures 6.10(a) to (c) were simulated. Owing to the efficiency deficit at high inclinations, the reconstruction underestimates the dipole amplitude. These plots correspond to 1,000 realisations of the fit illustrated in Figure 6.15.

tion, and the corresponding variant that evaluates the events' reconstructed zenith angles to understand the properties of the field of view.

In the following, the results for the variant 'p&a+$\vartheta$' are discussed, because it is the most advanced of the four variants. For the specific configuration simulated here, the error of the amplitude reconstruction (true value is 3%) amounts to approximately 0.32%, which is slightly worse than the value of the SAP method (0.30%), although these two values are still statistically compatible with each other: the difference corresponds to only $1.2\sigma$. The multipole expansion performs significantly better, with an error of only 0.24%. The error of the declination reconstruction is approximately 6.9°, which is better as compared with the SAP method (8.5°), but not as good as the multipole expansion method (5.6°). Finally, the dipole vector's right ascension is reconstructed with an error of 6.3°, which is slightly worse than SAP method (5.4°) and multipole expansion method (4.1°). The overall error of the direction reconstruction amounts to 8.8°, which is again in the range between SAP method (9.7°) and
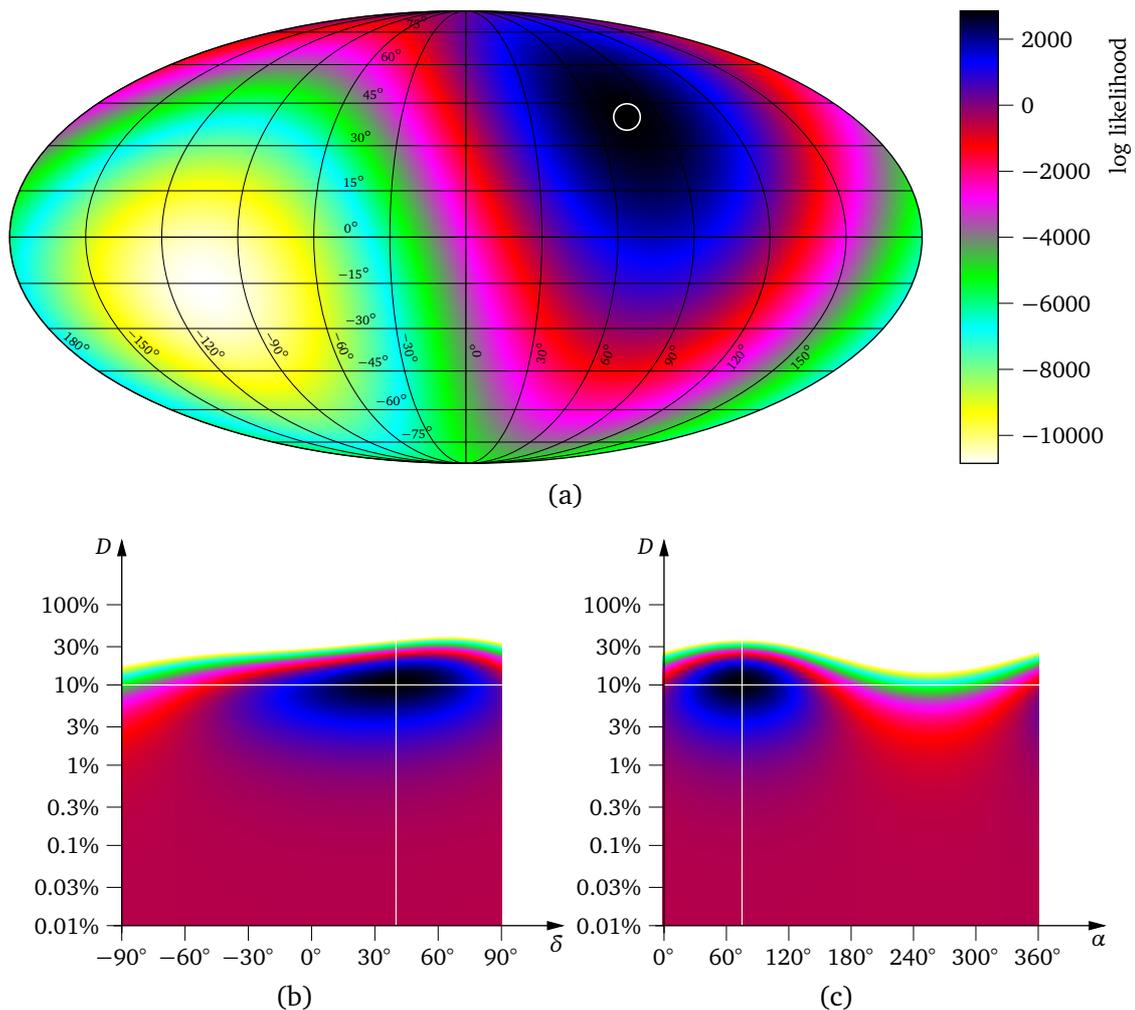
**Figure 6.17:** Horizontal Rayleigh analysis ('p&a+$\vartheta$') applied to a simulated data set with efficiency defect: log-likelihood map, illustrating the fit of the data displayed in Figures 6.10(a) to 6.10(c). Figure (a) displays log-likelihood values subject to dipole direction, for the true amplitude value (10%). The white circle marks the true dipole direction. Figure (b) displays log-likelihood values subject to amplitude and declination, for the true dipole right ascension (75°). Likewise, Figure (c) shows the amplitude/right ascension plane of the parameter space at $\delta = 40°$, which is the true declination value. The dotted lines mark the respective true values.

multipole expansion method (6.9°).

To summarise, the accuracies of the horizontal Rayleigh method compete well with those of the SAP method. However, the multipole method outperforms its competitors. While the difference in accuracy between SAP method and multipole method can be justified with the unfavourable weighting that the SAP method utilises, which overpronounces statistical fluctuations, this argument cannot serve as an explanation for the inferiority of the horizontal Rayleigh method, which, like the multipole expansion method, does not utilise weighting at all. It is difficult to give an exhaustive explanation for the different performances of these two methods, since the ways these methods work are very different. They do not use exactly the same parts of the data available. What they both use, they use in different ways: both methods can work with a list of arrival direction in horizontal coordinates and correspond-

| | |
|---|---|
| Entries | 1000 |
| Sample mean | $10.00 \pm 0.0044$ |
| Sample std. dev. | $0.138 \pm 0.0031$ |
| $q$ | $0.138 \pm 0.0029$ |

| | |
|---|---|
| Entries | 1000 |
| Sample mean | $39.97 \pm 0.025$ |
| Sample std. dev. | $0.800 \pm 0.018$ |
| $q$ | $0.800 \pm 0.017$ |

(a)  (b)

| | |
|---|---|
| Entries | 1000 |
| Sample mean | $75.10 \pm 0.027$ |
| Sample std. dev. | $0.849 \pm 0.019$ |
| $q$ | $0.854 \pm 0.019$ |

| | |
|---|---|
| Entries | 1000 |
| Sample mean | $0.920 \pm 0.015$ |
| Sample std. dev. | $0.471 \pm 0.011$ |
| $q$ | $1.034 \pm 0.016$ |

(c)  (d)
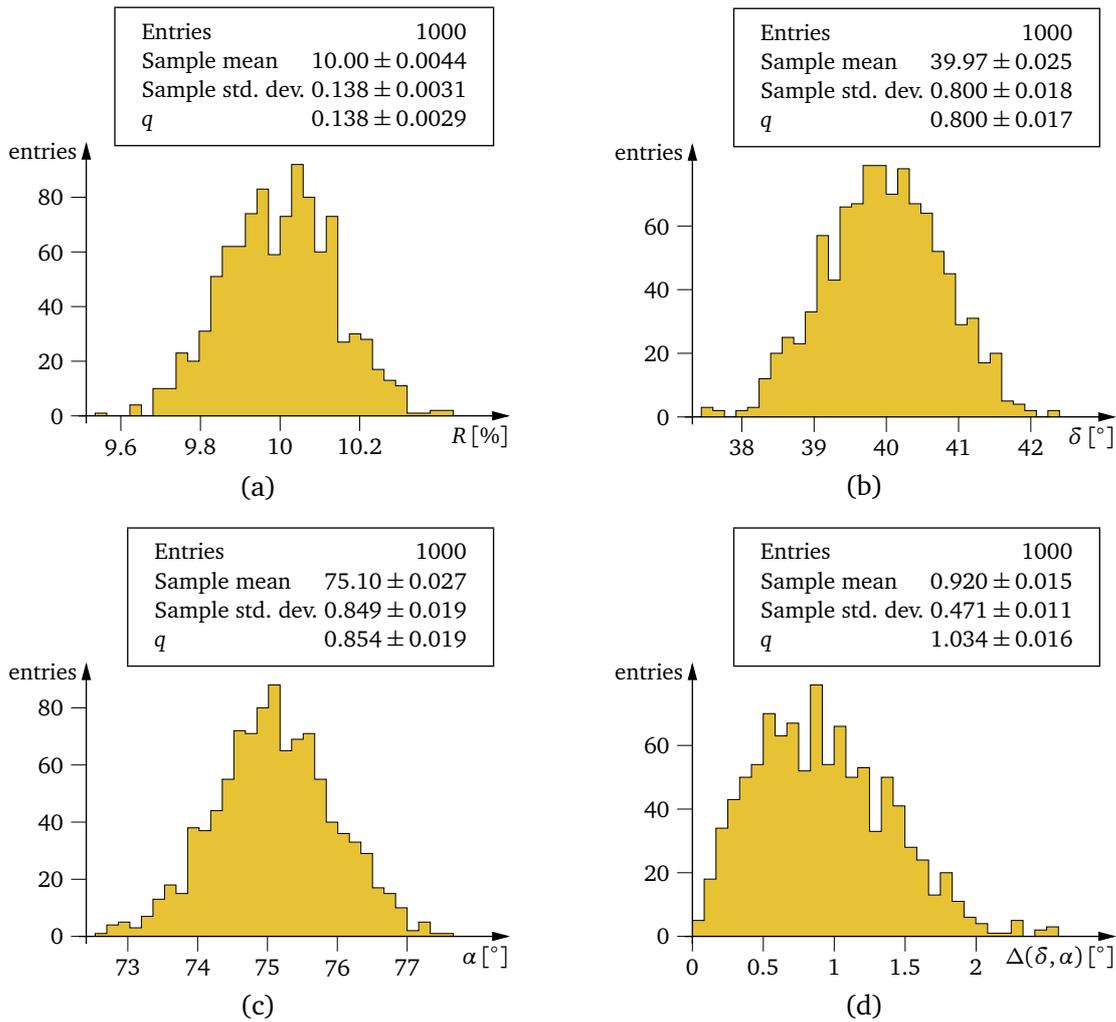
**Figure 6.18:** Horizontal Rayleigh analysis ('p&a+$\vartheta$') applied to simulated data sets with zenith efficiency defect: the same data sets as used for Figure 6.16 were analysed. The air showers' zenith angles were included in the analysis. The dipole amplitude is no longer underestimated as in Figure 6.16. These plots correspond to 1,000 realisations of the fit illustrated in Figure 6.17.

ing event time. The multipole expansion method, like the SAP method, needs the event time only for the conversion of the arrival direction from horizontal to equatorial coordinates. It does not make use of the information contained in the distribution of event times in sidereal time, which could provide knowledge about the change of the event rate, e.g. induced by metereological effects. Instead, it assumes constant measurement conditions in the same way as it assumes a well-formed field of view, i.e. constant efficiency for all arrival directions. In this sense, the multipole method can make use of additional information, that is not given to the horizontal Rayleigh method, this information being the assumptions incorporated into the method. How valuable or how harmful the utilisation of these assumptions is, depends on the specific parameters of the dipole, as well as on the presence of experimental effects. In case of simulations with the standard configuration, the assumptions do apply well. However, certain experimental effects can render the assumptions false. Based on false assumptions, the methods produce considerably wrong results.

| Entries | 1000 |
|---|---|
| Sample mean | $3.020 \pm 0.010$ |
| Sample std. dev. | $0.315 \pm 0.0071$ |
| $q$ | $0.316 \pm 0.0071$ |

(a)

| Entries | 1000 |
|---|---|
| Sample mean | $29.6 \pm 0.22$ |
| Sample std. dev. | $6.86 \pm 0.15$ |
| $q$ | $6.87 \pm 0.16$ |

(b)

| Entries | 1000 |
|---|---|
| Sample mean | $74.7 \pm 0.20$ |
| Sample std. dev. | $6.27 \pm 0.14$ |
| $q$ | $6.28 \pm 0.14$ |

(c)

| Entries | 1000 |
|---|---|
| Sample mean | $7.76 \pm 0.13$ |
| Sample std. dev. | $4.05 \pm 0.091$ |
| $q$ | $8.76 \pm 0.15$ |

(d)
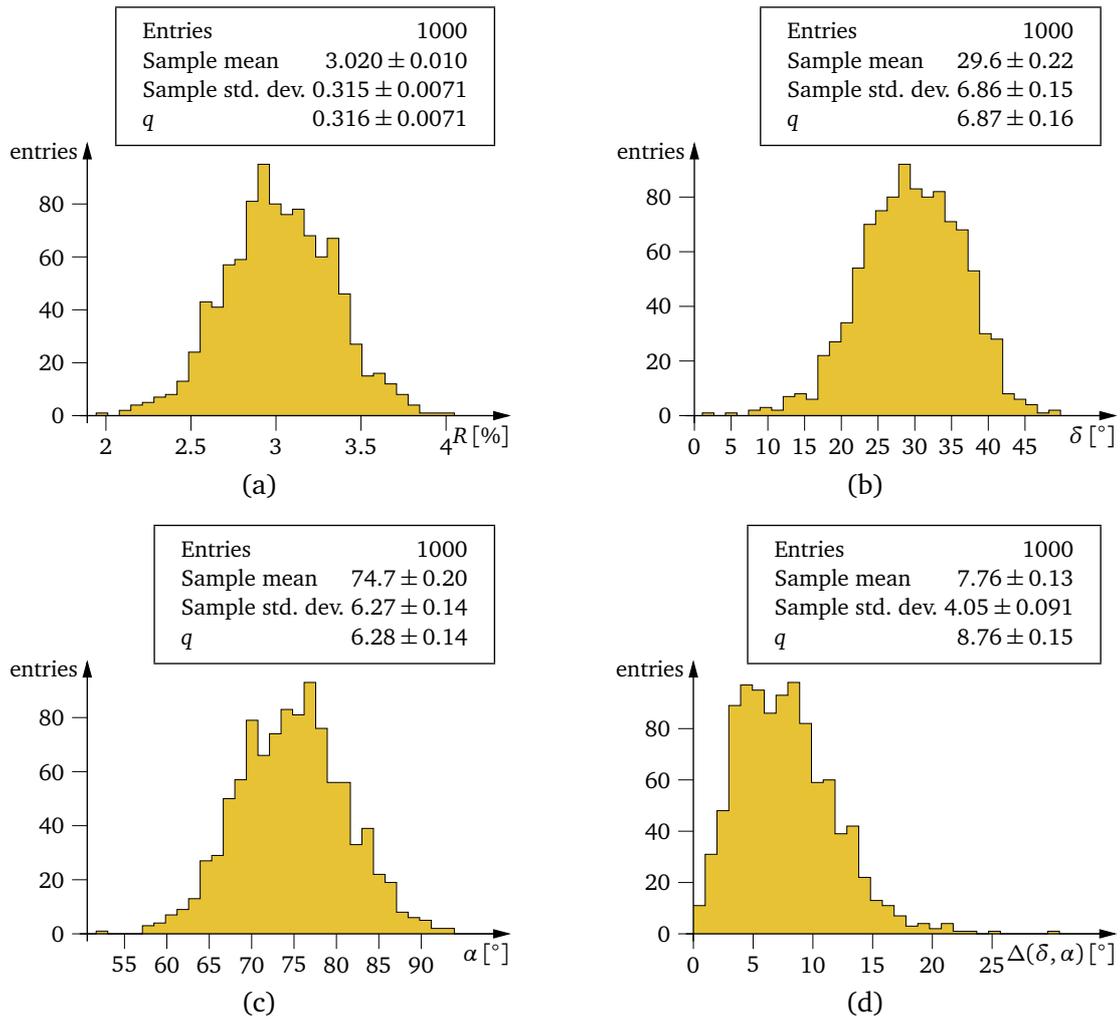
**Figure 6.19:** Horizontal Rayleigh analysis ('p&a+$\vartheta$' variant) applied to simulated data sets with standard configuration (see Section 5.3.2)

The behaviour of the four variants of the horizontal Rayleigh method related to dipole configuration and experimental parameters and effects shall be investigated with a series of Monte Carlo simulations, along the lines of Sections 5.4 and 5.5.

### 6.4.2.2   Number of Simulated Events

Figure 6.20 shows the reconstruction qualities for differently sized data sets. The grey data points for the Rayleigh, SAP and multipole expansion methods equal those in Figure 5.7 in the previous chapter and are shown here again to allow for comparison with the new horizontal Rayleigh method. The data points at $\log_{10} N = 6$ correspond to the distributions shown in Figure 6.19. The situation for data sets of larger or smaller sizes is not substantially different: the amplitude reconstruction is about as good as that of the SAP method, the quality of the declination reconstruction ranges between those of the SAP and multipole expansion method, and the reconstruction of the right ascension works slightly worse than with the other methods. Again, the variants of the horizontal method utilising amplitude information perform slightly better, while there is no noticeable difference between those variants that use the air shower's

| Method | R (true value: 3%) | | |
|---|---|---|---|
| | Sample mean | Sample std. dev. | $q$ |
| SAP | $3.016 \pm 0.0096$ | $0.304 \pm 0.0068$ | $0.304 \pm 0.0066$ |
| MP | $3.008 \pm 0.0075$ | $0.237 \pm 0.0053$ | $0.237 \pm 0.0053$ |
| HR (p) | $3.031 \pm 0.011$ | $0.352 \pm 0.0079$ | $0.353 \pm 0.0083$ |
| HR (p&a) | $3.020 \pm 0.010$ | $0.316 \pm 0.0071$ | $0.316 \pm 0.0071$ |
| HR (p+$\vartheta$) | $3.031 \pm 0.011$ | $0.351 \pm 0.0079$ | $0.352 \pm 0.0083$ |
| HR (p&a+$\vartheta$) | $3.020 \pm 0.010$ | $0.315 \pm 0.0071$ | $0.316 \pm 0.0071$ |

| Method | $\delta$ (true value: 30°) | | |
|---|---|---|---|
| | Sample mean | Sample std. dev. | $q$ |
| SAP | $28.5 \pm 0.27$ | $8.40 \pm 0.19$ | $8.5 \pm 0.20$ |
| MP | $29.51 \pm 0.18$ | $5.81 \pm 0.13$ | $5.83 \pm 0.14$ |
| HR (p) | $29.4 \pm 0.24$ | $7.65 \pm 0.17$ | $7.67 \pm 0.19$ |
| HR (p&a) | $29.6 \pm 0.22$ | $6.86 \pm 0.15$ | $6.87 \pm 0.16$ |
| HR (p+$\vartheta$) | $29.4 \pm 0.24$ | $7.64 \pm 0.17$ | $7.66 \pm 0.19$ |
| HR (p&a+$\vartheta$) | $29.6 \pm 0.22$ | $6.86 \pm 0.15$ | $6.87 \pm 0.16$ |

| Method | $\alpha$ (true value: 75°) | | |
|---|---|---|---|
| | Sample mean | Sample std. dev. | $q$ |
| Rayl. | $74.78 \pm 0.14$ | $4.45 \pm 0.099$ | $4.45 \pm 0.096$ |
| SAP | $74.75 \pm 0.17$ | $5.38 \pm 0.12$ | $5.38 \pm 0.12$ |
| MP | $74.78 \pm 0.13$ | $4.17 \pm 0.093$ | $4.18 \pm 0.090$ |
| HR (p) | $74.9 \pm 0.22$ | $6.99 \pm 0.16$ | $6.99 \pm 0.15$ |
| HR (p&a) | $74.8 \pm 0.20$ | $6.27 \pm 0.14$ | $6.27 \pm 0.14$ |
| HR (p+$\vartheta$) | $74.9 \pm 0.22$ | $6.99 \pm 0.16$ | $6.99 \pm 0.15$ |
| HR (p&a+$\vartheta$) | $74.7 \pm 0.20$ | $6.27 \pm 0.14$ | $6.28 \pm 0.14$ |

| Method | $\Delta(\delta, \alpha)$ (true value: 0°) | | |
|---|---|---|---|
| | Sample mean | Sample std. dev. | $q$ |
| SAP | $8.43 \pm 0.15$ | $4.88 \pm 0.11$ | $9.74 \pm 0.18$ |
| MP | $6.02 \pm 0.10$ | $3.29 \pm 0.074$ | $6.86 \pm 0.12$ |
| HR (p) | $8.60 \pm 0.15$ | $4.65 \pm 0.10$ | $9.77 \pm 0.17$ |
| HR (p&a) | $7.76 \pm 0.13$ | $4.05 \pm 0.091$ | $8.75 \pm 0.15$ |
| HR (p+$\vartheta$) | $8.60 \pm 0.15$ | $4.63 \pm 0.10$ | $9.76 \pm 0.17$ |
| HR (p&a+$\vartheta$) | $7.76 \pm 0.13$ | $4.05 \pm 0.091$ | $8.76 \pm 0.15$ |

**Table 6.1:** Reconstruction quality for simulated data set with standard configuration: 1,000 simulated data sets with standard configuration were analysed. Because the same data sets were used, the results for the different analysis methods are correlated.

reconstructed zenith angles and those that do not. There is, however, a marginal change of the conditions going to very small data sets. For data sets with 10,000 events or fewer, all four variants of the horizontal Rayleigh method are able to perform the reconstruction of both dipole declination and right ascension as well as the multipole expansion method. However, the direction reconstruction for data sets of such small sizes is generally poor, as the inaccuracies almost reach their maximum values as limited by geometry.

To summarise, the impact of the size of the data set is for the horizontal Rayleigh analysis about the same as for the other methods. There is no minimal size of the data set below which the horizontal Rayleigh method fails to work, at least not within the inspected range of data
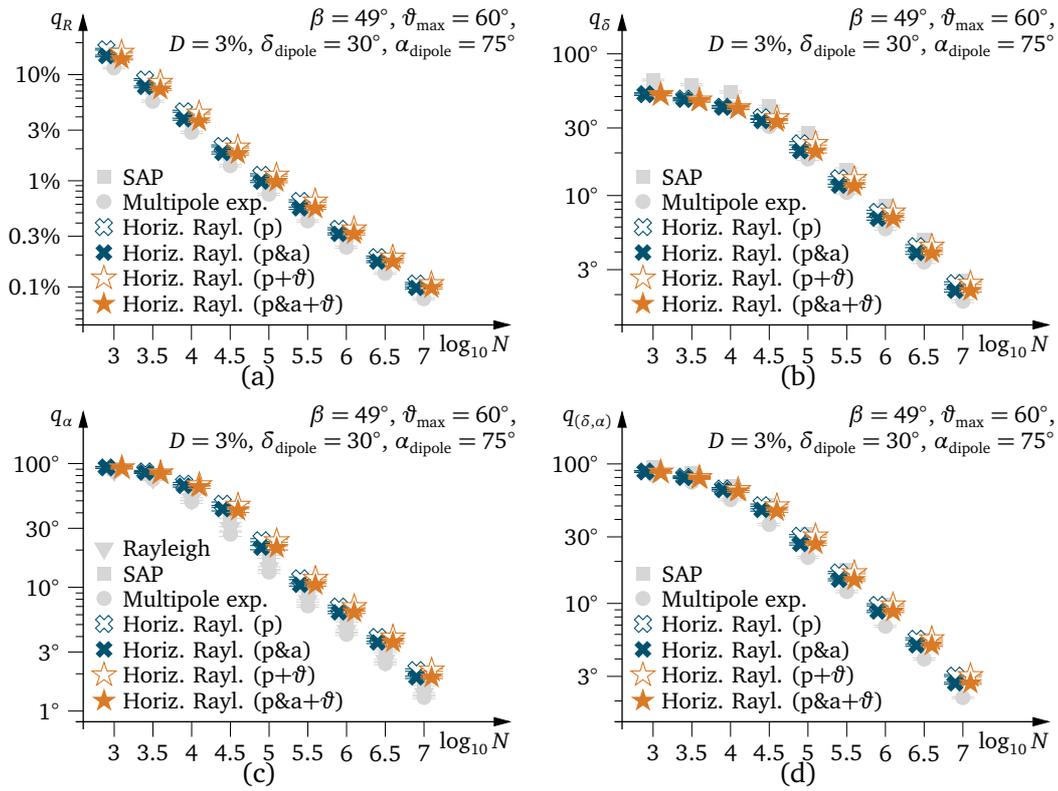
**Figure 6.20:** Horizontal Rayleigh analysis: reconstruction quality subject to number of simulated events

set sizes, starting at a size of 1,000 events.

### 6.4.2.3  Zenith Angle Limit

The relationship between reconstruction qualities and the experiment's zenith angle limit is depicted in Figure 6.21. The grey data points have already been shown in Figure 5.8. For each of the zenith limits, data sets with 1 million events each were simulated. The fact, that the choice of the zenith angle limit also influences the amount of statistics available for analysis is not taken into account. As it has been shown for the SAP and multipole methods in Section 5.4.2, a larger field of view is generally preferable, even without considering the gain in statistics. The effect is even more pronounced for the horizontal Rayleigh method, which apparently strongly disfavours a narrow field of view. A small opening angle poses a special problem for the horizontal Rayleigh method, as it is based on the analysis of azimuthal anisotropies. A low value of the zenith limit $\vartheta_{\max}$ implies, that only a small region of the sky close to the zenith is seen. Azimuthal anisotropies cannot be very pronounced within such a small region. Therefore, the azimuthal amplitudes are generally much smaller, and consequently both phases and amplitudes cannot be determined with good accuracy and so they scatter widely around their expected values. As a result, all parameters of the dipole configuration can only be vaguely estimated by the fit routine.

The other analysis methods follow a completely different mode of operation, with different implications of a small opening angle: Rayleigh, SAP and multipole expansion method all work with the equatorial coordinates of the showers' arrival directions. In equatorial coordinates, a low zenith limit $\vartheta_{\max}$ means, that only a narrow band of the sky with declinations in the range
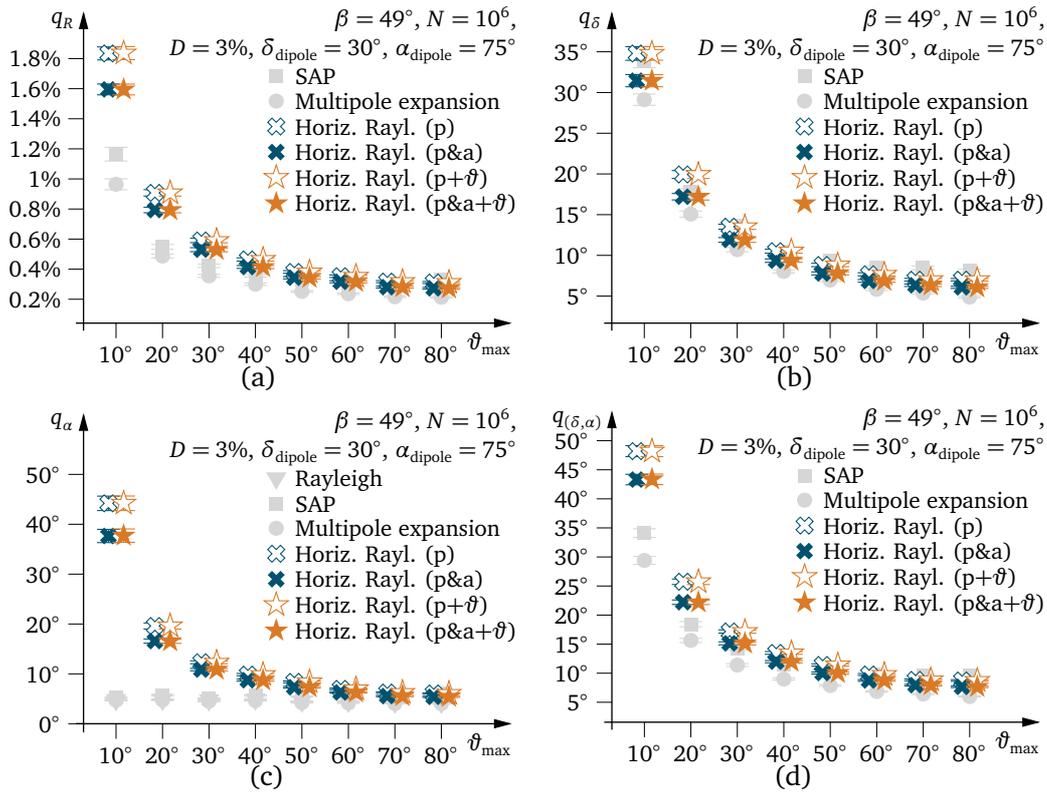
**Figure 6.21:** Horizontal Rayleigh analysis: reconstruction quality subject to zenith angle limit

between $\beta \pm \vartheta_{\max}$ can be seen. ($\beta$ denotes the experiment's geographical latitude.) Due to the fact that the visible sky only spans a small region along the North-South dimension, the North-South component of the dipole vector can only be reconstructed with large inaccuracy, which limits the accuracy of both dipole amplitude and declination reconstruction. However, it does not affect the right ascension reconstruction: the experiment practically scans the complete right ascension range during a sidereal day. The correct dipole right ascension can easily be identified through the excess that is seen at the corresponding time of the sidereal day.

To summarise, the horizontal Rayleigh method performs best with a large field of view. The influence of the zenith angle limit on the reconstruction quality is similar to the influence on other methods, with the exception of the right ascension reconstruction, which is degraded by a narrow field of view only in the case of the horizontal Rayleigh method.

### 6.4.2.4 Geographical Latitude

For the discussion of the influence of the experiment's geographical latitude on the reconstruction quality, a series of simulated data sets was generated for a selection of locations. The performances of the established analysis methods have been discussed in Section 5.4.3 and depicted in Figure 5.10. The plots illustrating the reconstruction accuracies of the horizontal Rayleigh methods are displayed in Figure 6.22. These plots contain no data points for the horizontal Rayleigh analysis for simulations of experiments located at one of the Earth's poles, since the method is not applicable to experiments at the Earth's North or South Pole. The horizontal Rayleigh method extracts the dipole vector's direction, both declination and right ascension, from the time development of the azimuth angle of the dipole vector in horizontal coordinates (Eq. 6.51) by means of a log-likelihood fit. For an experiment located at either
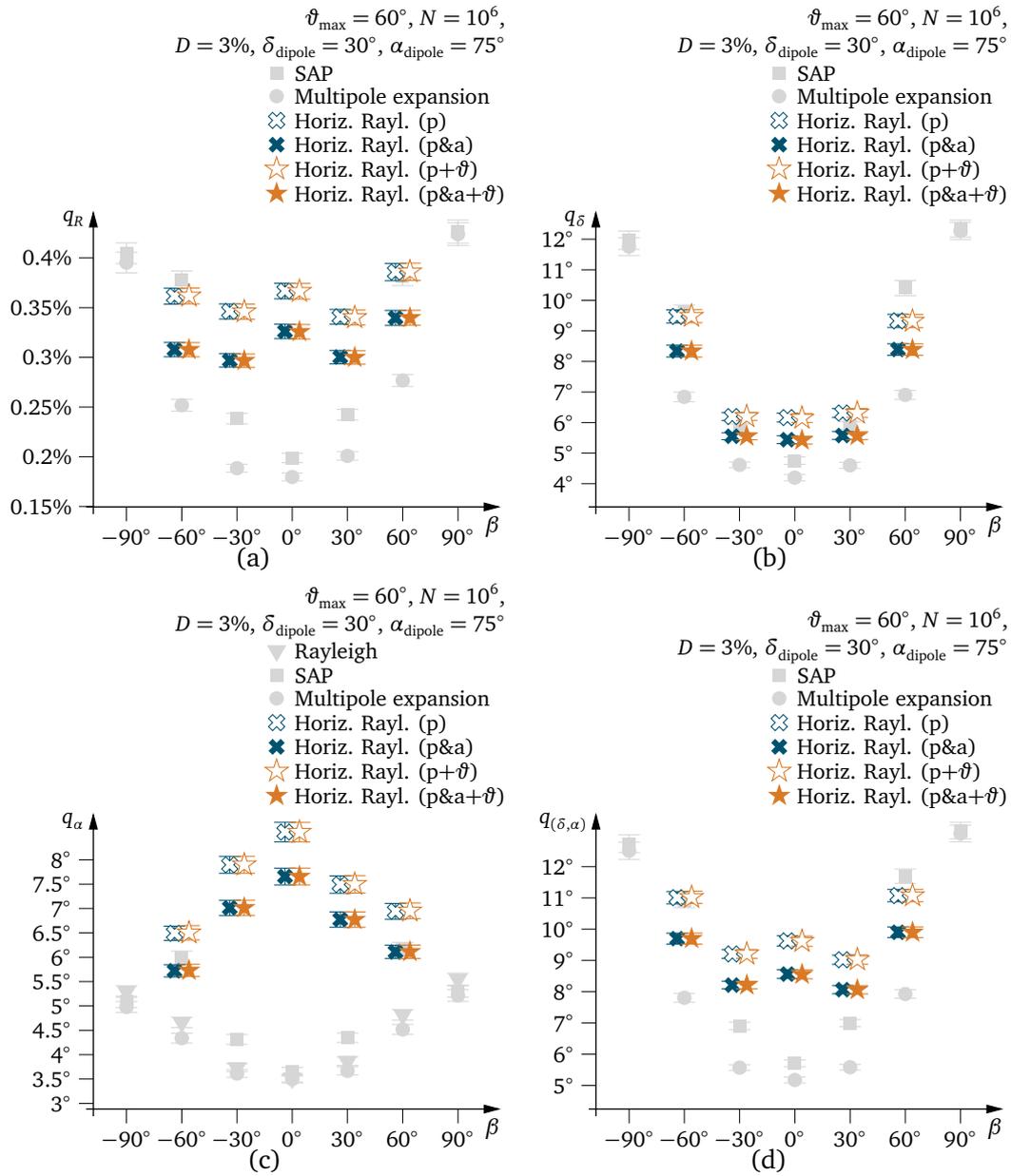
**Figure 6.22:** Horizontal Rayleigh analysis: reconstruction quality subject to experiment's geographical latitude

North or South Pole ($\beta = \pm 90°$), Equation 6.51 can be simplified by setting $\cos\beta = 0$ and $\sin\beta = \pm 1$:

$$
\begin{aligned}
\varphi_{\text{dipole}}(t) &= \arg(\mp \cos\delta_{\text{dipole}} \cos h_{\text{dipole}}(t) - i \cos\delta_{\text{dipole}} \sin h_{\text{dipole}}(t)) \\
&= \begin{cases}
\pi + h_{\text{dipole}}(t) &= \pi + local\ mean\ sidereal\ time(t) - \alpha_{\text{dipole}} & \text{(North Pole)} \\
-h_{\text{dipole}}(t) &= -local\ mean\ sidereal\ time(t) + \alpha_{\text{dipole}} & \text{(South Pole)} .
\end{cases}
\end{aligned}
$$

$$(6.73)$$

Thus, the fit function does not depend on the dipole vector's declination in this case. An experiment set up at one of the Earth's poles will always see the dipole vector turn continously and uniformly clockwise (North Pole) or anti-clockwise (South Pole). Care has to be taken

to have consistent definitions of the azimuth angle and the local mean sidereal time, as the concepts of both compass direction and local time are not directly applicable to polar locations, but can be defined by convention. The Rayleigh amplitudes extracted from the individual time bins do still relate to the dipole declination (shown here is the analytical description of the azimuthal amplitude as a function of time, the upper sign corresponds to the North Pole):

$$D'(t) = \frac{D \cos \delta_{\text{dipole}} \, \mathscr{E}_{21}(t)}{\mathscr{E}_{11}(t) \pm D \sin \delta_{\text{dipole}} \, \mathscr{E}_{12}(t)} \, . \tag{6.74}$$

However, at polar locations, the constant declination of the dipole vector translates into a constant zenith angle. Apart from possible variations of the $\mathscr{E}_{ij}$-functions, the above expression is a constant in time. Hence, it is not possible to obtain the two unknown quantities $D$ and $\delta_{\text{dipole}}$ from this relation.

The dipole vector's right ascension can be extracted from the Rayleigh phases, as it determines the offset between local time and reconstructed dipole azimuth angle. However, the implementation of the horizontal Rayleigh method used here cannot achieve this, because the fit routine often fails, owing to diverging fit parameters. A special implementation on the basis of the idea presented here could be crafted for dipole right ascension reconstruction with data from experiments located at one of the Earth's poles. However, this shall not be the subject of the discussion presented here.

Simulations were also carried out with experiment locations on latitudes between 60° South and 60° North. The results of the analyses of these sets with the horizontal Rayleigh analysis are depicted in Figure 6.22. Unlike for other methods, the choice of the geographical location of the experiment has no significant effect on the dipole amplitude reconstruction for the horizontal Rayleigh method. For the latitude values simulated, the error of the amplitude reconstruction ranges between 0.30° and 0.34° (numbers given here are for the 'p&a+$\vartheta$' variant, the true value is 3%). The reconstruction of the dipole vector's declination performs better at location closer to the equator. The closer the experiment is located to the equator, the smaller is the range of declination values for which the dipole vector's azimuth performs a clockwise or anti-clockwise movement throughout the sidereal day (Fig. 6.8(c)), as this is the case if $|\delta_{\text{dipole}}| < |\beta|$. Outside this range, the azimuth value continuously oscillates around either the North or South direction (Fig. 6.8(a) and 6.8(e)). In the former case, the specific value of the declination influences the shape of the azimuth as a function of time. In the latter case, the range of the azimuth oscillation characterises the declination. For the standard configuration with $\delta_{\text{dipole}} = 30°$, which was used here, the latter is the case when the latitude $\beta$ is between $-30°$ and $30°$. The plots in Figure 6.22(b) show, that the fit algorithm can determine the declination with better precision in the latter of the two cases, thus when $|\beta| < |\delta_{\text{dipole}}|$. The opposite is the case for the reconstruction of the dipole vector's right ascension, which determines the offset of the specific azimuth function (shown in Figure 6.8) with respect to the time axis. The strictly monotonic shapes of the function allow for better determination of this offset than the oscillating ones.

As a result of the combination of these opposite behaviours, the precision of the combined direction reconstruction varies only mildly in the range between 8.6° and 9.9°.

### 6.4.2.5   Dipole Amplitude

The influence of the true value of the dipole amplitude on the reconstruction accuracies is shown in Figure 6.23. The corresponding plots for the established reconstruction methods have been discussed in Section 5.4.4 and displayed in Figure 5.11. As for the other methods,
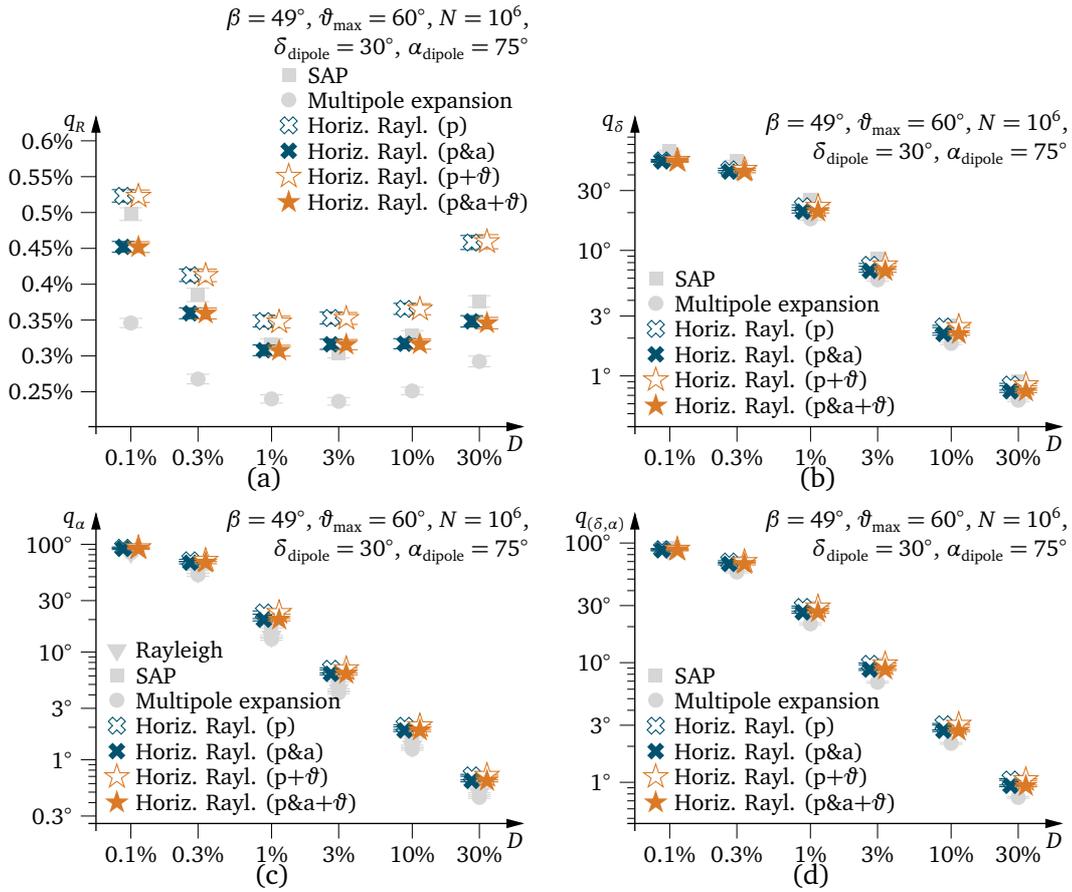
**Figure 6.23:** Horizontal Rayleigh analysis: reconstruction quality subject to dipole amplitude

a larger dipole amplitude results in a greater anisotropy signal and therefore allows for more precise reconstruction of the dipole parameters. The data points at $D = 3\%$ relate to the standard simulation configuration, for which the performance of the various methods has already been discussed. The situation for the various other dipole amplitudes is essentially the same: the horizontal Rayleigh method ('p&a+$\vartheta$') performs the amplitude reconstruction similarly well as the SAP method, is slightly better than the SAP method for declination reconstruction, but slightly worse for right ascension reconstruction. The dependency of the accuracies on the strength of the dipole is for the horizontal Rayleigh analysis very much the same as for the other methods, for which it has been discussed in Section 5.4.4. The saturation effect for the errors of the two directional parameters in case of very low anisotropy signals causes not only SAP and multipole expansion method to achieve the same accuracy, but also the horizontal Rayleigh method with all its variants. However, this is not really a remarkable outcome, as the errors are indeed so large that the results delivered by the methods are basically arbitrary. Only those simulations with dipole amplitudes of at least 1% (other parameters are given by the standard configuration, notably the number of events amounts to 1 million) yielded errors for the amplitude reconstruction, that are considerably lower than the true amplitude value. One peculiarity of the 'p' and 'p+$\vartheta$' variants can be observed in Figure 6.23(a): these extract the dipole amplitude from the amount of scatter in the reconstructed Ralyeigh phases per time bin (as in Figure 6.9(a)). In case of very large dipole amplitudes, the scatter is very narrow and the resulting absolute error of the amplitude determination is larger than for smaller amplitudes. The two variants, that do not utilise the reconstructed Rayleigh amplitudes in the
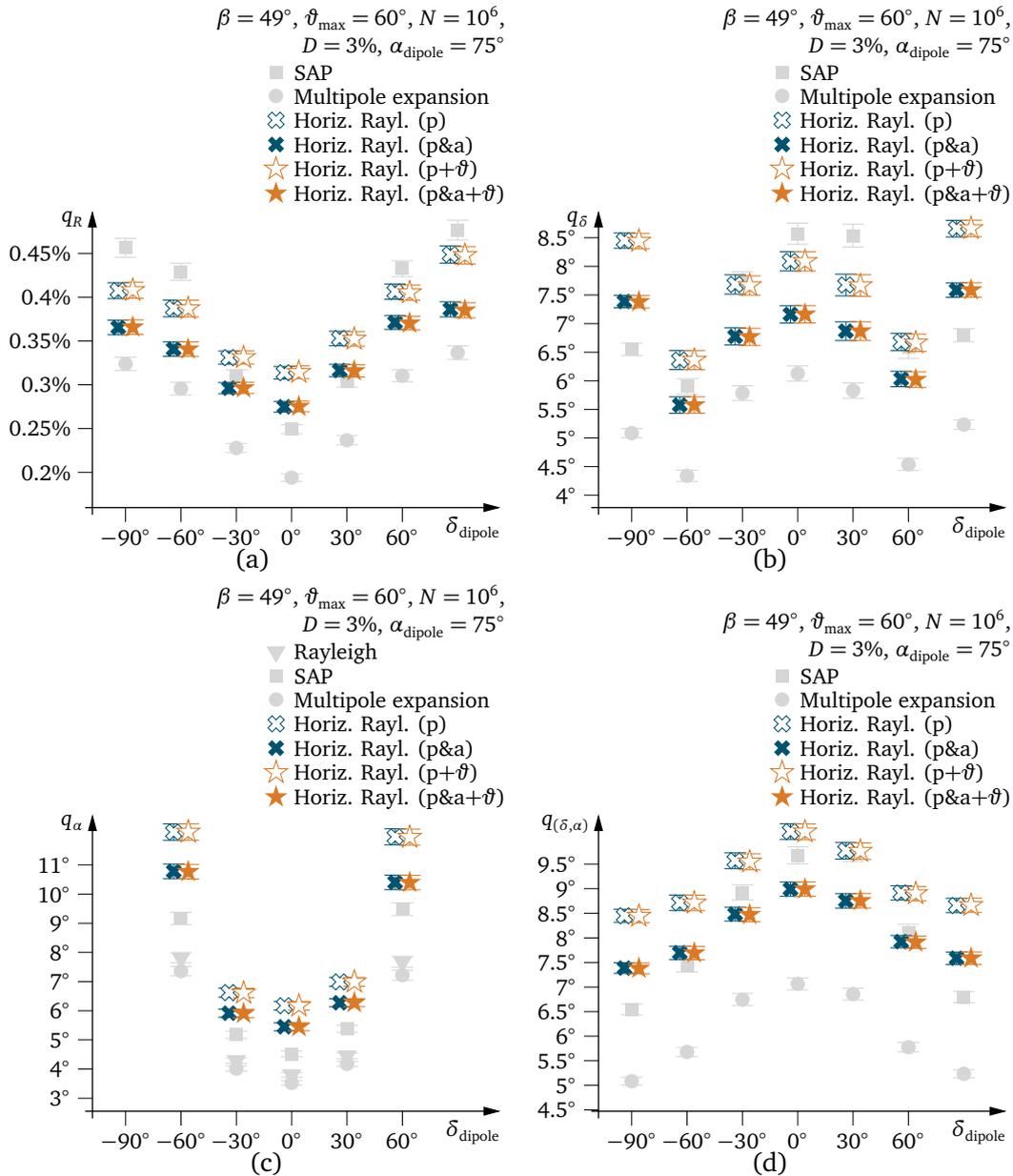
**Figure 6.24:** Horizontal Rayleigh analysis: reconstruction quality subject to dipole declination

individual time bins, perform here considerably worse. A similar effect is seen for the lowest dipole amplitude, but it is not statistically significant.

To summarise, the impact of the true dipole amplitude on the reconstruction accuracies is very similar for the horizontal Rayleigh method as compared to the established methods.

### 6.4.2.6 Dipole Declination

Figure 6.24 shows the results of the simulations with various values of the dipole declination. The behaviour of the Rayleigh, SAP and multipole expansion methods has been discussed in Section 5.4.5 and depicted in Figure 5.12. The influence of the dipole declination on the horizontal Rayleigh method is largely the same as on the other methods: the reconstruction of the
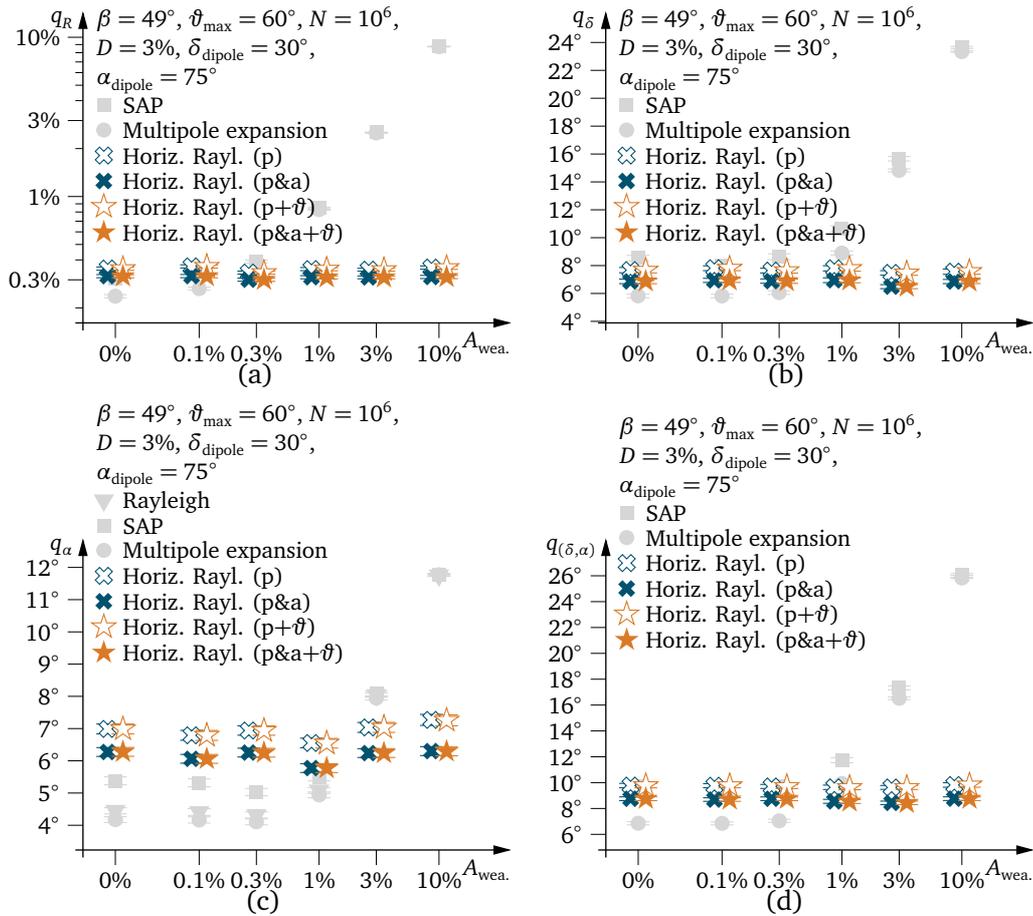
**Figure 6.25:** Horizontal Rayleigh analysis: reconstruction quality subject to spurious rate variation

dipole amplitude works best for equatorial dipoles, whereas the reconstruction of the dipole direction performs best with polar dipoles. However, the differences are generally not very large, and the horizontal Rayleigh method appears to be even more balanced. Over the full declination range from South to North Pole, the reconstruction error of the dipole amplitude (with the 'p&a+$\vartheta$' variant) varies only between 0.28% and 0.39% (the true value is 3%). The overall error of the direction determination ranges between 7.4° for polar dipoles and 9.0° for equatorial dipoles. Over the whole range of declination values, the horizontal Rayleigh analysis performs slightly worse than the multipole expansion method. It delivers results comparably good as those of the SAP method: of these two methods each one outperforms the other for certain ranges of the dipole declination.

To summarise, the impact of the dipole vector's declination value on the reconstruction quality is very similar for all methods involved. The general tendency that the horizontal Rayleigh method performs similarly well as the SAP method, and hence slightly worse than the multipole expansion method, is also valid here.

### 6.4.2.7  Rate Variations Due To Metereological Effects

The effects of spurious variations of the measurement rate, induced e.g. by metereological effects, have been investigated in Section 5.5.2. For a precise description of the nature of these effects and the way they are simulated, see the discussion there. The results for the

Rayleigh, SAP and multipole expansion methods have been presented in Figure 5.16. The same data sets were also analysed with the four variants of the horizontal Rayleigh method. The obtained reconstruction accuracies (Fig. 6.25), reveal a major advantage of the horizontal Rayleigh method: weather effects, as they have been defined here, do not influence the dipole reconstruction at all. The Monte Carlo code simulates the weather effect in the form of a harmonic variation of the event rate with sidereal time, of which $A_{\text{weather}}$ denotes the amplitude. When performing the analysis with any of the established methods, the effect is, that parts of the right ascension range are overrepresented in the data set, while others are underrepresented. While this is a purely experimental effect, the dipole reconstruction methods hold the cosmic ray flux distribution responsible for the inequality. Consequently, an artificial anisotropy is seen, which interferes with and superposes the actual cosmic ray flux distribution. For the horizontal Rayleigh method, on the other hand, any kind of variation of the event rate, whether it is caused by spurious effects or by actual anisotropy, merely affects the number of events entering the subset of data for the current sidereal time. Such variations do not influence the horizontal Rayleigh amplitudes or phases obtained for the various subsets. The number of events in a subset determines the spread of amplitude and phase in the subset. However, the implementation of the horizontal Rayleigh method keeps track of the number of events in each subset, and accounts correctly for the spread.

In summary, variations of the event rate, even if the cause of spurious metereological effects, do not affect the performance of the horizontal Rayleigh analysis.

### 6.4.2.8 Angular Resolution

A series of Monte Carlo simulations was conducted in order to examine the effect of limited angular resolution of the experiment. These have been the subject of Section 5.5.3, where the results for the established methods have been discussed, as shown in Figure 5.17. The results for the horizontal Rayleigh methods are depicted in Figure 6.26. As for the other methods, the effect of limited accuracy for the reconstruction of individual air showers' arrival directions has no effect on the dipole reconstruction. The plots show the results for the standard configuration ($\Delta = 0°$) and for four different values for the angular resolution $\Delta$, in the relevant range between $0.1°$ and $3°$. The reconstruction qualities, obtained from the Monte Carlo data sets with simulated angular resolution effect, are always compatible with those of the standard configuration, which assumes perfectly precise air shower reconstruction.

### 6.4.2.9 Inclination Dependent Efficiency Defect

The implications of an inclination dependent efficiency defect have been discussed in Section 5.5.4 and illustrated in Figure 5.19. It has been shown, that such an effect can seriously degrade the dipole reconstruction and introduce large biases. Figure 6.27 contains the corresponding plots for the horizontal Rayleigh analysis. As can be seen in that figure, such an efficiency deficit only leads to a mild decrease of accuracy, when the analysis is carried out with the horizontal Rayleigh method. The bad quality values for the other reconstruction methods do not arise from large statistical fluctuations but from systematic deviations. These substantial deviations do not occur in the case of the horizontal Rayleigh analysis. With one exception, all parameters match their respective true values on average, when obtained with the horizontal Rayleigh method. The mentioned exception is the amplitude reconstruction with the 'p' and 'p&a' variants. These variants assume full efficiency for the relation between azimuthal anisotropy amplitudes and the global dipol amplitude. If this assumption is false, it may affect the amplitude estimate. In case of lacking efficiency at high inclination, like it was simulated
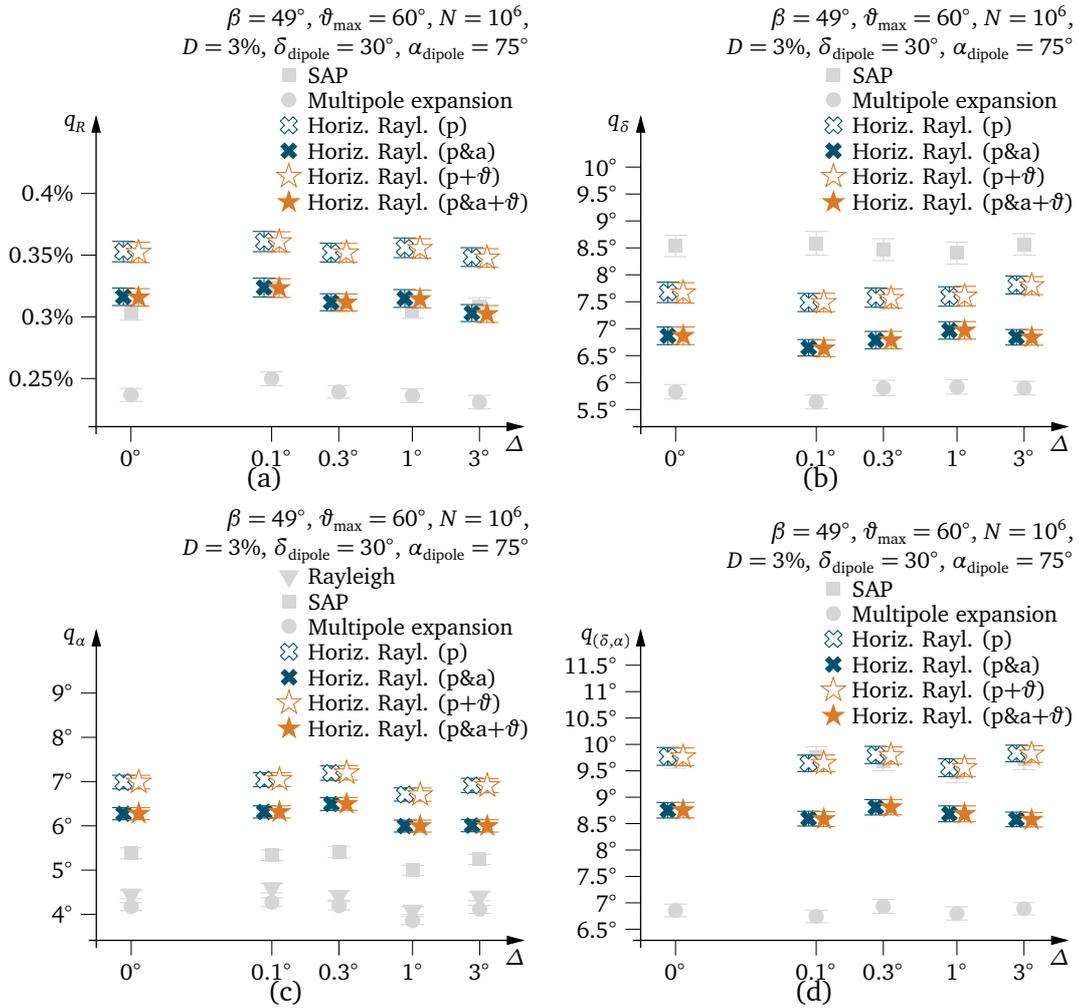
**Figure 6.26:** Horizontal Rayleigh analysis: reconstruction quality subject to the experiment's angular resolution

here, this circumstance leads to an underestimation of the amplitude: for $\vartheta_{\text{f.e.}} = 30°$, the mean reconstructed amplitude amounts to 2.2%, instead of the true value of 3%. By utilising the air showers' reconstructed zenith angles, the remaining two variants ('p+$\vartheta$' and 'p&a+$\vartheta$') can go without implicitly assuming full efficiency. As a result, these two variants do not underestimate the amplitude. They produce a negligible overestimation, with a maximum amplitude of 3.09%. The deviation is much smaller than the statistical fluctuations of the amplitude reconstruction. The reconstruction of the direction parameters is unbiased in case of each of the four variants. Therefore, the limited accuracy of declination and right ascension reconstructions are caused by the statistical fluctuations alone. As can be seen in the corresponding plots, the efficiency defect leads to a very moderate increase of the declination error, but also to a noticeable degradation of the right ascension reconstruction. The reason for this increase of the width of statistical fluctuations can be explained by the effective narrowing of the field of view: in the most drastic case of $\vartheta_{\text{f.e.}} = 30°$, for instance, there are very few events with inclinations above 40° in the data set, and nearly none with $\vartheta > 50°$. It has been discussed in Section 6.4.2.3, that a narrower field of view leads to worse reconstruction quality. The decrease of quality observed here is another manifestation of that effect.

In the case of an experiment, that uses a zenith limit of 60°, full efficiency thresholds at
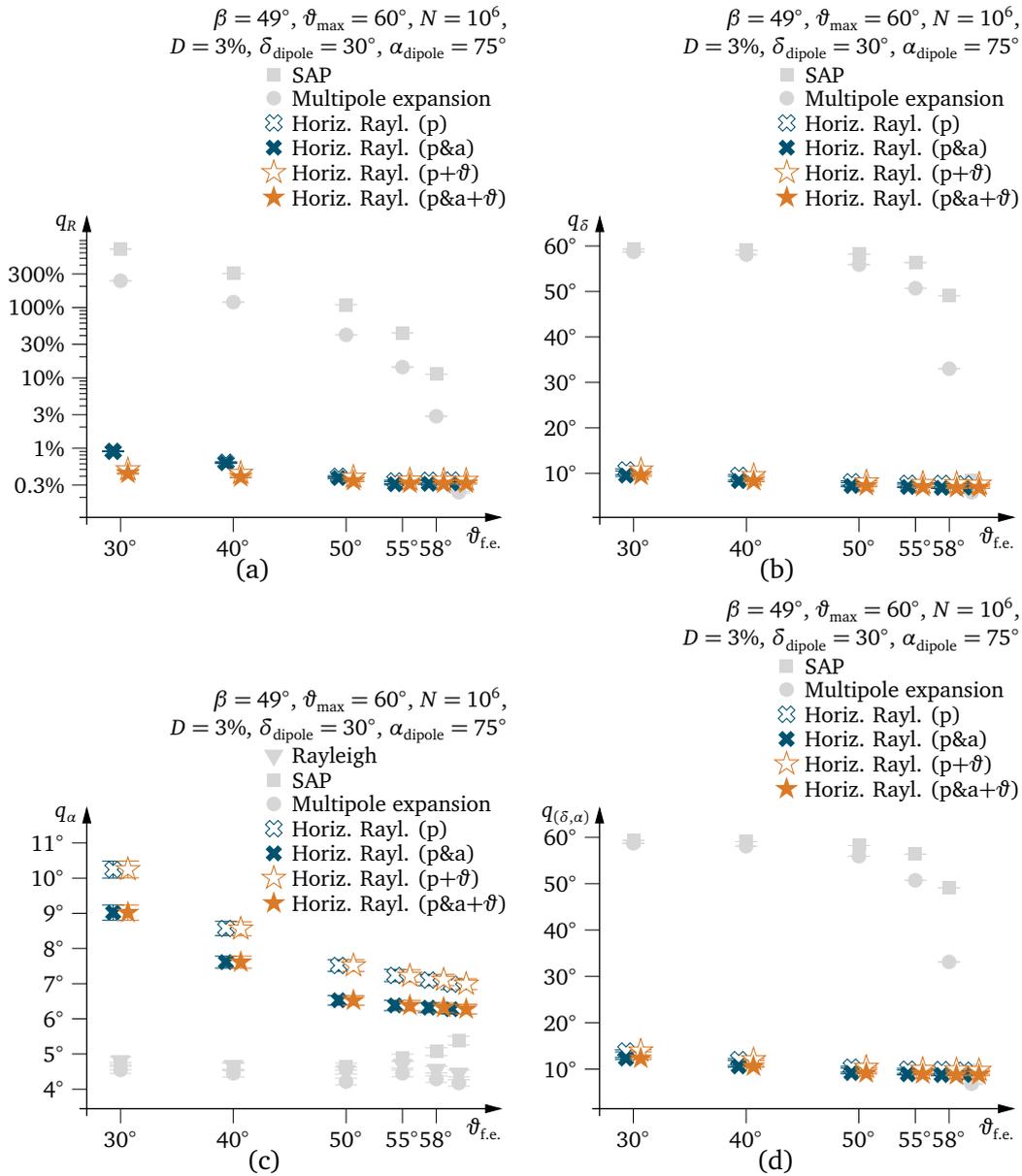
**Figure 6.27:** Horizontal Rayleigh analysis: reconstruction quality subject to the extent of the efficiency defect: the rightmost data point in each of the plots refers to the case of full efficiency for the whole field of view, thus for the absence of the efficiency defect.

zenith angles as low as $30°$ or $40°$ will not occur. An efficiency deficit of such an extent would certainly be noticed in any data set. These values were simulated only to demonstrate the robustness of the horizontal Rayleigh method. Less exaggerated cases, with $\vartheta_{\text{f.e.}} = 58°$ and $\vartheta_{\text{f.e.}} = 50°$ have been discussed in Section 5.5.4 with the aid of plots showing the distributions of reconstructed amplitude and declination values (Fig. 5.20). The corresponding plots for the horizontal Rayleigh method are shown in Figure 6.28. The plots in both figures have identical scales on the x-axes. Figures 6.28(a) to (d) illustrate the case of $\vartheta_{\text{f.e.}} = 58°$, whereas $\vartheta_{\text{f.e.}}$ is set to $50°$ in Figures 6.28(e) to (h). The 'p&a' variant was used to produce the plots in Figures 6.28(a), (b), (e) and (f). The remaining plots were produced with the 'p&a+$\vartheta$' variant. As can be seen, all distributions are well-shaped. The horizontal Rayleigh method

| Entries | 1000 |
|---|---|
| Sample mean | $2.994 \pm 0.0099$ |
| Sample std. dev. | $0.313 \pm 0.0070$ |
| $q$ | $0.312 \pm 0.0068$ |

(a) HR 'p&a', $\vartheta_{\text{f.e.}} = 58°$

| Entries | 1000 |
|---|---|
| Sample mean | $29.7 \pm 0.22$ |
| Sample std. dev. | $6.81 \pm 0.15$ |
| $q$ | $6.81 \pm 0.15$ |

(b) HR 'p&a', $\vartheta_{\text{f.e.}} = 58°$

| Sample mean | $3.018 \pm 0.010$ |
|---|---|
| Sample std. dev. | $0.315 \pm 0.0071$ |
| $q$ | $0.316 \pm 0.0069$ |

(c) HR 'p&a+$\vartheta$', $\vartheta_{\text{f.e.}} = 58°$

| Sample mean | $29.7 \pm 0.22$ |
|---|---|
| Sample std. dev. | $6.80 \pm 0.15$ |
| $q$ | $6.80 \pm 0.15$ |

(d) HR 'p&a+$\vartheta$', $\vartheta_{\text{f.e.}} = 58°$

| Sample mean | $2.789 \pm 0.0099$ |
|---|---|
| Sample std. dev. | $0.314 \pm 0.0070$ |
| $q$ | $0.378 \pm 0.0082$ |

(e) HR 'p&a', $\vartheta_{\text{f.e.}} = 50°$

| Sample mean | $29.6 \pm 0.23$ |
|---|---|
| Sample std. dev. | $7.22 \pm 0.16$ |
| $q$ | $7.23 \pm 0.18$ |

(f) HR 'p&a', $\vartheta_{\text{f.e.}} = 50°$

| Sample mean | $3.038 \pm 0.011$ |
|---|---|
| Sample std. dev. | $0.342 \pm 0.0076$ |
| $q$ | $0.344 \pm 0.0080$ |

(g) HR 'p&a+$\vartheta$', $\vartheta_{\text{f.e.}} = 50°$

| Sample mean | $29.5 \pm 0.23$ |
|---|---|
| Sample std. dev. | $7.23 \pm 0.16$ |
| $q$ | $7.24 \pm 0.18$ |

(h) HR 'p&a+$\vartheta$', $\vartheta_{\text{f.e.}} = 50°$

**Figure 6.28:** Horizontal Rayleigh method applied to data sets with efficiency defect

yields practically unbiased results, except for the moderate underestimations of the amplitudes produced by the variants not utilising zenith angle data, as the 'p&a' variant in Figures 6.28(e).

To summarise, the horizontal Rayleigh analysis provides an unbiased reconstruction of the dipole direction, independent of possible efficiency deficits. The 'p+$\vartheta$' and 'p&a+$\vartheta$' variants also provide an unbiased amplitude reconstruction, whereas the 'p' and 'p&a' may underestimate the strength of the dipole as a consequence of the efficiency defect. An efficiency defect may lead to larger statistical fluctuation, but that is a consequence of the effectively narrower field of view.

### 6.4.3 Summary

In this section, a new method for the reconstruction of the parameters of a dipole-like cosmic ray flux distribution has been proposed. The method divides the available data set into many subsets, each covering a small period of the sidereal day, typically one sidereal minute or less. Within these subsets, the Rayleigh analysis method is applied to the air showers' reconstructed azimuth angles. Amplitudes and phases of the first harmonic of the azimuthal anisotropy are obtained for each of the subsets. The parameters of the dipole-like flux distribution can be estimated by means of a log-likelihood fit, since the precise probability density functions are available, that describe the statistics of the Rayleigh amplitudes and phases at any time of the sidereal day on the basis of an assumed dipole configuration. The new method employs the Rayleigh analysis procedure in the horizontal coordinate system. Hence, it has been referred to as the "horizontal Rayleigh method".

The method has been discussed and its performance has been evaluated by means of extensive Monte Carlo simulation studies. It has been shown to work stably and to provide similar accuracy as the established methods. The Monte Carlo simulations also revealed a central advantage of the new method: the horizontal Rayleigh method appears to be vulnerable to neither spurious variations of the event rate nor a dependency of the experiment's sensitivity on shower inclination. The horizontal Rayleigh method does not implicitly assume constant measurement conditions or a precise shape of the field of view, other than demanding azimuthal symmetry. Corresponding effects have proven to be harmful to other reconstruction methods. In case of the horizontal Rayleigh method, they may influence the extent of statistical fluctuation, but they introduce no bias to the reconstruction.

## 6.5  Concluding Comparison of the Available Methods

Over the course of the last two chapters, a variety of experimental effects have been introduced and discussed at length. Some of them led to severe problems, others turned out to be irrelevant. These effects were always studied one at a time, in order to understand the influence of particular effects. It has also been shown, that combinations of different effects can cause additional problems. It is almost impossible to examine every possible combination of effects, experimental parameters and dipole configurations. In order to provide a concluding comparison of the methods discussed in this thesis, another series of Monte Carlo simulations was performed, the configuration of which was chosen to reflect a realistic scenario. The simulated dipole configuration and the experimental setup equal those of the standard configuration:

- a dipole distribution with an amplitude of 3%,

- the dipole vector points to $\delta_{\text{dipole}} = 30°$, $\alpha_{\text{dipole}} = 75°$,

- the experiment is located at $\beta = 49°$ Northern latitude,

- the field of view spans the zenith angle range up to a maximum value of $\vartheta_{\mathrm{max}} = 60°$,

- and data sets containing 1 million events each.

In contrast to the standard configuration, various experimental effects were taken into account. The severity of each of the effects is meant to reflect typical values for real data taking. However, these values are only a rough estimate, and depending on the experimental setup may differ substantially from the actual orders of magnitude:

- the simulated data taking was subject to occasional interruptions, and the sidereal day coverage used was again the one depicted in Figure 5.13, of the simulated cosmic ray flux,

- the resolution of the experiment's arrival direction reconstruction was simulated to be $1°$,

- full efficiency was only provided for shower inclinations up to $\vartheta_{\mathrm{f.e.}} = 58°$ (Fig. 5.18(e) for an illustration of the efficiency function),

- spurious rate variations led to a harmonic variation of the experiment's sensitivity with an amplitude of $A_{\mathrm{weather}} = 1\%$ in sidereal time.

1,000 data sets were generated with this configuration. The results are listed in Table 6.2. The SAP method overestimates the dipole amplitude almost by a factor of five. It suspects the dipole vector at declination $75°$ and right ascension $79.5°$. This adds up to an average deviation of the reconstructed dipole direction of $45°$.

The Rayleigh analysis was used for right ascension reconstruction only. The mean of the values obtained amounts to ca. $80°$, which is about half a degree worse than with the SAP method.

The multipole expansion method and the modified SAP method, with both direction and time based weighting, deliver practically identically results: the problems are the same as with the SAP method, but they tend to be less severe. The amplitude is overestimated by only a factor of two. The dipole declination is also shifted up North, but with a final value of $56°$ not as far as with the SAP method. The right ascension reconstructed by these methods is approximately the same as with the SAP method. The modified SAP method can gain one degree towards the true value when using time based weighting. The angular distance between the reconstructed dipole direction and the true one ends up at approximately $27°$.

While the mean values differ significantly from the true values, the amount of scatter in all these distributions is moderate. For example, the multipole expansion method reconstructs the dipole declination (true value is $30°$) on average as $56.4°$, with a standard deviation of only $2.3°$. I.e. the methods give significantly wrong results.

The horizontal Rayleigh method, on the other hand, reveals no noteworthy bias. The four variants yield a mean reconstructed amplitude between $3.02\%$ and $3.06\%$ (the true value is $3\%$). While this overestimation may be a statistically significant result of the Monte Carlo simulations, as the uncertainty of said mean values is only about $0.01\%$, its magnitude is too small to be relevant. The reconstructed dipole declination and right ascension values match their respective true values similarly well. In the absence of systematic deviations, the reconstruction quality is determined by the widths of the distributions of reconstructed values. Of the four variants, those utilising amplitude information (i.e. 'p&a' and 'p&a+$\vartheta$') generally yield more precise results. With the configuration used here, there is no observable difference between variants that do and do not use zenith angle data (as indicated by the '+$\vartheta$').

The standard deviations of reconstructed amplitude values are in the range between 0.29% and 0.33% (the true value is 3%). The distributions of reconstructed declination values have standard deviations of either 7.7° (for those variants that do not utilise horizontal Rayleigh amplitudes) or 6.9° (for those variants that do). Similarly, reconstructed dipole right ascension values scatter with standard deviations of 6.2° or 7.0°.

As a result, the horizontal Rayleigh methods is much more reliable (in terms of no bias) than other available methods. As a consequence, it offers the best reconstruction for dipole amplitude and declination in case of the simulation configuration used here. However, the right ascension reconstructions of the other methods outperform the horizontal Rayleigh method: the results of SAP, modified SAP and the multipole expansion methods are systematically off by about 5°, but the extent of statistical fluctuations are lower than for the horizontal Rayleigh method. The best right ascension reconstruction is achieved by the modified SAP method with time based weighting, with an overall reconstruction error of 5°.

However, all numbers quoted here do only apply to this specific series of Monte Carlo simulations. Other configurations will lead to different numbers. Of course, the conditions in real world experiments might differ substantially from the models and the assumptions made here. Still, the discussion in this section, and also the extensive Monte Carlo studies presented in this chapter and the previous chapter, should give the reader an impression of the strengths and the weaknesses of the various available reconstruction methods.

| Method | $R$ (true value: 3%) | | |
| | Sample mean | Sample std. dev. | $q$ |
|---|---|---|---|
| SAP | $14.686 \pm 0.014$ | $0.452 \pm 0.010$ | $11.695 \pm 0.014$ |
| MP | $6.451 \pm 0.0094$ | $0.297 \pm 0.0066$ | $3.464 \pm 0.0094$ |
| mSAP (d.b.w.) | $6.452 \pm 0.0094$ | $0.297 \pm 0.0066$ | $3.465 \pm 0.0094$ |
| mSAP (t.b.w.) | $6.455 \pm 0.0094$ | $0.297 \pm 0.0066$ | $3.468 \pm 0.0094$ |
| HR (p) | $3.031 \pm 0.010$ | $0.325 \pm 0.0073$ | $0.326 \pm 0.0068$ |
| HR (p&a) | $3.022 \pm 0.0093$ | $0.293 \pm 0.0066$ | $0.294 \pm 0.0066$ |
| HR (p+$\vartheta$) | $3.056 \pm 0.010$ | $0.328 \pm 0.0073$ | $0.332 \pm 0.0069$ |
| HR (p&a+$\vartheta$) | $3.047 \pm 0.0093$ | $0.295 \pm 0.0066$ | $0.299 \pm 0.0067$ |

| Method | $\delta$ (true value: 30°) | | |
| | Sample mean | Sample std. dev. | $q$ |
|---|---|---|---|
| SAP | $75.61 \pm 0.032$ | $1.02 \pm 0.023$ | $45.62 \pm 0.032$ |
| MP | $56.41 \pm 0.072$ | $2.26 \pm 0.051$ | $26.50 \pm 0.071$ |
| mSAP (d.b.w.) | $56.38 \pm 0.072$ | $2.27 \pm 0.051$ | $26.48 \pm 0.071$ |
| mSAP (t.b.w.) | $56.32 \pm 0.072$ | $2.27 \pm 0.051$ | $26.42 \pm 0.071$ |
| HR (p) | $29.6 \pm 0.24$ | $7.66 \pm 0.17$ | $7.67 \pm 0.17$ |
| HR (p&a) | $29.6 \pm 0.22$ | $6.90 \pm 0.15$ | $6.90 \pm 0.15$ |
| HR (p+$\vartheta$) | $29.6 \pm 0.24$ | $7.66 \pm 0.17$ | $7.67 \pm 0.17$ |
| HR (p&a+$\vartheta$) | $29.6 \pm 0.22$ | $6.90 \pm 0.15$ | $6.91 \pm 0.15$ |

| Method | $\alpha$ (true value: 75°) | | |
| | Sample mean | Sample std. dev. | $q$ |
|---|---|---|---|
| Rayl. | $79.97 \pm 0.11$ | $3.38 \pm 0.076$ | $6.01 \pm 0.095$ |
| SAP | $79.51 \pm 0.12$ | $3.89 \pm 0.087$ | $5.96 \pm 0.11$ |
| MP | $79.88 \pm 0.10$ | $3.18 \pm 0.071$ | $5.82 \pm 0.090$ |
| mSAP (d.b.w.) | $79.72 \pm 0.10$ | $3.18 \pm 0.071$ | $5.69 \pm 0.089$ |
| mSAP (t.b.w.) | $78.78 \pm 0.10$ | $3.17 \pm 0.071$ | $4.94 \pm 0.086$ |
| HR (p) | $74.8 \pm 0.22$ | $7.04 \pm 0.16$ | $7.03 \pm 0.17$ |
| HR (p&a) | $74.7 \pm 0.20$ | $6.17 \pm 0.14$ | $6.17 \pm 0.14$ |
| HR (p+$\vartheta$) | $74.9 \pm 0.22$ | $7.04 \pm 0.16$ | $7.04 \pm 0.17$ |
| HR (p&a+$\vartheta$) | $74.8 \pm 0.20$ | $6.18 \pm 0.14$ | $6.18 \pm 0.14$ |

| Method | $\Delta(\delta, \alpha)$ (true value: 0°) | | |
| | Sample mean | Sample std. dev. | $q$ |
|---|---|---|---|
| SAP | $45.71 \pm 0.033$ | $1.03 \pm 0.023$ | $45.72 \pm 0.033$ |
| MP | $26.72 \pm 0.072$ | $2.26 \pm 0.051$ | $26.82 \pm 0.071$ |
| mSAP (d.b.w.) | $26.68 \pm 0.072$ | $2.27 \pm 0.051$ | $26.78 \pm 0.071$ |
| mSAP (t.b.w.) | $26.55 \pm 0.072$ | $2.27 \pm 0.051$ | $26.64 \pm 0.071$ |
| HR (p) | $8.61 \pm 0.15$ | $4.65 \pm 0.10$ | $9.78 \pm 0.16$ |
| HR (p&a) | $7.69 \pm 0.13$ | $4.11 \pm 0.092$ | $8.72 \pm 0.14$ |
| HR (p+$\vartheta$) | $8.61 \pm 0.15$ | $4.65 \pm 0.10$ | $9.79 \pm 0.16$ |
| HR (p&a+$\vartheta$) | $7.70 \pm 0.13$ | $4.11 \pm 0.092$ | $8.73 \pm 0.14$ |

**Table 6.2:** Reconstruction quality for simulated data sets with a typical extent of experimental effects (for details see the text): 1,000 simulated data sets were analysed. Because the same data sets were used, the results for the different analysis methods are correlated.

# Chapter 7

# Summary and Conclusions

In this thesis, several methods for the data analysis of cosmic ray experiments with regard to large scale anisotropies, particularly to the reconstruction of dipole flux distributions, have been discussed. Existing methods have been explained, and new methods have been proposed. Both existing and new methods have been investigated and benchmarked by means of Monte Carlo simulated data sets. Special attention has been paid to examining the influence of experimental parameters. It has been shown, that certain effects, which are not unlikely to occur, can have a negative impact on the performance of the established methods, whereas the newly proposed methods have proven to be immune to these specific effects.

Anisotropy studies are generally based on the statistical evaluation of the arrival directions of cosmic ray particles, as detected and reconstructed in cosmic ray air shower experiments. The established methods discussed in this thesis—the Rayleigh analysis, the SAP method, and the multipole expansion method—all convert the arrival directions from local viewing directions (horizontal coordinates, zenith and azimuth angles) to a celestial coordinate system (equatorial coordinates, declination and right ascension angles). The frequency of observations from any given celestial direction is evaluated with respect to the exposure, which is the time-integrated detection area exposed towards that direction. The exposure as a function of declination and right ascension can be computed from the geometrical properties of the experiment (location, field of view) and the measurement times. At the first sight, it seems to be the natural choice to use the equatorial coordinate system, because the cosmic ray flux is fixed to the celestial sphere, and can therefore be regarded as a function of equatorial coordinates. On the other hand, the atmosphere and the experiment are part of an earthbound system of reference. Experimental effects can be described best by horizontal coordinates.

Given the exposure function, and assuming that the cosmic ray flux distribution has dipolar shape, the SAP method and the multipole expansion method (used as a dipole reconstruction method, thus going to first multipole order only) can reconstruct the dipole parameters. The Rayleigh method can only reconstruct the dipole vector's right ascension and the Rayleigh amplitude. The Rayleigh amplitude is loosely connected to the dipole amplitude, but is rather a measure for the evidence of the anisotropy. However, all these methods rely on the correctness of the calculated exposure. The calculation of the exposure has to take the shape of the field of view into account. Usually, a data selection cut—typically on some kind of estimated primary energy—is applied to the data set, that assures full detection and reconstruction efficiency for the whole field of view within the bounds of the cut. The calculation of the exposure is then based on the assumption of full efficiency. Another assumption often made is that of constant measurement conditions. Generally, measurement conditions are not constant, as e.g. the atmospheric conditions are subject to variations, most notably the day-night cycle. The hope is,

that these variations average out over time, so that any moment of the sidereal day is effectively equally well represented in the data set. The experimenter may also apply a correction, using recorded atmospheric data (for instance temperature, barometric pressure). It is questionable, whether such corrections can indeed free the data set completely of these variations. If either of these two assumptions—full efficiency and constant measurement conditions—is false, the calculated exposure is not correct, in the sense, that it does not reflect the experimental conditions properly.

A Monte Carlo generator has been developed for this thesis, which can produce simulated data sets, that reflect a given flux distribution and an experimental set-up. The experimental parameters can be chosen freely, and several experimental effects can be simulated. The available analysis methods have been thoroughly tested by means of Monte Carlo simulations. Under ideal circumstances, thus in absence of special experimental effects, all available methods reproduce the dipole parameters correctly. The accuracy is limited by statistical fluctuations. The choice of the dipole configuration (amplitude, orientation) and the experimental parameters (amount of statistics, location, size of the field of view) influence the width of the fluctuations. Generally, the multipole expansion method provides more accurate results than the SAP method and the Rayleigh analysis (the latter only yields the dipole right ascension). The situation is much different, when either of the aforementioned experimental effects (an efficiency deficit or varying sensitivity) are simulated: the tested methods produce severely biased results. They see phantom dipoles, that arise from the comparison of the data set with an exposure function, which does not correctly reflect the experimental circumstances. These artificial dipoles interfere with the real ones and—depending on the strength of the effect—may dominate the results. A typical symptom of this problem is, that dipoles are falsely reconstructed as pointing very close to either the North or the South Pole of the equatorial coordinate system.

In this thesis, four new ideas concerning dipole reconstruction have been discussed: two of them are modifications of the existing methods, the remaining two are completely new methods.

Firstly, an alternative way for weighting individual events in the Rayleigh analysis has been proposed. The weighting is needed to correct for different coverages of right ascension regions. The conventional weighting is based on a function of the reconstructed arrival directions and uses the calculated exposure functions. The proposed alternative uses weighting factors as a function of the sidereal time of day. It has been shown, that the performance of both methods is equally good. However, a false assumption of full efficiency for all shower inclinations can lead to erroneous results with the conventional weighting, where the newly proposed weighting yields correct results.

Secondly, a modification of the SAP method has been proposed. Once again, the modification concerns the weighting of individual air shower events. The original SAP method uses the inverse exposure function for weighting events, which means, that all directions within the visible sky contribute equally much to the resulting dipole vector estimator. Events coming from parts of the sky with very low exposure are drastically upweighted. As a consequence, the weighting factors may span several orders of magnitude, which is statistically unfavourable. The modification proposed uses the same weighting factors as for the Rayleigh analysis—either conventional direction based weights, or the newly proposed time based weights—which are of the order of one. As a result, the modified SAP method produces more accurate results. In fact, the results' widths of fluctuation have become identical to those of the multipole expansion method, which is related to the fact, that the modified SAP method is mathematically very similar to the multipole expansion method. It has been shown, that these two methods are the

same in the special case of an exposure function that does not vary with right ascension.

Thirdly, the Slice method has been introduced as a new method. It is based on dividing the visible sky into slices along the declination axis. The data set is separated into subsets accordingly, and the Rayleigh analysis is carried out for each of these subsets. The dipole parameters are determined by means of a log-likelihood fit of the Rayleigh amplitudes and phases obtained for the individual declination slices. However, it has been shown, that the Slice method is practically unusable, because large regions in the parameter space of dipole configurations yield almost identical likelihood values. The true configuration cannot reliably be determined by the fit procedure. Often it returns unphysically high amplitudes with dipole vectors pointing to the North or South Pole.

Fourthly, and most importantly, another new method has been proposed, that has been referred to as the horizontal Rayleigh method. It is based on the Rayleigh analysis formalism, but unlike the established Rayleigh analysis, it processes the arrival directions of recorded air showers in horizontal coordinates, thus in the local viewing directions at the location of the experiment. In doing so, it can take advantage of the symmetries in the local coordinate system: experimental effects and atmospheric conditions may vary for air showers with different inclinations. However, these influences should not discriminate between air showers arriving from different compass directions. Thus, azimuthal symmetry is assumed. Analysis methods, that convert the air showers' arrival directions into a sidereal coordinate system, can hardly profit from this symmetry. In order to see the dipole anisotropy in the horizontal coordinate system, the available data set is divided into many subsets, each spanning a short period of the sidereal day. Within each period, the dipole vector is constant even when represented in horizontal coordinates. The Rayleigh analyses yield the amplitudes of azimuthal anisotropy, and the phases, which can be identified with the dipole vector's azimuth coordinate. A log-likelihood fit is performed to obtain the dipole configuration from the results of the individual Rayleigh analyses. It has been shown, that this method reliably reconstructs the correct dipole parameters, except for experiments situated at the Earth's North or South Poles for geometrical reasons. The accuracy of the new method is similar to those of the established methods, depending on the particular dipole configuration and experimental properties. Typically, it performs comparably well with the SAP method.

The major advantage of the horizontal Rayleigh method is, that it even produces unbiased results when either or both of the aforementioned experimental effects—incomplete efficiency and varying sensitivity—is simulated. The new method is not influenced by these effects. This is no random coincidence, but a consequence of the fact, that its design is not based on the assumption of full efficiency or constant measurement conditions. The presence of such effects can have a moderate influence on the width of the fluctuation of the analysis results, but they introduce no systematic deviation.

As a consequence, the horizontal Rayleigh method can even be applied without any of those data selection cuts that aim at assuring full efficiency across the complete field of view. However, basic quality cuts need be applied, that can assure working reconstruction of showers' arrival directions and azimuthal symmetry. Still, without the demand of full efficiency up to the zenith angle limit, the analysis can be expanded towards lower primary energies and profit from larger statistics.

Four different variants of the horizontal Rayleigh method have been discussed. The one referred to in the text as the 'p&a+$\vartheta$' variant is the most advanced one, which has all the features mentioned here. Three other variants are intermediate stages of the development, which have been useful to trace back the impact of the design ideas.

Extensive Monte Carlo studies have been carried out to benchmark the new method and

compare its performance with those of the established methods. The horizontal Rayleigh method performs similarly well as the established methods under ideal measurement circumstances. Depending on the specific parameters, the statistical precision can be worse than that of other methods. However, the new method is not vulnerable to some relevant experimental effects. If such effects affect the data taking, the horizontal Rayleigh method yields substantially better results.

The horizontal Rayleigh method is a valuable new analysis method for the reconstruction of the parameters of a dipole-like cosmic ray flux distribution from a set of reconstructed arrival directions as recorded by a cosmic ray experiment. It is not meant to replace existing methods, but to complement them. Obtaining results compatible with both the established methods and the new horizontal Rayleigh method would be a strong indication that the properties of the experiment and the data set have been fully understood. Contradicting results would be evidence for the presence of experimental effects, that have not been considered correctly in the data analysis.

An important next step would be the application of the horizontal Rayleigh method to real experimental data, and the comparison of its results with those of other methods. Tracing back the reasons and the origins for the differences, if there were any, would certainly improve the understanding of the data. It might reveal shortcomings of the new method, and lead to its further development.

# Appendix A

# Definition of Spherical Harmonic Functions

The spherical harmonic functions as used in this thesis are constructed in a way to satisfy the following demands:

- They comply with the spherical coordinate system as used in this thesis. The latitude-like angle $\beta$ is measured from the equatorial plane, not from the North Pole of the coordinate system.

- They are purely real.

- They are normalised such that their square integrals equal $4\pi$.

The unit vector of the spherical coordinate system is defined as

$$\hat{e}(\beta, \lambda) = \begin{pmatrix} \cos\beta\cos\lambda \\ \cos\beta\sin\lambda \\ \sin\beta \end{pmatrix},$$

with the solid angle element given by

$$d\Omega = \cos\beta \, d\beta \, d\lambda.$$

The Legendre polynomials are defined as

$$P_n(x) = \frac{1}{2^n n!} \frac{d^n}{dx^n} \left[ (x^2 - 1)^n \right].$$

Based on these, the associated Legendre functions are given by

$$P_\ell^m(x) = (1 - x^2)^{m/2} \frac{d^m}{dx^m} \left( P_\ell(x) \right).$$

Finally, the spherical harmonic function of degree $\ell$ and order $m$ is given by

$$Y_{\ell m}(\beta, \lambda) = \begin{cases} \sqrt{2\ell + 1} \, P_\ell^0(\sin\beta) & (m = 0) \\[2ex] \sqrt{\dfrac{2(2\ell + 1)(\ell - m)!}{(\ell + m)!}} \cos(m\lambda) \, P_\ell^m(\sin\beta) & (m > 0) \\[2ex] -\sqrt{\dfrac{2(2\ell + 1)(\ell + m)!}{(\ell - m)!}} \sin(m\lambda) \, P_\ell^{-m}(\sin\beta) & (m < 0) \end{cases}.$$

This set of functions forms a complete orthonormal system on the unit sphere. Since all functions are purely real, complex conjugation needs not be taken into account in the following calculation:

$$
\begin{aligned}
\langle Y_{\ell m}, Y_{\ell' m'} \rangle &= \int \mathrm{d}\Omega \, Y_{\ell m} Y_{\ell' m'} \\
&= \int_{\beta=-\pi/2}^{\pi/2} \int_{\lambda=0}^{2\pi} \cos\beta \, \mathrm{d}\beta \, \mathrm{d}\lambda \, Y_{\ell m}(\beta,\lambda) \, Y_{\ell' m'}(\beta,\lambda) \\
&= 4\pi \delta_{\ell\ell'} \delta_{mm'} \, .
\end{aligned}
$$

| $Y_{\ell m}(\beta,\lambda)$ | $m=-1$ | $m=0$ | $m=1$ |
|---|---|---|---|
| $\ell=0$ | | $1$ | |
| $\ell=1$ | $\sqrt{3}\cos\beta\sin\lambda$ | $\sqrt{3}\sin\beta$ | $\sqrt{3}\cos\beta\cos\lambda$ |
| $\ell=2$ | $\sqrt{15}\sin\beta\cos\beta\sin\lambda$ | $-\sqrt{5}\left(\dfrac{1}{2}-\dfrac{3}{2}\sin^2\beta\right)$ | $\sqrt{15}\sin\beta\cos\beta\cos\lambda$ |
| $\ell=3$ | $-\sqrt{\dfrac{7}{6}}\cos\beta\left(\dfrac{15}{2}\cos^2\beta-6\right)\sin\lambda$ | $-\sqrt{7}\sin\beta\left(\dfrac{3}{2}-\dfrac{5}{2}\sin^2\beta\right)$ | $-\sqrt{\dfrac{7}{6}}\cos\beta\left(\dfrac{15}{2}\cos^2\beta-6\right)\cos\lambda$ |

| | $m=-3$ | $m=-2$ | $m=2$ | $m=3$ |
|---|---|---|---|---|
| $\ell=2$ | | $\dfrac{1}{2}\sqrt{15}\cos^2\beta\sin 2\lambda$ | $\dfrac{1}{2}\sqrt{15}\cos^2\beta\cos 2\lambda$ | |
| $\ell=3$ | $\dfrac{5}{2}\sqrt{\dfrac{7}{10}}\cos^3\beta\sin 3\lambda$ | $\dfrac{1}{2}\sqrt{105}\cos^2\beta\sin\beta\sin 2\lambda$ | $\dfrac{1}{2}\sqrt{105}\cos^2\beta\sin\beta\cos 2\lambda$ | $\dfrac{5}{2}\sqrt{\dfrac{7}{10}}\cos^3\beta\cos 3\lambda$ |

**Table A.1:** Spherical harmonic functions up to degree three

# Appendix B

# An Unbiased Estimator for the Quality Measure

## B.1 Derivation of the Estimators

The quality estimator $q^2$ has been defined in Section 5.3.1 as the mean square deviation of a reconstructed quantity $x$ from its true value $x_{\text{true}}$:

$$q^2 = \overline{(x - x_{\text{true}})^2}.$$

It is identical to the second algebraic moment $\mu'_2$ of the random variable $x - x_{\text{true}}$. The $r$-th algebraic moment is defined as:

$$\mu'_r = \overline{(x - x_{\text{true}})^r} = \mathrm{E}\left[(x - x_{\text{true}})^r\right].$$

The $\mu'_r$ denote the algebraic moments of the true distribution. For a given sample of $N$ observations $x_i$, the sample moments can be computed numerically:

$$m'_r = \frac{1}{N}\sum_{i=1}^{N}(x - x_{\text{true}})^r.$$

The sample moments are unbiased estimators for the moments of the underlying distribution:

$$\mathrm{E}\left[m'_r\right] = \mathrm{E}\left[\frac{1}{N}\sum_{i=1}^{N}(x - x_{\text{true}})^r\right] = \frac{1}{N}N \cdot \mathrm{E}\left[(x - x_{\text{true}})^r\right] = \mu'_r.$$

The expectation values of the squares of the sample moments can be calculated as follows:

$$\mathrm{E}\left[m'_r{}^2\right] = \mathrm{E}\left[\left(\frac{1}{N}\sum_{i=1}^{N}(x - x_{\text{true}})^r\right)^2\right] = \mathrm{E}\left[\frac{1}{N}\sum_{i=1}^{N}\frac{1}{N}\sum_{j=1}^{N}(x_i - x_{\text{true}})^r \cdot (x_i - x_{\text{true}})^r\right]$$

$$= \frac{1}{N^2}\cdot\left(\mathrm{E}\left[\sum_{i=1}^{N}(x_i - x_{\text{true}})^{2r}\right] + \mathrm{E}\left[\sum_{i=1}^{N}\sum_{j\neq i}(x_i - x_{\text{true}})^r \cdot (x_j - x_{\text{true}})^r\right]\right)$$

$$= \frac{1}{N^2}\cdot\left(N \cdot \mathrm{E}\left[(x - x_{\text{true}})^{2r}\right] + N \cdot (N-1)\cdot \mathrm{E}\left[(x - x_{\text{true}})^r\right]^2\right)$$

$$= \frac{1}{N^2} \cdot \left( N \cdot \mu'_{2r} + N \cdot (N-1) \cdot \mu'^{2}_r \right) = \frac{1}{N} \mu'_{2r} + \frac{N-1}{N} \mu'^{2}_r.$$

The variance of the estimator for $q^2$, $m'_2$, can be calculated as follows:

$$\mathrm{V}\left[ m'_2 \right] = \mathrm{E}\left[ \left( m'_2 - \mathrm{E}\left[ m'_2 \right] \right)^2 \right] = \mathrm{E}\left[ (m'_2 - \mu'_2)^2 \right] = \mathrm{E}\left[ m'^{2}_2 - 2 m'_2 \mu'_2 + \mu'^{2}_2 \right]$$

$$= \mathrm{E}\left[ m'^{2}_2 \right] - 2\mu'_2 \mathrm{E}\left[ m'_2 \right] + \mu'^{2}_2 = \frac{1}{N}\mu'_4 + \frac{N-1}{N}\mu'^{2}_2 - 2\mu'^{2}_2 + \mu'^{2}_2 = \frac{1}{N}\left( \mu'_4 - \mu'^{2}_2 \right)$$

Thus, the variance of the estimator for $q^2$ depends on the fourth and the second algebraic moment of the underlying distribution. Since these moments are unknown, an estimator is needed that can be computed from a sample. The sought-after estimator is given by $(m'_4 - m'^{2}_2)/(N-1)$, as it can be shown that its expectation value turns out to be the variance of $m'_2$:

$$\mathrm{E}\left[ \frac{1}{N-1} \cdot \left( m'_4 - m'^{2}_2 \right) \right] = \frac{1}{N-1} \cdot \left( \mu'_4 - \mathrm{E}\left[ m'^{2}_2 \right] \right)$$

$$= \frac{1}{N-1} \cdot \left( \mu'_4 - \left( \frac{1}{N}\mu'_4 + \frac{N-1}{N}\mu'^{2}_2 \right) \right) = \frac{1}{N}\left( \mu'_4 - \mu'^{2}_2 \right) = \mathrm{V}\left[ m'_2 \right].$$

## B.2 Summary

An unbiased estimator for the quality measure $q^2$ can be computed from a sample. The variance of the estimator yields the statistical error of the estimation, which is by definition the square root of the variance. The final result can be given as:

$$q^2_{\text{est}} = m'_2 \pm \sqrt{ \frac{1}{N-1} \cdot \left( m'_4 - m'^{2}_2 \right) }.$$

# Appendix C

# Tabulated Results of the Monte Carlo Studies

| Legend | |
|---|---|
| Rayl. | Rayleigh analysis |
| SAP | SAP method |
| MP | Multipole expansion method |
| HR (p) | Horizontal Rayleigh analysis, phase fit |
| HR (p&a) | Horizontal Rayleigh analysis, phase and amplitude fit |
| HR (p+$\vartheta$) | Horizontal Rayleigh analysis, phase fit, using reconstructed zenith angles |
| HR (p&a+$\vartheta$) | Horizontal Rayleigh analysis, phase and amplitude fit, using reconstructed zenith angles |
| Rayl. st. | Rayleigh analysis, steady data taking |
| Rayl. int. | Rayleigh analysis, occasionally interrupted data taking |
| SAP st. | SAP method, steady data taking |
| SAP int. | SAP method, occasionally interrupted data taking |
| MP st. | Multipole expansion method, steady data taking |
| MP int. | Multipole expansion method, occasionally interrupted data taking |

| Method | $\log_{10} N$ | $\bar{R}$ True | $\bar{R}$ Sample mean | $\bar{R}$ Sample std. dev. | $\bar{R}$ $q$ | $\bar{\delta}$ True | $\bar{\delta}$ Sample mean | $\bar{\delta}$ Sample std. dev. | $\bar{\delta}$ $q$ | $\bar{\alpha}$ True | $\bar{\alpha}$ Sample mean | $\bar{\alpha}$ Sample std. dev. | $\bar{\alpha}$ $q$ | $\Delta(\delta,\alpha)$ Sample mean | $\Delta(\delta,\alpha)$ Sample std. dev. | $\Delta(\delta,\alpha)$ $q$ |
|---|---|---|---|---|---|---|---|---|---|---|---|---|---|---|---|---|
| Rayl. | 3 | | | | | | | | | 75° | 74 ± 2.8 | 87 ± 2.0 | 87.4 ± 2.0 | | | |
| Rayl. | 3.5 | | | | | | | | | 75° | 73 ± 2.4 | 76.1 ± 1.7 | 76.1 ± 1.6 | | | |
| Rayl. | 4 | | | | | | | | | 75° | 74.6 ± 1.6 | 51.6 ± 1.2 | 51.6 ± 1.5 | | | |
| Rayl. | 4.5 | | | | | | | | | 75° | 75.4 ± 0.94 | 29.8 ± 0.67 | 29.7 ± 1.1 | | | |
| Rayl. | 5 | | | | | | | | | 75° | 74.8 ± 0.25 | 14.3 ± 0.32 | 14.3 ± 0.36 | | | |
| Rayl. | 5.5 | | | | | | | | | 75° | 74.99 ± 0.081 | 7.77 ± 0.17 | 7.77 ± 0.17 | | | |
| Rayl. | 6 | | | | | | | | | 75° | 74.97 ± 0.044 | 4.45 ± 0.099 | 4.45 ± 0.096 | | | |
| Rayl. | 6.5 | | | | | | | | | 75° | | 2.56 ± 0.057 | 2.55 ± 0.055 | | | |
| Rayl. | 7 | | | | | | | | | 75° | | 1.38 ± 0.031 | 1.38 ± 0.030 | | | |
| SAP | 3 | 3% | 16.2 ± 0.24 | 7.58 ± 0.17 | 15.2 ± 0.29 | 30° | −13.5 ± 1.5 | 48.9 ± 1.1 | 65.4 ± 0.94 | 75° | 72 ± 2.9 | 91 ± 2.0 | 90.9 ± 1.6 | 87.4 ± 1.2 | 36.7 ± 0.82 | 94.8 ± 1.1 |
| SAP | 3.5 | 3% | 9.15 ± 0.14 | 4.28 ± 0.096 | 7.49 ± 0.15 | 30° | −6.3 ± 1.5 | 48.5 ± 1.1 | 60.5 ± 0.95 | 75° | 75 ± 2.6 | 80.9 ± 1.8 | 80.8 ± 1.6 | 77.9 ± 1.1 | 36.2 ± 0.81 | 85.9 ± 1.1 |
| SAP | 4 | 3% | 5.78 ± 0.080 | 2.53 ± 0.057 | 3.76 ± 0.085 | 30° | 2.9 ± 1.5 | 46.6 ± 1.0 | 53.9 ± 0.96 | 75° | 71.1 ± 1.8 | 58.2 ± 1.3 | 58.3 ± 1.3 | 61.8 ± 1.0 | 32.6 ± 0.73 | 69.8 ± 1.1 |
| SAP | 4.5 | 3% | 3.93 ± 0.048 | 1.52 ± 0.034 | 1.78 ± 0.047 | 30° | 10.4 ± 1.2 | 37.8 ± 0.85 | 42.5 ± 0.86 | 75° | 74.1 ± 1.1 | 34.6 ± 0.77 | 34.6 ± 1.3 | 44.3 ± 0.78 | 24.7 ± 0.55 | 50.7 ± 0.87 |
| SAP | 5 | 3% | 3.28 ± 0.028 | 0.90 ± 0.020 | 0.94 ± 0.023 | 30° | 20.4 ± 0.82 | 25.8 ± 0.58 | 27.5 ± 0.68 | 75° | 75.6 ± 0.56 | 17.6 ± 0.39 | 17.6 ± 0.53 | 26.5 ± 0.53 | 16.7 ± 0.37 | 31.4 ± 0.64 |
| SAP | 5.5 | 3% | 3.052 ± 0.017 | 0.543 ± 0.012 | 0.545 ± 0.015 | 30° | 25.8 ± 0.46 | 14.7 ± 0.33 | 15.3 ± 0.39 | 75° | 74.7 ± 0.30 | 9.4 ± 0.20 | 9.4 ± 0.20 | 14.8 ± 0.29 | 9.1 ± 0.20 | 17.3 ± 0.35 |
| SAP | 6 | 3% | 3.016 ± 0.0096 | 0.304 ± 0.0068 | 0.304 ± 0.0066 | 30° | 28.5 ± 0.27 | 8.40 ± 0.19 | 8.5 ± 0.20 | 75° | 74.75 ± 0.17 | 5.38 ± 0.12 | 5.38 ± 0.12 | 8.43 ± 0.15 | 4.88 ± 0.12 | 9.74 ± 0.18 |
| SAP | 6.5 | 3% | 3.000 ± 0.0055 | 0.175 ± 0.0039 | 0.175 ± 0.0039 | 30° | 29.18 ± 0.15 | 4.79 ± 0.11 | 4.86 ± 0.12 | 75° | 75.05 ± 0.096 | 3.03 ± 0.068 | 3.03 ± 0.067 | 4.77 ± 0.088 | 2.79 ± 0.062 | 5.53 ± 0.11 |
| SAP | 7 | 3% | 2.996 ± 0.0033 | 0.104 ± 0.0023 | 0.104 ± 0.0023 | 30° | 29.73 ± 0.099 | 2.51 ± 0.056 | 2.52 ± 0.058 | 75° | 74.95 ± 0.052 | 1.64 ± 0.037 | 1.64 ± 0.036 | 2.53 ± 0.044 | 1.40 ± 0.031 | 2.89 ± 0.052 |
| MP | 3 | 3% | 12.90 ± 0.19 | 6.00 ± 0.13 | 11.6 ± 0.22 | 30° | 6.8 ± 1.6 | 49.2 ± 1.1 | 54.4 ± 1.0 | 75° | 73 ± 2.7 | 86.7 ± 1.5 | 87 ± 1.9 | 75.1 ± 1.1 | 36.3 ± 0.81 | 83.4 ± 1.1 |
| MP | 3.5 | 3% | 7.44 ± 0.11 | 3.43 ± 0.077 | 5.61 ± 0.13 | 30° | 11.9 ± 1.5 | 46.3 ± 1.0 | 49.7 ± 0.94 | 75° | 72 ± 2.4 | 74.5 ± 1.6 | 74.4 ± 1.7 | 65.6 ± 1.1 | 34.1 ± 0.76 | 73.9 ± 1.1 |
| MP | 4 | 3% | 4.96 ± 0.066 | 2.08 ± 0.047 | 2.86 ± 0.070 | 30° | 19.6 ± 1.3 | 40.4 ± 0.90 | 41.7 ± 0.87 | 75° | 74.7 ± 1.5 | 49.1 ± 1.1 | 49.1 ± 1.1 | 48.4 ± 0.85 | 27.0 ± 0.60 | 55.4 ± 0.97 |
| MP | 4.5 | 3% | 3.65 ± 0.039 | 1.23 ± 0.027 | 1.39 ± 0.036 | 30° | 23.4 ± 0.95 | 30.0 ± 0.67 | 30.7 ± 0.75 | 75° | 74.9 ± 0.85 | 26.9 ± 1.1 | 26.9 ± 1.1 | 31.6 ± 0.60 | 18.9 ± 0.42 | 36.8 ± 0.70 |
| MP | 5 | 3% | 3.20 ± 0.023 | 0.719 ± 0.016 | 0.747 ± 0.016 | 30° | 27.3 ± 0.57 | 17.9 ± 0.40 | 18.1 ± 0.44 | 75° | 75.6 ± 0.42 | 13.3 ± 0.30 | 13.3 ± 0.33 | 18.5 ± 0.34 | 10.7 ± 0.24 | 21.4 ± 0.40 |
| MP | 5.5 | 3% | 3.061 ± 0.013 | 0.414 ± 0.0093 | 0.419 ± 0.010 | 30° | 28.7 ± 0.33 | 10.4 ± 0.23 | 10.5 ± 0.25 | 75° | 74.8 ± 0.22 | 7.07 ± 0.15 | 7.07 ± 0.15 | 10.5 ± 0.19 | 6.10 ± 0.14 | 12.2 ± 0.23 |
| MP | 6 | 3% | 3.008 ± 0.0075 | 0.237 ± 0.0053 | 0.237 ± 0.0053 | 30° | 29.51 ± 0.18 | 5.81 ± 0.14 | 5.83 ± 0.14 | 75° | 74.78 ± 0.13 | 4.18 ± 0.090 | 4.18 ± 0.093 | 6.02 ± 0.10 | 3.29 ± 0.074 | 6.86 ± 0.12 |
| MP | 6.5 | 3% | 3.002 ± 0.0043 | 0.134 ± 0.0030 | 0.134 ± 0.0029 | 30° | 29.66 ± 0.11 | 3.38 ± 0.076 | 3.39 ± 0.081 | 75° | 74.98 ± 0.076 | 2.42 ± 0.054 | 2.42 ± 0.052 | 3.46 ± 0.063 | 1.99 ± 0.044 | 3.99 ± 0.073 |
| MP | 7 | 3% | 2.997 ± 0.0024 | 0.0774 ± 0.0017 | 0.0775 ± 0.0018 | 30° | 29.77 ± 0.056 | 1.78 ± 0.040 | 1.79 ± 0.037 | 75° | 74.99 ± 0.041 | 1.29 ± 0.028 | 1.29 ± 0.029 | 1.88 ± 0.031 | 0.97 ± 0.022 | 2.11 ± 0.033 |
| HR (p) | 3 | 3% | 18.2 ± 0.27 | 8.44 ± 0.19 | 17.3 ± 0.33 | 30° | 4.2 ± 1.4 | 45.0 ± 1.0 | 51.9 ± 0.95 | 75° | 77 ± 2.9 | 93 ± 2.1 | 93.1 ± 1.5 | 80.0 ± 1.2 | 37.1 ± 0.83 | 88.2 ± 1.1 |
| HR (p) | 3.5 | 3% | 10.64 ± 0.15 | 4.75 ± 0.11 | 9.00 ± 0.18 | 30° | 8.7 ± 1.4 | 43.4 ± 0.97 | 48.3 ± 0.95 | 75° | 73 ± 2.7 | 86 ± 1.9 | 86.4 ± 1.6 | 72.1 ± 1.2 | 36.7 ± 0.82 | 80.9 ± 1.2 |
| HR (p) | 4 | 3% | 6.52 ± 0.090 | 2.84 ± 0.064 | 4.52 ± 0.096 | 30° | 17.0 ± 1.3 | 34.4 ± 0.77 | 35.7 ± 0.83 | 75° | 73.4 ± 1.5 | 68.8 ± 1.5 | 68.8 ± 1.5 | 58.3 ± 1.0 | 32.3 ± 0.72 | 66.6 ± 1.1 |
| HR (p) | 4.5 | 3% | 4.34 ± 0.052 | 1.65 ± 0.037 | 2.13 ± 0.045 | 30° | 20.3 ± 1.1 | 23.2 ± 0.52 | | 75° | | 47.3 ± 1.1 | 47.4 ± 1.5 | 43.6 ± 0.81 | 25.7 ± 0.58 | 50.7 ± 0.95 |
| HR (p) | 5 | 3% | 3.16 ± 0.020 | 1.05 ± 0.023 | 1.14 ± 0.026 | 30° | 26.8 ± 0.73 | 13.2 ± 0.29 | 13.3 ± 0.32 | 75° | 74.9 ± 0.37 | 24.0 ± 0.54 | 24.0 ± 0.68 | 26.3 ± 0.49 | 15.6 ± 0.35 | 30.6 ± 0.61 |
| HR (p) | 5.5 | 3% | 3.031 ± 0.011 | 0.626 ± 0.014 | 0.646 ± 0.015 | 30° | 28.4 ± 0.42 | 7.65 ± 0.17 | | 75° | 74.9 ± 0.22 | 11.8 ± 0.26 | 11.8 ± 0.28 | 14.6 ± 0.25 | 7.99 ± 0.18 | 16.7 ± 0.30 |
| HR (p) | 6 | 3% | 3.010 ± 0.0060 | 0.352 ± 0.0079 | 0.353 ± 0.0083 | 30° | 29.72 ± 0.22 | 4.39 ± 0.10 | 4.40 ± 0.10 | 75° | 74.96 ± 0.13 | 6.99 ± 0.16 | 6.99 ± 0.16 | 8.60 ± 0.15 | 4.65 ± 0.10 | 9.77 ± 0.17 |
| HR (p) | 6.5 | 3% | 3.005 ± 0.0034 | 0.191 ± 0.0043 | 0.191 ± 0.0041 | 30° | | | | 75° | | | 3.97 ± 0.090 | 4.93 ± 0.083 | 2.62 ± 0.059 | 5.58 ± 0.096 |
| HR (p) | 7 | 3% | | 0.108 ± 0.0024 | 0.108 ± 0.0025 | 30° | 29.94 ± 0.068 | 2.41 ± 0.054 | 2.41 ± 0.051 | 75° | 74.99 ± 0.068 | 2.15 ± 0.048 | 2.14 ± 0.048 | 2.69 ± 0.045 | 1.42 ± 0.032 | 3.04 ± 0.048 |
| HR (pα) | 3 | 3% | 16.1 ± 0.23 | 7.32 ± 0.16 | 15.0 ± 0.28 | 30° | 4.3 ± 1.4 | 45.3 ± 1.0 | 52.1 ± 0.96 | 75° | 78 ± 2.9 | 93 ± 2.1 | 93.1 ± 1.5 | 79.6 ± 1.2 | 37.5 ± 0.84 | 88.0 ± 1.2 |
| HR (pα) | 3.5 | 3% | 9.44 ± 0.13 | 4.15 ± 0.093 | 7.60 ± 0.15 | 30° | 9.0 ± 1.3 | 42.7 ± 0.95 | 47.6 ± 0.95 | 75° | 72 ± 2.1 | 84.6 ± 1.9 | 84.6 ± 1.6 | 71.2 ± 1.1 | 31.6 ± 0.80 | 79.6 ± 1.1 |
| HR (pα) | 4 | 3% | 5.85 ± 0.080 | 2.50 ± 0.056 | 3.80 ± 0.082 | 30° | 17.1 ± 1.3 | 39.9 ± 0.89 | 33.6 ± 0.82 | 75° | 75.3 ± 1.4 | 64.0 ± 1.6 | 64.1 ± 1.5 | 57.1 ± 0.98 | 31.1 ± 0.70 | 65.6 ± 1.1 |
| HR (pα) | 4.5 | 3% | 4.04 ± 0.048 | 1.50 ± 0.034 | 1.83 ± 0.043 | 30° | 21.8 ± 1.0 | 32.6 ± 0.73 | 20.6 ± 0.52 | 75° | 75.5 ± 0.66 | 42.8 ± 0.96 | 42.8 ± 1.5 | 39.9 ± 0.77 | 24.5 ± 0.55 | 46.8 ± 0.94 |
| HR (pα) | 5 | 3% | 3.32 ± 0.029 | 0.93 ± 0.021 | 0.98 ± 0.021 | 30° | 27.3 ± 0.65 | 20.4 ± 0.46 | 11.8 ± 0.27 | 75° | 75.5 ± 0.66 | 20.9 ± 0.47 | 20.9 ± 0.81 | 23.2 ± 0.42 | 13.3 ± 0.30 | 26.7 ± 0.49 |
| HR (pα) | 5.5 | 3% | 3.122 ± 0.017 | 0.538 ± 0.012 | 0.551 ± 0.013 | 30° | 28.9 ± 0.37 | 11.7 ± 0.26 | 6.87 ± 0.16 | 75° | 74.8 ± 0.33 | 10.5 ± 0.24 | 10.5 ± 0.26 | 13.1 ± 0.22 | 6.94 ± 0.16 | 14.8 ± 0.25 |
| HR (pα) | 6 | 3% | 3.020 ± 0.010 | 0.316 ± 0.0071 | 0.316 ± 0.0071 | 30° | 29.6 ± 0.22 | 6.86 ± 0.15 | 3.93 ± 0.088 | 75° | 74.8 ± 0.20 | 6.27 ± 0.14 | 6.27 ± 0.14 | 7.76 ± 0.13 | 4.05 ± 0.091 | 8.75 ± 0.15 |
| HR (pα) | 6.5 | 3% | 3.009 ± 0.0055 | 0.191 ± 0.0043 | 0.191 ± 0.0039 | 30° | 29.75 ± 0.12 | 3.93 ± 0.088 | 2.13 ± 0.045 | 75° | 75.00 ± 0.12 | 3.59 ± 0.079 | 3.59 ± 0.079 | 4.05 ± 0.091 | 2.37 ± 0.053 | 5.01 ± 0.081 |
| HR (pα) | 7 | 3% | 3.002 ± 0.0031 | 0.098 ± 0.0022 | 0.098 ± 0.0021 | 30° | 29.92 ± 0.067 | 2.13 ± 0.048 | | 75° | 75.03 ± 0.059 | 1.87 ± 0.042 | 1.87 ± 0.040 | 2.37 ± 0.039 | 1.24 ± 0.028 | 2.68 ± 0.041 |
| HR (p+f) | 3 | 3% | 17.3 ± 0.24 | 7.73 ± 0.17 | 16.2 ± 0.28 | 30° | 4.4 ± 1.4 | 44.6 ± 1.0 | 51.5 ± 0.94 | 75° | 78 ± 2.9 | 92 ± 2.1 | 92.4 ± 1.6 | 79.2 ± 1.2 | 37.0 ± 0.83 | 87.4 ± 1.2 |
| HR (p+f) | 3.5 | 3% | 10.18 ± 0.14 | 4.49 ± 0.11 | 8.47 ± 0.16 | 30° | 9.5 ± 1.3 | 42.6 ± 0.95 | 47.2 ± 0.93 | 75° | 74 ± 2.7 | 84.2 ± 1.9 | 84.1 ± 1.6 | 70.9 ± 1.2 | 36.9 ± 0.83 | 79.9 ± 1.2 |
| HR (p+f) | 4 | 3% | 6.36 ± 0.087 | 2.75 ± 0.061 | 4.34 ± 0.094 | 30° | 18.0 ± 1.3 | 39.9 ± 0.89 | 41.7 ± 0.89 | 75° | 74.7 ± 1.5 | 67.5 ± 1.5 | 67.4 ± 1.4 | 57.0 ± 1.0 | 32.3 ± 0.72 | 65.5 ± 1.1 |
| HR (p+f) | 4.5 | 3% | 4.28 ± 0.052 | 1.64 ± 0.037 | 2.08 ± 0.044 | 30° | 20.5 ± 1.1 | 34.2 ± 0.76 | 35.4 ± 0.82 | 75° | 75.6 ± 0.75 | 46.1 ± 1.1 | 46.1 ± 1.4 | 43.0 ± 0.81 | 25.7 ± 0.57 | 50.1 ± 0.97 |
| HR (p+f) | 5 | 3% | 3.44 ± 0.033 | 1.04 ± 0.023 | 1.13 ± 0.026 | 30° | 26.8 ± 0.73 | 23.1 ± 0.52 | 23.3 ± 0.63 | 75° | 74.9 ± 0.37 | 23.8 ± 0.53 | 23.8 ± 0.67 | 26.2 ± 0.49 | 15.6 ± 0.35 | 30.5 ± 0.60 |
| HR (p+f) | 5.5 | 3% | 3.16 ± 0.020 | 0.625 ± 0.014 | 0.645 ± 0.015 | 30° | 28.4 ± 0.41 | 13.1 ± 0.29 | 13.2 ± 0.32 | 75° | 74.9 ± 0.22 | 11.8 ± 0.26 | 11.8 ± 0.28 | 14.6 ± 0.25 | 7.95 ± 0.18 | 16.6 ± 0.30 |
| HR (p+f) | 6 | 3% | 3.031 ± 0.011 | 0.351 ± 0.0079 | 0.352 ± 0.0083 | 30° | 29.4 ± 0.24 | 7.64 ± 0.17 | 7.66 ± 0.19 | 75° | 74.96 ± 0.13 | 6.99 ± 0.16 | 6.99 ± 0.15 | 8.60 ± 0.15 | 4.63 ± 0.10 | 9.76 ± 0.17 |
| HR (p+f) | 6.5 | 3% | 3.010 ± 0.0060 | 0.191 ± 0.0041 | 0.191 ± 0.0041 | 30° | 29.72 ± 0.14 | 4.39 ± 0.098 | 4.39 ± 0.10 | 75° | 74.99 ± 0.068 | 3.97 ± 0.090 | 3.97 ± 0.090 | 4.93 ± 0.083 | 2.62 ± 0.059 | 5.58 ± 0.095 |
| HR (p+f) | 7 | 3% | 3.005 ± 0.0034 | 0.107 ± 0.0024 | 0.108 ± 0.0025 | 30° | 29.94 ± 0.068 | 2.41 ± 0.054 | 2.41 ± 0.051 | 75° | 74.99 ± 0.068 | 2.14 ± 0.048 | 2.14 ± 0.048 | 2.69 ± 0.045 | 1.42 ± 0.032 | 3.04 ± 0.048 |
| HR (pα+f) | 3 | 3% | 15.3 ± 0.21 | 6.75 ± 0.15 | 14.0 ± 0.24 | 30° | 4.5 ± 1.4 | 45.0 ± 1.0 | 51.7 ± 0.94 | 75° | 76 ± 2.9 | 92 ± 2.1 | 91.9 ± 1.6 | 78.8 ± 1.2 | 36.9 ± 0.83 | 87.0 ± 1.2 |
| HR (pα+f) | 3.5 | 3% | 9.06 ± 0.13 | 3.98 ± 0.089 | 7.25 ± 0.15 | 30° | 10.0 ± 1.3 | 42.0 ± 0.94 | 46.5 ± 0.93 | 75° | 74 ± 2.6 | 83.5 ± 1.9 | 83.4 ± 1.6 | 69.7 ± 1.2 | 36.5 ± 0.82 | 78.7 ± 1.2 |
| HR (pα+f) | 4 | 3% | 5.70 ± 0.077 | 2.44 ± 0.055 | 3.64 ± 0.081 | 30° | 18.1 ± 1.2 | 39.5 ± 0.88 | 41.3 ± 0.87 | 75° | 73 ± 2.0 | 64.6 ± 1.4 | 64.7 ± 1.4 | 55.6 ± 0.98 | 30.9 ± 0.69 | 63.6 ± 1.1 |
| HR (pα+f) | 4.5 | 3% | 4.00 ± 0.047 | 1.49 ± 0.033 | 1.79 ± 0.042 | 30° | 21.8 ± 1.0 | 32.1 ± 0.72 | 33.1 ± 0.82 | 75° | 75.9 ± 0.66 | 41.7 ± 0.93 | 41.7 ± 1.4 | 39.2 ± 0.76 | 23.9 ± 0.54 | 45.9 ± 0.92 |
| HR (pα+f) | 5 | 3% | 3.32 ± 0.029 | 0.93 ± 0.021 | 0.98 ± 0.021 | 30° | 26.8 ± 0.73 | 20.3 ± 0.45 | 20.5 ± 0.52 | 75° | 74.9 ± 0.33 | 20.8 ± 0.47 | 20.8 ± 0.81 | 23.1 ± 0.42 | 13.2 ± 0.30 | 26.6 ± 0.49 |
| HR (pα+f) | 5.5 | 3% | 3.121 ± 0.017 | 0.537 ± 0.012 | 0.550 ± 0.013 | 30° | 28.8 ± 0.37 | 11.6 ± 0.26 | 11.7 ± 0.27 | 75° | 74.7 ± 0.20 | 10.5 ± 0.23 | 10.5 ± 0.24 | 13.0 ± 0.22 | 6.93 ± 0.15 | 14.7 ± 0.25 |
| HR (pα+f) | 6 | 3% | 3.020 ± 0.010 | 0.315 ± 0.0071 | 0.316 ± 0.0071 | 30° | 29.6 ± 0.22 | 6.86 ± 0.15 | 6.87 ± 0.16 | 75° | 75.00 ± 0.11 | 6.27 ± 0.14 | 6.28 ± 0.14 | 7.76 ± 0.13 | 4.05 ± 0.091 | 8.76 ± 0.15 |
| HR (pα+f) | 6.5 | 3% | 3.009 ± 0.0060 | 0.173 ± 0.0039 | 0.173 ± 0.0039 | 30° | 29.75 ± 0.12 | 3.92 ± 0.088 | 3.93 ± 0.088 | 75° | 75.00 ± 0.11 | 3.59 ± 0.080 | 3.59 ± 0.078 | 4.41 ± 0.075 | 2.37 ± 0.053 | 5.01 ± 0.081 |
| HR (pα+f) | 7 | 3% | 3.002 ± 0.0031 | 0.098 ± 0.0022 | 0.098 ± 0.0021 | 30° | 29.92 ± 0.067 | 2.13 ± 0.048 | 2.13 ± 0.045 | 75° | 75.02 ± 0.059 | 1.87 ± 0.042 | 1.87 ± 0.040 | 2.37 ± 0.039 | 1.24 ± 0.028 | 2.68 ± 0.041 |

**Table C.1:** Tabulated data for Figures 5.7 and 6.20: $\beta = 49°$, $\vartheta_{\max} = 60°$, $D = 3\%$, $\delta_{\text{dipole}} = 30°$, $\alpha_{\text{dipole}} = 75°$

| Method | $\theta_{max}$ True | $R$ Sample mean | $R$ Sample std. dev | $R$ q | $\delta$ True | $\delta$ Sample mean | $\delta$ Sample std. dev | $\delta$ q | $\alpha$ True | $\alpha$ Sample mean | $\alpha$ Sample std. dev | $\alpha$ q | $\Delta(\delta,\alpha)$ Sample mean | $\Delta(\delta,\alpha)$ Sample std. dev | $\Delta(\delta,\alpha)$ q |
|---|---|---|---|---|---|---|---|---|---|---|---|---|---|---|---|
| Rayl. | 10° | | | | | | | | 75° | 75.00 ± 0.15 | 4.78 ± 0.11 | 4.77 ± 0.12 | | | |
| Rayl. | 20° | | | | | | | | 75° | 75.02 ± 0.15 | 4.85 ± 0.11 | 4.84 ± 0.11 | | | |
| Rayl. | 30° | | | | | | | | 75° | 75.02 ± 0.15 | 4.73 ± 0.11 | 4.73 ± 0.11 | | | |
| Rayl. | 40° | | | | | | | | 75° | 74.86 ± 0.15 | 4.90 ± 0.11 | 4.90 ± 0.11 | | | |
| Rayl. | 50° | | | | | | | | 75° | 74.83 ± 0.14 | 4.50 ± 0.10 | 4.51 ± 0.099 | | | |
| Rayl. | 60° | | | | | | | | 75° | 74.78 ± 0.14 | 4.45 ± 0.099 | 4.45 ± 0.096 | | | |
| Rayl. | 70° | | | | | | | | 75° | 74.92 ± 0.14 | 4.27 ± 0.096 | 4.27 ± 0.092 | | | |
| Rayl. | 80° | | | | | | | | 75° | 75.12 ± 0.13 | 4.26 ± 0.095 | 4.26 ± 0.090 | | | |
| SAP | 10° | 3.48 ± 0.034 | 1.06 ± 0.024 | 1.16 ± 0.046 | 30° | 19.5 ± 1.0 | 32.2 ± 0.72 | 33.8 ± 0.75 | 75° | 74.98 ± 0.17 | 5.27 ± 0.12 | 5.27 ± 0.13 | 27.6 ± 0.63 | 20.1 ± 0.45 | 34.1 ± 0.75 |
| SAP | 20° | 3.126 ± 0.017 | 0.534 ± 0.012 | 0.548 ± 0.016 | 30° | 26.7 ± 0.55 | 17.4 ± 0.39 | 17.7 ± 0.46 | 75° | 74.96 ± 0.18 | 5.73 ± 0.13 | 5.73 ± 0.13 | 15.0 ± 0.34 | 10.7 ± 0.24 | 18.4 ± 0.44 |
| SAP | 30° | 3.046 ± 0.013 | 0.420 ± 0.0094 | 0.422 ± 0.011 | 30° | 27.0 ± 0.42 | 13.3 ± 0.30 | 13.6 ± 0.34 | 75° | 75.11 ± 0.16 | 5.07 ± 0.11 | 5.07 ± 0.11 | 11.8 ± 0.25 | 8.05 ± 0.18 | 14.3 ± 0.32 |
| SAP | 40° | 3.027 ± 0.011 | 0.355 ± 0.0079 | 0.356 ± 0.0087 | 30° | 28.4 ± 0.33 | 10.3 ± 0.23 | 10.4 ± 0.25 | 75° | 74.89 ± 0.18 | 5.63 ± 0.12 | 5.63 ± 0.12 | 9.89 ± 0.19 | 5.90 ± 0.13 | 11.5 ± 0.23 |
| SAP | 50° | 3.019 ± 0.010 | 0.328 ± 0.0073 | 0.328 ± 0.0077 | 30° | 28.4 ± 0.29 | 9.2 ± 0.21 | 9.3 ± 0.24 | 75° | 74.95 ± 0.17 | 5.44 ± 0.13 | 5.44 ± 0.13 | 8.89 ± 0.17 | 5.51 ± 0.12 | 10.5 ± 0.22 |
| SAP | 60° | 3.016 ± 0.0096 | 0.304 ± 0.0068 | 0.304 ± 0.0066 | 30° | 28.5 ± 0.27 | 8.40 ± 0.19 | 8.5 ± 0.20 | 75° | 74.75 ± 0.17 | 5.38 ± 0.12 | 5.38 ± 0.12 | 8.43 ± 0.15 | 4.88 ± 0.11 | 9.74 ± 0.13 |
| SAP | 70° | 3.003 ± 0.0097 | 0.306 ± 0.0068 | 0.306 ± 0.0073 | 30° | 28.3 ± 0.26 | 8.29 ± 0.19 | 8.5 ± 0.22 | 75° | 74.97 ± 0.17 | 5.33 ± 0.12 | 5.32 ± 0.12 | 8.31 ± 0.15 | 4.90 ± 0.11 | 9.6 ± 0.20 |
| SAP | 80° | 3.013 ± 0.010 | 0.328 ± 0.0073 | 0.328 ± 0.0077 | 30° | 28.7 ± 0.25 | 7.99 ± 0.18 | 8.1 ± 0.20 | 75° | 75.0 ± 0.17 | 6.07 ± 0.14 | 6.06 ± 0.14 | 8.43 ± 0.15 | 4.72 ± 0.11 | 9.66 ± 0.18 |
| MP | 10° | 3.35 ± 0.028 | 0.90 ± 0.020 | 0.96 ± 0.036 | 30° | 22.3 ± 0.89 | 28.1 ± 0.63 | 29.1 ± 0.69 | 75° | 75.02 ± 0.15 | 4.74 ± 0.11 | 4.74 ± 0.12 | 23.5 ± 0.56 | 17.6 ± 0.39 | 29.4 ± 0.68 |
| MP | 20° | 3.104 ± 0.015 | 0.476 ± 0.011 | 0.487 ± 0.013 | 30° | 27.7 ± 0.47 | 14.9 ± 0.33 | 15.1 ± 0.38 | 75° | 75.00 ± 0.15 | 4.79 ± 0.11 | 4.79 ± 0.10 | 12.9 ± 0.28 | 8.9 ± 0.20 | 15.6 ± 0.37 |
| MP | 30° | 3.054 ± 0.011 | 0.351 ± 0.010 | 0.355 ± 0.010 | 30° | 28.7 ± 0.34 | 10.6 ± 0.24 | 10.7 ± 0.26 | 75° | 75.02 ± 0.15 | 4.53 ± 0.10 | 4.53 ± 0.10 | 9.6 ± 0.20 | 6.17 ± 0.14 | 11.4 ± 0.25 |
| MP | 40° | 3.027 ± 0.0095 | 0.299 ± 0.0067 | 0.300 ± 0.0075 | 30° | 29.3 ± 0.25 | 8.00 ± 0.18 | 8.03 ± 0.19 | 75° | 74.86 ± 0.15 | 4.66 ± 0.11 | 4.66 ± 0.11 | 7.76 ± 0.14 | 4.54 ± 0.10 | 8.99 ± 0.17 |
| MP | 50° | 3.021 ± 0.0079 | 0.251 ± 0.0056 | 0.252 ± 0.0055 | 30° | 29.3 ± 0.22 | 6.94 ± 0.16 | 6.97 ± 0.16 | 75° | 74.85 ± 0.13 | 4.24 ± 0.097 | 4.24 ± 0.097 | 6.80 ± 0.13 | 3.97 ± 0.089 | 7.88 ± 0.15 |
| MP | 60° | 3.008 ± 0.0075 | 0.237 ± 0.0053 | 0.237 ± 0.0053 | 30° | 29.51 ± 0.18 | 5.81 ± 0.13 | 5.83 ± 0.14 | 75° | 74.78 ± 0.13 | 4.17 ± 0.093 | 4.18 ± 0.090 | 6.02 ± 0.10 | 3.29 ± 0.074 | 6.86 ± 0.12 |
| MP | 70° | 3.013 ± 0.0068 | 0.216 ± 0.0048 | 0.217 ± 0.0051 | 30° | 29.79 ± 0.17 | 5.37 ± 0.12 | 5.37 ± 0.12 | 75° | 74.82 ± 0.13 | 4.06 ± 0.091 | 4.06 ± 0.088 | 5.63 ± 0.098 | 3.10 ± 0.069 | 6.42 ± 0.11 |
| MP | 80° | 3.027 ± 0.0067 | 0.212 ± 0.0048 | 0.213 ± 0.0048 | 30° | 29.99 ± 0.15 | 4.88 ± 0.11 | 4.87 ± 0.11 | 75° | 75.0 ± 0.13 | 4.04 ± 0.090 | 4.04 ± 0.087 | 5.30 ± 0.089 | 2.80 ± 0.063 | 5.99 ± 0.095 |
| HR (p) | 10° | 4.05 ± 0.048 | 1.50 ± 0.034 | 1.83 ± 0.043 | 30° | 19.3 ± 1.0 | 33.1 ± 0.74 | 34.8 ± 0.83 | 75° | 79.3 ± 1.4 | 44.0 ± 0.98 | 44.2 ± 1.4 | 41.3 ± 0.78 | 24.8 ± 0.56 | 48.2 ± 0.94 |
| HR (p) | 20° | 3.29 ± 0.027 | 0.86 ± 0.019 | 0.91 ± 0.021 | 30° | 27.3 ± 0.62 | 19.8 ± 0.44 | 19.9 ± 0.48 | 75° | 73.7 ± 0.62 | 19.6 ± 0.44 | 19.6 ± 0.61 | 22.3 ± 0.41 | 12.9 ± 0.29 | 25.7 ± 0.47 |
| HR (p) | 30° | 3.139 ± 0.018 | 0.574 ± 0.013 | 0.591 ± 0.014 | 30° | 28.9 ± 0.43 | 13.5 ± 0.30 | 13.5 ± 0.31 | 75° | 75.0 ± 0.39 | 12.3 ± 0.29 | 12.3 ± 0.29 | 15.2 ± 0.25 | 8.03 ± 0.18 | 17.2 ± 0.28 |
| HR (p) | 40° | 3.060 ± 0.012 | 0.459 ± 0.011 | 0.464 ± 0.011 | 30° | 29.2 ± 0.33 | 10.5 ± 0.23 | 10.5 ± 0.25 | 75° | 74.3 ± 0.31 | 9.8 ± 0.22 | 9.9 ± 0.23 | 11.8 ± 0.20 | 6.46 ± 0.14 | 13.5 ± 0.23 |
| HR (p) | 50° | 3.060 ± 0.011 | 0.377 ± 0.0084 | 0.381 ± 0.0087 | 30° | 29.6 ± 0.28 | 8.8 ± 0.20 | 8.8 ± 0.21 | 75° | 74.9 ± 0.27 | 8.40 ± 0.19 | 8.39 ± 0.18 | 10.08 ± 0.17 | 5.35 ± 0.12 | 11.4 ± 0.19 |
| HR (p) | 60° | 3.039 ± 0.010 | 0.352 ± 0.0079 | 0.353 ± 0.0083 | 30° | 29.4 ± 0.24 | 7.65 ± 0.17 | 7.67 ± 0.19 | 75° | 74.9 ± 0.22 | 6.99 ± 0.16 | 6.99 ± 0.15 | 8.60 ± 0.15 | 4.65 ± 0.10 | 9.77 ± 0.15 |
| HR (p) | 70° | 3.031 ± 0.011 | 0.315 ± 0.0070 | 0.317 ± 0.0071 | 30° | 29.8 ± 0.22 | 7.01 ± 0.16 | 7.01 ± 0.17 | 75° | 74.7 ± 0.20 | 6.25 ± 0.14 | 6.26 ± 0.15 | 7.72 ± 0.14 | 4.31 ± 0.096 | 8.84 ± 0.15 |
| HR (p) | 80° | 3.048 ± 0.0097 | 0.308 ± 0.0069 | 0.311 ± 0.0067 | 30° | 29.8 ± 0.22 | 7.01 ± 0.16 | 7.01 ± 0.15 | 75° | 75.3 ± 0.19 | 6.07 ± 0.14 | 6.07 ± 0.14 | 7.71 ± 0.13 | 4.13 ± 0.092 | 8.75 ± 0.14 |
| HR (p&a) | 10° | 3.81 ± 0.044 | 1.38 ± 0.031 | 1.60 ± 0.036 | 30° | 21.5 ± 0.96 | 30.3 ± 0.68 | 31.5 ± 0.75 | 75° | 78.9 ± 1.2 | 37.5 ± 0.84 | 37.6 ± 1.3 | 37.1 ± 0.71 | 22.4 ± 0.50 | 43.3 ± 0.90 |
| HR (p&a) | 20° | 3.25 ± 0.024 | 0.754 ± 0.017 | 0.793 ± 0.018 | 30° | 28.0 ± 0.54 | 17.1 ± 0.38 | 17.2 ± 0.39 | 75° | 74.3 ± 0.52 | 16.6 ± 0.37 | 16.6 ± 0.42 | 19.4 ± 0.34 | 10.8 ± 0.24 | 22.2 ± 0.38 |
| HR (p&a) | 30° | 3.115 ± 0.016 | 0.517 ± 0.012 | 0.530 ± 0.013 | 30° | 29.0 ± 0.38 | 11.9 ± 0.27 | 11.4 ± 0.29 | 75° | 74.5 ± 0.28 | 10.9 ± 0.24 | 10.9 ± 0.24 | 13.4 ± 0.22 | 7.11 ± 0.16 | 15.1 ± 0.26 |
| HR (p&a) | 40° | 3.058 ± 0.013 | 0.410 ± 0.0092 | 0.444 ± 0.0095 | 30° | 29.5 ± 0.30 | 9.3 ± 0.21 | 9.4 ± 0.21 | 75° | 74.8 ± 0.20 | 8.7 ± 0.19 | 8.7 ± 0.20 | 10.55 ± 0.18 | 5.69 ± 0.13 | 12.03 ± 0.17 |
| HR (p&a) | 50° | 3.044 ± 0.011 | 0.341 ± 0.0078 | 0.343 ± 0.0078 | 30° | 29.6 ± 0.28 | 7.77 ± 0.17 | 7.78 ± 0.18 | 75° | 74.9 ± 0.24 | 7.32 ± 0.16 | 7.31 ± 0.16 | 8.80 ± 0.15 | 4.81 ± 0.11 | 10.03 ± 0.17 |
| HR (p&a) | 60° | 3.031 ± 0.011 | 0.316 ± 0.0071 | 0.316 ± 0.0071 | 30° | 29.5 ± 0.22 | 6.86 ± 0.15 | 6.87 ± 0.16 | 75° | 74.8 ± 0.18 | 6.27 ± 0.14 | 6.26 ± 0.15 | 7.76 ± 0.13 | 4.05 ± 0.091 | 8.75 ± 0.15 |
| HR (p&a) | 70° | 3.022 ± 0.0088 | 0.280 ± 0.0063 | 0.280 ± 0.0063 | 30° | 29.9 ± 0.20 | 6.33 ± 0.14 | 6.33 ± 0.15 | 75° | 74.7 ± 0.17 | 6.25 ± 0.14 | 6.28 ± 0.14 | 6.98 ± 0.12 | 3.78 ± 0.085 | 7.94 ± 0.14 |
| HR (p&a) | 80° | 3.038 ± 0.0085 | 0.270 ± 0.0060 | 0.273 ± 0.0058 | 30° | 29.7 ± 0.19 | 6.08 ± 0.14 | 6.08 ± 0.13 | 75° | 75.16 ± 0.17 | 5.40 ± 0.12 | 6.07 ± 0.14 | 6.77 ± 0.11 | 3.57 ± 0.080 | 7.65 ± 0.13 |
| HR (p+f) | 10° | 4.05 ± 0.048 | 1.38 ± 0.031 | 1.84 ± 0.043 | 30° | 19.3 ± 1.0 | 33.1 ± 0.68 | 34.8 ± 0.84 | 75° | 79.3 ± 1.4 | 44.0 ± 0.98 | 44.2 ± 1.5 | 41.3 ± 0.79 | 22.4 ± 0.50 | 48.2 ± 0.94 |
| HR (p+f) | 20° | 3.25 ± 0.027 | 0.86 ± 0.019 | 0.91 ± 0.021 | 30° | 27.3 ± 0.62 | 19.8 ± 0.44 | 19.9 ± 0.49 | 75° | 73.7 ± 0.62 | 19.6 ± 0.44 | 19.6 ± 0.63 | 19.4 ± 0.34 | 10.8 ± 0.24 | 25.7 ± 0.48 |
| HR (p+f) | 30° | 3.138 ± 0.018 | 0.574 ± 0.013 | 0.590 ± 0.014 | 30° | 28.9 ± 0.43 | 13.5 ± 0.30 | 13.5 ± 0.30 | 75° | 75.0 ± 0.39 | 12.3 ± 0.28 | 9.8 ± 0.23 | 15.2 ± 0.25 | 8.02 ± 0.18 | 17.2 ± 0.29 |
| HR (p+f) | 40° | 3.071 ± 0.015 | 0.459 ± 0.010 | 0.464 ± 0.011 | 30° | 29.2 ± 0.33 | 10.5 ± 0.23 | 10.5 ± 0.25 | 75° | 74.3 ± 0.31 | 8.39 ± 0.18 | 8.39 ± 0.23 | 11.8 ± 0.20 | 6.47 ± 0.14 | 13.5 ± 0.24 |
| HR (p+f) | 50° | 3.060 ± 0.012 | 0.376 ± 0.0084 | 0.381 ± 0.0087 | 30° | 29.6 ± 0.28 | 8.8 ± 0.20 | 8.8 ± 0.21 | 75° | 74.9 ± 0.27 | 6.99 ± 0.16 | 6.99 ± 0.15 | 10.07 ± 0.17 | 5.36 ± 0.12 | 11.4 ± 0.19 |
| HR (p+f) | 60° | 3.031 ± 0.011 | 0.351 ± 0.0079 | 0.352 ± 0.0083 | 30° | 29.4 ± 0.22 | 7.64 ± 0.17 | 7.66 ± 0.19 | 75° | 74.9 ± 0.22 | 6.26 ± 0.15 | 6.26 ± 0.15 | 8.60 ± 0.15 | 4.63 ± 0.10 | 9.76 ± 0.17 |
| HR (p+f) | 70° | 3.039 ± 0.010 | 0.315 ± 0.0070 | 0.317 ± 0.0071 | 30° | 29.8 ± 0.22 | 7.01 ± 0.17 | 7.01 ± 0.17 | 75° | 74.7 ± 0.17 | 6.26 ± 0.14 | 6.26 ± 0.15 | 7.73 ± 0.14 | 4.30 ± 0.096 | 8.85 ± 0.15 |
| HR (p+f) | 80° | 3.048 ± 0.0097 | 0.307 ± 0.0069 | 0.311 ± 0.0067 | 30° | 29.7 ± 0.19 | 7.01 ± 0.16 | 7.01 ± 0.15 | 75° | 75.3 ± 0.19 | 6.07 ± 0.14 | 6.07 ± 0.14 | 7.71 ± 0.13 | 4.12 ± 0.092 | 8.74 ± 0.14 |
| HR (p&a+f) | 10° | 3.81 ± 0.044 | 1.38 ± 0.031 | 1.59 ± 0.036 | 30° | 21.5 ± 0.96 | 30.3 ± 0.68 | 31.4 ± 0.74 | 75° | 78.6 ± 1.2 | 37.6 ± 0.84 | 37.7 ± 1.3 | 37.1 ± 0.71 | 22.4 ± 0.50 | 43.4 ± 0.90 |
| HR (p&a+f) | 20° | 3.25 ± 0.024 | 0.754 ± 0.017 | 0.793 ± 0.018 | 30° | 28.0 ± 0.54 | 17.1 ± 0.38 | 17.2 ± 0.40 | 75° | 74.2 ± 0.52 | 16.5 ± 0.37 | 16.6 ± 0.42 | 19.4 ± 0.34 | 10.8 ± 0.24 | 22.2 ± 0.39 |
| HR (p&a+f) | 30° | 3.114 ± 0.016 | 0.516 ± 0.012 | 0.528 ± 0.013 | 30° | 29.0 ± 0.37 | 11.8 ± 0.27 | 11.9 ± 0.29 | 75° | 74.8 ± 0.34 | 10.9 ± 0.24 | 10.9 ± 0.24 | 13.3 ± 0.23 | 7.12 ± 0.16 | 15.1 ± 0.26 |
| HR (p&a+f) | 40° | 3.058 ± 0.013 | 0.410 ± 0.0092 | 0.414 ± 0.0095 | 30° | 29.5 ± 0.25 | 9.4 ± 0.21 | 9.4 ± 0.21 | 75° | 74.5 ± 0.28 | 8.7 ± 0.19 | 8.7 ± 0.23 | 10.54 ± 0.18 | 5.71 ± 0.13 | 12.0 ± 0.20 |
| HR (p&a+f) | 50° | 3.042 ± 0.011 | 0.340 ± 0.0076 | 0.343 ± 0.0077 | 30° | 29.6 ± 0.20 | 7.79 ± 0.17 | 7.80 ± 0.18 | 75° | 74.9 ± 0.23 | 7.31 ± 0.16 | 7.31 ± 0.16 | 8.80 ± 0.15 | 4.83 ± 0.11 | 10.04 ± 0.17 |
| HR (p&a+f) | 60° | 3.020 ± 0.010 | 0.315 ± 0.0071 | 0.316 ± 0.0071 | 30° | 29.6 ± 0.20 | 6.86 ± 0.15 | 6.87 ± 0.15 | 75° | 74.7 ± 0.20 | 6.27 ± 0.14 | 6.28 ± 0.14 | 7.76 ± 0.13 | 4.05 ± 0.091 | 8.76 ± 0.091 |
| HR (p&a+f) | 70° | 3.022 ± 0.0088 | 0.280 ± 0.0063 | 0.280 ± 0.0063 | 30° | 29.9 ± 0.20 | 6.33 ± 0.14 | 6.33 ± 0.15 | 75° | 74.78 ± 0.18 | 5.56 ± 0.13 | 5.56 ± 0.13 | 6.98 ± 0.12 | 3.78 ± 0.085 | 7.94 ± 0.14 |
| HR (p&a+f) | 80° | 3.038 ± 0.0085 | 0.270 ± 0.0060 | 0.272 ± 0.0058 | 30° | 29.7 ± 0.19 | 6.07 ± 0.14 | 6.07 ± 0.13 | 75° | 75.16 ± 0.17 | 5.40 ± 0.12 | 5.40 ± 0.12 | 6.77 ± 0.11 | 3.57 ± 0.080 | 7.65 ± 0.12 |

**Table C.2:** Tabulated data for Figures 5.8 and 6.21: $\beta = 49°$, $N = 10^6$, $D = 3\%$, $\delta_{dipole} = 30°$, $\alpha_{dipole} = 75°$

| Method | $\vartheta_{max}$ | R True | R Sample mean | R Sample std. dev. | R q | $\delta$ True | $\delta$ Sample mean | $\delta$ Sample std. dev. | $\delta$ q | $\alpha$ True | $\alpha$ Sample mean | $\alpha$ Sample std. dev. | $\alpha$ q | $\Delta(\delta,\alpha)$ Sample mean | $\Delta(\delta,\alpha)$ Sample std. dev. | $\Delta(\delta,\alpha)$ q |
|---|---|---|---|---|---|---|---|---|---|---|---|---|---|---|---|---|
| Rayl. | 10° | | | | | | | | | 75° | 75.5±0.92 | 28.9±0.65 | 28.9±1.0 | | | |
| Rayl. | 20° | | | | | | | | | 75° | 74.5±0.41 | 13.0±0.29 | 13.0±0.31 | | | |
| Rayl. | 30° | | | | | | | | | 75° | 74.8±0.27 | 8.6±0.19 | 8.6±0.20 | | | |
| Rayl. | 40° | | | | | | | | | 75° | 74.6±0.19 | 6.13±0.14 | 6.14±0.15 | | | |
| Rayl. | 50° | | | | | | | | | 75° | 75.00±0.16 | 4.99±0.11 | 4.99±0.11 | | | |
| Rayl. | 60° | | | | | | | | | 75° | 74.78±0.14 | 4.45±0.099 | 4.45±0.096 | | | |
| Rayl. | 70° | | | | | | | | | 75° | 75.12±0.13 | 4.01±0.090 | 4.01±0.088 | | | |
| Rayl. | 80° | | | | | | | | | 75° | 74.91±0.12 | 3.82±0.085 | 3.82±0.080 | | | |
| SAP | 10° | 3% | 9.15±0.18 | 5.78±0.13 | 8.4±0.25 | 30° | 7±2.1 | 64.9±1.5 | 68.9±0.98 | 75° | 75.7±0.98 | 31.0±0.69 | 31.0±1.0 | 64.4±0.98 | 31.1±0.70 | 71.5±0.96 |
| SAP | 20° | 3% | 3.79±0.043 | 1.36±0.030 | 1.57±0.059 | 30° | 16.0±1.2 | 37.6±0.84 | 40.1±0.83 | 75° | 74.7±0.46 | 14.5±0.33 | 14.5±0.36 | 35.2±0.72 | 22.7±0.51 | 41.9±0.80 |
| SAP | 30° | 3% | 3.19±0.023 | 0.715±0.016 | 0.74±0.023 | 30° | 24.6±0.66 | 20.8±0.47 | 21.5±0.53 | 75° | 74.6±0.31 | 9.7±0.22 | 9.7±0.23 | 19.4±0.39 | 12.5±0.28 | 23.1±0.50 |
| SAP | 40° | 3% | 3.055±0.015 | 0.475±0.011 | 0.478±0.012 | 30° | 26.7±0.45 | 14.3±0.32 | 14.7±0.34 | 75° | 74.6±0.23 | 7.36±0.16 | 7.37±0.18 | 13.7±0.26 | 8.20±0.18 | 16.0±0.32 |
| SAP | 50° | 3% | 3.028±0.012 | 0.390±0.0087 | 0.391±0.0088 | 30° | 28.3±0.33 | 10.3±0.23 | 10.4±0.24 | 75° | 75.0±0.19 | 6.03±0.13 | 6.03±0.15 | 10.11±0.18 | 5.84±0.13 | 11.7±0.22 |
| SAP | 60° | 3% | 3.016±0.0096 | 0.304±0.0066 | 0.304±0.0066 | 30° | 28.5±0.27 | 8.40±0.19 | 8.5±0.20 | 75° | 74.75±0.17 | 5.38±0.12 | 5.38±0.12 | 8.43±0.15 | 4.88±0.11 | 9.74±0.18 |
| SAP | 70° | 3% | 3.000±0.0089 | 0.281±0.0063 | 0.280±0.0060 | 30° | 28.7±0.23 | 7.41±0.17 | 7.52±0.18 | 75° | 75.23±0.16 | 5.04±0.12 | 5.04±0.12 | 7.45±0.14 | 4.48±0.11 | 8.69±0.16 |
| SAP | 80° | 3% | 3.004±0.0095 | 0.302±0.0068 | 0.302±0.0069 | 30° | 28.5±0.24 | 7.63±0.17 | 7.77±0.18 | 75° | 74.99±0.16 | 5.10±0.11 | 5.09±0.11 | 7.77±0.14 | 4.46±0.10 | 8.96±0.16 |
| MP | 10° | 3% | 8.17±0.17 | 5.26±0.12 | 7.4±0.21 | 30° | 9±2.0 | 61.7±1.4 | 65.3±0.97 | 75° | 75.3±0.91 | 28.6±0.64 | 28.6±0.97 | 60.8±0.97 | 30.6±0.69 | 68.0±0.96 |
| MP | 20° | 3% | 3.63±0.038 | 1.21±0.027 | 1.36±0.047 | 30° | 20.0±1.1 | 33.5±0.75 | 35.0±0.75 | 75° | 74.6±0.41 | 12.8±0.29 | 12.8±0.30 | 30.6±0.63 | 20.1±0.45 | 36.6±0.73 |
| MP | 30° | 3% | 3.15±0.019 | 0.605±0.014 | 0.623±0.018 | 30° | 26.8±0.55 | 17.4±0.39 | 17.7±0.46 | 75° | 74.8±0.26 | 8.22±0.18 | 8.22±0.19 | 16.0±0.33 | 10.5±0.23 | 19.1±0.43 |
| MP | 40° | 3% | 3.047±0.013 | 0.401±0.0090 | 0.404±0.0092 | 30° | 28.7±0.35 | 10.9±0.24 | 11.0±0.25 | 75° | 74.72±0.19 | 5.95±0.13 | 5.95±0.14 | 10.5±0.19 | 6.14±0.14 | 12.2±0.23 |
| MP | 50° | 3% | 3.030±0.0097 | 0.305±0.0068 | 0.307±0.0069 | 30° | 29.7±0.24 | 7.56±0.17 | 7.56±0.18 | 75° | 75.06±0.15 | 4.73±0.11 | 4.73±0.11 | 7.44±0.14 | 4.31±0.096 | 8.60±0.16 |
| MP | 60° | 3% | 3.008±0.0075 | 0.237±0.0053 | 0.237±0.0053 | 30° | 29.51±0.18 | 5.81±0.13 | 5.83±0.14 | 75° | 74.78±0.13 | 4.17±0.093 | 4.18±0.090 | 6.02±0.10 | 3.29±0.074 | 6.86±0.12 |
| MP | 70° | 3% | 3.009±0.0063 | 0.200±0.0045 | 0.200±0.0044 | 30° | 29.79±0.16 | 4.93±0.11 | 4.93±0.14 | 75° | 75.13±0.12 | 3.72±0.083 | 3.72±0.082 | 5.19±0.088 | 2.79±0.062 | 5.89±0.099 |
| MP | 80° | 3% | 3.010±0.0059 | 0.187±0.0042 | 0.187±0.0046 | 30° | 29.90±0.14 | 4.29±0.096 | 4.29±0.10 | 75° | 74.96±0.11 | 3.62±0.081 | 3.61±0.076 | 4.66±0.081 | 2.55±0.057 | 5.31±0.092 |
| HR (p) | 10° | 3% | 14.2±0.20 | 6.38±0.14 | 12.9±0.23 | 30° | 4.4±1.4 | 44.2±0.99 | 51.1±0.92 | 75° | 71±2.9 | 90±2.0 | 90.4±1.6 | 79.2±1.2 | 36.9±0.82 | 87.4±1.2 |
| HR (p) | 20° | 3% | 4.53±0.059 | 1.88±0.042 | 2.42±0.057 | 30° | 16.9±1.1 | 36.1±0.81 | 38.4±0.85 | 75° | 74.8±1.7 | 53.7±1.2 | 53.6±1.5 | 48.5±0.91 | 28.6±0.64 | 56.3±1.0 |
| HR (p) | 30° | 3% | 3.37±0.031 | 0.97±0.022 | 1.04±0.023 | 30° | 26.9±0.70 | 22.0±0.49 | 22.2±0.52 | 75° | 74.6±0.73 | 23.1±0.52 | 23.1±0.79 | 25.4±0.45 | 14.3±0.32 | 29.1±0.53 |
| HR (p) | 40° | 3% | 3.12±0.021 | 0.649±0.015 | 0.660±0.014 | 30° | 28.8±0.44 | 14.0±0.31 | 14.0±0.32 | 75° | 74.9±0.41 | 12.8±0.29 | 12.8±0.31 | 15.6±0.27 | 8.5±0.19 | 17.8±0.30 |
| HR (p) | 50° | 3% | 3.072±0.014 | 0.443±0.0099 | 0.449±0.010 | 30° | 29.4±0.31 | 9.8±0.22 | 9.8±0.23 | 75° | 75.1±0.29 | 9.1±0.20 | 9.1±0.21 | 11.0±0.19 | 6.05±0.14 | 12.6±0.22 |
| HR (p) | 60° | 3% | 3.031±0.011 | 0.352±0.0079 | 0.353±0.0083 | 30° | 29.6±0.24 | 7.65±0.17 | 7.67±0.19 | 75° | 74.9±0.22 | 6.99±0.15 | 6.99±0.15 | 8.60±0.15 | 4.65±0.10 | 9.77±0.17 |
| HR (p) | 70° | 3% | 3.023±0.0096 | 0.305±0.0068 | 0.306±0.0067 | 30° | 29.8±0.21 | 6.55±0.15 | 6.55±0.15 | 75° | 75.18±0.19 | 5.85±0.14 | 5.85±0.14 | 7.28±0.12 | 3.94±0.088 | 8.27±0.14 |
| HR (p) | 80° | 3% | 3.028±0.0085 | 0.270±0.0060 | 0.271±0.0062 | 30° | 29.5±0.20 | 6.18±0.14 | 6.19±0.14 | 75° | 75.03±0.17 | 5.45±0.12 | 5.45±0.13 | 6.87±0.12 | 3.65±0.082 | 7.78±0.13 |
| HR (p&a) | 10° | 3% | 12.78±0.18 | 5.83±0.13 | 11.4±0.22 | 30° | 4.1±1.4 | 44.2±0.99 | 51.2±0.91 | 75° | 73±2.8 | 89±2.0 | 89.1±1.5 | 78.5±1.2 | 37.1±0.83 | 86.9±1.2 |
| HR (p&a) | 20° | 3% | 4.23±0.054 | 1.71±0.038 | 2.10±0.049 | 30° | 18.6±1.1 | 35.8±0.80 | 37.6±0.85 | 75° | 75.0±1.5 | 48.4±1.1 | 48.4±1.4 | 45.3±0.82 | 26.0±0.58 | 52.3±0.98 |
| HR (p&a) | 30° | 3% | 3.28±0.028 | 0.89±0.020 | 0.94±0.021 | 30° | 27.1±0.63 | 19.8±0.44 | 20.0±0.48 | 75° | 74.7±0.65 | 20.7±0.46 | 20.6±0.84 | 23.0±0.40 | 12.8±0.29 | 26.3±0.49 |
| HR (p&a) | 40° | 3% | 3.093±0.018 | 0.577±0.013 | 0.584±0.013 | 30° | 29.0±0.39 | 12.3±0.28 | 12.3±0.27 | 75° | 75.1±0.36 | 11.4±0.25 | 11.4±0.26 | 13.8±0.24 | 7.50±0.17 | 15.7±0.26 |
| HR (p&a) | 50° | 3% | 3.059±0.013 | 0.404±0.0090 | 0.408±0.0095 | 30° | 29.9±0.28 | 8.8±0.20 | 8.8±0.21 | 75° | 75.0±0.25 | 8.05±0.18 | 8.0±0.19 | 9.80±0.17 | 5.40±0.12 | 11.2±0.19 |
| HR (p&a) | 60° | 3% | 3.020±0.010 | 0.316±0.0071 | 0.316±0.0071 | 30° | 29.6±0.22 | 6.86±0.15 | 6.87±0.13 | 75° | 74.8±0.20 | 6.27±0.14 | 6.27±0.14 | 7.76±0.13 | 4.05±0.091 | 8.75±0.15 |
| HR (p&a) | 70° | 3% | 3.023±0.0085 | 0.269±0.0059 | 0.269±0.0059 | 30° | 29.82±0.19 | 5.87±0.13 | 5.87±0.13 | 75° | 75.30±0.16 | 5.00±0.11 | 5.00±0.11 | 6.40±0.11 | 3.50±0.078 | 7.30±0.12 |
| HR (p&a) | 80° | 3% | 3.022±0.0076 | 0.239±0.0054 | 0.240±0.0058 | 30° | 29.71±0.17 | 5.29±0.12 | 5.29±0.12 | 75° | 75.10±0.15 | 4.79±0.11 | 4.79±0.11 | 5.95±0.099 | 3.13±0.070 | 6.72±0.11 |
| HR (p+f) | 10° | 3% | 14.1±0.20 | 6.37±0.14 | 12.8±0.24 | 30° | 4.8±1.4 | 44.1±0.99 | 50.8±0.92 | 75° | 71±2.8 | 90±2.0 | 90.1±1.5 | 78.7±1.1 | 36.3±0.81 | 86.7±1.1 |
| HR (p+f) | 20° | 3% | 4.52±0.059 | 1.87±0.042 | 2.41±0.057 | 30° | 17.0±1.1 | 36.0±0.80 | 38.2±0.85 | 75° | 75.4±1.7 | 54.3±1.2 | 54.3±1.6 | 48.4±0.90 | 28.6±0.64 | 56.2±1.0 |
| HR (p+f) | 30° | 3% | 3.37±0.031 | 0.97±0.022 | 1.04±0.023 | 30° | 27.0±0.69 | 21.9±0.49 | 22.1±0.52 | 75° | 74.6±0.74 | 23.3±0.46 | 23.3±0.96 | 25.3±0.45 | 14.1±0.32 | 29.0±0.53 |
| HR (p+f) | 40° | 3% | 3.13±0.020 | 0.647±0.014 | 0.659±0.014 | 30° | 28.8±0.44 | 13.9±0.31 | 14.0±0.32 | 75° | 74.9±0.41 | 12.8±0.31 | 12.8±0.31 | 15.6±0.27 | 8.5±0.19 | 17.8±0.30 |
| HR (p+f) | 50° | 3% | 3.071±0.014 | 0.442±0.0099 | 0.448±0.010 | 30° | 29.6±0.31 | 9.8±0.22 | 9.8±0.23 | 75° | 75.1±0.29 | 9.1±0.20 | 9.1±0.22 | 11.0±0.19 | 6.03±0.14 | 12.6±0.22 |
| HR (p+f) | 60° | 3% | 3.031±0.011 | 0.351±0.0079 | 0.352±0.0083 | 30° | 29.4±0.24 | 7.64±0.17 | 7.66±0.19 | 75° | 74.7±0.20 | 6.99±0.15 | 6.99±0.15 | 8.60±0.15 | 4.63±0.10 | 9.76±0.17 |
| HR (p+f) | 70° | 3% | 3.017±0.0096 | 0.305±0.0068 | 0.306±0.0066 | 30° | 29.8±0.21 | 6.55±0.15 | 6.55±0.15 | 75° | 75.18±0.18 | 5.85±0.13 | 5.85±0.13 | 7.27±0.12 | 3.94±0.088 | 8.27±0.14 |
| HR (p+f) | 80° | 3% | 3.028±0.0085 | 0.270±0.0060 | 0.271±0.0062 | 30° | 29.6±0.20 | 6.17±0.14 | 6.19±0.14 | 75° | 75.03±0.17 | 5.45±0.12 | 5.44±0.13 | 6.87±0.12 | 3.65±0.082 | 7.77±0.13 |
| HR (p&a+f) | 10° | 3% | 12.59±0.18 | 5.77±0.13 | 11.2±0.21 | 30° | 4.6±1.4 | 44.1±0.99 | 50.9±0.93 | 75° | 72±2.8 | 89±2.0 | 88.6±1.5 | 77.9±1.2 | 36.7±0.82 | 86.1±1.2 |
| HR (p&a+f) | 20° | 3% | 4.22±0.054 | 1.71±0.038 | 2.10±0.049 | 30° | 18.7±1.1 | 35.6±0.80 | 37.4±0.85 | 75° | 75.1±1.5 | 48.4±1.1 | 48.4±1.4 | 45.3±0.83 | 26.2±0.59 | 52.4±0.99 |
| HR (p&a+f) | 30° | 3% | 3.29±0.028 | 0.89±0.020 | 0.94±0.021 | 30° | 27.1±0.62 | 19.7±0.44 | 19.9±0.48 | 75° | 74.7±0.65 | 20.5±0.46 | 20.5±0.79 | 22.9±0.40 | 12.7±0.28 | 26.2±0.48 |
| HR (p&a+f) | 40° | 3% | 3.094±0.018 | 0.576±0.013 | 0.583±0.013 | 30° | 29.0±0.39 | 12.3±0.27 | 12.3±0.27 | 75° | 75.1±0.36 | 11.4±0.26 | 11.4±0.26 | 13.8±0.24 | 7.48±0.17 | 15.7±0.25 |
| HR (p&a+f) | 50° | 3% | 3.059±0.013 | 0.403±0.0090 | 0.407±0.0095 | 30° | 29.9±0.28 | 8.8±0.20 | 8.8±0.21 | 75° | 75.0±0.25 | 8.04±0.18 | 8.0±0.19 | 9.80±0.17 | 5.38±0.12 | 11.4±0.19 |
| HR (p&a+f) | 60° | 3% | 3.020±0.010 | 0.316±0.0071 | 0.316±0.0071 | 30° | 29.6±0.22 | 6.86±0.15 | 6.87±0.13 | 75° | 74.7±0.20 | 6.28±0.14 | 6.28±0.14 | 7.76±0.13 | 4.05±0.091 | 8.75±0.15 |
| HR (p&a+f) | 70° | 3% | 3.017±0.0085 | 0.268±0.0058 | 0.269±0.0058 | 30° | 29.82±0.19 | 5.87±0.13 | 5.87±0.13 | 75° | 75.31±0.16 | 5.07±0.11 | 5.08±0.11 | 6.41±0.11 | 3.50±0.078 | 7.30±0.12 |
| HR (p&a+f) | 80° | 3% | 3.022±0.0076 | 0.239±0.0054 | 0.240±0.0058 | 30° | 29.72±0.17 | 5.28±0.12 | 5.28±0.12 | 75° | 75.09±0.15 | 4.79±0.11 | 4.79±0.11 | 5.94±0.099 | 3.13±0.070 | 6.71±0.11 |

**Table C.3:** Tabulated data for Figure 5.9: $\beta = 49°$, $N \propto \sin^2 \vartheta_{max}$, $N(\vartheta_{max} = 60°) = 10^6$, $D = 3\%$, $\delta_{dipole} = 30°$, $\alpha_{dipole} = 75°$.

**Table C.4:** Tabulated data for Figures 5.10 and 6.22: $\vartheta_{max} = 60°$, $N = 10^6$, $D = 3\%$, $\delta_{dipole} = 30°$, $\alpha_{dipole} = 75°$

| Method | β | $\bar{R}$ True | $\bar{R}$ Sample mean | $\bar{R}$ Sample std. dev. | $\bar{R}$ q | δ True | δ Sample mean | δ Sample std. dev. | δ q | α True | α Sample mean | α Sample std. dev. | α q | Δ(δ, α) Sample mean | Δ(δ, α) Sample std. dev. | Δ(δ, α) q |
|---|---|---|---|---|---|---|---|---|---|---|---|---|---|---|---|---|
| Rayl. | −90° | | | | | | | | | 75° | 74.84 ± 0.17 | 5.30 ± 0.12 | 5.29 ± 0.12 | | | |
| Rayl. | −60° | | | | | | | | | 75° | 75.13 ± 0.15 | 4.66 ± 0.10 | 4.66 ± 0.11 | | | |
| Rayl. | −30° | | | | | | | | | 75° | 75.17 ± 0.12 | 3.73 ± 0.080 | 3.73 ± 0.080 | | | |
| Rayl. | 0° | | | | | | | | | 75° | 75.08 ± 0.11 | 3.52 ± 0.082 | 3.52 ± 0.082 | | | |
| Rayl. | 30° | | | | | | | | | 75° | 74.73 ± 0.12 | 3.86 ± 0.086 | 3.86 ± 0.086 | | | |
| Rayl. | 60° | | | | | | | | | 75° | 75.11 ± 0.15 | 4.82 ± 0.11 | 4.82 ± 0.11 | | | |
| Rayl. | 90° | | | | | | | | | 75° | 75.07 ± 0.18 | 5.55 ± 0.12 | 5.54 ± 0.13 | | | |
| SAP | −90° | 3% | 3.074 ± 0.013 | 0.398 ± 0.0089 | 0.405 ± 0.010 | 30° | 29.1 ± 0.38 | 11.9 ± 0.27 | 12.0 ± 0.30 | 75° | 74.86 ± 0.16 | 5.09 ± 0.11 | 5.09 ± 0.12 | 10.7 ± 0.22 | 6.86 ± 0.15 | 12.7 ± 0.29 |
| SAP | −60° | 3% | 3.101 ± 0.012 | 0.365 ± 0.0082 | 0.378 ± 0.0086 | 30° | 30.5 ± 0.30 | 9.6 ± 0.22 | 9.6 ± 0.23 | 75° | 75.37 ± 0.19 | 5.97 ± 0.13 | 5.98 ± 0.14 | 9.36 ± 0.18 | 5.58 ± 0.12 | 10.9 ± 0.21 |
| SAP | −30° | 3% | 3.043 ± 0.0074 | 0.235 ± 0.0052 | 0.238 ± 0.0053 | 30° | 30.65 ± 0.18 | 5.78 ± 0.13 | 5.82 ± 0.13 | 75° | 75.16 ± 0.14 | 4.31 ± 0.096 | 4.31 ± 0.10 | 6.05 ± 0.11 | 3.32 ± 0.074 | 6.90 ± 0.12 |
| SAP | 0° | 3% | 3.019 ± 0.0063 | 0.198 ± 0.0044 | 0.199 ± 0.0047 | 30° | 29.78 ± 0.15 | 4.75 ± 0.11 | 4.75 ± 0.12 | 75° | 75.07 ± 0.12 | 3.65 ± 0.082 | 3.65 ± 0.089 | 4.94 ± 0.090 | 2.85 ± 0.064 | 5.71 ± 0.11 |
| SAP | 30° | 3% | 3.021 ± 0.0076 | 0.241 ± 0.0054 | 0.242 ± 0.0054 | 30° | 29.55 ± 0.19 | 5.89 ± 0.13 | 5.90 ± 0.12 | 75° | 74.67 ± 0.14 | 4.34 ± 0.097 | 4.35 ± 0.096 | 6.18 ± 0.10 | 3.28 ± 0.073 | 7.00 ± 0.11 |
| SAP | 60° | 3% | 3.017 ± 0.012 | 0.381 ± 0.0085 | 0.381 ± 0.0091 | 30° | 28.0 ± 0.32 | 10.2 ± 0.23 | 10.4 ± 0.25 | 75° | 75.2 ± 0.19 | 6.16 ± 0.14 | 6.16 ± 0.14 | 10.05 ± 0.19 | 6.00 ± 0.13 | 11.7 ± 0.23 |
| SAP | 90° | 3% | 3.094 ± 0.013 | 0.416 ± 0.0093 | 0.426 ± 0.012 | 30° | 29.2 ± 0.39 | 12.3 ± 0.28 | 12.3 ± 0.28 | 75° | 75.15 ± 0.17 | 5.30 ± 0.12 | 5.30 ± 0.12 | 11.1 ± 0.22 | 7.04 ± 0.16 | 13.2 ± 0.26 |
| MP | −90° | 3% | 3.071 ± 0.012 | 0.389 ± 0.0087 | 0.395 ± 0.010 | 30° | 29.2 ± 0.37 | 11.7 ± 0.26 | 11.8 ± 0.29 | 75° | 74.88 ± 0.16 | 4.98 ± 0.11 | 4.98 ± 0.11 | 10.5 ± 0.21 | 6.77 ± 0.15 | 12.5 ± 0.28 |
| MP | −60° | 3% | 3.026 ± 0.0079 | 0.251 ± 0.0056 | 0.252 ± 0.0059 | 30° | 29.3 ± 0.22 | 6.80 ± 0.15 | 6.84 ± 0.16 | 75° | 75.13 ± 0.14 | 4.34 ± 0.097 | 4.34 ± 0.10 | 6.78 ± 0.12 | 3.88 ± 0.087 | 7.81 ± 0.14 |
| MP | −30° | 3% | 3.014 ± 0.0059 | 0.188 ± 0.0042 | 0.189 ± 0.0040 | 30° | 30.06 ± 0.15 | 4.62 ± 0.10 | 4.61 ± 0.095 | 75° | 75.15 ± 0.11 | 3.61 ± 0.081 | 3.61 ± 0.079 | 4.94 ± 0.081 | 2.57 ± 0.057 | 5.57 ± 0.088 |
| MP | 0° | 3% | 3.015 ± 0.0057 | 0.179 ± 0.0040 | 0.180 ± 0.0039 | 30° | 29.76 ± 0.13 | 4.19 ± 0.094 | 4.20 ± 0.11 | 75° | 75.07 ± 0.11 | 3.50 ± 0.078 | 3.50 ± 0.080 | 4.49 ± 0.081 | 2.57 ± 0.057 | 5.18 ± 0.095 |
| MP | 30° | 3% | 3.024 ± 0.0063 | 0.199 ± 0.0045 | 0.201 ± 0.0043 | 30° | 30.08 ± 0.15 | 4.60 ± 0.10 | 4.60 ± 0.099 | 75° | 74.76 ± 0.12 | 3.66 ± 0.082 | 3.67 ± 0.081 | 4.93 ± 0.083 | 2.62 ± 0.059 | 5.59 ± 0.091 |
| MP | 60° | 3% | 3.030 ± 0.0087 | 0.275 ± 0.0062 | 0.277 ± 0.0060 | 30° | 30.1 ± 0.22 | 6.91 ± 0.15 | 6.91 ± 0.15 | 75° | 75.04 ± 0.14 | 4.52 ± 0.10 | 4.52 ± 0.10 | 6.96 ± 0.12 | 3.80 ± 0.085 | 7.93 ± 0.14 |
| MP | 90° | 3% | 3.090 ± 0.013 | 0.415 ± 0.0093 | 0.424 ± 0.011 | 30° | 29.2 ± 0.39 | 12.3 ± 0.27 | 12.3 ± 0.28 | 75° | 75.14 ± 0.16 | 5.22 ± 0.12 | 5.22 ± 0.12 | 11.0 ± 0.22 | 7.01 ± 0.16 | 13.1 ± 0.27 |
| HR (p) | −60° | 3% | 3.050 ± 0.011 | 0.358 ± 0.0080 | 0.362 ± 0.0080 | 30° | 29.2 ± 0.30 | 9.4 ± 0.21 | 9.5 ± 0.21 | 75° | 74.9 ± 0.21 | 6.49 ± 0.15 | 6.49 ± 0.15 | 9.61 ± 0.17 | 5.36 ± 0.12 | 11.0 ± 0.20 |
| HR (p) | −30° | 3% | 3.035 ± 0.011 | 0.345 ± 0.0077 | 0.346 ± 0.0076 | 30° | 30.0 ± 0.20 | 6.20 ± 0.14 | 6.20 ± 0.13 | 75° | 75.1 ± 0.25 | 7.90 ± 0.18 | 7.90 ± 0.17 | 8.18 ± 0.13 | 4.22 ± 0.094 | 9.21 ± 0.14 |
| HR (p) | 0° | 3% | 3.035 ± 0.012 | 0.365 ± 0.0082 | 0.367 ± 0.0078 | 30° | 29.6 ± 0.19 | 6.15 ± 0.14 | 6.16 ± 0.14 | 75° | 74.4 ± 0.27 | 8.6 ± 0.20 | 8.6 ± 0.20 | 8.43 ± 0.15 | 4.65 ± 0.10 | 9.63 ± 0.16 |
| HR (p) | 30° | 3% | 3.060 ± 0.011 | 0.336 ± 0.0075 | 0.341 ± 0.0075 | 30° | 30.1 ± 0.20 | 6.31 ± 0.14 | 6.31 ± 0.15 | 75° | 74.7 ± 0.24 | 7.49 ± 0.18 | 7.49 ± 0.18 | 7.93 ± 0.14 | 4.30 ± 0.096 | 9.02 ± 0.15 |
| HR (p) | 60° | 3% | 3.073 ± 0.012 | 0.379 ± 0.0085 | 0.386 ± 0.0087 | 30° | 29.9 ± 0.30 | 9.3 ± 0.21 | 9.3 ± 0.22 | 75° | 75.1 ± 0.22 | 6.95 ± 0.16 | 6.94 ± 0.16 | 9.64 ± 0.17 | 5.46 ± 0.12 | 11.1 ± 0.20 |
| HR (p&a) | −60° | 3% | 3.028 ± 0.0097 | 0.307 ± 0.0069 | 0.308 ± 0.0072 | 30° | 29.1 ± 0.26 | 8.30 ± 0.19 | 8.3 ± 0.19 | 75° | 74.98 ± 0.18 | 5.72 ± 0.13 | 5.72 ± 0.13 | 8.44 ± 0.15 | 4.79 ± 0.11 | 9.70 ± 0.17 |
| HR (p&a) | −30° | 3% | 3.023 ± 0.0094 | 0.296 ± 0.0066 | 0.297 ± 0.0067 | 30° | 30.01 ± 0.18 | 5.55 ± 0.12 | 5.55 ± 0.11 | 75° | 75.1 ± 0.22 | 7.01 ± 0.16 | 7.01 ± 0.16 | 7.35 ± 0.12 | 3.67 ± 0.082 | 8.21 ± 0.12 |
| HR (p&a) | 0° | 3% | 3.029 ± 0.010 | 0.325 ± 0.0073 | 0.326 ± 0.0073 | 30° | 29.83 ± 0.17 | 5.44 ± 0.12 | 5.44 ± 0.13 | 75° | 74.6 ± 0.24 | 7.65 ± 0.17 | 7.66 ± 0.17 | 7.55 ± 0.13 | 4.05 ± 0.091 | 8.56 ± 0.14 |
| HR (p&a) | 30° | 3% | 3.046 ± 0.0094 | 0.297 ± 0.0066 | 0.300 ± 0.0067 | 30° | 30.10 ± 0.18 | 5.58 ± 0.12 | 5.58 ± 0.13 | 75° | 74.8 ± 0.21 | 6.77 ± 0.15 | 6.77 ± 0.16 | 7.08 ± 0.12 | 3.87 ± 0.086 | 8.07 ± 0.13 |
| HR (p&a) | 60° | 3% | 3.048 ± 0.011 | 0.336 ± 0.0075 | 0.340 ± 0.0075 | 30° | 29.9 ± 0.27 | 8.39 ± 0.19 | 8.39 ± 0.19 | 75° | 75.0 ± 0.19 | 6.11 ± 0.14 | 6.11 ± 0.14 | 8.72 ± 0.15 | 4.69 ± 0.10 | 9.90 ± 0.17 |
| HR (p+f) | −60° | 3% | 3.051 ± 0.011 | 0.358 ± 0.0080 | 0.362 ± 0.0080 | 30° | 29.2 ± 0.30 | 9.4 ± 0.21 | 9.5 ± 0.21 | 75° | 74.9 ± 0.21 | 6.50 ± 0.15 | 6.50 ± 0.15 | 9.62 ± 0.17 | 5.38 ± 0.12 | 11.0 ± 0.20 |
| HR (p+f) | −30° | 3% | 3.036 ± 0.011 | 0.344 ± 0.0077 | 0.346 ± 0.0076 | 30° | 30.0 ± 0.20 | 6.20 ± 0.14 | 6.20 ± 0.13 | 75° | 75.1 ± 0.25 | 7.90 ± 0.18 | 7.90 ± 0.17 | 8.18 ± 0.13 | 4.23 ± 0.095 | 9.21 ± 0.14 |
| HR (p+f) | 0° | 3% | 3.035 ± 0.012 | 0.365 ± 0.0082 | 0.366 ± 0.0078 | 30° | 29.6 ± 0.19 | 6.14 ± 0.14 | 6.15 ± 0.15 | 75° | 74.4 ± 0.27 | 8.6 ± 0.20 | 8.6 ± 0.20 | 8.42 ± 0.15 | 4.65 ± 0.10 | 9.62 ± 0.17 |
| HR (p+f) | 30° | 3% | 3.060 ± 0.011 | 0.335 ± 0.0075 | 0.340 ± 0.0074 | 30° | 30.1 ± 0.20 | 6.32 ± 0.14 | 6.31 ± 0.15 | 75° | 74.7 ± 0.24 | 7.49 ± 0.17 | 7.50 ± 0.18 | 7.94 ± 0.14 | 4.30 ± 0.096 | 9.03 ± 0.15 |
| HR (p+f) | 60° | 3% | 3.073 ± 0.012 | 0.379 ± 0.0085 | 0.386 ± 0.0087 | 30° | 29.9 ± 0.29 | 9.3 ± 0.21 | 9.3 ± 0.21 | 75° | 75.1 ± 0.22 | 6.96 ± 0.16 | 6.95 ± 0.16 | 9.64 ± 0.17 | 5.45 ± 0.12 | 11.1 ± 0.20 |
| HR (p&a+f) | −60° | 3% | 3.028 ± 0.0097 | 0.307 ± 0.0069 | 0.308 ± 0.0071 | 30° | 29.1 ± 0.26 | 8.29 ± 0.19 | 8.3 ± 0.19 | 75° | 74.98 ± 0.18 | 5.73 ± 0.13 | 5.73 ± 0.13 | 8.44 ± 0.15 | 4.79 ± 0.11 | 9.70 ± 0.18 |
| HR (p&a+f) | −30° | 3% | 3.023 ± 0.0094 | 0.296 ± 0.0066 | 0.297 ± 0.0067 | 30° | 29.99 ± 0.18 | 5.55 ± 0.12 | 5.55 ± 0.11 | 75° | 75.1 ± 0.22 | 7.01 ± 0.16 | 7.01 ± 0.16 | 7.35 ± 0.12 | 3.67 ± 0.082 | 8.21 ± 0.12 |
| HR (p&a+f) | 0° | 3% | 3.029 ± 0.010 | 0.325 ± 0.0073 | 0.326 ± 0.0073 | 30° | 29.82 ± 0.17 | 5.43 ± 0.12 | 5.43 ± 0.13 | 75° | 74.6 ± 0.24 | 7.65 ± 0.17 | 7.66 ± 0.17 | 7.54 ± 0.13 | 4.05 ± 0.091 | 8.56 ± 0.14 |
| HR (p&a+f) | 30° | 3% | 3.046 ± 0.0094 | 0.296 ± 0.0066 | 0.300 ± 0.0068 | 30° | 30.12 ± 0.18 | 5.57 ± 0.12 | 5.57 ± 0.13 | 75° | 74.8 ± 0.21 | 6.77 ± 0.15 | 6.77 ± 0.16 | 7.07 ± 0.12 | 3.87 ± 0.087 | 8.06 ± 0.13 |
| HR (p&a+f) | 60° | 3% | 3.048 ± 0.011 | 0.337 ± 0.0075 | 0.340 ± 0.0075 | 30° | 29.9 ± 0.27 | 8.39 ± 0.19 | 8.39 ± 0.19 | 75° | 75.0 ± 0.19 | 6.12 ± 0.14 | 6.11 ± 0.14 | 8.72 ± 0.15 | 4.70 ± 0.11 | 9.90 ± 0.17 |

| Method | D | R̄ True | R̄ Sample mean | R̄ Sample std. dev | R̄ q | δ True | δ Sample mean | δ Sample std. dev | δ q | ᾱ True | ᾱ Sample mean | ᾱ Sample std. dev | ᾱ q | Δ(δ,α) Sample mean | Δ(δ,α) Sample std. dev | Δ(δ,α) q |
|---|---|---|---|---|---|---|---|---|---|---|---|---|---|---|---|---|
| Rayl. | 0.1% | | | | | | | | | 75° | 83±2.7 | 83.8±1.9 | 84.2±1.5 | | | |
| Rayl. | 0.3% | | | | | | | | | 75° | 76.6±1.8 | 55.5±1.2 | 55.5±1.6 | | | |
| Rayl. | 1% | | | | | | | | | 75° | 75.2±0.44 | 14.0±0.31 | 14.0±0.32 | | | |
| Rayl. | 3% | | | | | | | | | 75° | 74.78±0.14 | 4.45±0.099 | 4.45±0.096 | | | |
| Rayl. | 10% | | | | | | | | | 75° | 74.98±0.042 | 1.33±0.030 | 1.33±0.030 | | | |
| Rayl. | 30% | | | | | | | | | 75° | 74.995±0.015 | 0.486±0.011 | 0.485±0.011 | | | |
| SAP | 0.1% | 0.1% | 0.530±0.0079 | 0.251±0.0056 | 0.498±0.0089 | 30° | −6.2±1.6 | 50.3±1.1 | 62.0±0.97 | 75° | 82±2.8 | 88±2.0 | 88.6±1.5 | 84.1±1.1 | 36.3±0.81 | 91.6±1.1 |
| SAP | 0.3% | 0.3% | 0.586±0.0082 | 0.258±0.0058 | 0.385±0.0094 | 30° | 8.3±1.5 | 46.6±1.0 | 51.4±0.97 | 75° | 79±1.9 | 60.3±1.4 | 60.4±1.5 | 60.3±1.0 | 31.7±0.71 | 68.1±1.1 |
| SAP | 1% | 1% | 1.095±0.0095 | 0.302±0.0067 | 0.316±0.0080 | 30° | 23.0±0.76 | 24.1±0.54 | 25.1±0.62 | 75° | 75.3±0.54 | 17.1±0.38 | 17.1±0.45 | 24.9±0.47 | 15.0±0.34 | 29.1±0.58 |
| SAP | 3% | 3% | 3.016±0.0096 | 0.304±0.0068 | 0.304±0.0066 | 30° | 28.5±0.27 | 8.40±0.19 | 8.5±0.20 | 75° | 74.75±0.17 | 5.38±0.12 | 5.38±0.12 | 8.43±0.15 | 4.88±0.11 | 9.74±0.18 |
| SAP | 10% | 10% | 9.978±0.010 | 0.328±0.0073 | 0.328±0.0072 | 30° | 29.61±0.079 | 2.51±0.056 | 2.53±0.058 | 75° | 74.95±0.051 | 1.62±0.036 | 1.62±0.039 | 2.51±0.046 | 1.45±0.032 | 2.90±0.053 |
| SAP | 30% | 30% | 29.952±0.012 | 0.373±0.0083 | 0.376±0.0080 | 30° | 29.91±0.028 | 0.90±0.020 | 0.90±0.020 | 75° | 75.017±0.017 | 0.545±0.012 | 0.545±0.012 | 0.885±0.016 | 0.502±0.011 | 1.017±0.018 |
| MP | 0.1% | 0.1% | 0.394±0.0058 | 0.182±0.0041 | 0.346±0.0064 | 30° | 3.4±1.5 | 48.6±1.2 | 55.4±0.98 | 75° | 82±2.6 | 83.4±1.9 | 83.7±1.6 | 75.4±1.1 | 35.7±0.80 | 83.4±1.1 |
| MP | 0.3% | 0.3% | 0.482±0.0062 | 0.197±0.0044 | 0.268±0.0067 | 30° | 18.8±1.3 | 40.5±0.91 | 42.0±0.93 | 75° | 76.1±1.6 | 52.1±1.2 | 52.0±1.5 | 49.5±0.91 | 28.6±0.64 | 57.2±1.0 |
| MP | 1% | 1% | 1.057±0.0074 | 0.233±0.0052 | 0.240±0.0058 | 30° | 27.2±0.56 | 17.6±0.39 | 17.9±0.46 | 75° | 75.3±0.42 | 13.2±0.29 | 13.2±0.31 | 18.2±0.34 | 10.8±0.24 | 21.1±0.43 |
| MP | 3% | 3% | 3.008±0.0075 | 0.237±0.0053 | 0.237±0.0053 | 30° | 29.51±0.18 | 5.81±0.13 | 5.83±0.14 | 75° | 74.78±0.13 | 4.17±0.093 | 4.18±0.090 | 6.02±0.10 | 3.29±0.074 | 6.86±0.12 |
| MP | 10% | 10% | 10.001±0.0079 | 0.251±0.0056 | 0.251±0.0053 | 30° | 29.91±0.057 | 1.82±0.041 | 1.82±0.040 | 75° | 74.96±0.040 | 1.25±0.028 | 1.25±0.027 | 1.84±0.033 | 1.04±0.023 | 2.12±0.036 |
| MP | 30% | 30% | 29.989±0.0092 | 0.292±0.0065 | 0.292±0.0074 | 30° | 30.00±0.020 | 0.640±0.014 | 0.639±0.014 | 75° | 75.000±0.014 | 0.447±0.010 | 0.447±0.0094 | 0.654±0.011 | 0.362±0.0081 | 0.748±0.013 |
| HR (p) | 0.1% | 0.1% | 0.559±0.0079 | 0.250±0.0056 | 0.523±0.0087 | 30° | 3.7±1.4 | 45.1±1.0 | 52.2±0.96 | 75° | 82±2.9 | 93±2.1 | 92.9±1.5 | 80.6±1.2 | 37.3±0.84 | 88.8±1.2 |
| HR (p) | 0.3% | 0.3% | 0.618±0.0083 | 0.263±0.0059 | 0.413±0.0087 | 30° | 13.7±1.3 | 41.1±0.92 | 44.2±0.92 | 75° | 75±2.2 | 71.0±1.6 | 71.0±1.6 | 61.1±1.1 | 34.1±0.76 | 70.0±1.2 |
| HR (p) | 1% | 1% | 1.130±0.010 | 0.324±0.0072 | 0.349±0.0082 | 30° | 26.5±0.70 | 22.2±0.50 | 22.5±0.57 | 75° | 75.7±0.74 | 23.2±0.52 | 23.2±0.79 | 25.4±0.46 | 14.5±0.32 | 29.2±0.54 |
| HR (p) | 3% | 3% | 3.031±0.011 | 0.352±0.0079 | 0.353±0.0083 | 30° | 29.4±0.24 | 7.65±0.17 | 7.67±0.19 | 75° | 74.9±0.22 | 6.99±0.15 | 6.99±0.15 | 8.60±0.15 | 4.65±0.10 | 9.77±0.17 |
| HR (p) | 10% | 10% | 10.011±0.012 | 0.366±0.0082 | 0.366±0.0077 | 30° | 29.89±0.078 | 2.48±0.055 | 2.48±0.053 | 75° | 74.97±0.065 | 2.07±0.046 | 2.07±0.048 | 2.71±0.045 | 1.42±0.032 | 3.06±0.048 |
| HR (p) | 30% | 30% | 30.090±0.014 | 0.450±0.010 | 0.458±0.0098 | 30° | 30.03±0.027 | 0.85±0.019 | 0.854±0.018 | 75° | 75.02±0.023 | 0.716±0.016 | 0.716±0.015 | 0.939±0.015 | 0.481±0.011 | 1.055±0.017 |
| HR (pκα) | 0.1% | 0.1% | 0.495±0.0070 | 0.221±0.0049 | 0.452±0.0076 | 30° | 4.0±1.4 | 44.3±0.99 | 51.4±0.96 | 75° | 82±2.9 | 91±2.0 | 91.0±1.5 | 78.9±1.2 | 36.8±0.82 | 87.1±1.1 |
| HR (pκα) | 0.3% | 0.3% | 0.570±0.0075 | 0.238±0.0053 | 0.359±0.0076 | 30° | 15.9±1.3 | 40.1±0.90 | 42.5±0.90 | 75° | 76±2.1 | 67.5±1.5 | 67.4±1.6 | 58.0±1.0 | 33.2±0.74 | 66.9±1.2 |
| HR (pκα) | 1% | 1% | 1.098±0.0092 | 0.292±0.0065 | 0.308±0.0075 | 30° | 26.5±0.64 | 20.1±0.45 | 20.4±0.51 | 75° | 75.6±0.63 | 19.9±0.45 | 19.9±0.51 | 22.9±0.41 | 12.9±0.29 | 26.3±0.49 |
| HR (pκα) | 3% | 3% | 3.020±0.010 | 0.316±0.0071 | 0.316±0.0071 | 30° | 29.6±0.22 | 6.86±0.15 | 6.87±0.16 | 75° | 74.8±0.20 | 6.27±0.14 | 6.27±0.14 | 7.76±0.13 | 4.05±0.091 | 8.75±0.15 |
| HR (pκα) | 10% | 10% | 10.002±0.010 | 0.317±0.0071 | 0.317±0.0071 | 30° | 29.90±0.068 | 2.16±0.048 | 2.16±0.048 | 75° | 74.93±0.059 | 1.87±0.042 | 1.87±0.043 | 2.39±0.040 | 1.26±0.028 | 2.70±0.043 |
| HR (pκα) | 30% | 30% | 29.991±0.011 | 0.348±0.0078 | 0.348±0.0079 | 30° | 30.00±0.024 | 0.755±0.017 | 0.755±0.017 | 75° | 75.03±0.020 | 0.636±0.014 | 0.636±0.013 | 0.825±0.014 | 0.439±0.0098 | 0.934±0.015 |
| HR (p+θ̄) | 0.1% | 0.1% | 0.559±0.0079 | 0.250±0.0056 | 0.523±0.0087 | 30° | 3.7±1.4 | 45.1±1.0 | 52.2±0.96 | 75° | 81±2.9 | 93±2.1 | 92.9±1.5 | 80.5±1.2 | 37.5±0.84 | 88.8±1.2 |
| HR (p+θ̄) | 0.3% | 0.3% | 0.618±0.0083 | 0.263±0.0059 | 0.412±0.0087 | 30° | 13.7±1.3 | 41.2±0.92 | 44.3±0.93 | 75° | 74±2.2 | 71.1±1.6 | 71.1±1.6 | 61.1±1.1 | 34.2±0.77 | 70.0±1.2 |
| HR (p+θ̄) | 1% | 1% | 1.129±0.010 | 0.323±0.0072 | 0.347±0.0081 | 30° | 26.5±0.70 | 22.2±0.50 | 22.5±0.57 | 75° | 75.7±0.74 | 23.3±0.52 | 23.3±0.80 | 25.4±0.46 | 14.5±0.32 | 29.2±0.54 |
| HR (p+θ̄) | 3% | 3% | 3.031±0.011 | 0.351±0.0079 | 0.352±0.0083 | 30° | 29.4±0.24 | 7.64±0.17 | 7.66±0.19 | 75° | 74.9±0.22 | 6.99±0.15 | 6.99±0.15 | 8.60±0.15 | 4.63±0.10 | 9.76±0.17 |
| HR (p+θ̄) | 10% | 10% | 10.012±0.012 | 0.365±0.0082 | 0.365±0.0077 | 30° | 29.90±0.078 | 2.48±0.055 | 2.48±0.053 | 75° | 74.97±0.065 | 2.07±0.046 | 2.07±0.048 | 2.71±0.045 | 1.42±0.032 | 3.06±0.048 |
| HR (p+θ̄) | 30% | 30% | 30.104±0.014 | 0.447±0.010 | 0.459±0.0099 | 30° | 30.03±0.027 | 0.852±0.019 | 0.852±0.018 | 75° | 75.02±0.023 | 0.717±0.016 | 0.717±0.015 | 0.937±0.015 | 0.482±0.011 | 1.054±0.017 |
| HR (pκα+θ̄) | 0.1% | 0.1% | 0.495±0.0070 | 0.220±0.0049 | 0.452±0.0076 | 30° | 4.0±1.4 | 44.3±0.99 | 51.4±0.96 | 75° | 82±2.9 | 91±2.0 | 91.1±1.5 | 78.9±1.2 | 37.0±0.83 | 87.2±1.2 |
| HR (pκα+θ̄) | 0.3% | 0.3% | 0.569±0.0075 | 0.238±0.0053 | 0.359±0.0076 | 30° | 15.9±1.3 | 40.1±0.90 | 42.5±0.90 | 75° | 75±2.1 | 67.6±1.5 | 67.6±1.6 | 58.0±1.0 | 33.2±0.74 | 66.8±1.2 |
| HR (pκα+θ̄) | 1% | 1% | 1.097±0.0092 | 0.292±0.0065 | 0.307±0.0075 | 30° | 26.5±0.64 | 20.1±0.45 | 20.4±0.51 | 75° | 75.6±0.63 | 20.0±0.45 | 20.0±0.51 | 22.9±0.41 | 13.0±0.29 | 26.3±0.49 |
| HR (pκα+θ̄) | 3% | 3% | 3.020±0.010 | 0.315±0.0071 | 0.316±0.0071 | 30° | 29.6±0.22 | 6.86±0.15 | 6.87±0.16 | 75° | 74.7±0.20 | 6.27±0.14 | 6.28±0.14 | 7.76±0.13 | 4.05±0.091 | 8.76±0.15 |
| HR (pκα+θ̄) | 10% | 10% | 10.002±0.010 | 0.317±0.0071 | 0.316±0.0071 | 30° | 29.90±0.068 | 2.16±0.048 | 2.16±0.048 | 75° | 74.93±0.059 | 1.87±0.042 | 1.87±0.043 | 2.38±0.040 | 1.26±0.028 | 2.70±0.043 |
| HR (pκα+θ̄) | 30% | 30% | 29.992±0.011 | 0.346±0.0077 | 0.346±0.0080 | 30° | 30.00±0.024 | 0.753±0.017 | 0.752±0.016 | 75° | 75.02±0.020 | 0.636±0.014 | 0.636±0.013 | 0.823±0.014 | 0.439±0.0098 | 0.933±0.015 |

**Table C.5:** Tabulated data for Figures 5.11 and 6.23: $\beta = 49°$, $\vartheta_{max} = 60°$, $N = 10^6$, $\delta_{dipole} = 30°$, $\alpha_{dipole} = 75°$.

Table C.6 — Tabulated data. Column groups: **D** (True, Sample mean, Sample std. dev., q), **δ** (True, Sample mean, Sample std. dev., q), **α** (True, Sample mean, Sample std. dev., q), **Δ(δ, α)** (Sample mean, Sample std. dev., q).

| Method | $\delta_{dipole}$ | D True | D Sample mean | D Sample std. dev. | D q | δ True | δ Sample mean | δ Sample std. dev. | δ q | α True | α Sample mean | α Sample std. dev. | α q | Δ Sample mean | Δ Sample std. dev. | Δ q |
|---|---|---|---|---|---|---|---|---|---|---|---|---|---|---|---|---|
| Rayl. | −60° | | | | | | | | | 75° | 74.8 ± 0.25 | 7.81 ± 0.17 | 7.81 ± 0.17 | | | |
| Rayl. | −30° | | | | | | | | | 75° | 75.16 ± 0.14 | 4.29 ± 0.096 | 4.29 ± 0.094 | | | |
| Rayl. | 0° | | | | | | | | | 75° | 74.98 ± 0.12 | 3.80 ± 0.085 | 3.80 ± 0.080 | | | |
| Rayl. | 30° | | | | | | | | | 75° | 74.78 ± 0.14 | 4.45 ± 0.099 | 4.45 ± 0.096 | | | |
| Rayl. | 60° | | | | | | | | | 75° | 75.4 ± 0.24 | 7.67 ± 0.17 | 7.68 ± 0.18 | | | |
| SAP | −90° | 3% | 3.060 ± 0.014 | 0.453 ± 0.010 | 0.456 ± 0.011 | −90° | −84.23 ± 0.098 | 3.10 ± 0.069 | 6.55 ± 0.11 | 75° | 74.6 ± 0.29 | 9.2 ± 0.20 | 9.2 ± 0.21 | 5.77 ± 0.098 | 3.10 ± 0.069 | 6.55 ± 0.11 |
| SAP | −60° | 3% | 3.097 ± 0.013 | 0.418 ± 0.0094 | 0.429 ± 0.0096 | −60° | −59.85 ± 0.19 | 5.90 ± 0.13 | 5.90 ± 0.14 | 75° | 75.18 ± 0.16 | 5.18 ± 0.12 | 5.18 ± 0.12 | 6.52 ± 0.11 | 3.57 ± 0.080 | 7.43 ± 0.13 |
| SAP | −30° | 3% | 3.074 ± 0.0095 | 0.301 ± 0.0067 | 0.249 ± 0.0051 | −30° | −30.6 ± 0.24 | 7.72 ± 0.17 | 7.74 ± 0.17 | 75° | 75.10 ± 0.14 | 4.52 ± 0.10 | 4.52 ± 0.099 | 8.38 ± 0.15 | 4.84 ± 0.11 | 8.93 ± 0.15 |
| SAP | 0° | 3% | 3.041 ± 0.0078 | 0.246 ± 0.0055 | 0.304 ± 0.0066 | 0° | −0.8 ± 0.27 | 8.5 ± 0.19 | 8.57 ± 0.19 | 75° | | | | 8.43 ± 0.15 | 4.88 ± 0.11 | 9.68 ± 0.17 |
| SAP | 30° | 3% | 3.016 ± 0.0096 | 0.304 ± 0.0068 | 0.432 ± 0.0091 | 30° | 28.5 ± 0.27 | 8.40 ± 0.11 | 8.5 ± 0.20 | 75° | | | | 8.43 ± 0.15 | 4.88 ± 0.11 | 9.74 ± 0.18 |
| SAP | 60° | 3% | 2.996 ± 0.014 | 0.433 ± 0.0097 | — | 60° | 58.6 ± 0.20 | 6.43 ± 0.14 | 6.6 ± 0.19 | 75° | 74.75 ± 0.17 | 5.38 ± 0.12 | 5.38 ± 0.12 | 7.05 ± 0.13 | 4.01 ± 0.090 | 8.11 ± 0.17 |
| SAP | 90° | 3% | 2.949 ± 0.015 | 0.474 ± 0.011 | 0.477 ± 0.011 | 90° | 84.02 ± 0.10 | 3.24 ± 0.072 | 6.80 ± 0.11 | 75° | 75.4 ± 0.30 | 9.5 ± 0.21 | 9.5 ± 0.21 | 5.98 ± 0.10 | 3.24 ± 0.072 | 6.80 ± 0.11 |
| MP | −90° | 3% | 3.013 ± 0.010 | 0.324 ± 0.0072 | 0.324 ± 0.0076 | −90° | −85.48 ± 0.074 | 2.33 ± 0.052 | 5.08 ± 0.080 | 75° | 74.7 ± 0.23 | 7.36 ± 0.16 | 7.36 ± 0.16 | 4.52 ± 0.074 | 2.33 ± 0.052 | 5.08 ± 0.080 |
| MP | −60° | 3% | 3.025 ± 0.0093 | 0.295 ± 0.0066 | 0.296 ± 0.0073 | −60° | −59.66 ± 0.14 | 4.33 ± 0.097 | 4.34 ± 0.099 | 75° | 75.13 ± 0.13 | 4.02 ± 0.093 | 4.02 ± 0.093 | 5.04 ± 0.083 | 2.62 ± 0.059 | 5.68 ± 0.091 |
| MP | −30° | 3% | 3.027 ± 0.0072 | 0.226 ± 0.0051 | 0.228 ± 0.0051 | −30° | −29.87 ± 0.18 | 5.79 ± 0.13 | 5.78 ± 0.13 | 75° | 75.01 ± 0.11 | 3.52 ± 0.073 | 3.52 ± 0.073 | 5.83 ± 0.11 | 3.40 ± 0.076 | 6.75 ± 0.12 |
| MP | 0° | 3% | 3.020 ± 0.0061 | 0.193 ± 0.0043 | 0.194 ± 0.0044 | 0° | 0.3 ± 0.19 | 6.12 ± 0.14 | 6.13 ± 0.13 | 75° | | | | 6.18 ± 0.11 | 3.43 ± 0.077 | 7.06 ± 0.12 |
| MP | 30° | 3% | 3.008 ± 0.0075 | 0.237 ± 0.0053 | 0.237 ± 0.0053 | 30° | 29.51 ± 0.18 | 5.81 ± 0.13 | 5.83 ± 0.14 | 75° | | | | 6.02 ± 0.10 | 3.29 ± 0.074 | 6.86 ± 0.12 |
| MP | 60° | 3% | 3.022 ± 0.0098 | 0.310 ± 0.0069 | 0.310 ± 0.0067 | 60° | 59.67 ± 0.14 | 4.53 ± 0.10 | 4.54 ± 0.11 | 75° | 74.78 ± 0.13 | 4.18 ± 0.090 | 4.18 ± 0.090 | 5.09 ± 0.087 | 2.74 ± 0.061 | 5.78 ± 0.096 |
| MP | 90° | 3% | 3.012 ± 0.011 | 0.337 ± 0.0075 | 0.337 ± 0.0078 | 90° | 85.35 ± 0.076 | 2.41 ± 0.054 | 5.23 ± 0.083 | 75° | 75.3 ± 0.23 | 7.22 ± 0.17 | 7.22 ± 0.17 | 4.65 ± 0.076 | 2.41 ± 0.054 | 5.23 ± 0.083 |
| HR (p) | −90° | 3% | 3.041 ± 0.013 | 0.406 ± 0.0091 | 0.407 ± 0.0091 | −90° | −82.51 ± 0.12 | 3.91 ± 0.087 | 8.45 ± 0.13 | 75° | 74.2 ± 0.38 | 12.1 ± 0.27 | 12.1 ± 0.28 | 7.49 ± 0.12 | 3.91 ± 0.087 | 8.45 ± 0.13 |
| HR (p) | −60° | 3% | 3.034 ± 0.012 | 0.386 ± 0.0086 | 0.387 ± 0.0096 | −60° | −59.2 ± 0.20 | 6.31 ± 0.14 | 6.36 ± 0.17 | 75° | 75.1 ± 0.21 | 6.62 ± 0.15 | 6.62 ± 0.16 | 7.67 ± 0.13 | 4.13 ± 0.092 | 8.71 ± 0.16 |
| HR (p) | −30° | 3% | 3.055 ± 0.010 | 0.326 ± 0.0073 | 0.331 ± 0.0075 | −30° | −29.5 ± 0.24 | 7.67 ± 0.17 | 7.68 ± 0.17 | 75° | 75.0 ± 0.20 | 6.17 ± 0.14 | 6.17 ± 0.15 | 9.05 ± 0.15 | 4.60 ± 0.10 | 9.57 ± 0.16 |
| HR (p) | 0° | 3% | 3.036 ± 0.0099 | 0.312 ± 0.0070 | 0.314 ± 0.0073 | 0° | 0.7 ± 0.25 | 8.06 ± 0.18 | 8.09 ± 0.17 | 75° | | | | 9.05 ± 0.15 | 4.63 ± 0.10 | 10.16 ± 0.16 |
| HR (p) | 30° | 3% | 3.031 ± 0.011 | 0.352 ± 0.0079 | 0.353 ± 0.0083 | 30° | 29.4 ± 0.24 | 7.65 ± 0.15 | 7.67 ± 0.15 | 75° | | | | 8.60 ± 0.15 | 4.65 ± 0.10 | 9.77 ± 0.17 |
| HR (p) | 60° | 3% | 3.050 ± 0.013 | 0.403 ± 0.0090 | 0.406 ± 0.0086 | 60° | 59.4 ± 0.21 | 6.65 ± 0.15 | 6.68 ± 0.15 | 75° | 74.9 ± 0.22 | 6.99 ± 0.16 | 6.99 ± 0.16 | 7.85 ± 0.13 | 4.22 ± 0.094 | 8.92 ± 0.14 |
| HR (p) | 90° | 3% | 3.050 ± 0.014 | 0.446 ± 0.010 | 0.449 ± 0.0099 | 90° | 82.40 ± 0.13 | 4.15 ± 0.093 | 8.66 ± 0.15 | 75° | 74.8 ± 0.38 | 12.0 ± 0.27 | 12.0 ± 0.28 | 7.60 ± 0.13 | 4.15 ± 0.093 | 8.66 ± 0.15 |
| HR (p&a) | −90° | 3% | 3.016 ± 0.012 | 0.365 ± 0.0082 | 0.365 ± 0.0083 | −90° | −83.40 ± 0.10 | 3.31 ± 0.074 | 7.39 ± 0.11 | 75° | 74.3 ± 0.34 | 10.8 ± 0.24 | 10.8 ± 0.25 | 6.60 ± 0.10 | 3.31 ± 0.074 | 7.39 ± 0.11 |
| HR (p&a) | −60° | 3% | 3.030 ± 0.011 | 0.340 ± 0.0076 | 0.341 ± 0.0083 | −60° | −59.28 ± 0.17 | 5.53 ± 0.12 | 5.58 ± 0.14 | 75° | 75.05 ± 0.19 | 5.92 ± 0.13 | 5.92 ± 0.14 | 6.74 ± 0.12 | 3.71 ± 0.083 | 7.70 ± 0.14 |
| HR (p&a) | −30° | 3% | 3.026 ± 0.0087 | 0.294 ± 0.0066 | 0.296 ± 0.0064 | −30° | −29.6 ± 0.21 | 6.77 ± 0.15 | 6.78 ± 0.15 | 75° | 74.75 ± 0.17 | 5.45 ± 0.12 | 5.45 ± 0.14 | 7.96 ± 0.13 | 4.17 ± 0.093 | 8.99 ± 0.14 |
| HR (p&a) | 0° | 3% | 3.020 ± 0.010 | 0.274 ± 0.0061 | 0.275 ± 0.0061 | 0° | 0.6 ± 0.23 | 7.14 ± 0.16 | 7.16 ± 0.15 | 75° | | | | 7.42 ± 0.13 | 4.11 ± 0.092 | 8.48 ± 0.14 |
| HR (p&a) | 30° | 3% | — | 0.316 ± 0.0071 | 0.316 ± 0.0071 | 30° | 29.6 ± 0.22 | 6.86 ± 0.15 | 6.87 ± 0.16 | 75° | | | | 7.76 ± 0.13 | 4.05 ± 0.091 | 8.75 ± 0.15 |
| HR (p&a) | 60° | 3% | 3.045 ± 0.012 | 0.369 ± 0.0082 | 0.371 ± 0.0078 | 60° | 59.61 ± 0.19 | 6.02 ± 0.13 | 6.03 ± 0.14 | 75° | 74.8 ± 0.20 | 6.27 ± 0.14 | 6.27 ± 0.14 | 7.00 ± 0.12 | 3.71 ± 0.083 | 7.92 ± 0.13 |
| HR (p&a) | 90° | 3% | 3.042 ± 0.012 | 0.384 ± 0.0086 | 0.386 ± 0.0086 | 90° | 83.33 ± 0.11 | 3.62 ± 0.081 | 7.59 ± 0.13 | 75° | 75.0 ± 0.33 | 10.4 ± 0.23 | 10.4 ± 0.25 | 6.67 ± 0.11 | 3.62 ± 0.081 | 7.59 ± 0.13 |
| HR (p+ϑ̂) | −90° | 3% | 3.040 ± 0.013 | 0.406 ± 0.0091 | 0.408 ± 0.0091 | −90° | −82.52 ± 0.12 | 3.92 ± 0.088 | 8.44 ± 0.13 | 75° | 74.3 ± 0.38 | 12.1 ± 0.27 | 12.1 ± 0.28 | 7.48 ± 0.12 | 3.92 ± 0.088 | 8.44 ± 0.13 |
| HR (p+ϑ̂) | −60° | 3% | 3.034 ± 0.012 | 0.386 ± 0.0086 | 0.387 ± 0.0095 | −60° | −59.2 ± 0.20 | 6.31 ± 0.14 | 6.36 ± 0.17 | 75° | 75.1 ± 0.21 | 6.61 ± 0.16 | 6.61 ± 0.16 | 7.66 ± 0.13 | 4.14 ± 0.093 | 8.71 ± 0.16 |
| HR (p+ϑ̂) | −30° | 3% | 3.055 ± 0.010 | 0.327 ± 0.0073 | 0.331 ± 0.0075 | −30° | −29.5 ± 0.24 | 7.65 ± 0.17 | 7.67 ± 0.17 | 75° | 75.0 ± 0.20 | 6.17 ± 0.14 | 6.17 ± 0.15 | 9.05 ± 0.15 | 4.60 ± 0.10 | 9.55 ± 0.16 |
| HR (p+ϑ̂) | 0° | 3% | 3.036 ± 0.0099 | 0.312 ± 0.0070 | 0.314 ± 0.0073 | 0° | 0.7 ± 0.25 | 8.06 ± 0.18 | 8.09 ± 0.17 | 75° | | | | 9.05 ± 0.15 | 4.62 ± 0.10 | 10.16 ± 0.16 |
| HR (p+ϑ̂) | 30° | 3% | 3.031 ± 0.011 | 0.351 ± 0.0079 | 0.352 ± 0.0083 | 30° | 29.4 ± 0.24 | 7.64 ± 0.15 | 7.66 ± 0.15 | 75° | | | | 8.60 ± 0.15 | 4.63 ± 0.10 | 9.76 ± 0.17 |
| HR (p+ϑ̂) | 60° | 3% | 3.050 ± 0.013 | 0.402 ± 0.0090 | 0.405 ± 0.0086 | 60° | 59.4 ± 0.21 | 6.64 ± 0.15 | 6.66 ± 0.15 | 75° | 74.9 ± 0.22 | 6.99 ± 0.16 | 6.99 ± 0.16 | 7.84 ± 0.13 | 4.21 ± 0.094 | 8.90 ± 0.14 |
| HR (p+ϑ̂) | 90° | 3% | 3.050 ± 0.014 | 0.445 ± 0.010 | 0.448 ± 0.0099 | 90° | 82.40 ± 0.13 | 4.16 ± 0.093 | 8.66 ± 0.15 | 75° | 74.8 ± 0.38 | 12.0 ± 0.27 | 12.0 ± 0.27 | 7.60 ± 0.13 | 4.16 ± 0.093 | 8.66 ± 0.15 |
| HR (p&a+ϑ̂) | −90° | 3% | 3.016 ± 0.012 | 0.366 ± 0.0082 | 0.366 ± 0.0083 | −90° | −83.41 ± 0.10 | 3.32 ± 0.074 | 7.38 ± 0.11 | 75° | 74.3 ± 0.34 | 10.8 ± 0.24 | 10.8 ± 0.25 | 6.59 ± 0.10 | 3.32 ± 0.074 | 7.38 ± 0.11 |
| HR (p&a+ϑ̂) | −60° | 3% | 3.030 ± 0.011 | 0.339 ± 0.0076 | 0.341 ± 0.0083 | −60° | −59.29 ± 0.17 | 5.53 ± 0.12 | 5.58 ± 0.14 | 75° | 75.04 ± 0.19 | 5.91 ± 0.14 | 5.91 ± 0.14 | 6.74 ± 0.12 | 3.71 ± 0.083 | 7.69 ± 0.14 |
| HR (p&a+ϑ̂) | −30° | 3% | 3.037 ± 0.0093 | 0.294 ± 0.0066 | 0.296 ± 0.0064 | −30° | −29.6 ± 0.21 | 6.76 ± 0.15 | 6.77 ± 0.15 | 75° | 74.75 ± 0.17 | 5.45 ± 0.12 | 5.45 ± 0.13 | 7.97 ± 0.13 | 4.10 ± 0.092 | 8.47 ± 0.14 |
| HR (p&a+ϑ̂) | 0° | 3% | 3.020 ± 0.010 | 0.315 ± 0.0071 | 0.316 ± 0.0071 | 0° | 0.6 ± 0.23 | 6.86 ± 0.15 | 6.87 ± 0.16 | 75° | | | | 7.41 ± 0.13 | 4.17 ± 0.093 | 8.99 ± 0.14 |
| HR (p&a+ϑ̂) | 30° | 3% | 3.045 ± 0.012 | 0.368 ± 0.0082 | 0.370 ± 0.0078 | 30° | 29.6 ± 0.22 | 6.01 ± 0.13 | 6.02 ± 0.14 | 75° | | | | 7.76 ± 0.13 | 4.05 ± 0.091 | 8.76 ± 0.15 |
| HR (p&a+ϑ̂) | 60° | 3% | 3.043 ± 0.012 | 0.383 ± 0.0086 | 0.385 ± 0.0086 | 60° | 59.63 ± 0.19 | 6.01 ± 0.13 | 6.02 ± 0.14 | 75° | 74.7 ± 0.20 | 6.27 ± 0.14 | 6.28 ± 0.14 | 6.99 ± 0.12 | 3.70 ± 0.083 | 7.91 ± 0.13 |
| HR (p&a+ϑ̂) | 90° | 3% | 3.043 ± 0.012 | 0.383 ± 0.0086 | 0.385 ± 0.0086 | 90° | 83.33 ± 0.11 | 3.63 ± 0.081 | 7.59 ± 0.13 | 75° | 75.0 ± 0.33 | 10.4 ± 0.23 | 10.4 ± 0.25 | 6.67 ± 0.11 | 3.63 ± 0.081 | 7.59 ± 0.13 |

**Table C.6:** Tabulated data for Figures 5.12 and 6.24: $\beta = 49°$, $\vartheta_{max} = 60°$, $N = 10^6$, $D = 3\%$, $\alpha_{dipole} = 75°$

| Method | $\log_{10} N$ | $R$ | | | | $\delta$ | | | | $\alpha$ | | | | $\Delta(\delta,\alpha)$ | | |
|---|---|---|---|---|---|---|---|---|---|---|---|---|---|---|---|---|
| | | True | Sample mean | Sample std. dev | $q$ | True | Sample mean | Sample std. dev | $q$ | True | Sample mean | Sample std. dev | $q$ | Sample mean | Sample std. dev | $q$ |
| Rayl. st. | 3 | | | | | | | | | 75° | 74 ± 2.8 | 87 ± 2.0 | 87.4 ± 1.6 | | | |
| Rayl. st. | 3.5 | | | | | | | | | 75° | 73 ± 2.4 | 76.1 ± 1.7 | 76.1 ± 1.6 | | | |
| Rayl. st. | 4 | | | | | | | | | 75° | 74.6 ± 1.6 | 51.6 ± 1.2 | 51.6 ± 1.5 | | | |
| Rayl. st. | 4.5 | | | | | | | | | 75° | 75.4 ± 0.45 | 29.8 ± 0.67 | 29.7 ± 1.1 | | | |
| Rayl. st. | 5 | | | | | | | | | 75° | 75.6 ± 0.45 | 14.3 ± 0.32 | 14.3 ± 0.36 | | | |
| Rayl. st. | 5.5 | | | | | | | | | 75° | 74.8 ± 0.25 | 7.77 ± 0.17 | 7.77 ± 0.17 | | | |
| Rayl. st. | 6 | | | | | | | | | 75° | 74.78 ± 0.14 | 4.45 ± 0.099 | 4.45 ± 0.096 | | | |
| Rayl. st. | 6.5 | | | | | | | | | 75° | 74.99 ± 0.081 | 2.56 ± 0.057 | 2.55 ± 0.055 | | | |
| Rayl. st. | 7 | | | | | | | | | 75° | 74.97 ± 0.044 | 1.38 ± 0.031 | 1.38 ± 0.030 | | | |
| SAP st. | 3 | 3% | 16.2 ± 0.24 | 7.58 ± 0.17 | 15.2 ± 0.29 | 30° | −13.5 ± 1.5 | 48.9 ± 1.1 | 65.4 ± 0.94 | 75° | 72 ± 2.9 | 91 ± 2.0 | 90.9 ± 1.6 | 87.4 ± 1.2 | 36.7 ± 0.82 | 94.8 ± 1.1 |
| SAP st. | 3.5 | 3% | 9.15 ± 0.14 | 4.28 ± 0.096 | 7.49 ± 0.15 | 30° | −6.3 ± 1.5 | 48.5 ± 1.1 | 60.5 ± 0.95 | 75° | 75 ± 2.6 | 80.9 ± 1.8 | 80.8 ± 1.6 | 77.9 ± 1.1 | 36.2 ± 0.81 | 85.9 ± 1.1 |
| SAP st. | 4 | 3% | 5.78 ± 0.080 | 2.53 ± 0.057 | 3.76 ± 0.085 | 30° | 2.9 ± 1.5 | 46.6 ± 1.0 | 53.9 ± 0.96 | 75° | 71.1 ± 1.8 | 58.2 ± 1.3 | 58.3 ± 1.5 | 61.8 ± 1.0 | 32.6 ± 0.73 | 69.8 ± 1.1 |
| SAP st. | 4.5 | 3% | 3.93 ± 0.048 | 1.52 ± 0.034 | 1.78 ± 0.047 | 30° | 10.4 ± 1.2 | 37.8 ± 0.85 | 42.5 ± 0.86 | 75° | 75.6 ± 0.56 | 34.6 ± 1.3 | 34.6 ± 1.5 | 44.3 ± 0.78 | 24.7 ± 0.55 | 50.7 ± 0.87 |
| SAP st. | 5 | 3% | 3.28 ± 0.028 | 0.90 ± 0.020 | 0.94 ± 0.023 | 30° | 20.4 ± 0.82 | 25.8 ± 0.58 | 27.5 ± 0.68 | 75° | 74.7 ± 0.30 | 17.6 ± 0.39 | 17.6 ± 0.45 | 26.5 ± 0.53 | 16.7 ± 0.37 | 31.4 ± 0.64 |
| SAP st. | 5.5 | 3% | 3.052 ± 0.017 | 0.543 ± 0.012 | 0.545 ± 0.015 | 30° | 25.8 ± 0.46 | 14.7 ± 0.33 | 15.3 ± 0.39 | 75° | 74.8 ± 0.21 | 9.4 ± 0.21 | 9.4 ± 0.20 | 14.8 ± 0.29 | 9.1 ± 0.20 | 17.3 ± 0.35 |
| SAP st. | 6 | 3% | 3.016 ± 0.0096 | 0.304 ± 0.0068 | 0.304 ± 0.0066 | 30° | 28.5 ± 0.27 | 8.40 ± 0.19 | 8.5 ± 0.20 | 75° | 74.75 ± 0.17 | 5.38 ± 0.12 | 5.38 ± 0.12 | 8.43 ± 0.15 | 4.88 ± 0.11 | 9.74 ± 0.18 |
| SAP st. | 6.5 | 3% | 3.000 ± 0.0055 | 0.175 ± 0.0039 | 0.175 ± 0.0039 | 30° | 29.18 ± 0.15 | 4.79 ± 0.11 | 4.86 ± 0.12 | 75° | 75.05 ± 0.096 | 3.03 ± 0.068 | 3.03 ± 0.067 | 4.77 ± 0.088 | 2.79 ± 0.062 | 5.53 ± 0.11 |
| SAP st. | 7 | 3% | 2.996 ± 0.0033 | 0.104 ± 0.0023 | 0.104 ± 0.0024 | 30° | 29.73 ± 0.079 | 2.51 ± 0.056 | 2.52 ± 0.058 | 75° | 74.95 ± 0.052 | 1.64 ± 0.037 | 1.64 ± 0.036 | 2.53 ± 0.044 | 1.40 ± 0.031 | 2.89 ± 0.052 |
| MP st. | 3 | 3% | 12.90 ± 0.19 | 6.00 ± 0.13 | 11.6 ± 0.22 | 30° | 6.8 ± 1.6 | 49.2 ± 1.1 | 54.4 ± 1.0 | 75° | 72 ± 2.7 | 87 ± 1.9 | 86.7 ± 1.5 | 75.1 ± 1.1 | 36.3 ± 0.81 | 83.4 ± 1.1 |
| MP st. | 3.5 | 3% | 7.44 ± 0.11 | 3.43 ± 0.077 | 5.61 ± 0.13 | 30° | 11.9 ± 1.5 | 46.3 ± 1.0 | 49.7 ± 0.94 | 75° | 72 ± 2.4 | 49.1 ± 1.1 | 74.5 ± 1.6 | 65.6 ± 1.1 | 34.1 ± 0.76 | 73.9 ± 1.1 |
| MP st. | 4 | 3% | 4.96 ± 0.066 | 2.08 ± 0.047 | 2.86 ± 0.070 | 30° | 19.6 ± 1.3 | 40.4 ± 0.90 | 41.7 ± 0.87 | 75° | 74.7 ± 1.6 | 49.1 ± 1.1 | 49.1 ± 1.5 | 48.4 ± 0.85 | 27.0 ± 0.60 | 55.4 ± 0.97 |
| MP st. | 4.5 | 3% | 3.65 ± 0.039 | 1.23 ± 0.027 | 1.39 ± 0.036 | 30° | 23.4 ± 0.95 | 30.0 ± 0.67 | 30.7 ± 0.75 | 75° | 74.9 ± 0.85 | 26.9 ± 1.1 | 26.9 ± 1.1 | 31.6 ± 0.60 | 18.9 ± 0.42 | 36.8 ± 0.70 |
| MP st. | 5 | 3% | 3.20 ± 0.023 | 0.719 ± 0.016 | 0.747 ± 0.016 | 30° | 27.3 ± 0.57 | 17.9 ± 0.40 | 18.1 ± 0.44 | 75° | 75.6 ± 0.42 | 13.3 ± 0.30 | 13.3 ± 0.33 | 18.5 ± 0.34 | 10.7 ± 0.24 | 21.4 ± 0.40 |
| MP st. | 5.5 | 3% | 3.061 ± 0.013 | 0.414 ± 0.0093 | 0.419 ± 0.010 | 30° | 28.7 ± 0.33 | 10.4 ± 0.23 | 10.5 ± 0.25 | 75° | 74.8 ± 0.22 | 7.07 ± 0.16 | 7.07 ± 0.15 | 10.5 ± 0.19 | 6.10 ± 0.14 | 12.2 ± 0.23 |
| MP st. | 6 | 3% | 3.008 ± 0.0075 | 0.237 ± 0.0053 | 0.237 ± 0.0053 | 30° | 29.51 ± 0.18 | 5.81 ± 0.13 | 5.83 ± 0.14 | 75° | 74.78 ± 0.13 | 4.17 ± 0.093 | 4.18 ± 0.090 | 6.02 ± 0.10 | 3.29 ± 0.074 | 6.86 ± 0.12 |
| MP st. | 6.5 | 3% | 3.002 ± 0.0043 | 0.134 ± 0.0030 | 0.134 ± 0.0029 | 30° | 29.66 ± 0.11 | 3.38 ± 0.076 | 3.39 ± 0.081 | 75° | 74.98 ± 0.076 | 2.42 ± 0.052 | 2.42 ± 0.054 | 3.46 ± 0.063 | 1.99 ± 0.044 | 3.99 ± 0.073 |
| MP st. | 7 | 3% | 2.997 ± 0.0024 | 0.0774 ± 0.0017 | 0.0775 ± 0.0018 | 30° | 29.77 ± 0.056 | 1.78 ± 0.040 | 1.79 ± 0.037 | 75° | 74.99 ± 0.041 | 1.29 ± 0.029 | 1.29 ± 0.028 | 1.88 ± 0.031 | 0.97 ± 0.022 | 2.11 ± 0.033 |
| Rayl. int. | 3 | | | | | | | | | 75° | 76 ± 2.8 | 88 ± 2.0 | 88.4 ± 1.6 | | | |
| Rayl. int. | 3.5 | | | | | | | | | 75° | 79 ± 2.4 | 74.7 ± 1.7 | 74.7 ± 1.6 | | | |
| Rayl. int. | 4 | | | | | | | | | 75° | 75.5 ± 1.7 | 54.1 ± 1.2 | 54.1 ± 1.6 | | | |
| Rayl. int. | 4.5 | | | | | | | | | 75° | 76.6 ± 0.95 | 30.0 ± 0.67 | 30.1 ± 1.0 | | | |
| Rayl. int. | 5 | | | | | | | | | 75° | 74.7 ± 0.25 | 14.5 ± 0.46 | 14.5 ± 0.34 | | | |
| Rayl. int. | 5.5 | | | | | | | | | 75° | 74.9 ± 0.25 | 8.01 ± 0.18 | 8.01 ± 0.18 | | | |
| Rayl. int. | 6 | | | | | | | | | 75° | 75.02 ± 0.15 | 4.60 ± 0.10 | 4.59 ± 0.11 | | | |
| Rayl. int. | 6.5 | | | | | | | | | 75° | 74.88 ± 0.083 | 2.62 ± 0.059 | 2.62 ± 0.064 | | | |
| Rayl. int. | 7 | | | | | | | | | 75° | 74.97 ± 0.045 | 1.41 ± 0.032 | 1.41 ± 0.032 | | | |
| SAP int. | 3 | 3% | 16.2 ± 0.23 | 7.19 ± 0.16 | 15.0 ± 0.28 | 30° | −13.0 ± 1.6 | 49.1 ± 1.1 | 65.3 ± 0.94 | 75° | 77 ± 2.9 | 92 ± 2.1 | 91.7 ± 1.6 | 88.1 ± 1.1 | 36.3 ± 0.81 | 95.3 ± 1.1 |
| SAP int. | 3.5 | 3% | 9.49 ± 0.15 | 4.71 ± 0.11 | 8.0 ± 0.27 | 30° | −5.1 ± 1.5 | 48.7 ± 1.1 | 60.0 ± 0.95 | 75° | 76 ± 2.5 | 79.9 ± 1.8 | 79.8 ± 1.6 | 76.9 ± 1.1 | 34.8 ± 0.78 | 84.4 ± 1.1 |
| SAP int. | 4 | 3% | 5.80 ± 0.081 | 2.55 ± 0.057 | 3.78 ± 0.090 | 30° | 2.6 ± 1.5 | 46.9 ± 1.0 | 54.3 ± 0.98 | 75° | 75.7 ± 1.2 | 61.6 ± 1.4 | 61.6 ± 1.6 | 63.0 ± 1.0 | 33.2 ± 0.74 | 71.2 ± 1.1 |
| SAP int. | 4.5 | 3% | 4.11 ± 0.049 | 1.55 ± 0.035 | 1.91 ± 0.063 | 30° | 13.2 ± 1.2 | 38.3 ± 0.86 | 41.8 ± 0.87 | 75° | 75.1 ± 0.58 | 37.2 ± 0.83 | 37.1 ± 1.2 | 44.2 ± 0.82 | 25.9 ± 0.58 | 51.2 ± 0.92 |
| SAP int. | 5 | 3% | 3.27 ± 0.028 | 0.88 ± 0.020 | 0.92 ± 0.023 | 30° | 20.8 ± 0.82 | 26.0 ± 0.58 | 27.6 ± 0.66 | 75° | 74.9 ± 0.31 | 18.2 ± 0.41 | 18.2 ± 0.42 | 27.2 ± 0.51 | 16.2 ± 0.36 | 31.7 ± 0.61 |
| SAP int. | 5.5 | 3% | 3.051 ± 0.017 | 0.535 ± 0.012 | 0.588 ± 0.013 | 30° | 26.2 ± 0.47 | 14.8 ± 0.33 | 15.3 ± 0.39 | 75° | 75.1 ± 0.58 | 9.8 ± 0.22 | 9.8 ± 0.23 | 15.0 ± 0.28 | 9.0 ± 0.20 | 17.5 ± 0.36 |
| SAP int. | 6 | 3% | 3.011 ± 0.0098 | 0.310 ± 0.0069 | 0.310 ± 0.0074 | 30° | 28.3 ± 0.27 | 8.39 ± 0.19 | 8.6 ± 0.20 | 75° | 75.07 ± 0.18 | 5.56 ± 0.12 | 5.56 ± 0.13 | 8.51 ± 0.16 | 4.92 ± 0.11 | 9.83 ± 0.18 |
| SAP int. | 6.5 | 3% | 3.003 ± 0.0057 | 0.179 ± 0.0040 | 0.179 ± 0.0041 | 30° | 29.48 ± 0.15 | 4.67 ± 0.10 | 4.70 ± 0.10 | 75° | 74.76 ± 0.10 | 3.17 ± 0.071 | 3.17 ± 0.071 | 4.73 ± 0.085 | 2.69 ± 0.060 | 5.44 ± 0.096 |
| SAP int. | 7 | 3% | 2.997 ± 0.0031 | 0.099 ± 0.0022 | 0.099 ± 0.0021 | 30° | 29.87 ± 0.083 | 2.62 ± 0.059 | 2.63 ± 0.062 | 75° | 74.99 ± 0.053 | 1.69 ± 0.038 | 1.69 ± 0.037 | 2.61 ± 0.047 | 1.49 ± 0.033 | 3.00 ± 0.055 |
| MP int. | 3 | 3% | 13.0 ± 0.19 | 6.15 ± 0.14 | 11.7 ± 0.25 | 30° | 4.5 ± 1.5 | 48.5 ± 1.1 | 54.7 ± 0.96 | 75° | 75 ± 2.8 | 88 ± 2.0 | 87.8 ± 1.6 | 77.3 ± 1.2 | 37.2 ± 0.83 | 85.8 ± 1.2 |
| MP int. | 3.5 | 3% | 7.59 ± 0.11 | 3.48 ± 0.078 | 5.76 ± 0.12 | 30° | 13.0 ± 1.4 | 45.7 ± 1.0 | 48.7 ± 0.95 | 75° | 77 ± 2.3 | 73.3 ± 1.6 | 73.3 ± 1.6 | 64.5 ± 1.1 | 33.9 ± 0.76 | 72.9 ± 1.1 |
| MP int. | 4 | 3% | 4.93 ± 0.066 | 2.09 ± 0.047 | 2.84 ± 0.071 | 30° | 17.4 ± 1.3 | 41.4 ± 0.93 | 43.3 ± 0.91 | 75° | 76.3 ± 0.83 | 51.3 ± 1.1 | 51.3 ± 1.5 | 50.0 ± 0.89 | 28.2 ± 0.63 | 57.4 ± 1.0 |
| MP int. | 4.5 | 3% | 3.69 ± 0.040 | 1.28 ± 0.029 | 1.45 ± 0.039 | 30° | 24.2 ± 0.90 | 28.5 ± 0.64 | 29.1 ± 0.71 | 75° | 74.8 ± 0.44 | 26.2 ± 0.59 | 26.2 ± 0.76 | 31.4 ± 0.58 | 18.4 ± 0.41 | 36.4 ± 0.73 |
| MP int. | 5 | 3% | 3.24 ± 0.022 | 0.710 ± 0.016 | 0.749 ± 0.018 | 30° | 27.1 ± 0.60 | 19.0 ± 0.42 | 19.2 ± 0.44 | 75° | 74.8 ± 0.24 | 13.8 ± 0.33 | 13.8 ± 0.33 | 19.6 ± 0.35 | 11.1 ± 0.25 | 22.5 ± 0.41 |
| MP int. | 5.5 | 3% | 3.065 ± 0.013 | 0.422 ± 0.0094 | 0.427 ± 0.010 | 30° | 29.2 ± 0.32 | 10.2 ± 0.23 | 10.2 ± 0.25 | 75° | 74.8 ± 0.24 | 7.59 ± 0.17 | 7.58 ± 0.16 | 10.59 ± 0.19 | 5.92 ± 0.13 | 12.1 ± 0.23 |
| MP int. | 6 | 3% | 3.031 ± 0.0075 | 0.237 ± 0.0053 | 0.239 ± 0.0054 | 30° | 29.79 ± 0.19 | 5.90 ± 0.13 | 5.90 ± 0.12 | 75° | 74.98 ± 0.14 | 4.34 ± 0.097 | 4.34 ± 0.097 | 6.13 ± 0.11 | 3.36 ± 0.075 | 6.99 ± 0.12 |
| MP int. | 6.5 | 3% | 3.007 ± 0.0042 | 0.133 ± 0.0030 | 0.133 ± 0.0028 | 30° | 29.89 ± 0.10 | 3.28 ± 0.073 | 3.28 ± 0.073 | 75° | 74.87 ± 0.078 | 2.47 ± 0.055 | 2.47 ± 0.059 | 3.41 ± 0.061 | 1.93 ± 0.043 | 3.91 ± 0.067 |
| MP int. | 7 | 3% | 2.997 ± 0.0023 | 0.0736 ± 0.0016 | 0.0736 ± 0.0018 | 30° | 29.88 ± 0.057 | 1.79 ± 0.040 | 1.79 ± 0.043 | 75° | 74.98 ± 0.042 | 1.33 ± 0.030 | 1.33 ± 0.030 | 1.83 ± 0.034 | 1.08 ± 0.024 | 2.13 ± 0.040 |

**Table C.7:** Tabulated data for Figure 5.14: $\beta = 49°$, $\vartheta_{\max} = 60°$, $D = 3\%$, $\delta_{\mathrm{dipole}} = 30°$, $\alpha_{\mathrm{dipole}} = 75°$

| Method | $\alpha_{dipole}$ | True | $R$ Sample mean | Sample std. dev | $q$ | True | $\delta$ Sample mean | Sample std. dev | $q$ | True | $\alpha$ Sample mean | Sample std. dev | $q$ | $\Delta(\delta,\alpha)$ Sample mean | $q$ |
|---|---|---|---|---|---|---|---|---|---|---|---|---|---|---|---|
| Rayl. | 0° | | | | | | | | | 0° | $0.13 \pm 0.14$ | $4.41 \pm 0.099$ | $4.41 \pm 0.10$ | | |
| Rayl. | 45° | | | | | | | | | 45° | $45.09 \pm 0.14$ | $4.42 \pm 0.099$ | $4.42 \pm 0.10$ | | |
| Rayl. | 90° | | | | | | | | | 90° | $90.07 \pm 0.14$ | $4.27 \pm 0.096$ | $4.27 \pm 0.095$ | | |
| Rayl. | 135° | | | | | | | | | 135° | $135.12 \pm 0.14$ | $4.53 \pm 0.10$ | $4.53 \pm 0.11$ | | |
| Rayl. | 180° | | | | | | | | | 180° | $180.11 \pm 0.14$ | $4.50 \pm 0.10$ | $4.50 \pm 0.11$ | | |
| Rayl. | 225° | | | | | | | | | 225° | $225.24 \pm 0.14$ | $4.34 \pm 0.097$ | $4.35 \pm 0.097$ | | |
| Rayl. | 270° | | | | | | | | | 270° | $269.78 \pm 0.14$ | $4.44 \pm 0.099$ | $4.45 \pm 0.095$ | | |
| Rayl. | 315° | | | | | | | | | 315° | $314.90 \pm 0.14$ | $4.39 \pm 0.098$ | $4.39 \pm 0.099$ | | |
| SAP | 0° | 3% | $3.006 \pm 0.0099$ | $0.314 \pm 0.0070$ | $0.314 \pm 0.0074$ | 30° | $28.4 \pm 0.27$ | $8.39 \pm 0.19$ | $8.5 \pm 0.21$ | 0° | $-0.22 \pm 0.17$ | $5.40 \pm 0.12$ | $5.40 \pm 0.13$ | $4.97 \pm 0.11$ | $9.74 \pm 0.19$ |
| SAP | 45° | 3% | $3.001 \pm 0.010$ | $0.316 \pm 0.0071$ | $0.316 \pm 0.0072$ | 30° | $28.2 \pm 0.27$ | $8.49 \pm 0.19$ | $8.7 \pm 0.21$ | 45° | $45.13 \pm 0.17$ | $5.39 \pm 0.12$ | $5.39 \pm 0.13$ | $5.08 \pm 0.11$ | $9.9 \pm 0.19$ |
| SAP | 90° | 3% | $3.021 \pm 0.010$ | $0.327 \pm 0.0073$ | $0.327 \pm 0.0075$ | 30° | $28.3 \pm 0.27$ | $8.5 \pm 0.19$ | $8.7 \pm 0.21$ | 90° | $90.18 \pm 0.16$ | $5.19 \pm 0.12$ | $5.19 \pm 0.12$ | $5.08 \pm 0.11$ | $9.8 \pm 0.20$ |
| SAP | 135° | 3% | $3.011 \pm 0.010$ | $0.319 \pm 0.0071$ | $0.326 \pm 0.0075$ | 30° | $28.4 \pm 0.26$ | $8.03 \pm 0.18$ | $8.2 \pm 0.22$ | 135° | $134.96 \pm 0.17$ | $5.47 \pm 0.12$ | $5.26 \pm 0.12$ | $4.83 \pm 0.11$ | $9.5 \pm 0.20$ |
| SAP | 180° | 3% | $3.004 \pm 0.010$ | $0.326 \pm 0.0073$ | $0.319 \pm 0.0077$ | 30° | $28.2 \pm 0.26$ | $8.18 \pm 0.18$ | $8.4 \pm 0.20$ | 180° | $180.32 \pm 0.17$ | $5.25 \pm 0.12$ | $5.66 \pm 0.13$ | $4.87 \pm 0.11$ | $9.55 \pm 0.19$ |
| SAP | 225° | 3% | $3.003 \pm 0.010$ | $0.319 \pm 0.0071$ | $0.319 \pm 0.0077$ | 30° | $28.3 \pm 0.26$ | $8.06 \pm 0.18$ | $8.23 \pm 0.18$ | 225° | $225.48 \pm 0.18$ | $5.64 \pm 0.13$ | $5.66 \pm 0.13$ | $4.79 \pm 0.11$ | $9.59 \pm 0.17$ |
| SAP | 270° | 3% | $3.011 \pm 0.0098$ | $0.309 \pm 0.0069$ | $0.309 \pm 0.0067$ | 30° | $28.2 \pm 0.26$ | $8.33 \pm 0.19$ | $8.5 \pm 0.21$ | 270° | $269.75 \pm 0.17$ | $5.37 \pm 0.12$ | $5.37 \pm 0.13$ | $5.02 \pm 0.11$ | $9.7 \pm 0.20$ |
| SAP | 315° | 3% | $3.016 \pm 0.0098$ | $0.309 \pm 0.0069$ | $0.309 \pm 0.0071$ | 30° | $28.3 \pm 0.26$ | $8.32 \pm 0.19$ | $8.5 \pm 0.21$ | 315° | $314.88 \pm 0.17$ | $5.34 \pm 0.12$ | $5.33 \pm 0.12$ | $4.94 \pm 0.11$ | $9.67 \pm 0.19$ |
| MP | 0° | 3% | $3.014 \pm 0.0076$ | $0.241 \pm 0.0054$ | $0.242 \pm 0.0057$ | 30° | $29.71 \pm 0.18$ | $5.80 \pm 0.13$ | $5.81 \pm 0.14$ | 0° | $0.05 \pm 0.13$ | $4.20 \pm 0.094$ | $4.20 \pm 0.096$ | $3.28 \pm 0.073$ | $6.84 \pm 0.13$ |
| MP | 45° | 3% | $3.015 \pm 0.0073$ | $0.232 \pm 0.0052$ | $0.232 \pm 0.0050$ | 30° | $29.51 \pm 0.18$ | $5.81 \pm 0.13$ | $5.83 \pm 0.13$ | 45° | $45.11 \pm 0.13$ | $4.14 \pm 0.093$ | $4.14 \pm 0.099$ | $3.29 \pm 0.074$ | $6.84 \pm 0.13$ |
| MP | 90° | 3% | $3.023 \pm 0.0080$ | $0.253 \pm 0.0057$ | $0.254 \pm 0.0060$ | 30° | $29.5 \pm 0.19$ | $6.09 \pm 0.14$ | $6.12 \pm 0.15$ | 90° | $90.15 \pm 0.13$ | $4.04 \pm 0.092$ | $4.04 \pm 0.092$ | $3.51 \pm 0.079$ | $7.04 \pm 0.13$ |
| MP | 135° | 3% | $3.012 \pm 0.0074$ | $0.235 \pm 0.0053$ | $0.235 \pm 0.0050$ | 30° | $29.57 \pm 0.18$ | $5.71 \pm 0.13$ | $5.72 \pm 0.15$ | 135° | $135.10 \pm 0.14$ | $4.30 \pm 0.096$ | $4.30 \pm 0.10$ | $3.38 \pm 0.076$ | $6.83 \pm 0.13$ |
| MP | 180° | 3% | $3.015 \pm 0.0078$ | $0.246 \pm 0.0054$ | $0.247 \pm 0.0054$ | 30° | $29.48 \pm 0.18$ | $5.75 \pm 0.13$ | $5.77 \pm 0.14$ | 180° | $180.13 \pm 0.13$ | $4.16 \pm 0.093$ | $4.16 \pm 0.093$ | $3.37 \pm 0.075$ | $6.80 \pm 0.12$ |
| MP | 225° | 3% | $3.024 \pm 0.0077$ | $0.243 \pm 0.0054$ | $0.244 \pm 0.0056$ | 30° | $29.61 \pm 0.18$ | $5.79 \pm 0.13$ | $5.80 \pm 0.13$ | 225° | $225.26 \pm 0.13$ | $4.19 \pm 0.094$ | $4.19 \pm 0.094$ | $3.34 \pm 0.075$ | $6.84 \pm 0.12$ |
| MP | 270° | 3% | $3.019 \pm 0.0074$ | $0.234 \pm 0.0052$ | $0.235 \pm 0.0049$ | 30° | $29.53 \pm 0.18$ | $5.76 \pm 0.13$ | $5.77 \pm 0.13$ | 270° | $269.80 \pm 0.13$ | $4.24 \pm 0.095$ | $4.24 \pm 0.093$ | $3.28 \pm 0.073$ | $6.85 \pm 0.12$ |
| MP | 315° | 3% | $3.018 \pm 0.0074$ | $0.234 \pm 0.0052$ | $0.234 \pm 0.0056$ | 30° | $29.59 \pm 0.19$ | $5.87 \pm 0.13$ | $5.88 \pm 0.13$ | 315° | $314.91 \pm 0.13$ | $4.15 \pm 0.093$ | $4.15 \pm 0.093$ | $3.33 \pm 0.075$ | $6.89 \pm 0.12$ |
| HR (p) | 0° | 3% | $3.054 \pm 0.010$ | $0.330 \pm 0.0074$ | $0.334 \pm 0.0077$ | 30° | $29.7 \pm 0.24$ | $7.71 \pm 0.17$ | $7.71 \pm 0.18$ | 0° | $-0.01 \pm 0.22$ | $6.85 \pm 0.16$ | $6.85 \pm 0.16$ | $4.64 \pm 0.10$ | $9.71 \pm 0.17$ |
| HR (p) | 45° | 3% | $3.055 \pm 0.011$ | $0.333 \pm 0.0075$ | $0.338 \pm 0.0073$ | 30° | $29.4 \pm 0.25$ | $7.80 \pm 0.17$ | $7.82 \pm 0.17$ | 45° | $45.4 \pm 0.22$ | $6.91 \pm 0.15$ | $6.92 \pm 0.16$ | $4.72 \pm 0.11$ | $9.84 \pm 0.16$ |
| HR (p) | 90° | 3% | $3.051 \pm 0.011$ | $0.359 \pm 0.0080$ | $0.362 \pm 0.0081$ | 30° | $29.3 \pm 0.26$ | $8.08 \pm 0.18$ | $8.11 \pm 0.19$ | 90° | $90.0 \pm 0.21$ | $6.79 \pm 0.15$ | $6.78 \pm 0.16$ | $4.92 \pm 0.11$ | $9.99 \pm 0.16$ |
| HR (p) | 135° | 3% | $3.039 \pm 0.011$ | $0.359 \pm 0.0076$ | $0.340 \pm 0.0074$ | 30° | $29.3 \pm 0.24$ | $7.62 \pm 0.17$ | $7.64 \pm 0.18$ | 135° | $134.9 \pm 0.23$ | $7.31 \pm 0.16$ | $6.87 \pm 0.15$ | $4.65 \pm 0.10$ | $9.91 \pm 0.16$ |
| HR (p) | 180° | 3% | $3.045 \pm 0.011$ | $0.362 \pm 0.0081$ | $0.364 \pm 0.0081$ | 30° | $29.4 \pm 0.24$ | $7.66 \pm 0.17$ | $7.7 \pm 0.20$ | 180° | $180.0 \pm 0.22$ | $6.88 \pm 0.15$ | $6.99 \pm 0.16$ | $4.64 \pm 0.10$ | $9.71 \pm 0.17$ |
| HR (p) | 225° | 3% | $3.051 \pm 0.011$ | $0.362 \pm 0.0081$ | $0.366 \pm 0.0086$ | 30° | $29.4 \pm 0.25$ | $7.80 \pm 0.17$ | $7.79 \pm 0.18$ | 225° | $225.4 \pm 0.22$ | $7.04 \pm 0.16$ | $7.05 \pm 0.17$ | $4.64 \pm 0.11$ | $9.89 \pm 0.17$ |
| HR (p) | 270° | 3% | $3.033 \pm 0.011$ | $0.354 \pm 0.0079$ | $0.355 \pm 0.0074$ | 30° | $29.4 \pm 0.25$ | $7.80 \pm 0.17$ | $7.82 \pm 0.17$ | 270° | $269.9 \pm 0.22$ | $6.99 \pm 0.16$ | $6.99 \pm 0.16$ | $4.76 \pm 0.11$ | $9.89 \pm 0.17$ |
| HR (p) | 315° | 3% | $3.025 \pm 0.011$ | $0.342 \pm 0.0076$ | $0.343 \pm 0.0077$ | 30° | $29.6 \pm 0.24$ | $7.69 \pm 0.17$ | $7.69 \pm 0.17$ | 315° | $315.1 \pm 0.19$ | $6.97 \pm 0.16$ | $6.97 \pm 0.16$ | $4.63 \pm 0.10$ | $9.76 \pm 0.16$ |
| HR (p&a) | 0° | 3% | $3.036 \pm 0.0094$ | $0.299 \pm 0.0067$ | $0.301 \pm 0.0066$ | 30° | $29.8 \pm 0.21$ | $6.77 \pm 0.15$ | $6.76 \pm 0.16$ | 0° | $0.07 \pm 0.19$ | $6.06 \pm 0.14$ | $6.05 \pm 0.14$ | $4.04 \pm 0.090$ | $8.54 \pm 0.15$ |
| HR (p&a) | 45° | 3% | $3.033 \pm 0.0096$ | $0.303 \pm 0.0068$ | $0.304 \pm 0.0061$ | 30° | $29.5 \pm 0.21$ | $6.73 \pm 0.15$ | $6.75 \pm 0.15$ | 45° | $45.2 \pm 0.19$ | $6.12 \pm 0.14$ | $6.12 \pm 0.14$ | $4.03 \pm 0.090$ | $8.58 \pm 0.15$ |
| HR (p&a) | 90° | 3% | $3.032 \pm 0.0095$ | $0.322 \pm 0.0072$ | $0.324 \pm 0.0075$ | 30° | $29.3 \pm 0.21$ | $7.25 \pm 0.16$ | $7.28 \pm 0.16$ | 90° | $90.0 \pm 0.21$ | $5.82 \pm 0.14$ | $5.81 \pm 0.14$ | $4.36 \pm 0.097$ | $8.84 \pm 0.15$ |
| HR (p&a) | 135° | 3% | $3.037 \pm 0.010$ | $0.322 \pm 0.0072$ | $0.324 \pm 0.0074$ | 30° | $29.6 \pm 0.21$ | $6.73 \pm 0.15$ | $6.74 \pm 0.16$ | 135° | $135.0 \pm 0.20$ | $6.24 \pm 0.14$ | $6.23 \pm 0.14$ | $4.06 \pm 0.091$ | $8.62 \pm 0.14$ |
| HR (p&a) | 180° | 3% | $3.038 \pm 0.0098$ | $0.323 \pm 0.0072$ | $0.324 \pm 0.0068$ | 30° | $29.6 \pm 0.21$ | $6.44 \pm 0.14$ | $6.45 \pm 0.14$ | 180° | $180.0 \pm 0.20$ | $6.21 \pm 0.14$ | $6.21 \pm 0.14$ | $4.02 \pm 0.090$ | $8.39 \pm 0.15$ |
| HR (p&a) | 225° | 3% | $3.030 \pm 0.0097$ | $0.311 \pm 0.0070$ | $0.324 \pm 0.0068$ | 30° | $29.8 \pm 0.21$ | $6.45 \pm 0.14$ | $6.45 \pm 0.14$ | 225° | $225.4 \pm 0.22$ | $6.44 \pm 0.14$ | $6.44 \pm 0.14$ | $4.15 \pm 0.093$ | $8.79 \pm 0.15$ |
| HR (p&a) | 270° | 3% | $3.033 \pm 0.011$ | $0.308 \pm 0.0069$ | $0.309 \pm 0.0063$ | 30° | $29.6 \pm 0.22$ | $6.79 \pm 0.15$ | $6.82 \pm 0.16$ | 270° | $269.9 \pm 0.22$ | $6.44 \pm 0.14$ | $6.44 \pm 0.14$ | $4.08 \pm 0.091$ | $8.64 \pm 0.14$ |
| HR (p&a) | 315° | 3% | $3.017 \pm 0.0096$ | $0.305 \pm 0.0068$ | $0.305 \pm 0.0067$ | 30° | $29.7 \pm 0.22$ | $6.91 \pm 0.15$ | $6.91 \pm 0.15$ | 315° | $315.1 \pm 0.22$ | $6.16 \pm 0.14$ | $6.16 \pm 0.13$ | $4.00 \pm 0.090$ | $8.72 \pm 0.13$ |
| HR (p+θ) | 0° | 3% | $3.053 \pm 0.010$ | $0.329 \pm 0.0074$ | $0.333 \pm 0.0076$ | 30° | $29.7 \pm 0.24$ | $7.72 \pm 0.17$ | $7.72 \pm 0.18$ | 0° | $-0.01 \pm 0.22$ | $6.85 \pm 0.15$ | $6.85 \pm 0.16$ | $4.65 \pm 0.10$ | $9.72 \pm 0.17$ |
| HR (p+θ) | 45° | 3% | $3.055 \pm 0.011$ | $0.333 \pm 0.0075$ | $0.338 \pm 0.0073$ | 30° | $29.4 \pm 0.25$ | $7.78 \pm 0.17$ | $7.80 \pm 0.17$ | 45° | $45.4 \pm 0.22$ | $6.91 \pm 0.15$ | $6.91 \pm 0.16$ | $4.71 \pm 0.11$ | $9.82 \pm 0.16$ |
| HR (p+θ) | 90° | 3% | $3.039 \pm 0.011$ | $0.338 \pm 0.0080$ | $0.361 \pm 0.0081$ | 30° | $29.3 \pm 0.26$ | $8.08 \pm 0.18$ | $8.11 \pm 0.19$ | 90° | $90.0 \pm 0.21$ | $6.79 \pm 0.15$ | $6.79 \pm 0.16$ | $4.91 \pm 0.11$ | $9.99 \pm 0.16$ |
| HR (p+θ) | 135° | 3% | $3.045 \pm 0.011$ | $0.338 \pm 0.0076$ | $0.340 \pm 0.0074$ | 30° | $29.4 \pm 0.24$ | $7.60 \pm 0.17$ | $7.63 \pm 0.18$ | 135° | $134.9 \pm 0.23$ | $7.31 \pm 0.16$ | $7.31 \pm 0.16$ | $4.64 \pm 0.10$ | $9.89 \pm 0.16$ |
| HR (p+θ) | 180° | 3% | $3.051 \pm 0.011$ | $0.361 \pm 0.0081$ | $0.364 \pm 0.0081$ | 30° | $29.3 \pm 0.24$ | $7.65 \pm 0.17$ | $7.7 \pm 0.20$ | 180° | $180.0 \pm 0.22$ | $6.89 \pm 0.15$ | $6.99 \pm 0.17$ | $4.64 \pm 0.10$ | $9.71 \pm 0.17$ |
| HR (p+θ) | 225° | 3% | $3.033 \pm 0.011$ | $0.354 \pm 0.0079$ | $0.365 \pm 0.0085$ | 30° | $29.6 \pm 0.25$ | $7.79 \pm 0.17$ | $7.80 \pm 0.18$ | 225° | $225.4 \pm 0.22$ | $7.05 \pm 0.16$ | $7.06 \pm 0.17$ | $4.75 \pm 0.11$ | $9.90 \pm 0.17$ |
| HR (p+θ) | 270° | 3% | $3.033 \pm 0.011$ | $0.354 \pm 0.0079$ | $0.355 \pm 0.0075$ | 30° | $29.5 \pm 0.25$ | $7.79 \pm 0.17$ | $7.81 \pm 0.19$ | 270° | $269.9 \pm 0.22$ | $7.00 \pm 0.16$ | $6.99 \pm 0.16$ | $4.75 \pm 0.11$ | $9.89 \pm 0.17$ |
| HR (p+θ) | 315° | 3% | $3.025 \pm 0.011$ | $0.342 \pm 0.0076$ | $0.342 \pm 0.0077$ | 30° | $29.6 \pm 0.24$ | $7.67 \pm 0.17$ | $7.68 \pm 0.17$ | 315° | $315.1 \pm 0.22$ | $6.97 \pm 0.16$ | $6.97 \pm 0.16$ | $4.63 \pm 0.10$ | $9.75 \pm 0.16$ |
| HR (p&a+θ) | 0° | 3% | $3.036 \pm 0.0094$ | $0.298 \pm 0.0067$ | $0.300 \pm 0.0066$ | 30° | $29.8 \pm 0.21$ | $6.77 \pm 0.15$ | $6.77 \pm 0.16$ | 0° | $0.07 \pm 0.19$ | $6.06 \pm 0.14$ | $6.06 \pm 0.14$ | $4.05 \pm 0.091$ | $8.54 \pm 0.15$ |
| HR (p&a+θ) | 45° | 3% | $3.032 \pm 0.0096$ | $0.303 \pm 0.0068$ | $0.304 \pm 0.0061$ | 30° | $29.5 \pm 0.21$ | $6.72 \pm 0.15$ | $6.74 \pm 0.15$ | 45° | $45.2 \pm 0.19$ | $6.11 \pm 0.14$ | $6.11 \pm 0.14$ | $4.02 \pm 0.090$ | $8.56 \pm 0.13$ |
| HR (p&a+θ) | 90° | 3% | $3.039 \pm 0.010$ | $0.321 \pm 0.0072$ | $0.323 \pm 0.0074$ | 30° | $29.4 \pm 0.23$ | $7.25 \pm 0.16$ | $7.27 \pm 0.16$ | 90° | $90.01 \pm 0.18$ | $5.82 \pm 0.13$ | $5.82 \pm 0.14$ | $4.35 \pm 0.097$ | $8.83 \pm 0.15$ |
| HR (p&a+θ) | 135° | 3% | $3.032 \pm 0.0095$ | $0.321 \pm 0.0072$ | $0.323 \pm 0.0073$ | 30° | $29.6 \pm 0.21$ | $6.72 \pm 0.15$ | $6.73 \pm 0.16$ | 135° | $135.0 \pm 0.20$ | $6.22 \pm 0.14$ | $6.21 \pm 0.15$ | $4.05 \pm 0.091$ | $8.61 \pm 0.14$ |
| HR (p&a+θ) | 180° | 3% | $3.037 \pm 0.010$ | $0.321 \pm 0.0072$ | $0.323 \pm 0.0073$ | 30° | $29.5 \pm 0.20$ | $6.43 \pm 0.14$ | $6.45 \pm 0.16$ | 180° | $180.0 \pm 0.20$ | $6.23 \pm 0.14$ | $6.22 \pm 0.14$ | $4.03 \pm 0.090$ | $8.39 \pm 0.15$ |
| HR (p&a+θ) | 225° | 3% | $3.038 \pm 0.0098$ | $0.313 \pm 0.0068$ | $0.313 \pm 0.0068$ | 30° | $29.8 \pm 0.21$ | $6.79 \pm 0.15$ | $6.79 \pm 0.17$ | 225° | $225.4 \pm 0.22$ | $6.45 \pm 0.14$ | $6.46 \pm 0.15$ | $4.16 \pm 0.093$ | $8.80 \pm 0.15$ |
| HR (p&a+θ) | 270° | 3% | $3.030 \pm 0.0097$ | $0.308 \pm 0.0069$ | $0.309 \pm 0.0063$ | 30° | $29.5 \pm 0.22$ | $6.80 \pm 0.15$ | $6.81 \pm 0.16$ | 270° | $269.9 \pm 0.19$ | $6.14 \pm 0.14$ | $6.14 \pm 0.14$ | $4.07 \pm 0.091$ | $8.64 \pm 0.14$ |
| HR (p&a+θ) | 315° | 3% | $3.017 \pm 0.0096$ | $0.304 \pm 0.0068$ | $0.305 \pm 0.0067$ | 30° | $29.7 \pm 0.22$ | $6.90 \pm 0.15$ | $6.90 \pm 0.15$ | 315° | $315.1 \pm 0.19$ | $6.17 \pm 0.14$ | $6.16 \pm 0.13$ | $4.01 \pm 0.090$ | $8.71 \pm 0.13$ |

**Table C.8:** Tabulated data for Figure 5.15: $\beta = 49°$, $\vartheta_{max} = 60°$, $N = 10^6$, $D = 3\%$, $\delta_{dipole} = 30°$

| Method | $A_{\text{wss}}$ | True | $\bar{R}$ Sample mean | $\bar{R}$ Sample std. dev | $\bar{R}$ q | $\bar{\delta}$ True | $\bar{\delta}$ Sample mean | $\bar{\delta}$ Sample std. dev | $\bar{\delta}$ q | $\bar{\alpha}$ True | $\bar{\alpha}$ Sample mean | $\bar{\alpha}$ Sample std. dev | $\bar{\alpha}$ q | $\Delta(\bar{\delta},\bar{\alpha})$ Sample mean | $\Delta(\bar{\delta},\bar{\alpha})$ Sample std. dev | $\Delta(\bar{\delta},\bar{\alpha})$ q |
|---|---|---|---|---|---|---|---|---|---|---|---|---|---|---|---|---|
| Rayl. | 0% | | | | | | | | | 75° | 74.78 ± 0.14 | 4.45 ± 0.099 | 4.45 ± 0.096 | | | |
| Rayl. | 0.1% | | | | | | | | | 75° | 75.69 ± 0.14 | 4.36 ± 0.098 | 4.41 ± 0.11 | | | |
| Rayl. | 0.3% | | | | | | | | | 75° | 76.25 ± 0.13 | 4.14 ± 0.093 | 4.32 ± 0.098 | | | |
| Rayl. | 1% | | | | | | | | | 75° | 78.89 ± 0.10 | 3.26 ± 0.073 | 5.08 ± 0.093 | | | |
| Rayl. | 3% | | | | | | | | | 75° | 82.73 ± 0.070 | 2.21 ± 0.049 | 8.04 ± 0.068 | | | |
| Rayl. | 10% | | | | | | | | | 75° | 86.71 ± 0.032 | 1.00 ± 0.022 | 11.75 ± 0.032 | | | |
| SAP | 0% | 3% | 3.016 ± 0.0096 | 0.304 ± 0.0068 | 0.304 ± 0.0066 | 30° | 28.5 ± 0.27 | 8.40 ± 0.19 | 8.5 ± 0.20 | 75° | 74.75 ± 0.17 | 5.38 ± 0.12 | 5.38 ± 0.12 | 8.43 ± 0.15 | 4.88 ± 0.11 | 9.74 ± 0.18 |
| SAP | 0.1% | 3% | 3.108 ± 0.010 | 0.326 ± 0.0073 | 0.343 ± 0.0082 | 30° | 28.3 ± 0.25 | 7.82 ± 0.17 | 8.00 ± 0.17 | 75° | 75.70 ± 0.17 | 5.27 ± 0.12 | 5.32 ± 0.12 | 8.09 ± 0.14 | 4.46 ± 0.10 | 9.23 ± 0.16 |
| SAP | 0.3% | 3% | 3.240 ± 0.0098 | 0.309 ± 0.0069 | 0.391 ± 0.0085 | 30° | 26.3 ± 0.25 | 7.80 ± 0.17 | 8.6 ± 0.20 | 75° | 76.26 ± 0.15 | 4.87 ± 0.11 | 5.03 ± 0.11 | 8.30 ± 0.16 | 5.03 ± 0.11 | 9.71 ± 0.19 |
| SAP | 1% | 3% | 3.795 ± 0.0094 | 0.297 ± 0.0066 | 0.849 ± 0.0093 | 30° | 21.7 ± 0.21 | 6.69 ± 0.15 | 10.7 ± 0.21 | 75° | 78.80 ± 0.13 | 3.96 ± 0.089 | 5.49 ± 0.12 | 10.38 ± 0.17 | 5.47 ± 0.12 | 11.7 ± 0.20 |
| SAP | 3% | 3% | 5.513 ± 0.0086 | 0.272 ± 0.0061 | 2.527 ± 0.0086 | 30° | 15.17 ± 0.16 | 5.04 ± 0.11 | 15.66 ± 0.16 | 75° | 82.66 ± 0.081 | 2.56 ± 0.057 | 8.08 ± 0.081 | 16.69 ± 0.15 | 4.66 ± 0.10 | 17.33 ± 0.15 |
| SAP | 10% | 3% | 11.754 ± 0.0079 | 0.250 ± 0.0056 | 8.757 ± 0.0079 | 30° | 6.47 ± 0.074 | 2.33 ± 0.052 | 23.65 ± 0.074 | 75° | 86.71 ± 0.038 | 1.21 ± 0.027 | 11.77 ± 0.038 | 26.02 ± 0.069 | 2.19 ± 0.049 | 26.11 ± 0.069 |
| MP | 0% | 3% | 3.008 ± 0.0075 | 0.237 ± 0.0053 | 0.237 ± 0.0053 | 30° | 29.51 ± 0.18 | 5.81 ± 0.13 | 5.83 ± 0.14 | 75° | 74.78 ± 0.13 | 4.17 ± 0.093 | 4.18 ± 0.090 | 6.02 ± 0.10 | 3.29 ± 0.074 | 6.86 ± 0.12 |
| MP | 0.1% | 3% | 3.108 ± 0.0076 | 0.241 ± 0.0054 | 0.264 ± 0.0060 | 30° | 29.06 ± 0.18 | 5.75 ± 0.13 | 5.82 ± 0.13 | 75° | 75.73 ± 0.13 | 4.10 ± 0.092 | 4.16 ± 0.095 | 5.99 ± 0.11 | 3.32 ± 0.074 | 6.85 ± 0.12 |
| MP | 0.3% | 3% | 3.234 ± 0.0072 | 0.228 ± 0.0051 | 0.327 ± 0.0064 | 30° | 27.20 ± 0.17 | 5.38 ± 0.12 | 6.06 ± 0.14 | 75° | 76.25 ± 0.12 | 3.91 ± 0.088 | 4.11 ± 0.093 | 6.13 ± 0.11 | 3.48 ± 0.078 | 7.05 ± 0.13 |
| MP | 1% | 3% | 3.796 ± 0.0072 | 0.228 ± 0.0051 | 0.828 ± 0.0071 | 30° | 22.52 ± 0.15 | 4.83 ± 0.11 | 8.90 ± 0.15 | 75° | 78.87 ± 0.097 | 3.08 ± 0.069 | 4.94 ± 0.090 | 9.06 ± 0.13 | 4.07 ± 0.091 | 9.94 ± 0.14 |
| MP | 3% | 3% | 5.498 ± 0.0066 | 0.209 ± 0.0047 | 2.507 ± 0.0066 | 30° | 15.56 ± 0.11 | 3.37 ± 0.075 | 14.83 ± 0.11 | 75° | 82.69 ± 0.064 | 2.02 ± 0.045 | 7.95 ± 0.062 | 16.22 ± 0.10 | 3.15 ± 0.071 | 16.52 ± 0.10 |
| MP | 10% | 3% | 11.714 ± 0.0061 | 0.194 ± 0.0043 | 8.716 ± 0.0061 | 30° | 6.72 ± 0.053 | 1.68 ± 0.038 | 23.34 ± 0.053 | 75° | 86.73 ± 0.030 | 0.95 ± 0.021 | 11.77 ± 0.030 | 25.78 ± 0.050 | 1.58 ± 0.035 | 25.83 ± 0.050 |
| HR (p) | 0% | 3% | 3.031 ± 0.011 | 0.352 ± 0.0079 | 0.353 ± 0.0083 | 30° | 29.4 ± 0.24 | 7.65 ± 0.17 | 7.67 ± 0.19 | 75° | 74.9 ± 0.22 | 6.99 ± 0.16 | 6.99 ± 0.15 | 8.60 ± 0.15 | 4.65 ± 0.10 | 9.77 ± 0.17 |
| HR (p) | 0.1% | 3% | 3.048 ± 0.011 | 0.361 ± 0.0081 | 0.364 ± 0.0084 | 30° | 29.8 ± 0.25 | 7.81 ± 0.17 | 7.81 ± 0.17 | 75° | 75.3 ± 0.21 | 6.79 ± 0.15 | 6.79 ± 0.15 | 8.64 ± 0.14 | 4.55 ± 0.10 | 9.76 ± 0.16 |
| HR (p) | 0.3% | 3% | 3.029 ± 0.010 | 0.332 ± 0.0074 | 0.333 ± 0.0072 | 30° | 30.0 ± 0.24 | 7.64 ± 0.17 | 7.64 ± 0.17 | 75° | 74.7 ± 0.22 | 6.94 ± 0.16 | 6.94 ± 0.15 | 8.59 ± 0.14 | 4.51 ± 0.10 | 9.70 ± 0.16 |
| HR (p) | 1% | 3% | 3.035 ± 0.011 | 0.349 ± 0.0078 | 0.350 ± 0.0079 | 30° | 29.0 ± 0.24 | 7.74 ± 0.17 | 7.80 ± 0.19 | 75° | 74.8 ± 0.21 | 6.55 ± 0.15 | 6.55 ± 0.15 | 8.44 ± 0.15 | 4.65 ± 0.10 | 9.64 ± 0.17 |
| HR (p) | 3% | 3% | 3.039 ± 0.011 | 0.345 ± 0.0077 | 0.347 ± 0.0072 | 30° | 30.0 ± 0.24 | 7.48 ± 0.17 | 7.47 ± 0.16 | 75° | 74.9 ± 0.22 | 7.04 ± 0.16 | 7.04 ± 0.15 | 8.56 ± 0.14 | 4.41 ± 0.099 | 9.63 ± 0.15 |
| HR (p) | 10% | 3% | 3.054 ± 0.011 | 0.354 ± 0.0079 | 0.358 ± 0.0086 | 30° | 29.6 ± 0.24 | 7.56 ± 0.17 | 7.56 ± 0.19 | 75° | 75.3 ± 0.23 | 7.26 ± 0.16 | 7.27 ± 0.17 | 8.62 ± 0.15 | 4.70 ± 0.11 | 9.82 ± 0.17 |
| HR (pκa) | 0% | 3% | 3.020 ± 0.010 | 0.316 ± 0.0071 | 0.316 ± 0.0071 | 30° | 29.6 ± 0.22 | 6.86 ± 0.15 | 6.87 ± 0.16 | 75° | 74.8 ± 0.20 | 6.27 ± 0.14 | 6.27 ± 0.14 | 7.76 ± 0.13 | 4.05 ± 0.091 | 8.75 ± 0.15 |
| HR (pκa) | 0.1% | 3% | 3.038 ± 0.0099 | 0.315 ± 0.0070 | 0.317 ± 0.0073 | 30° | 29.9 ± 0.22 | 6.94 ± 0.16 | 6.94 ± 0.15 | 75° | 75.2 ± 0.19 | 6.06 ± 0.14 | 6.06 ± 0.14 | 7.71 ± 0.13 | 4.00 ± 0.090 | 8.69 ± 0.14 |
| HR (pκa) | 0.3% | 3% | 3.014 ± 0.0095 | 0.300 ± 0.0067 | 0.301 ± 0.0067 | 30° | 29.9 ± 0.22 | 6.89 ± 0.15 | 6.89 ± 0.15 | 75° | 74.9 ± 0.20 | 6.26 ± 0.14 | 6.26 ± 0.14 | 7.71 ± 0.13 | 4.14 ± 0.093 | 8.75 ± 0.14 |
| HR (pκa) | 1% | 3% | 3.023 ± 0.0098 | 0.311 ± 0.0070 | 0.311 ± 0.0070 | 30° | 29.1 ± 0.22 | 6.90 ± 0.15 | 6.95 ± 0.17 | 75° | 75.00 ± 0.18 | 5.78 ± 0.13 | 5.77 ± 0.14 | 7.49 ± 0.13 | 4.13 ± 0.092 | 8.55 ± 0.15 |
| HR (pκa) | 3% | 3% | 3.024 ± 0.0098 | 0.310 ± 0.0069 | 0.311 ± 0.0062 | 30° | 30.0 ± 0.21 | 6.49 ± 0.15 | 6.49 ± 0.14 | 75° | 74.8 ± 0.20 | 6.24 ± 0.14 | 6.24 ± 0.14 | 7.45 ± 0.13 | 3.96 ± 0.089 | 8.43 ± 0.14 |
| HR (pκa) | 10% | 3% | 3.037 ± 0.0098 | 0.311 ± 0.0069 | 0.313 ± 0.0072 | 30° | 29.5 ± 0.22 | 6.85 ± 0.15 | 6.86 ± 0.15 | 75° | 75.4 ± 0.20 | 6.29 ± 0.14 | 6.30 ± 0.14 | 7.76 ± 0.13 | 4.07 ± 0.091 | 8.76 ± 0.14 |
| HR (p+ϑ) | 0% | 3% | 3.031 ± 0.011 | 0.351 ± 0.0079 | 0.352 ± 0.0083 | 30° | 29.4 ± 0.24 | 7.64 ± 0.17 | 7.66 ± 0.19 | 75° | 74.9 ± 0.22 | 6.99 ± 0.16 | 6.99 ± 0.15 | 8.60 ± 0.15 | 4.63 ± 0.10 | 9.76 ± 0.17 |
| HR (p+ϑ) | 0.1% | 3% | 3.048 ± 0.011 | 0.361 ± 0.0081 | 0.364 ± 0.0083 | 30° | 29.8 ± 0.25 | 7.81 ± 0.17 | 7.81 ± 0.17 | 75° | 75.3 ± 0.21 | 6.78 ± 0.15 | 6.79 ± 0.15 | 8.64 ± 0.14 | 4.55 ± 0.10 | 9.76 ± 0.16 |
| HR (p+ϑ) | 0.3% | 3% | 3.029 ± 0.010 | 0.331 ± 0.0074 | 0.333 ± 0.0072 | 30° | 30.0 ± 0.24 | 7.64 ± 0.17 | 7.63 ± 0.17 | 75° | 74.7 ± 0.22 | 6.94 ± 0.16 | 6.94 ± 0.15 | 8.58 ± 0.14 | 4.51 ± 0.10 | 9.70 ± 0.16 |
| HR (p+ϑ) | 1% | 3% | 3.035 ± 0.011 | 0.348 ± 0.0078 | 0.350 ± 0.0078 | 30° | 29.0 ± 0.24 | 7.73 ± 0.17 | 7.79 ± 0.19 | 75° | 74.8 ± 0.21 | 6.55 ± 0.15 | 6.54 ± 0.15 | 8.43 ± 0.15 | 4.64 ± 0.10 | 9.62 ± 0.17 |
| HR (p+ϑ) | 3% | 3% | 3.039 ± 0.011 | 0.345 ± 0.0077 | 0.347 ± 0.0071 | 30° | 30.0 ± 0.24 | 7.47 ± 0.17 | 7.47 ± 0.16 | 75° | 74.9 ± 0.22 | 7.04 ± 0.16 | 7.04 ± 0.15 | 8.55 ± 0.14 | 4.42 ± 0.099 | 9.62 ± 0.15 |
| HR (p+ϑ) | 10% | 3% | 3.055 ± 0.011 | 0.354 ± 0.0079 | 0.358 ± 0.0086 | 30° | 29.6 ± 0.24 | 7.57 ± 0.17 | 7.57 ± 0.17 | 75° | 75.3 ± 0.23 | 7.25 ± 0.16 | 7.26 ± 0.17 | 8.62 ± 0.15 | 4.70 ± 0.11 | 9.82 ± 0.17 |
| HR (pκa+ϑ) | 0% | 3% | 3.020 ± 0.010 | 0.315 ± 0.0071 | 0.316 ± 0.0071 | 30° | 29.6 ± 0.22 | 6.86 ± 0.15 | 6.87 ± 0.16 | 75° | 74.7 ± 0.20 | 6.27 ± 0.14 | 6.28 ± 0.14 | 7.76 ± 0.13 | 4.05 ± 0.091 | 8.76 ± 0.15 |
| HR (pκa+ϑ) | 0.1% | 3% | 3.038 ± 0.0099 | 0.314 ± 0.0070 | 0.316 ± 0.0073 | 30° | 29.9 ± 0.22 | 6.94 ± 0.16 | 6.94 ± 0.15 | 75° | 75.3 ± 0.19 | 6.06 ± 0.14 | 6.06 ± 0.14 | 7.71 ± 0.13 | 4.01 ± 0.090 | 8.69 ± 0.14 |
| HR (pκa+ϑ) | 0.3% | 3% | 3.014 ± 0.0095 | 0.300 ± 0.0067 | 0.300 ± 0.0067 | 30° | 29.9 ± 0.22 | 6.88 ± 0.15 | 6.88 ± 0.15 | 75° | 74.9 ± 0.20 | 6.25 ± 0.14 | 6.25 ± 0.14 | 7.71 ± 0.13 | 4.14 ± 0.093 | 8.75 ± 0.14 |
| HR (pκa+ϑ) | 1% | 3% | 3.023 ± 0.0098 | 0.310 ± 0.0069 | 0.311 ± 0.0070 | 30° | 29.1 ± 0.22 | 6.89 ± 0.15 | 6.94 ± 0.17 | 75° | 75.00 ± 0.18 | 5.77 ± 0.13 | 5.77 ± 0.14 | 7.48 ± 0.13 | 4.12 ± 0.093 | 8.54 ± 0.15 |
| HR (pκa+ϑ) | 3% | 3% | 3.024 ± 0.0098 | 0.310 ± 0.0069 | 0.311 ± 0.0062 | 30° | 30.0 ± 0.21 | 6.49 ± 0.15 | 6.49 ± 0.14 | 75° | 74.8 ± 0.20 | 6.24 ± 0.14 | 6.24 ± 0.14 | 7.45 ± 0.13 | 3.96 ± 0.089 | 8.43 ± 0.14 |
| HR (pκa+ϑ) | 10% | 3% | 3.038 ± 0.0098 | 0.310 ± 0.0069 | 0.312 ± 0.0072 | 30° | 29.5 ± 0.22 | 6.85 ± 0.15 | 6.86 ± 0.15 | 75° | 75.4 ± 0.20 | 6.28 ± 0.14 | 6.29 ± 0.14 | 7.75 ± 0.13 | 4.07 ± 0.091 | 8.75 ± 0.14 |

**Table C.9:** Tabulated data for Figures 5.16 and 6.25: $\beta = 49°$, $\vartheta_{\max} = 60°$, $N = 10^6$, $D = 3\%$, $\delta_{\text{dipole}} = 30°$, $\alpha_{\text{dipole}} = 75°$

| Method | Δ | R True | R Sample mean | R Sample std. dev. | R q | δ True | δ Sample mean | δ Sample std. dev. | δ q | α True | α Sample mean | α Sample std. dev. | α q | Δ(δ,α) Sample mean | Δ(δ,α) Sample std. dev. | Δ(δ,α) q |
|---|---|---|---|---|---|---|---|---|---|---|---|---|---|---|---|---|
| Rayl. | 0° | | | | | | | | | 75° | 74.78 ± 0.14 | 4.45 ± 0.099 | 4.45 ± 0.096 | | | |
| Rayl. | 0.1° | | | | | | | | | 75° | 74.93 ± 0.15 | 4.60 ± 0.10 | 4.59 ± 0.11 | | | |
| Rayl. | 0.3° | | | | | | | | | 75° | 75.02 ± 0.14 | 4.42 ± 0.099 | 4.42 ± 0.10 | | | |
| Rayl. | 1° | | | | | | | | | 75° | 74.71 ± 0.13 | 4.08 ± 0.091 | 4.09 ± 0.091 | | | |
| Rayl. | 3° | | | | | | | | | 75° | 75.02 ± 0.14 | 4.41 ± 0.099 | 4.41 ± 0.099 | | | |
| SAP | 0° | 3% | 3.016 ± 0.0096 | 0.304 ± 0.0068 | 0.304 ± 0.0066 | 30° | 28.5 ± 0.27 | 8.40 ± 0.19 | 8.5 ± 0.20 | 75° | 74.75 ± 0.17 | 5.38 ± 0.12 | 5.38 ± 0.12 | 8.43 ± 0.15 | 4.88 ± 0.11 | 9.74 ± 0.18 |
| SAP | 0.1° | 3% | 3.013 ± 0.010 | 0.323 ± 0.0072 | 0.323 ± 0.0079 | 30° | 28.1 ± 0.26 | 8.38 ± 0.19 | 8.6 ± 0.22 | 75° | 74.93 ± 0.17 | 5.34 ± 0.12 | 5.34 ± 0.12 | 8.36 ± 0.16 | 5.04 ± 0.11 | 9.8 ± 0.20 |
| SAP | 0.3° | 3% | 3.013 ± 0.0098 | 0.310 ± 0.0069 | 0.310 ± 0.0067 | 30° | 28.2 ± 0.26 | 8.27 ± 0.19 | 8.5 ± 0.20 | 75° | 75.16 ± 0.17 | 5.41 ± 0.12 | 5.41 ± 0.13 | 8.30 ± 0.15 | 5.00 ± 0.11 | 9.69 ± 0.19 |
| SAP | 1° | 3% | 3.011 ± 0.0097 | 0.305 ± 0.0068 | 0.306 ± 0.0067 | 30° | 28.2 ± 0.26 | 8.21 ± 0.18 | 8.4 ± 0.20 | 75° | 74.80 ± 0.16 | 4.99 ± 0.11 | 5.00 ± 0.11 | 8.11 ± 0.15 | 4.88 ± 0.11 | 9.46 ± 0.19 |
| SAP | 3° | 3% | 3.004 ± 0.0097 | 0.308 ± 0.0069 | 0.308 ± 0.0074 | 30° | 28.1 ± 0.26 | 8.35 ± 0.19 | 8.6 ± 0.20 | 75° | 75.17 ± 0.17 | 5.24 ± 0.12 | 5.24 ± 0.11 | 8.38 ± 0.16 | 4.92 ± 0.11 | 9.71 ± 0.19 |
| MP | 0° | 3% | 3.008 ± 0.0075 | 0.237 ± 0.0053 | 0.237 ± 0.0053 | 30° | 29.51 ± 0.18 | 5.81 ± 0.13 | 5.83 ± 0.14 | 75° | 74.78 ± 0.13 | 4.17 ± 0.093 | 4.18 ± 0.090 | 6.02 ± 0.10 | 3.29 ± 0.074 | 6.86 ± 0.12 |
| MP | 0.1° | 3% | 3.030 ± 0.0078 | 0.248 ± 0.0056 | 0.250 ± 0.0056 | 30° | 29.76 ± 0.18 | 5.64 ± 0.13 | 5.64 ± 0.13 | 75° | 74.98 ± 0.14 | 4.28 ± 0.096 | 4.27 ± 0.097 | 5.89 ± 0.10 | 3.29 ± 0.074 | 6.74 ± 0.12 |
| MP | 0.3° | 3% | 3.024 ± 0.0075 | 0.238 ± 0.0053 | 0.239 ± 0.0051 | 30° | 29.36 ± 0.19 | 5.87 ± 0.13 | 5.90 ± 0.14 | 75° | 75.10 ± 0.13 | 4.19 ± 0.094 | 4.19 ± 0.095 | 6.06 ± 0.11 | 3.37 ± 0.075 | 6.93 ± 0.13 |
| MP | 1° | 3% | 3.019 ± 0.0074 | 0.235 ± 0.0053 | 0.236 ± 0.0055 | 30° | 29.18 ± 0.19 | 5.86 ± 0.13 | 5.92 ± 0.13 | 75° | 74.78 ± 0.12 | 3.85 ± 0.086 | 3.86 ± 0.086 | 5.88 ± 0.11 | 3.41 ± 0.076 | 6.80 ± 0.12 |
| MP | 3° | 3% | 3.018 ± 0.0073 | 0.230 ± 0.0052 | 0.231 ± 0.0055 | 30° | 29.63 ± 0.19 | 5.89 ± 0.13 | 5.90 ± 0.13 | 75° | 75.08 ± 0.13 | 4.11 ± 0.092 | 4.11 ± 0.091 | 6.06 ± 0.10 | 3.27 ± 0.073 | 6.89 ± 0.11 |
| HR (p) | 0° | 3% | 3.031 ± 0.011 | 0.352 ± 0.0079 | 0.353 ± 0.0083 | 30° | 29.4 ± 0.24 | 7.65 ± 0.17 | 7.67 ± 0.19 | 75° | 74.9 ± 0.22 | 6.99 ± 0.16 | 6.99 ± 0.15 | 8.60 ± 0.15 | 4.65 ± 0.10 | 9.77 ± 0.17 |
| HR (p) | 0.1° | 3% | 3.068 ± 0.011 | 0.355 ± 0.0079 | 0.361 ± 0.0082 | 30° | 29.7 ± 0.24 | 7.48 ± 0.17 | 7.49 ± 0.17 | 75° | 75.1 ± 0.22 | 7.05 ± 0.16 | 7.04 ± 0.16 | 8.55 ± 0.14 | 4.47 ± 0.10 | 9.64 ± 0.16 |
| HR (p) | 0.3° | 3% | 3.046 ± 0.011 | 0.349 ± 0.0078 | 0.352 ± 0.0076 | 30° | 29.4 ± 0.24 | 7.55 ± 0.17 | 7.58 ± 0.18 | 75° | 75.1 ± 0.23 | 7.19 ± 0.16 | 7.19 ± 0.16 | 8.71 ± 0.14 | 4.50 ± 0.10 | 9.80 ± 0.16 |
| HR (p) | 1° | 3% | 3.040 ± 0.011 | 0.354 ± 0.0079 | 0.356 ± 0.0080 | 30° | 29.2 ± 0.24 | 7.56 ± 0.17 | 7.60 ± 0.18 | 75° | 74.9 ± 0.21 | 6.71 ± 0.15 | 6.71 ± 0.15 | 8.38 ± 0.15 | 4.61 ± 0.10 | 9.56 ± 0.17 |
| HR (p) | 3° | 3% | 3.053 ± 0.011 | 0.344 ± 0.0077 | 0.348 ± 0.0076 | 30° | 29.5 ± 0.25 | 7.80 ± 0.17 | 7.81 ± 0.17 | 75° | 75.3 ± 0.22 | 6.91 ± 0.15 | 6.91 ± 0.16 | 8.70 ± 0.14 | 4.58 ± 0.10 | 9.83 ± 0.16 |
| HR (p&α) | 0° | 3% | 3.020 ± 0.010 | 0.316 ± 0.0071 | 0.316 ± 0.0071 | 30° | 29.6 ± 0.22 | 6.86 ± 0.15 | 6.87 ± 0.16 | 75° | 74.8 ± 0.20 | 6.27 ± 0.14 | 6.27 ± 0.14 | 7.76 ± 0.13 | 4.05 ± 0.091 | 8.75 ± 0.15 |
| HR (p&α) | 0.1° | 3% | 3.052 ± 0.010 | 0.320 ± 0.0072 | 0.324 ± 0.0076 | 30° | 29.9 ± 0.21 | 6.65 ± 0.15 | 6.65 ± 0.15 | 75° | 75.1 ± 0.20 | 6.32 ± 0.14 | 6.31 ± 0.14 | 7.60 ± 0.13 | 4.01 ± 0.090 | 8.59 ± 0.14 |
| HR (p&α) | 0.3° | 3% | 3.036 ± 0.0098 | 0.310 ± 0.0069 | 0.312 ± 0.0069 | 30° | 29.5 ± 0.21 | 6.77 ± 0.15 | 6.79 ± 0.16 | 75° | 75.2 ± 0.21 | 6.49 ± 0.15 | 6.49 ± 0.15 | 7.82 ± 0.13 | 4.06 ± 0.091 | 8.81 ± 0.15 |
| HR (p&α) | 1° | 3% | 3.034 ± 0.0099 | 0.313 ± 0.0070 | 0.315 ± 0.0072 | 30° | 29.2 ± 0.22 | 6.93 ± 0.15 | 6.97 ± 0.16 | 75° | 74.89 ± 0.19 | 6.00 ± 0.13 | 5.99 ± 0.13 | 7.60 ± 0.13 | 4.20 ± 0.094 | 8.68 ± 0.15 |
| HR (p&α) | 3° | 3% | 3.048 ± 0.0095 | 0.299 ± 0.0067 | 0.303 ± 0.0069 | 30° | 29.6 ± 0.22 | 6.83 ± 0.15 | 6.84 ± 0.14 | 75° | 75.17 ± 0.19 | 6.01 ± 0.13 | 6.01 ± 0.14 | 7.56 ± 0.13 | 4.06 ± 0.091 | 8.58 ± 0.14 |
| HR (p+ϑ) | 0° | 3% | 3.031 ± 0.011 | 0.351 ± 0.0079 | 0.352 ± 0.0083 | 30° | 29.4 ± 0.24 | 7.64 ± 0.17 | 7.66 ± 0.19 | 75° | 74.9 ± 0.22 | 6.99 ± 0.16 | 6.99 ± 0.15 | 8.60 ± 0.15 | 4.63 ± 0.10 | 9.76 ± 0.17 |
| HR (p+ϑ) | 0.1° | 3% | 3.067 ± 0.011 | 0.355 ± 0.0079 | 0.361 ± 0.0082 | 30° | 29.7 ± 0.24 | 7.48 ± 0.17 | 7.48 ± 0.17 | 75° | 75.1 ± 0.22 | 7.05 ± 0.16 | 7.05 ± 0.16 | 8.54 ± 0.14 | 4.47 ± 0.10 | 9.64 ± 0.16 |
| HR (p+ϑ) | 0.3° | 3% | 3.046 ± 0.011 | 0.349 ± 0.0078 | 0.352 ± 0.0076 | 30° | 29.4 ± 0.24 | 7.54 ± 0.17 | 7.56 ± 0.18 | 75° | 75.1 ± 0.23 | 7.20 ± 0.16 | 7.20 ± 0.16 | 8.70 ± 0.14 | 4.50 ± 0.10 | 9.79 ± 0.16 |
| HR (p+ϑ) | 1° | 3% | 3.040 ± 0.011 | 0.353 ± 0.0079 | 0.355 ± 0.0079 | 30° | 29.2 ± 0.24 | 7.57 ± 0.17 | 7.60 ± 0.18 | 75° | 74.9 ± 0.21 | 6.71 ± 0.15 | 6.70 ± 0.15 | 8.38 ± 0.15 | 4.61 ± 0.10 | 9.56 ± 0.17 |
| HR (p+ϑ) | 3° | 3% | 3.053 ± 0.011 | 0.344 ± 0.0077 | 0.348 ± 0.0076 | 30° | 29.5 ± 0.25 | 7.79 ± 0.17 | 7.80 ± 0.17 | 75° | 75.3 ± 0.22 | 6.91 ± 0.15 | 6.91 ± 0.16 | 8.68 ± 0.14 | 4.58 ± 0.10 | 9.82 ± 0.16 |
| HR (p&α+ϑ) | 0° | 3% | 3.020 ± 0.010 | 0.315 ± 0.0071 | 0.316 ± 0.0071 | 30° | 29.6 ± 0.22 | 6.86 ± 0.15 | 6.87 ± 0.16 | 75° | 74.7 ± 0.20 | 6.28 ± 0.14 | 6.28 ± 0.14 | 7.76 ± 0.13 | 4.05 ± 0.091 | 8.76 ± 0.15 |
| HR (p&α+ϑ) | 0.1° | 3% | 3.051 ± 0.010 | 0.319 ± 0.0071 | 0.323 ± 0.0076 | 30° | 29.9 ± 0.21 | 6.64 ± 0.15 | 6.64 ± 0.15 | 75° | 75.1 ± 0.20 | 6.32 ± 0.14 | 6.31 ± 0.14 | 7.59 ± 0.13 | 4.01 ± 0.090 | 8.59 ± 0.14 |
| HR (p&α+ϑ) | 0.3° | 3% | 3.036 ± 0.0098 | 0.310 ± 0.0069 | 0.312 ± 0.0069 | 30° | 29.5 ± 0.21 | 6.77 ± 0.15 | 6.79 ± 0.16 | 75° | 75.2 ± 0.21 | 6.50 ± 0.15 | 6.50 ± 0.15 | 7.82 ± 0.13 | 4.06 ± 0.091 | 8.81 ± 0.15 |
| HR (p&α+ϑ) | 1° | 3% | 3.034 ± 0.0099 | 0.313 ± 0.0070 | 0.314 ± 0.0072 | 30° | 29.2 ± 0.22 | 6.93 ± 0.15 | 6.97 ± 0.16 | 75° | 74.90 ± 0.19 | 6.00 ± 0.13 | 5.99 ± 0.13 | 7.60 ± 0.13 | 4.21 ± 0.094 | 8.69 ± 0.15 |
| HR (p&α+ϑ) | 3° | 3% | 3.047 ± 0.0094 | 0.299 ± 0.0067 | 0.302 ± 0.0068 | 30° | 29.6 ± 0.22 | 6.83 ± 0.15 | 6.84 ± 0.14 | 75° | 75.17 ± 0.19 | 6.00 ± 0.13 | 6.00 ± 0.14 | 7.56 ± 0.13 | 4.05 ± 0.091 | 8.57 ± 0.14 |

**Table C.10:** Tabulated data for Figures 5.17 and 6.26: $\beta = 49°$, $\vartheta_{max} = 60°$, $N = 10^6$, $D = 3\%$, $\delta_{dipole} = 30°$, $\alpha_{dipole} = 75°$

| Method | $\vartheta_{l.e.}$ | R True | R Sample mean | R Sample std. dev. | R q | δ True | δ Sample mean | δ Sample std. dev. | δ q | α True | α Sample mean | α Sample std. dev. | α q | Δ(δ,α) Sample mean | Δ(δ,α) Sample std. dev. | Δ(δ,α) q |
|---|---|---|---|---|---|---|---|---|---|---|---|---|---|---|---|---|
| Rayl. | 30° | | | | | | | | | 75° | 75.09±0.15 | 4.81±0.11 | 4.80±0.11 | | | |
| Rayl. | 40° | | | | | | | | | 75° | 75.09±0.15 | 4.67±0.11 | 4.67±0.11 | | | |
| Rayl. | 50° | | | | | | | | | 75° | 75.06±0.15 | 4.53±0.10 | 4.53±0.10 | | | |
| Rayl. | 55° | | | | | | | | | 75° | 75.05±0.15 | 4.70±0.11 | 4.70±0.11 | | | |
| Rayl. | 58° | | | | | | | | | 75° | 74.87±0.14 | 4.56±0.096 | 4.56±0.096 | | | |
| Rayl. | 60° | | | | | | | | | 75° | 74.78±0.14 | 4.45±0.099 | 4.45±0.096 | | | |
| SAP | 30° | 3% | 681.87±0.15 | 4.68±0.10 | 678.89±0.15 | 30° | 89.3340±0.0017 | 0.0535±0.0012 | 59.3340±0.0017 | 75° | 75.11±0.15 | 4.66±0.10 | 4.66±0.10 | 59.3362±0.0017 | 0.0535±0.0012 | 59.3362±0.0017 |
| SAP | 40° | 3% | 307.31±0.11 | 3.58±0.080 | 304.33±0.11 | 30° | 89.063±0.0024 | 0.0762±0.0017 | 59.063±0.0024 | 75° | 75.13±0.15 | 4.63±0.11 | 4.63±0.11 | 59.066±0.0024 | 0.0761±0.0017 | 59.066±0.0024 |
| SAP | 50° | 3% | 112.72±0.035 | 1.12±0.025 | 109.73±0.035 | 30° | 88.215±0.0046 | 0.145±0.0032 | 58.215±0.0046 | 75° | 75.15±0.15 | 4.64±0.10 | 4.64±0.10 | 58.221±0.0046 | 0.145±0.0032 | 58.221±0.0046 |
| SAP | 55° | 3% | 46.613±0.018 | 0.579±0.013 | 43.617±0.018 | 30° | 86.355±0.0095 | 0.300±0.0067 | 56.356±0.0095 | 75° | 75.12±0.15 | 4.89±0.11 | 4.89±0.11 | 56.369±0.0095 | 0.300±0.0067 | 56.370±0.0095 |
| SAP | 58° | 3% | 14.267±0.014 | 0.450±0.010 | 11.276±0.014 | 30° | 79.04±0.030 | 0.96±0.022 | 49.05±0.030 | 75° | 74.91±0.16 | 5.07±0.11 | 5.07±0.11 | 49.09±0.030 | 0.96±0.022 | 49.10±0.030 |
| SAP | 60° | 3% | 3.016±0.0096 | 0.304±0.0068 | 0.304±0.0066 | 30° | 28.5±0.27 | 8.40±0.19 | 8.5±0.20 | 75° | 74.75±0.17 | 5.38±0.12 | 5.38±0.12 | 8.43±0.15 | 4.88±0.11 | 9.74±0.18 |
| MP | 30° | 3% | 243.33±0.042 | 1.33±0.030 | 240.33±0.042 | 30° | 88.699±0.0032 | 0.101±0.0023 | 58.699±0.0032 | 75° | 75.12±0.14 | 4.55±0.10 | 4.55±0.10 | 58.703±0.0032 | 0.101±0.0023 | 58.703±0.0032 |
| MP | 40° | 3% | 122.39±0.024 | 0.760±0.017 | 119.39±0.024 | 30° | 88.090±0.0046 | 0.147±0.0033 | 58.090±0.0046 | 75° | 75.17±0.14 | 4.45±0.099 | 4.45±0.10 | 58.096±0.0046 | 0.147±0.0033 | 58.096±0.0046 |
| MP | 50° | 3% | 43.889±0.015 | 0.468±0.010 | 40.892±0.015 | 30° | 85.908±0.0097 | 0.306±0.0068 | 55.909±0.0097 | 75° | 75.12±0.13 | 4.22±0.094 | 4.22±0.094 | 55.920±0.0097 | 0.307±0.0069 | 55.921±0.0097 |
| MP | 55° | 3% | 17.230±0.013 | 0.402±0.0090 | 14.236±0.013 | 30° | 80.70±0.021 | 0.672±0.015 | 50.70±0.021 | 75° | 75.07±0.14 | 4.45±0.10 | 4.45±0.095 | 50.73±0.021 | 0.671±0.015 | 50.73±0.021 |
| MP | 58° | 3% | 5.828±0.010 | 0.322±0.0072 | 2.847±0.010 | 30° | 62.94±0.070 | 2.23±0.050 | 33.02±0.070 | 75° | 74.92±0.14 | 4.29±0.096 | 4.29±0.095 | 33.06±0.070 | 2.22±0.050 | 33.13±0.070 |
| MP | 60° | 3% | 3.008±0.0075 | 0.237±0.0053 | 0.237±0.0053 | 30° | 29.51±0.18 | 5.81±0.13 | 5.83±0.14 | 75° | 74.78±0.13 | 4.17±0.093 | 4.18±0.090 | 6.02±0.10 | 3.29±0.074 | 6.86±0.12 |
| HR (p) | 30° | 3% | 2.164±0.011 | 0.342±0.0077 | 0.903±0.010 | 30° | 28.9±0.34 | 10.7±0.24 | 10.8±0.23 | 75° | 75.3±0.32 | 10.2±0.23 | 10.2±0.24 | 12.3±0.21 | 6.59±0.15 | 13.9±0.23 |
| HR (p) | 40° | 3% | 2.477±0.011 | 0.355±0.0079 | 0.632±0.010 | 30° | 29.8±0.30 | 9.5±0.21 | 9.5±0.21 | 75° | 75.1±0.27 | 8.6±0.19 | 8.6±0.20 | 10.59±0.16 | 5.78±0.13 | 12.1±0.20 |
| HR (p) | 50° | 3% | 2.813±0.011 | 0.353±0.0079 | 0.399±0.0090 | 30° | 29.7±0.26 | 8.15±0.18 | 8.2±0.19 | 75° | 75.0±0.24 | 7.52±0.17 | 7.52±0.17 | 8.80±0.15 | 4.98±0.11 | 10.42±0.18 |
| HR (p) | 55° | 3% | 2.958±0.011 | 0.340±0.0076 | 0.343±0.0074 | 30° | 29.8±0.25 | 7.81±0.17 | 7.81±0.17 | 75° | 75.1±0.23 | 7.24±0.16 | 7.23±0.17 | 8.79±0.15 | 4.73±0.11 | 9.99±0.17 |
| HR (p) | 58° | 3% | 3.004±0.011 | 0.350±0.0078 | 0.350±0.0075 | 30° | 29.6±0.25 | 7.79±0.17 | 7.80±0.17 | 75° | 75.0±0.22 | 7.11±0.16 | 7.10±0.16 | 8.60±0.15 | 4.59±0.10 | 9.91±0.16 |
| HR (p) | 60° | 3% | 3.031±0.011 | 0.352±0.0079 | 0.353±0.0083 | 30° | 29.4±0.24 | 7.65±0.17 | 7.67±0.19 | 75° | 74.9±0.22 | 6.99±0.15 | 6.99±0.15 | 8.60±0.15 | 4.65±0.10 | 9.77±0.17 |
| HR (p&a) | 30° | 3% | 2.152±0.0095 | 0.301±0.0067 | 0.900±0.0093 | 30° | 29.3±0.30 | 9.5±0.21 | 9.5±0.21 | 75° | 75.3±0.29 | 9.0±0.20 | 9.0±0.22 | 10.80±0.19 | 5.88±0.13 | 12.3±0.20 |
| HR (p&a) | 40° | 3% | 2.468±0.0099 | 0.312±0.0070 | 0.617±0.0094 | 30° | 30.1±0.26 | 8.32±0.19 | 8.32±0.17 | 75° | 75.2±0.24 | 7.61±0.17 | 7.61±0.17 | 9.37±0.16 | 4.94±0.11 | 10.59±0.17 |
| HR (p&a) | 50° | 3% | 2.789±0.0099 | 0.314±0.0070 | 0.378±0.0082 | 30° | 29.6±0.23 | 7.22±0.16 | 7.23±0.18 | 75° | 75.1±0.21 | 6.53±0.15 | 6.53±0.14 | 8.06±0.14 | 4.37±0.098 | 9.17±0.16 |
| HR (p&a) | 55° | 3% | 2.943±0.0096 | 0.303±0.0068 | 0.308±0.0066 | 30° | 29.8±0.22 | 7.02±0.16 | 7.02±0.15 | 75° | 75.0±0.20 | 6.38±0.14 | 6.38±0.15 | 7.90±0.13 | 4.13±0.092 | 8.91±0.14 |
| HR (p&a) | 58° | 3% | 2.994±0.0099 | 0.313±0.0070 | 0.312±0.0068 | 30° | 29.7±0.22 | 6.81±0.15 | 6.81±0.15 | 75° | 75.0±0.20 | 6.32±0.14 | 6.32±0.14 | 7.72±0.13 | 4.09±0.091 | 8.74±0.14 |
| HR (p&a) | 60° | 3% | 3.020±0.010 | 0.316±0.0071 | 0.316±0.0071 | 30° | 29.6±0.22 | 6.86±0.15 | 6.87±0.16 | 75° | 74.8±0.20 | 6.27±0.14 | 6.27±0.14 | 7.76±0.13 | 4.05±0.091 | 8.75±0.15 |
| HR (p+f) | 30° | 3% | 3.088±0.015 | 0.490±0.011 | 0.497±0.011 | 30° | 28.8±0.34 | 10.7±0.24 | 10.8±0.23 | 75° | 75.3±0.32 | 10.2±0.23 | 10.2±0.24 | 12.3±0.21 | 6.59±0.15 | 13.9±0.23 |
| HR (p+f) | 40° | 3% | 3.059±0.014 | 0.438±0.0098 | 0.442±0.010 | 30° | 29.7±0.30 | 9.6±0.21 | 9.6±0.21 | 75° | 75.1±0.27 | 8.6±0.19 | 8.6±0.20 | 10.60±0.18 | 5.77±0.13 | 12.1±0.20 |
| HR (p+f) | 50° | 3% | 3.064±0.012 | 0.384±0.0086 | 0.389±0.0092 | 30° | 29.7±0.26 | 8.16±0.18 | 8.2±0.19 | 75° | 75.0±0.24 | 7.52±0.17 | 7.51±0.17 | 8.81±0.15 | 4.99±0.11 | 10.43±0.18 |
| HR (p+f) | 55° | 3% | 3.056±0.011 | 0.352±0.0079 | 0.356±0.0078 | 30° | 29.8±0.25 | 7.84±0.17 | 7.84±0.17 | 75° | 75.1±0.23 | 7.22±0.16 | 7.22±0.17 | 8.79±0.15 | 4.74±0.11 | 10.00±0.17 |
| HR (p+f) | 58° | 3% | 3.029±0.011 | 0.353±0.0079 | 0.354±0.0076 | 30° | 29.6±0.25 | 7.78±0.17 | 7.79±0.17 | 75° | 75.0±0.22 | 7.11±0.16 | 7.11±0.16 | 8.60±0.15 | 4.58±0.10 | 9.91±0.16 |
| HR (p+f) | 60° | 3% | 3.031±0.011 | 0.351±0.0079 | 0.352±0.0083 | 30° | 29.4±0.24 | 7.64±0.17 | 7.66±0.19 | 75° | 74.9±0.22 | 6.99±0.15 | 6.99±0.15 | 8.60±0.15 | 4.63±0.10 | 9.76±0.17 |
| HR (p&a+f) | 30° | 3% | 3.070±0.014 | 0.431±0.0096 | 0.436±0.0094 | 30° | 29.2±0.30 | 9.5±0.21 | 9.5±0.20 | 75° | 75.3±0.29 | 9.0±0.20 | 9.0±0.22 | 10.83±0.19 | 5.88±0.13 | 12.3±0.20 |
| HR (p&a+f) | 40° | 3% | 3.049±0.012 | 0.386±0.0086 | 0.389±0.0090 | 30° | 30.0±0.26 | 8.34±0.19 | 8.34±0.18 | 75° | 75.2±0.24 | 7.61±0.17 | 7.61±0.17 | 9.39±0.16 | 4.94±0.11 | 10.61±0.17 |
| HR (p&a+f) | 50° | 3% | 3.038±0.011 | 0.342±0.0076 | 0.344±0.0080 | 30° | 29.5±0.23 | 7.23±0.16 | 7.24±0.18 | 75° | 75.1±0.21 | 6.52±0.15 | 6.52±0.17 | 8.06±0.14 | 4.38±0.098 | 9.17±0.16 |
| HR (p&a+f) | 55° | 3% | 3.041±0.0099 | 0.313±0.0070 | 0.316±0.0070 | 30° | 29.8±0.22 | 7.04±0.16 | 7.04±0.15 | 75° | 75.0±0.20 | 6.38±0.14 | 6.38±0.15 | 7.91±0.13 | 4.14±0.093 | 8.93±0.14 |
| HR (p&a+f) | 58° | 3% | 3.018±0.010 | 0.315±0.0071 | 0.316±0.0069 | 30° | 29.7±0.22 | 6.80±0.15 | 6.80±0.15 | 75° | 75.0±0.20 | 6.32±0.14 | 6.32±0.14 | 7.72±0.13 | 4.08±0.091 | 8.73±0.14 |
| HR (p&a+f) | 60° | 3% | 3.020±0.010 | 0.315±0.0071 | 0.316±0.0071 | 30° | 29.6±0.22 | 6.86±0.15 | 6.87±0.16 | 75° | 74.7±0.20 | 6.27±0.14 | 6.28±0.14 | 7.76±0.13 | 4.05±0.091 | 8.76±0.15 |

**Table C.11:** Tabulated data for Figures 5.19 and 6.27: $\beta = 49°$, $\vartheta_{max} = 60°$, $N = 10^6$, $D = 3\%$, $\delta_{dipole} = 30°$, $\alpha_{dipole} = 75°$

| Method | $\Delta$ | $R_{\text{Rayl.}}$ True | Sample mean | Sample std. dev. | $q$ | $\alpha$ True | Sample mean | Sample std. dev. | $q$ |
|---|---|---|---|---|---|---|---|---|---|
| Rayl. t.b.w. | 0° | 1.81856% | 1.828 ± 0.0044 | 0.139 ± 0.0031 | 0.139 ± 0.0030 | 75° | 75.01 ± 0.15 | 4.61 ± 0.10 | 4.61 ± 0.11 |
| Rayl. t.b.w. | 0.1° | 1.81856% | 1.830 ± 0.0044 | 0.139 ± 0.0031 | 0.139 ± 0.0030 | 75° | 75.11 ± 0.14 | 4.46 ± 0.10 | 4.46 ± 0.10 |
| Rayl. t.b.w. | 0.3° | 1.81856% | 1.820 ± 0.0045 | 0.142 ± 0.0032 | 0.142 ± 0.0032 | 75° | 75.11 ± 0.14 | 4.39 ± 0.098 | 4.39 ± 0.093 |
| Rayl. t.b.w. | 1° | 1.81856% | 1.822 ± 0.0045 | 0.141 ± 0.0032 | 0.141 ± 0.0031 | 75° | 74.98 ± 0.14 | 4.36 ± 0.098 | 4.36 ± 0.098 |
| Rayl. t.b.w. | 3° | 1.81856% | 1.826 ± 0.0043 | 0.135 ± 0.0030 | 0.136 ± 0.0031 | 75° | 74.94 ± 0.15 | 4.64 ± 0.10 | 4.64 ± 0.10 |
| Rayl. | 0° | 1.81856% | 1.829 ± 0.0044 | 0.139 ± 0.0031 | 0.139 ± 0.0030 | 75° | 75.02 ± 0.15 | 4.60 ± 0.10 | 4.59 ± 0.11 |
| Rayl. | 0.1° | 1.81856% | 1.829 ± 0.0044 | 0.139 ± 0.0031 | 0.139 ± 0.0029 | 75° | 75.11 ± 0.14 | 4.46 ± 0.10 | 4.46 ± 0.10 |
| Rayl. | 0.3° | 1.81856% | 1.820 ± 0.0045 | 0.142 ± 0.0032 | 0.142 ± 0.0032 | 75° | 75.10 ± 0.14 | 4.39 ± 0.098 | 4.39 ± 0.093 |
| Rayl. | 1° | 1.81856% | 1.822 ± 0.0045 | 0.141 ± 0.0032 | 0.141 ± 0.0031 | 75° | 74.98 ± 0.14 | 4.36 ± 0.098 | 4.36 ± 0.099 |
| Rayl. | 3° | 1.81856% | 1.826 ± 0.0043 | 0.135 ± 0.0030 | 0.136 ± 0.0031 | 75° | 74.95 ± 0.15 | 4.65 ± 0.10 | 4.64 ± 0.10 |

**Table C.12:** Tabulated data for Figure 6.1: $\beta = 49°$, $\vartheta_{\max} = 60°$, $N = 10^6$, $D = 3\%$, $\delta_{\text{dipole}} = 30°$, $\alpha_{\text{dipole}} = 75°$

| Method | $A_{\text{wea.}}$ | $R_{\text{Rayl.}}$ True | Sample mean | Sample std. dev. | $q$ | $\alpha$ True | Sample mean | Sample std. dev. | $q$ |
|---|---|---|---|---|---|---|---|---|---|
| Rayl. t.b.w. | 0% | 1.81856% | 1.828 ± 0.0044 | 0.139 ± 0.0031 | 0.139 ± 0.0030 | 75° | 75.01 ± 0.15 | 4.61 ± 0.10 | 4.61 ± 0.11 |
| Rayl. t.b.w. | 0.1% | 1.81856% | 1.889 ± 0.0046 | 0.146 ± 0.0033 | 0.162 ± 0.0036 | 75° | 75.32 ± 0.14 | 4.52 ± 0.10 | 4.53 ± 0.099 |
| Rayl. t.b.w. | 0.3% | 1.81856% | 1.999 ± 0.0046 | 0.144 ± 0.0032 | 0.231 ± 0.0041 | 75° | 76.56 ± 0.13 | 4.09 ± 0.091 | 4.37 ± 0.097 |
| Rayl. t.b.w. | 1% | 1.81856% | 2.444 ± 0.0045 | 0.143 ± 0.0032 | 0.641 ± 0.0045 | 75° | 78.80 ± 0.11 | 3.39 ± 0.076 | 5.09 ± 0.096 |
| Rayl. t.b.w. | 3% | 1.81856% | 3.691 ± 0.0044 | 0.139 ± 0.0031 | 1.878 ± 0.0044 | 75° | 82.63 ± 0.071 | 2.25 ± 0.050 | 7.95 ± 0.070 |
| Rayl. t.b.w. | 10% | 1.81856% | 8.115 ± 0.0044 | 0.139 ± 0.0031 | 6.298 ± 0.0044 | 75° | 86.64 ± 0.031 | 0.98 ± 0.022 | 11.68 ± 0.031 |
| Rayl. | 0% | 1.81856% | 1.829 ± 0.0044 | 0.139 ± 0.0031 | 0.139 ± 0.0030 | 75° | 75.02 ± 0.15 | 4.60 ± 0.10 | 4.59 ± 0.11 |
| Rayl. | 0.1% | 1.81856% | 1.889 ± 0.0046 | 0.146 ± 0.0033 | 0.162 ± 0.0036 | 75° | 75.30 ± 0.14 | 4.50 ± 0.10 | 4.51 ± 0.099 |
| Rayl. | 0.3% | 1.81856% | 2.000 ± 0.0046 | 0.144 ± 0.0032 | 0.232 ± 0.0042 | 75° | 76.52 ± 0.13 | 4.08 ± 0.091 | 4.35 ± 0.096 |
| Rayl. | 1% | 1.81856% | 2.447 ± 0.0045 | 0.143 ± 0.0032 | 0.644 ± 0.0045 | 75° | 78.69 ± 0.11 | 3.39 ± 0.076 | 5.01 ± 0.096 |
| Rayl. | 3% | 1.81856% | 3.699 ± 0.0044 | 0.139 ± 0.0031 | 1.885 ± 0.0044 | 75° | 82.41 ± 0.071 | 2.24 ± 0.050 | 7.74 ± 0.070 |
| Rayl. | 10% | 1.81856% | 8.136 ± 0.0044 | 0.139 ± 0.0031 | 6.319 ± 0.0044 | 75° | 86.29 ± 0.031 | 0.98 ± 0.022 | 11.34 ± 0.031 |

**Table C.13:** Tabulated data for Figure 6.2: $\beta = 49°$, $\vartheta_{\max} = 60°$, $N = 10^6$, $D = 3\%$, $\delta_{\text{dipole}} = 30°$, $\alpha_{\text{dipole}} = 75°$

| Method | $\vartheta_{f.e.}$ | $R_{\text{Rayl.}}$ True | Sample mean | Sample std. dev. | $q$ | $\alpha$ True | Sample mean | Sample std. dev. | $q$ |
|---|---|---|---|---|---|---|---|---|---|
| Rayl. t.b.w. | 30° | 1.81856% | 1.735 ± 0.0044 | 0.138 ± 0.0031 | 0.162 ± 0.0035 | 75° | 74.99 ± 0.15 | 4.81 ± 0.11 | 4.81 ± 0.11 |
| Rayl. t.b.w. | 40° | 1.81856% | 1.749 ± 0.0045 | 0.142 ± 0.0032 | 0.158 ± 0.0033 | 75° | 75.09 ± 0.15 | 4.71 ± 0.11 | 4.71 ± 0.10 |
| Rayl. t.b.w. | 50° | 1.81856% | 1.786 ± 0.0045 | 0.141 ± 0.0032 | 0.145 ± 0.0031 | 75° | 75.11 ± 0.14 | 4.51 ± 0.10 | 4.51 ± 0.10 |
| Rayl. t.b.w. | 55° | 1.81856% | 1.804 ± 0.0044 | 0.139 ± 0.0031 | 0.140 ± 0.0033 | 75° | 74.95 ± 0.14 | 4.55 ± 0.10 | 4.55 ± 0.10 |
| Rayl. t.b.w. | 58° | 1.81856% | 1.821 ± 0.0042 | 0.133 ± 0.0030 | 0.133 ± 0.0029 | 75° | 74.92 ± 0.15 | 4.60 ± 0.10 | 4.60 ± 0.11 |
| Rayl. t.b.w. | 60° | 1.81856% | 1.828 ± 0.0044 | 0.139 ± 0.0031 | 0.139 ± 0.0030 | 75° | 75.01 ± 0.15 | 4.61 ± 0.10 | 4.61 ± 0.11 |
| Rayl. | 30° | 1.81856% | 2.093 ± 0.0045 | 0.143 ± 0.0032 | 0.309 ± 0.0043 | 75° | 125.98 ± 0.12 | 3.83 ± 0.086 | 51.12 ± 0.12 |
| Rayl. | 40° | 1.81856% | 1.866 ± 0.0045 | 0.141 ± 0.0032 | 0.149 ± 0.0033 | 75° | 114.20 ± 0.14 | 4.43 ± 0.099 | 39.45 ± 0.14 |
| Rayl. | 50° | 1.81856% | 1.734 ± 0.0045 | 0.141 ± 0.0032 | 0.165 ± 0.0034 | 75° | 92.79 ± 0.15 | 4.63 ± 0.10 | 18.38 ± 0.14 |
| Rayl. | 55° | 1.81856% | 1.763 ± 0.0044 | 0.139 ± 0.0031 | 0.150 ± 0.0034 | 75° | 81.86 ± 0.15 | 4.65 ± 0.10 | 8.28 ± 0.14 |
| Rayl. | 58° | 1.81856% | 1.808 ± 0.0042 | 0.133 ± 0.0030 | 0.133 ± 0.0029 | 75° | 76.60 ± 0.15 | 4.64 ± 0.10 | 4.90 ± 0.12 |
| Rayl. | 60° | 1.81856% | 1.829 ± 0.0044 | 0.139 ± 0.0031 | 0.139 ± 0.0030 | 75° | 75.02 ± 0.15 | 4.60 ± 0.10 | 4.59 ± 0.11 |

**Table C.14:** Tabulated data for Figure 6.3: $\beta = 49°$, $\vartheta_{\max} = 60°$, $N = 10^6$, $D = 3\%$, $\delta_{\text{dipole}} = 30°$, $\alpha_{\text{dipole}} = 75°$

| Method | $\theta_{f.e.}$ | True | R Sample mean | R Sample std. dev. | R q | True | δ Sample mean | δ Sample std. dev. | δ q | True | α Sample mean | α Sample std. dev. | α q | Δ(δ,α) Sample mean | Δ(δ,α) Sample std. dev. | Δ(δ,α) q |
|---|---|---|---|---|---|---|---|---|---|---|---|---|---|---|---|---|
| Rayl. | 30° | | | | | | | | | 75° | 125.98 ± 0.12 | 3.83 ± 0.086 | 51.12 ± 0.12 | | | |
| Rayl. | 40° | | | | | | | | | 75° | 114.20 ± 0.14 | 4.43 ± 0.099 | 39.45 ± 0.14 | | | |
| Rayl. | 50° | | | | | | | | | 75° | 92.79 ± 0.15 | 4.65 ± 0.10 | 18.38 ± 0.14 | | | |
| Rayl. | 55° | | | | | | | | | 75° | 81.86 ± 0.15 | 4.64 ± 0.10 | 8.28 ± 0.14 | | | |
| Rayl. | 58° | | | | | | | | | 75° | 76.60 ± 0.15 | 4.90 ± 0.12 | 4.90 ± 0.12 | | | |
| Rayl. | 60° | | | | | | | | | 75° | 75.02 ± 0.15 | 4.60 ± 0.10 | 4.59 ± 0.11 | | | |
| Rayl. t.b.w | 30° | | | | | | | | | 75° | 74.99 ± 0.15 | 4.81 ± 0.11 | 4.81 ± 0.11 | | | |
| Rayl. t.b.w | 40° | | | | | | | | | 75° | 75.09 ± 0.15 | 4.71 ± 0.11 | 4.71 ± 0.10 | | | |
| Rayl. t.b.w | 50° | | | | | | | | | 75° | 75.11 ± 0.14 | 4.51 ± 0.10 | 4.51 ± 0.10 | | | |
| Rayl. t.b.w | 55° | | | | | | | | | 75° | 74.95 ± 0.14 | 4.55 ± 0.10 | 4.60 ± 0.11 | | | |
| Rayl. t.b.w | 58° | | | | | | | | | 75° | 74.92 ± 0.15 | 4.60 ± 0.10 | 4.60 ± 0.11 | | | |
| Rayl. t.b.w | 60° | | | | | | | | | 75° | 75.01 ± 0.15 | 4.61 ± 0.10 | 4.61 ± 0.11 | | | |
| SAP | 30° | 3% | 681.69 ± 0.16 | 5.00 ± 0.11 | 678.71 ± 0.16 | 30° | 89.3035 ± 0.0017 | 0.0533 ± 0.0012 | 59.3036 ± 0.0017 | 75° | 110.02 ± 0.14 | 4.45 ± 0.099 | 35.30 ± 0.14 | 59.4323 ± 0.0017 | 0.0524 ± 0.0012 | 59.4323 ± 0.0017 |
| SAP | 40° | 3% | 307.00 ± 0.12 | 3.83 ± 0.086 | 304.02 ± 0.12 | 30° | 89.072 ± 0.0025 | 0.0775 ± 0.0017 | 59.072 ± 0.0025 | 75° | 98.78 ± 0.15 | 4.76 ± 0.11 | 24.25 ± 0.15 | 59.155 ± 0.0024 | 0.0771 ± 0.0017 | 59.155 ± 0.0024 |
| SAP | 50° | 3% | 112.79 ± 0.034 | 1.09 ± 0.024 | 109.79 ± 0.034 | 30° | 88.263 ± 0.0047 | 0.148 ± 0.0033 | 58.263 ± 0.0047 | 75° | 85.37 ± 0.15 | 4.71 ± 0.11 | 11.39 ± 0.13 | 58.298 ± 0.0047 | 0.148 ± 0.0033 | 58.298 ± 0.0047 |
| SAP | 55° | 3% | 46.577 ± 0.017 | 0.539 ± 0.012 | 43.580 ± 0.017 | 30° | 86.394 ± 0.0093 | 0.294 ± 0.0066 | 56.393 ± 0.0093 | 75° | 79.22 ± 0.16 | 5.08 ± 0.11 | 6.60 ± 0.13 | 56.419 ± 0.0094 | 0.295 ± 0.0066 | 56.420 ± 0.0094 |
| SAP | 58° | 3% | 14.284 ± 0.015 | 0.478 ± 0.011 | 11.294 ± 0.015 | 30° | 79.07 ± 0.031 | 0.97 ± 0.022 | 49.08 ± 0.031 | 75° | 75.89 ± 0.16 | 5.12 ± 0.11 | 5.19 ± 0.12 | 49.13 ± 0.031 | 0.98 ± 0.022 | 49.13 ± 0.031 |
| SAP | 60° | 3% | 3.011 ± 0.0098 | 0.310 ± 0.0069 | 0.310 ± 0.0074 | 30° | 28.3 ± 0.27 | 8.39 ± 0.19 | 8.6 ± 0.20 | 75° | 75.07 ± 0.18 | 5.56 ± 0.12 | 5.56 ± 0.13 | 8.51 ± 0.16 | 4.92 ± 0.11 | 9.83 ± 0.18 |
| mSAP d.b.w | 30° | 3% | 243.24 ± 0.043 | 1.36 ± 0.030 | 240.25 ± 0.043 | 30° | 88.584 ± 0.0032 | 0.101 ± 0.0023 | 58.584 ± 0.0032 | 75° | 115.66 ± 0.13 | 4.12 ± 0.092 | 40.87 ± 0.13 | 58.933 ± 0.0031 | 0.099 ± 0.0022 | 58.933 ± 0.0031 |
| mSAP d.b.w | 40° | 3% | 122.32 ± 0.025 | 0.792 ± 0.018 | 119.32 ± 0.025 | 30° | 88.081 ± 0.0047 | 0.147 ± 0.0033 | 58.082 ± 0.0047 | 75° | 103.87 ± 0.14 | 4.43 ± 0.099 | 29.21 ± 0.14 | 58.329 ± 0.0047 | 0.147 ± 0.0033 | 58.330 ± 0.0047 |
| mSAP d.b.w | 50° | 3% | 43.896 ± 0.015 | 0.469 ± 0.010 | 40.899 ± 0.015 | 30° | 86.036 ± 0.0097 | 0.307 ± 0.0069 | 56.037 ± 0.0097 | 75° | 88.16 ± 0.14 | 4.34 ± 0.097 | 13.85 ± 0.13 | 56.156 ± 0.0097 | 0.307 ± 0.0069 | 56.157 ± 0.0097 |
| mSAP d.b.w | 55° | 3% | 17.220 ± 0.011 | 0.360 ± 0.0081 | 14.224 ± 0.011 | 30° | 80.84 ± 0.022 | 0.68 ± 0.015 | 50.84 ± 0.022 | 75° | 80.29 ± 0.14 | 4.39 ± 0.098 | 6.88 ± 0.12 | 50.91 ± 0.022 | 0.684 ± 0.015 | 50.91 ± 0.022 |
| mSAP d.b.w | 58° | 3% | 5.827 ± 0.010 | 0.327 ± 0.0073 | 2.846 ± 0.010 | 30° | 63.02 ± 0.071 | 2.25 ± 0.050 | 33.09 ± 0.070 | 75° | 76.24 ± 0.14 | 4.32 ± 0.097 | 4.49 ± 0.11 | 33.14 ± 0.071 | 2.25 ± 0.050 | 33.22 ± 0.071 |
| mSAP d.b.w | 60° | 3% | 3.031 ± 0.0075 | 0.237 ± 0.0053 | 0.239 ± 0.0054 | 30° | 29.79 ± 0.19 | 5.90 ± 0.13 | 5.90 ± 0.12 | 75° | 74.99 ± 0.14 | 4.34 ± 0.097 | 4.33 ± 0.10 | 6.13 ± 0.11 | 3.36 ± 0.075 | 6.99 ± 0.12 |
| mSAP t.b.w | 30° | 3% | 243.24 ± 0.043 | 1.36 ± 0.030 | 240.24 ± 0.043 | 30° | 88.695 ± 0.0031 | 0.098 ± 0.0022 | 58.695 ± 0.0031 | 75° | 75.07 ± 0.15 | 4.60 ± 0.10 | 4.60 ± 0.11 | 58.699 ± 0.0031 | 0.099 ± 0.0022 | 58.699 ± 0.0031 |
| mSAP t.b.w | 40° | 3% | 122.32 ± 0.025 | 0.793 ± 0.018 | 119.32 ± 0.025 | 30° | 88.089 ± 0.0047 | 0.147 ± 0.0033 | 58.089 ± 0.0047 | 75° | 75.11 ± 0.14 | 4.47 ± 0.099 | 4.47 ± 0.099 | 58.095 ± 0.0047 | 0.147 ± 0.0033 | 58.095 ± 0.0047 |
| mSAP t.b.w | 50° | 3% | 43.899 ± 0.015 | 0.468 ± 0.010 | 40.902 ± 0.015 | 30° | 85.915 ± 0.0097 | 0.307 ± 0.0069 | 55.915 ± 0.0097 | 75° | 74.97 ± 0.13 | 4.19 ± 0.095 | 4.19 ± 0.095 | 55.926 ± 0.0097 | 0.307 ± 0.0069 | 55.927 ± 0.0097 |
| mSAP t.b.w | 55° | 3% | 17.227 ± 0.011 | 0.361 ± 0.0081 | 14.231 ± 0.011 | 30° | 80.67 ± 0.022 | 0.683 ± 0.015 | 50.67 ± 0.022 | 75° | 74.97 ± 0.14 | 4.33 ± 0.096 | 4.33 ± 0.096 | 50.69 ± 0.022 | 0.685 ± 0.015 | 50.70 ± 0.022 |
| mSAP t.b.w | 58° | 3% | 5.834 ± 0.010 | 0.328 ± 0.0073 | 2.853 ± 0.010 | 30° | 62.89 ± 0.071 | 2.25 ± 0.050 | 32.96 ± 0.071 | 75° | 74.91 ± 0.14 | 4.29 ± 0.096 | 4.29 ± 0.10 | 33.00 ± 0.071 | 2.26 ± 0.050 | 33.08 ± 0.071 |
| mSAP t.b.w | 60° | 3% | 3.030 ± 0.0075 | 0.238 ± 0.0053 | 0.240 ± 0.0054 | 30° | 29.79 ± 0.19 | 5.91 ± 0.13 | 5.91 ± 0.13 | 75° | 74.98 ± 0.14 | 4.35 ± 0.097 | 4.35 ± 0.10 | 6.14 ± 0.11 | 3.37 ± 0.075 | 7.00 ± 0.12 |
| MP | 30° | 3% | 243.70 ± 0.043 | 1.37 ± 0.031 | 240.70 ± 0.043 | 30° | 88.518 ± 0.0032 | 0.101 ± 0.0023 | 58.518 ± 0.0032 | 75° | 121.56 ± 0.12 | 3.90 ± 0.087 | 46.73 ± 0.12 | 58.989 ± 0.0031 | 0.099 ± 0.0022 | 58.990 ± 0.0031 |
| MP | 40° | 3% | 122.46 ± 0.025 | 0.793 ± 0.018 | 119.46 ± 0.025 | 30° | 88.051 ± 0.0047 | 0.147 ± 0.0033 | 58.051 ± 0.0047 | 75° | 108.37 ± 0.14 | 4.36 ± 0.098 | 33.65 ± 0.14 | 58.383 ± 0.0047 | 0.147 ± 0.0033 | 58.383 ± 0.0047 |
| MP | 50° | 3% | 43.922 ± 0.015 | 0.468 ± 0.010 | 40.924 ± 0.015 | 30° | 86.051 ± 0.0097 | 0.307 ± 0.0069 | 56.052 ± 0.0097 | 75° | 90.28 ± 0.14 | 4.36 ± 0.098 | 15.89 ± 0.13 | 56.208 ± 0.0097 | 0.307 ± 0.0069 | 56.209 ± 0.0097 |
| MP | 55° | 3% | 17.224 ± 0.011 | 0.360 ± 0.0080 | 14.229 ± 0.011 | 30° | 80.87 ± 0.022 | 0.68 ± 0.015 | 50.88 ± 0.022 | 75° | 81.11 ± 0.14 | 4.40 ± 0.099 | 7.53 ± 0.13 | 50.96 ± 0.022 | 0.684 ± 0.015 | 50.96 ± 0.022 |
| MP | 58° | 3% | 5.827 ± 0.010 | 0.326 ± 0.0073 | 2.846 ± 0.010 | 30° | 63.05 ± 0.071 | 2.25 ± 0.050 | 33.12 ± 0.070 | 75° | 76.43 ± 0.14 | 4.32 ± 0.097 | 4.55 ± 0.11 | 33.18 ± 0.071 | 2.25 ± 0.050 | 33.25 ± 0.071 |
| MP | 60° | 3% | 3.031 ± 0.0075 | 0.237 ± 0.0053 | 0.239 ± 0.0054 | 30° | 29.79 ± 0.19 | 5.90 ± 0.13 | 5.90 ± 0.12 | 75° | 74.98 ± 0.14 | 4.34 ± 0.097 | 4.34 ± 0.10 | 6.13 ± 0.11 | 3.36 ± 0.075 | 6.99 ± 0.12 |

**Table C.15:** Tabulated data for Figure 6.5: $\beta = 49°$, $\vartheta_{max} = 60°$, $N = 10^6$, $D = 3\%$, $\delta_{\mathrm{dipole}} = 30°$, $\alpha_{\mathrm{dipole}} = 75°$

# List of Figures

# List of Tables

# Bibliography

[Abb08a]   R. Abbasi et al. (HiRes Collaboration), *Observation of the GZK cutoff by the HiRes experiment*, Phys. Rev. Lett. **100** (2008), 101101, astro-ph/0703099.

[Abb08b]   R. U. Abbasi et al., *Search for Correlations between HiRes Stereo Events and Active Galactic Nuclei*, Astropart. Phys. **30** (2008), 175–179, 0804.0382.

[Abd09]    A. A. Abdo et al., *The Large Scale Cosmic-Ray Anisotropy as Observed with Milagro*, Astrophys. J. **698** (2009), 2121–2130, 0806.2293.

[Abr04]    J. Abraham et al. (Pierre Auger Collaboration), *Properties and performance of the prototype instrument for the Pierre Auger Observatory*, Nucl. Instrum. Meth. **A523** (2004), 50–95.

[Abr08a]   J. Abraham et al. (Pierre Auger Collaboration), *Correlation of the highest-energy cosmic rays with the positions of nearby active galactic nuclei*, Astropart. Phys. **29** (2008), 188–204, 0712.2843.

[Abr08b]   J. Abraham et al. (Pierre Auger Collaboration), *Observation of the suppression of the flux of cosmic rays above $4 \times 10^{19} eV$*, Phys. Rev. Lett. **101** (2008), 061101, 0806.4302.

[Abr09]    J. Abraham et al. (Pierre Auger Collaboration), *Atmospheric effects on extensive air showers observed with the Surface Detector of the Pierre Auger Observatory*, Astropart. Phys. **32** (2009), 89, 0906.5497.

[Agl96]    M. Aglietta et al. (EAS-TOP Collaboration), *A measurement of the solar and sidereal cosmic ray anisotropy at E(0) approx. $10^{14}$ eV*, Astrophys. J. **470** (1996), 501–505.

[Ame05]    M. Amenomori et al. (Tibet AS Gamma Collaboration), *Large-scale sidereal anisotropy of galactic cosmic-ray intensity observed by the Tibet Air Shower Array*, Astrophys. J. **626** (2005), L29–L32, astro-ph/0505114.

[Ant03]    T. Antoni et al. (KASCADE Collaboration), *The Cosmic ray experiment KASCADE*, Nucl. Instrum. Meth. **A513** (2003), 490–510.

[Ant04]    T. Antoni et al. (The KASCADE Collaboration), *Large scale cosmic-ray anisotropy with KASCADE*, Astrophys. J. **604** (2004), 687–692, astro-ph/0312375.

[Ant05]    T. Antoni et al. (The KASCADE Collaboration), *KASCADE measurements of energy spectra for elemental groups of cosmic rays: Results and open problems*, Astropart. Phys. **24** (2005), 1–25, astro-ph/0505413.

[Arm08]   E. Armengaud (Pierre Auger Collaboration), *Search for large-scale anisotropies with the Auger Observatory*, Proceedings of the 30th International Cosmic Ray Conference (R. Caballero, J. C. D'Olivo, G. Medina-Tanco, L. Nellen, F. A. Sánchez, and J. F. Valdés-Galicia, eds.), Universidad Nacional Autónoma de México, Mexico City, Mexico, 2008, vol. 4 (HE part 1), pp. 555–558.

[Aub05]   J. Aublin and E. Parizot, *Generalised 3D-reconstruction method of a dipole anisotropy in cosmic-ray distributions*, Astronomy & Astrophysics **441** (2005), 407–415, astro-ph/0504575.

[Aug07]   Pierre Auger Collaboration, *Correlation of the Highest-Energy Cosmic Rays with Nearby Extragalactic Objects*, Science **318** (2007), 938–943.

[Bat09]   E. Battaner, J. Castellano, and M. Masip, *Galactic magnetic fields and the large-scale anisotropy at MILAGRO*, Astrophys. J. **703** (2009), L90–L93, 0907.2889.

[Bec09]   R. Beck, *Galactic and Extragalactic Magnetic Fields*, AIP Conf. Proc. **1085** (2009), 83–96, 0810.2923.

[Ber06]   V. S. Berezinsky, S. I. Grigoreva, and B. I. Hnatyk, *Extragalactic UHE proton spectrum and prediction of flux of iron-nuclei at $10^8$ GeV – $10^9$ GeV*, Nucl. Phys. Proc. Suppl. **151** (2006), 497–500.

[Bie97]   P. L. Biermann, *The origin of the highest energy cosmic rays*, J. Phys. **G23** (1997), 1–27.

[Bil08]   P. Billoir and O. Deligny, *Estimates of multipolar coefficients to search for cosmic ray anisotropies with non-uniform or partial sky coverage*, JCAP **0802** (2008), 009, 0710.2290.

[Bir94]   D. J. Bird et al. (HIRES Collaboration), *The Cosmic ray energy spectrum observed by the Fly's Eye*, Astrophys. J. **424** (1994), 491–502.

[Blu09]   J. Bluemer, R. Engel, and J. R. Hoerandel, *Cosmic Rays from the Knee to the Highest Energies*, Prog. Part. Nucl. Phys. **63** (2009), 293–338, 0904.0725.

[Bon07]   R. Bonino, *Study of the Ultra High Energy Cosmic Rays Arrival Directions*, PhD thesis, Università degli Studi di Torino, 2007.

[Bon09]   C. Bonifazi et al. (Pierre Auger Collaboration), *The angular resolution of the Pierre Auger Observatory*, Nucl. Phys. Proc. Suppl. **190** (2009), 20–25, 0901.3138.

[Com1935] A. H. Compton and I. A. Getting, *An Apparent Effect of Galactic Rotation on the Intensity of Cosmic Rays*, Phys. Rev. **47** (1935), no. 11, 817–821.

[DM03]    D. De Marco, P. Blasi, and A. V. Olinto, *On the statistical significance of the GZK feature in the spectrum of ultra high energy cosmic rays*, Astropart. Phys. **20** (2003), 53–65, astro-ph/0301497.

[Gai90]   see e.g. references in: T. K. Gaisser, *Cosmic Rays and Particle Physics*, Cambridge Univ. Press, 1990.

[Gal03]   M. Galassi, J. Davies, J. Theiler, B. Gough, G. Jungman, M. Booth, and F. Rossi, *GNU Scientific Library: Reference Manual*, Network Theory Ltd., February 2003.

[Ghi07]     P. Ghia (EAS-TOP Collaboration), *EAS-TOP: the cosmic ray anisotropy in the energy region $E_0 = 10^{14}$–$10^{15}$ eV*, Proc. 30th International Cosmic Ray Conference (ICRC 2007) (R. Caballero, J. C. D'Olivo, G. Medina-Tanco, L. Nellen, F. A. Sánchez, and J. F. Valdés-Galicia, eds.), 2007, vol. 4, pp. 51–54.

[Gre66]     K. Greisen, *End to the cosmic ray spectrum?*, Phys. Rev. Lett. **16** (1966), 748–750.

[Gru00]     see e.g. references in: C. Grupen, *Astroteilchenphysik*, Vieweg, Braunschweig/Wiesbaden, 2000.

[Gui07]     G. Guillian et al. (Super-Kamiokande Collaboration), *Observation of the anisotropy of 10-TeV primary cosmic ray nuclei flux with the Super-Kamiokande-I detector*, Phys. Rev. **D75** (2007), 062003, astro-ph/0508468.

[Han09]     J. L. Han, *Magnetic structure of our Galaxy: A review of observations*, Proceedings of the International Astronomical Union **4** (2009), no. S259, 455–466, 0901.1165.

[Hay99]     N. Hayashida et al. (AGASA Collaboration), *The anisotropy of cosmic ray arrival directions around $10^{18}$ eV*, Astropart. Phys. **10** (1999), 303–311, astro-ph/9807045.

[Hei95]     C. Heiles, *The Galactic B-Field (GBF)*, The Physics of the Interstellar Medium and Intergalactic Medium (A. Ferrara, C. F. McKee, C. Heiles, & P. R. Shapiro, ed.), 1995, Astronomical Society of the Pacific Conference Series, vol. 80, pp. 507–+.

[Hei96]     C. Heiles, *The Local Direction and Curvature of the Galactic Magnetic Field Derived from Starlight Polarization*, Astrophys. J. **462** (1996), 316–+.

[Hes1912]   V. F. Hess, *Über Beobachtungen der durchdringenden Strahlung bei sieben Freiballonfahrten*, Physik. Zeitschr. **13** (1912), 1084–1091.

[Hil84]     A. M. Hillas, *The Origin of Ultrahigh-Energy Cosmic Rays*, Ann. Rev. Astron. Astrophys. **22** (1984), 425–444.

[Hil85]     C. T. Hill and D. N. Schramm, *The Ultrahigh-Energy Cosmic Ray Spectrum*, Phys. Rev. **D31** (1985), 564.

[Hil05]     A. M. Hillas, *Can diffusive shock acceleration in supernova remnants account for high-energy galactic cosmic rays?*, J. Phys. **G31** (2005), R95–R131.

[Hoe03]     J. R. Hoerandel, *On the knee in the energy spectrum of cosmic rays*, Astropart. Phys. **19** (2003), 193–220, astro-ph/0210453.

[Hoe04]     J. R. Hoerandel, *Models of the knee in the energy spectrum of cosmic rays*, Astropart. Phys. **21** (2004), 241–265, astro-ph/0402356.

[Joh94]     N. L. Johnson, S. Kotz, and N. Balakrishnan, *Continuous Univariate Distributions, Vol. 1 (Wiley Series in Probability and Statistics)*, Wiley-Interscience, 1994.

[Lin75]     J. Linsley, *Fluctuation Effects on Directional Data*, Phys. Rev. Lett. **34** (1975), no. 24, 1530–1533.

[Mai04]     G. Maier, *Search for cosmic-ray anisotropy with KASCADE. (In German)*, FZKA-6951.

[Mol1805]   C. Mollweide, *Über die vom Prof. Schmidt in Giessen in der zweyten Abteilung seines Handbuchs der Naturlehre S. 595 angegebene Projection der Halbkugelfläche*, Zach's Monatliche Correspondenz **13** (1805), 152–163.

[Mol05]     S. Mollerach and E. Roulet, *A new method to search for a cosmic ray dipole anisotropy*, JCAP **0508** (2005), 004, astro-ph/0504630.

[Ove04]     S. Over, *Development and Commissioning of Data Acquisition Systems for the KASCADE-Grande Experiment*, diploma thesis, University of Siegen, 2004.

[Rao98]     see e.g. references in: M. V. S. Rao and B. V. Sreekantan, *Extensive Air Showers*, World Scientific Publishing, 1998.

[Ray1880]   L. Rayleigh, *On the Resultant of a large Number of Vibrations of the same Pitch and of arbitrary Phase*, Phil. Mag. **10** (1880), 73–78.

[Shi06]     K. Shinozaki (AGASA Collaboration), *AGASA results*, Nucl. Phys. Proc. Suppl. **151** (2006), 3–10.

[Sof86]     Y. Sofue, M. Fujimoto, and R. Wielebinski, *Global structure of magnetic fields in spiral galaxies*, Ann. Rev. Astron. Astrophys. **24** (1986), 459–497.

[Som01]     P. Sommers, *Cosmic Ray Anisotropy Analysis with a Full-Sky Observatory*, Astropart. Phys. **14** (2001), 271–286, astro-ph/0004016.

[Sta97]     T. Stanev, *Ultra high energy cosmic rays and the large scale structure of the galactic magnetic field*, Astrophys. J. **479** (1997), 290–295, astro-ph/9607086.

[Ste99]     F. W. Stecker and M. H. Salamon, *Photodisintegration of ultrahigh energy cosmic rays: A new determination*, Astrophys. J. **512** (1999), 521–526, astro-ph/9808110.

[Str07]     A. W. Strong, I. V. Moskalenko, and V. S. Ptuskin, *Cosmic-ray propagation and interactions in the Galaxy*, Ann. Rev. Nucl. Part. Sci. **57** (2007), 285–327, astro-ph/0701517.

[Stu07]     M. Stuempert, *Suche nach Anisotropie in der kosmischen Strahlung mit KASCADE-Grande*, PhD thesis, Universität Karlsruhe, 2007.

[Tad06]     J. Tada et al. (LAAS Collaboration), *Analysis of cosmic ray anisotropy around 10**15-eV using network observation data of air showers*, Nucl. Phys. Proc. Suppl. **151** (2006), 485–488.

[Wib05]     T. Wibig and A. W. Wolfendale, *At what particle energy do extragalactic cosmic rays start to predominate?*, J. Phys. **G31** (2005), 255–264, astro-ph/0410624.

[Zat66]     G. T. Zatsepin and V. A. Kuzmin, *Upper limit of the spectrum of cosmic rays*, JETP Lett. **4** (1966), 78–80.

[Zir05]     V. N. Zirakashvili, *Cosmic ray anisotropy problem*, Int. J. Mod. Phys. **A20** (2005), 6858–6860.

# Acknowledgement

I want to thank everyone who made this thesis possible with their assistance and their support. I also want to thank all my friends and colleagues who made the past years as enjoyable for me as they were. If I tried to list everyone who has helped me, I am almost certain that I would forget someone important. However, some people must not go unmentioned:

My supervisor Prof. Dr. Peter Buchholz, whom I want to thank for the trust he put in me over the past years. He introduced me to the KASCADE-Grande collaboration, and allowed me to stay at the vibrant place for the research of cosmic radiation that is the Karlsruhe Institute of Technology (known as "Research Centre Karlsruhe", or "Forschungszentrum Karlsruhe", at the time I began my work).

Prof. Dr. Claus Grupen, who kindly agreed to review and evaluate this thesis.

Dr. Ralph Engel, who helped me put my work activity on the right track. The discussions I had with him were extremely fruitful and inspiring.

Dr. Wolfgang Walkowiak, for his hospitality and helpfulness when hosting me during my stays in Siegen.

Dr. Andreas Haungs and his KASCADE-Grande group in Karlsruhe, who welcomed me as an external postgraduate student in their midst. I would also like to express my gratitude for funding a number of journeys, most notably one to Turin/Italy in Summer 2009. This visit gave me the opportunity to discuss my work with Prof. Dr. Gianni Navarra, only weeks before he passed away—sadly and way too soon. He was a pioneer of cosmic ray experiments, one of the initiators of the KASCADE-Grande project, an authority in the field of cosmic ray anisotropy, and truly a source of inspiration to me and so many others. He has gone, but will never be forgotten.

I would also like to thank my proof-readers: Dr. Paul Doll, Dr. Blair Edwards, Dr. Andreas Haungs, Dr. Markus Horn, Mandy Hughes, Dan Murnaghan and Michael Wommer. They sacrificed precious time to show me what stupid mistakes I can make and how confused my scribbling can be. Their help was highly appreciated.

Thanks also to my flatmates in Karlsruhe for putting up with me (current and former, in order of appearance): Achim, Florian, Kai, Peter. (No girls this time. Not intentionally. Cf. the acknowledgement in [Ove04].)

I am looking back at eleven years of physics in my life, and I still feel nothing but awe for this great science. It deals with nothing less than how the universe works. It can explain what keeps matter together, or what makes stars explode. As interesting as the answers, are the questions that arise. And in investigating the open questions that you come across as a physicist, it teaches you how to tell the relevant from the irrelevant. It makes you develop a feeling for judging the significance of things. And it gives you the opportunity to discuss with gifted, bright people from all over the world, in schools, conferences and meetings. Now that I look forward and seek new challenges in my life, I am glad I can draw on this wealth of experience. Once again, I say thank you to each and everyone, who made this exciting time possible: professors, assistants, staff, colleagues and (fellow) students. My fond wish is, that I was able to give the tiniest of contributions to physics, for it has given so much to me.